Understanding and Optimizing Dynamics in Hyperpolarized Magnetic Resonance

by

Jacob R. Lindale

Department of Chemistry
Duke University

Date:_____

Approved:

_____

Warren S. Warren, Advisor

_____

Hashim M. Al-Hashimi

_____

Thomas Theis

_____

Kevin D. Welsher

_____

Weitao Yang

Thesis submitted in partial fulfillment of
the requirements for the degree of Doctor
of Philosophy in the Department of
Chemistry in the Graduate School
of Duke University

2021

ABSTRACT

Understanding and Optimizing Dynamics in Hyperpolarized Magnetic Resonance

by

Jacob R. Lindale

Department of Chemistry
Duke University

Date:_____

Approved:

_____

Warren S. Warren, Advisor

_____

Hashim M. Al-Hashimi

_____

Thomas Theis

_____

Kevin D. Welsher

_____

Weitao Yang

An abstract of a dissertation submitted in partial
fulfillment of the requirements for the degree
of Doctor of Philosophy in the Department of
Chemistry in the Graduate School of
Duke University

2021

Abstract

Magnetic resonance techniques are among the most powerful methods for characterization. However, they inherently suffer from an intrinsically low signal-to-noise due to the weak interaction of the nuclear spin with external magnetic fields. Hyperpolarization methods circumvent this limitation by deriving non-equilibrium spin polarization from an external source of spin order, dramatically increasing the magnetic resonance signals. Signal Amplification By Reversible Exchange, or SABRE, is a relatively new and promising method that derives spin hyperpolarization from parahydrogen, the singlet spin isomer of dihydrogen, allowing it to operate at a fraction of the cost of other hyperpolarization methods. A target molecule and parahydrogen transiently bind an organometallic complex, during which time polarization is transferred from the parahydrogen to target nuclei. The reversible nature of this interaction makes the hyperpolarization method readily scalable, giving SABRE the potential to supplant older, more expensive techniques and bring hyperpolarization technology to a broader audience.

However, the current demonstrations of SABRE generate polarizations that are about an order of magnitude away from the upper theoretical limits of the technique, and variants of this experiment have been limited in target scope by the underlying physics. To address these limitations, this dissertation returns to examine the theoretical underpinnings of SABRE, and in doing so re-interrogates the unification of chemical exchange and quantum dynamics. We derive exact formulations of the chemical exchange interaction in both the magnetic resonance limits, which is used to construct a physically exhaustive computational model for

SABRE. This model then facilitates *in silico* exploration of the system and permits us to address experimental limitations of the method. In particular, this dissertation utilizes simulations to develop and expand the capabilities of SABRE performed at arbitrarily high magnetic fields. We show that the limitations in the scope of SABRE imposed by the spin physics under these conditions may be removed, culminating in the first demonstration of simultaneous hyperpolarization of multiple components. This expansion is a key step towards translating SABRE into areas of conventional magnetic resonance such as biomolecular NMR and metabonomics. The theoretical framework presented here provides access to new routes for optimizing SABRE hyperpolarization, and we demonstrate that sequences may be developed to generate up to a five-fold increase in performance. Finally, we extend the theoretical treatment of chemical exchange within the Lindblad formalism to obtain exact master equations that are valid in any physical limit.

Table of Contents

List of Tables

List of Figures

Acknowledgements

There are numerous people that I wish to thank for supporting me throughout graduate school, and chief among them is my advisor, Dr. Warren Warren. I could not be more grateful for his patience and encouragement as I explored the phase space of my research, his instruction when I got stuck in a local minimum, and his uncanny ability to identify unproductive trajectories. I must also thank my lab mate Shannon Eriksson, who was an outstanding research partner throughout graduate school and on whose ability to think critically I could always rely. Additionally, I want to thank the entire Warren group: Dr. Johannes Colell, who trained me in running SABRE experiments when I joined, Dr. Thomas Theis, Dr. Martin Fischer, Dr. David Grass, Dr. Guannan Zhang, Dr. Zijian Zhou, Dr. Jun Jiang, Dr. Xiaomeng Jia, Dr. Xiao Ji, Xiaoqing Li, Yuheng Liao, Yue Zhou, Ge Chen, and Heidi Kastenholz. I would also like to thank the three reviewers of my dissertation, Dr. David Grass, Shannon Eriksson, and Heidi Kastenholz. I have also had the pleasure of mentoring a fantastic group of undergraduate researchers in my time at Duke, including Christian Tanner, Grayson Clark, Meghana Iragavarapu, Rishi Subrahmanyan, Tingguang Li, Liang Cheng, and Clark Eriksson. Last, but not least, this research would not have been possible without our collaboration with Dr. Steven Malcolmson and Dr. Nathan Adamson in the Department of Chemistry at Duke, who provided our lab with the necessary with catalyst to perform our research.

Chapter 1: Introduction

Nuclear magnetic resonance has been considered among the most versatile and ubiquitous techniques in the natural and physical sciences for decades[1-4]. Broadly, these techniques interrogate the quantum mechanical property of nuclear spin and its magnetic interactions. Until the advent of the laser, magnetic resonance was the height of esoteric physics[5, 6], made possible by highly developed hardware coupled with a robust theoretical formalism[7]. As a spectroscopy, nuclear magnetic resonance (NMR) is second to none in its ability to coherently control the dynamics of quantum systems[4, 8, 9]. It is the only known technique that simultaneously boasts atomic resolution and the ability to monitor molecular dynamics across nearly fifteen orders of magnitude in time[4, 10]. Furthermore, magnetic resonance imaging (MRI) is among the most powerful medical imaging modalities, which, beyond its ability to non-invasively acquire high resolution *in vivo* images, can do such things like see thought (functional MRI[11-14]) and characterize regions of cerebral ischemia (diffusion weighted imaging[15-17]), critical in the treatment of vascular occlusions (**Fig. 1**).

Despite its broad applications in virtually every field of science, nuclear magnetic resonance is fundamentally limited by low signals that arise from weak interactions of nuclear spins with external magnetic fields. The observed signal in magnetic resonance is proportional to the spin polarization P, which for a nucleus such as ^{1}H in a magnetic field B_0 is,

$$P = \tanh\left(\frac{\gamma B_0}{2k_B T}\right) \tag{1.1}$$

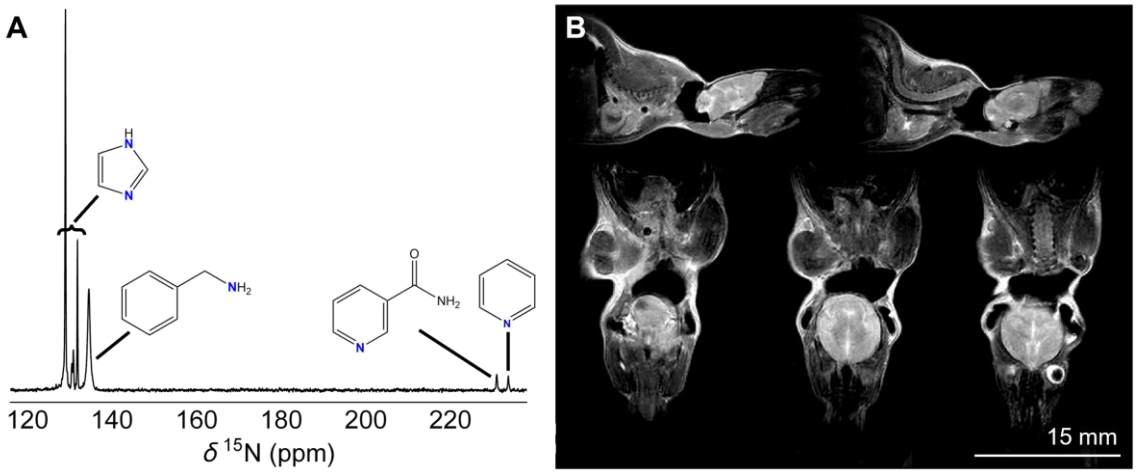

Figure 1: Nuclear magnetic resonance techniques. A. NMR spectroscopy is a powerful tool for materials characterization, as spectra are readily interpretable and can be correlated to molecular structure. Here, we show a spectrum of four different ^{15}N-labelled compounds, each having a unique signature in the spectrum. **B.** Magnetic resonance imaging (MRI) allows non-invasive *in vivo* imaging, and is an essential diagnostic clinical modality. Here, we show images of an asystolic mouse collected in a pre-clinical 1T imager.

where γ is the gyromagnetic ratio of the nucleus (its sensitivity to the magnetic field), k_B is the Boltzmann constant, and T is the temperature of the system. Equation 1.1 will be derived later from the Boltzmann distribution, but it is interesting to put the expression into context. To generate $P = 1\%$ on ^{1}H, which has the second-highest sensitivity to the magnetic field (tritium, ^{3}H, has the highest sensitivity but is only 10^{-18} abundant), requires a magnetic field of $B_0 \approx 3000\,T$ at room temperature (where the thermal energy is $k_B T \approx 207\,cm^{-1}$). For reference, the largest commercially available NMR spectrometer as of 2020[18] uses a $B_0 = 28.2\,T$ magnet, where $\gamma B_0 \approx 0.04\,cm^{-1}$ and thus $P \approx 0.01\%$. Detecting signals of nuclei like ^{15}N is even more difficult, as they only have $1/10$ the gyromagnetic ratio as ^{1}H, thus having a fraction the spin polarization, and are additionally $\sim 1/200$ as abundant. For conventional magnetic resonance, decades of engineering have been devoted to improving the sensitivity of the detection coils, such as the use of cryogenically cooled coils to reduce thermal noise. Even with state-of-the-art hardware, conventional techniques are still orders-of-magnitude removed

from the upper limit of the signals that would be possible if every spin contributed to the observable signal.

At the frontier of magnetic resonance are hyperpolarization techniques[19-52], which circumvent the inherently low signal strength by artificially inducing a large, non-equilibrium spin polarization on nuclear targets (Fig. 2A). Typically, this is done by deriving the hyperpolarized signal from a source of "spin order", which is prepared in a highly polarized state by a separate process. Under certain conditions, the source of spin order can be put into

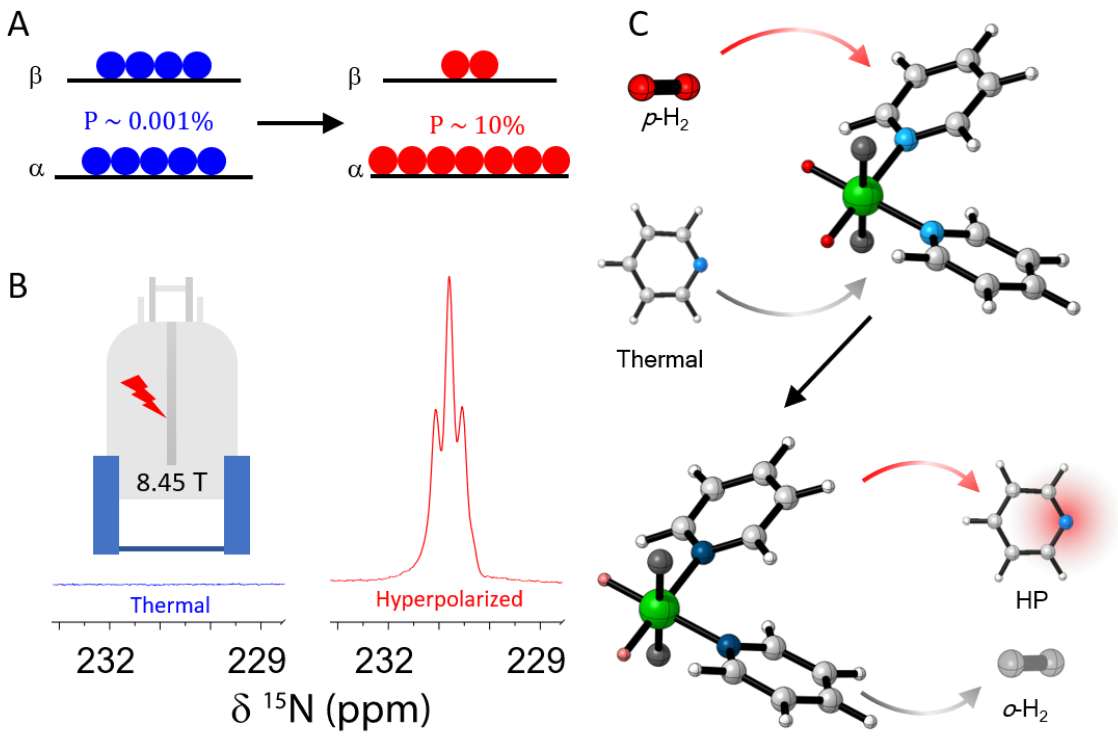

Figure 2: Hyperpolarized magnetic resonance. A. When thermally polarized at standard temperature (blue), spins nearly equally occupy the ground (α) and excited (β) spin states as the energy splitting between these states is much smaller than thermal energy ($k_B T$). Hyperpolarization aggravates this difference by deriving polarization (P) from an external source of spin order. **B.** At room temperature, signals arising from rare nuclei like ^{15}N are not detected with a single scan, even in a superconducting magnet. However, the hyperpolarized signal is clearly visible in a single scan, which was generated here using irradiation of a SABRE sample at 8.45T. **C.** SABRE generates hyperpolarization through transient interactions of parahydrogen and a substrate with an iridium catalyst. During this interaction, polarization flows to the target nuclei, after which the substrate dissociates to form hyperpolarized species in solution.

magnetic contact with the target nuclei and its polarization may be transferred to those spins, generating a hyperpolarized state. Hyperpolarized nuclei generate significantly larger NMR signals than are available under thermal conditions (Fig. 2B). The conditions under which hyperpolarization can be created are largely dependent on the source of spin order, the source complexity and its lifetime.

Dynamic Nuclear Polarization (DNP) is perhaps the most commonly encountered of the hyperpolarization methods, as the technique was first experimentally realized in the early 1950s[53-68]. This technique can be coupled with MRI to directly observe metabolic rates *in vivo*, giving clinicians a powerful tool in the detection of malignant lesions that would be difficult to demarcate in conventional MRI images[59, 69-75]. It has also been shown to couple with solid state NMR for the characterization of insensitive nuclei in materials[76, 77]. DNP derives nuclear hyperpolarization from an electron spin, which can be prepared with near unity polarization at low (1.5K) temperatures and modest (3T) magnetic fields. Polarization can be driven from the electron spin to nuclear spins in the presence of intense microwave irradiation, which is necessary as DNP-active transitions are nearly quantum-mechanically forbidden. This results in polarization being transferred to the target nuclei slowly, on the timescale of hours, and a large financial cost for the instrumentation required to manipulate the electron spin at cryogenic temperatures (the commercially available SpinLab DNP is $2.5M). For this reason, there are fewer than 50 SpinLab instruments in the world.

An alternative source of spin order is parahydrogen, the singlet (S_H^0) spin isomer of dihydrogen, as it can be prepared with modest cooling (40K) by the ton and is stable for years. The singlet state of H_2 has no angular momentum and no magnetic moment, whereas the triplet (T_H^+, T_H^0, T_H^-) states of H_2 have both angular momentum and magnetization. These states

are separated in energy by the large rotational constant of H_2, which makes it possible to enrich the parahydrogen state. Perhaps its most straightforward use is in ParaHydrogen Induced Polarization (PHIP) hyperpolarization experiments such as "Parahydrogen And Synthesis Allow Dramatically Enhanced Nuclear Alignment (PASADENA)[27, 28, 78-80], where parahydrogen is catalytically added across unsaturated bonds in organic molecules. As a hyperpolarization technique, PASADENA is limited as it often requires specialized reaction conditions and catalysts for different substrates. The substrate scope is additionally restrictive, as the experiment requires that the target has an unsaturated bond across which the parahydrogen may be added. To overcome the chemical restrictions of PHIP, the Duckett group introduced Signal Amplification By Reversible Exchange (SABRE), a non-hydrogenative PHIP variant that transiently permits magnetic contact between parahydrogen and a target ligand mediated by an iridium catalyst (Fig. 2C)[38, 81]. In this method, parahydrogen (H_2) binds the hyperpolarization catalyst and forms an iridium-dihydride (IrH_2) complex. During these transient interactions, the magnetic asymmetry induced by binding to the iridium complex allows the parahydrogen-derived hydride singlet state to be unlocked and hyperpolarization is transferred to target nuclei. This allows a more diverse target scope without chemical alteration.

SABRE has gained much attention over the last decade, as it has potential to overcome DNP as the preeminent hyperpolarization technique. In addition to having less stringent experimental conditions to generate parahydrogen, SABRE has been shown to generate polarizations exceeding 20% in less than a minute, orders of magnitude faster than DNP[49]. Furthermore, the initial setup cost for SABRE can be as low as a few hundred dollars, which is a small fraction of the cost for a commercial DNP. While the original implementation of SABRE targeted ^{1}H, work from Warren and coworkers extended SABRE to heteronuclei. In

2014, they introduced the Low Irradiation Generates Hyperpolarization Transfer for SABRE (LIGHT-SABRE) pulse sequence[52], which generates hyperpolarization directly in the NMR spectrometer using microwatt radiofrequency pulses to transfer the spin order from the parahydrogen singlet state into a magnetized state. Shortly thereafter, they also introduced the SABRE-SHEATH (SABRE in Shield Enables Alignment Transfer to Heteronuclei) experiment, which generates much larger hyperpolarization than LIGHT-SABRE using static, microTesla magnetic fields with even fewer experimental restrictions[51]. Hundreds of substrates have been hyperpolarized following these advancements, with typical polarization levels on the order of 2-5% for ^{15}N nuclei[44, 45, 48-51, 82-88]. Together, these experiments belong to the class of extended SABRE, or X-SABRE, experiments.

The original X-SABRE experiments were motivated from spin dynamics that have been understood for decades and it is beneficial to briefly introduce these concepts to frame the work presented here. We will use the LIGHT-SABRE experiment as an example, and will discuss how population flows both by coherent (quantum) interactions and by exchange (chemical) interactions to generate hyperpolarization (Fig. 3A). At the start of the experiment, the parahydrogen overpopulates a state proportional to the singlet state on the two hydrides, which is denoted as either $|S_H^0\alpha_L\rangle$ or $|S_H^0\beta_L\rangle$, which are populated nearly equally. The α_L and β_L part of these states refer to the aligned (up) spin (α_L) or anti-aligned (down) spin (β_L) states of the hyperpolarization target ligand, and the population difference between these states determines the polarization of the system. When in the NMR spectrometer, the populations are essentially locked in these states, which means that when the target dissociates, there is still essentially equal population in both $|\alpha_L\rangle$ and $|\beta_L\rangle$ and thus no hyperpolarization. However, a radiofrequency pulse with a magnitude approximately equal to the hydride-hydride coupling

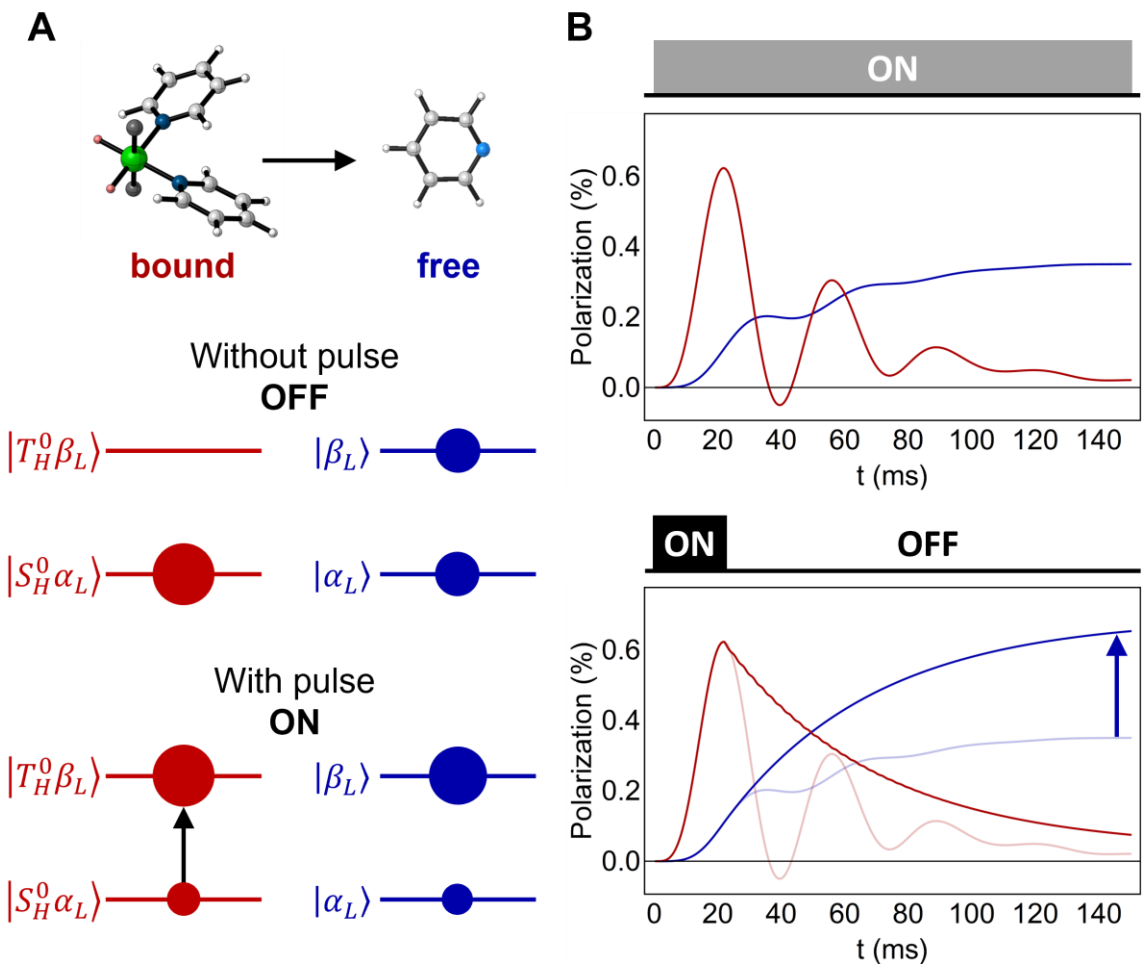

Figure 3: Coherent dynamics in the LIGHT-SABRE experiment. A. As hyperpolarization is generated on the iridium-bound species (red), it reversibly exchanges with free target (blue) in solution. In the absence of the pulse, population is locked in the original states. However, the pulse permits population transfer to a magnetized state, in this case $|T_H^0\beta_L\rangle$ that, when exchange occurs, generates hyperpolarized target in solution. **B.** (Top) The spin polarization oscillates as a result of quantum mechanical evolution in the system while exchange generates an accumulation of hyperpolarization. When continuously driving the matching condition, the resultant polarization is highly dependent on the residence time on the iridium complex as the destruction of polarization is allowed (decreasing polarization). However, by pumping the anti-crossing condition (bottom, darker lines), one can arrest the coherent dynamics and significantly improve the resultant hyperpolarization.

(μW powers) and a frequency slightly offset from the resonance frequency of the target nucleus can selectively transfer population from $|S_H^0\alpha_L\rangle \rightarrow |T_H^0\beta_L\rangle$, as shown in Fig. 3A, or can transfer population from $|S_H^0\beta_L\rangle \rightarrow |T_H^0\alpha_L\rangle$ depending on the carrier frequency of the pulse. If the $|S_H^0\alpha_L\rangle \rightarrow |T_H^0\beta_L\rangle$ transition is excited, upon exchange there will be more

population in the $|\beta_L\rangle$ state than there was in the $|\alpha_L\rangle$ state, generating hyperpolarization on the free species. The condition where population is allowed to flow between the initial and final states is referred to as a matching condition or resonance condition. Importantly, the $|S_H^0\alpha_L\rangle \rightarrow |T_H^0\beta_L\rangle$ and $|S_H^0\beta_L\rangle \rightarrow |T_H^0\alpha_L\rangle$ transitions have different matching conditions, which is what permits hyperpolarization. By holding the system at the matching condition, or in terms of the LIGHT-SABRE experiment continually irradiating the sample, one catalytically generates hyperpolarization while the targets reversibly bind the hyperpolarization catalyst, allowing for the bulk generation of hyperpolarized target in solution. Using this as the motivation, LIGHT-SABRE was shown to generate signals approximately $150\times$ the thermal ^{15}N-pyridine signal. This spin physics will be formally treated in Chapter 2.

While the initial flow of population at resonance transfers population into the magnetized state, the coherent dynamics will eventually reverse the flow of population and begin to destroy the target magnetization (Fig. 3B), which we will refer to as back-pumping. This oscillatory structure is the hallmark of coherent quantum dynamics. As exchange is occurring continuously throughout the SABRE process, the final polarization is strongly dictated by the residence time of the target on the iridium complex. For instance, if the target exchanges off the complex prior to the maximum in the coherent dynamics, then the polarization of the free species will be additive and the hyperpolarization will increase. However, if the lifetime of the target is much longer than the period of the coherent dynamics, then the resulting hyperpolarization will be largely attenuated by the back-pumping.

As the matching condition is only met when the heteronuclear target is irradiated, simply turning the pulse off after a fixed amount of time will effectively turn off the matching condition and prevent the destruction of polarization. Then, waiting for some time to permit

exchange off the catalyst can dramatically increase the resulting polarization, even though the time spent driving the transition diminished (Fig. 3B). This idea was experimentally demonstrated by comparing the resulting polarizations from the continuous LIGHT-SABRE and the pumped LIGHT-SABRE pulse sequences (Fig. 4)[89]. An approximate $2.5\times$ increase in the resulting hyperpolarization is observed when the $|S_H^0\beta_L\rangle \rightarrow |T_H^0\alpha_L\rangle$ transition is coherently pumped simply by preventing back- pumping of the system. Additionally, the coherent spin dynamics of the SABRE system were observed for the first time by scanning time that the system is at resonance, which is accomplished by changing the pulse length t_p and monitoring the resulting hyperpolarized signal. This provided access to the underling

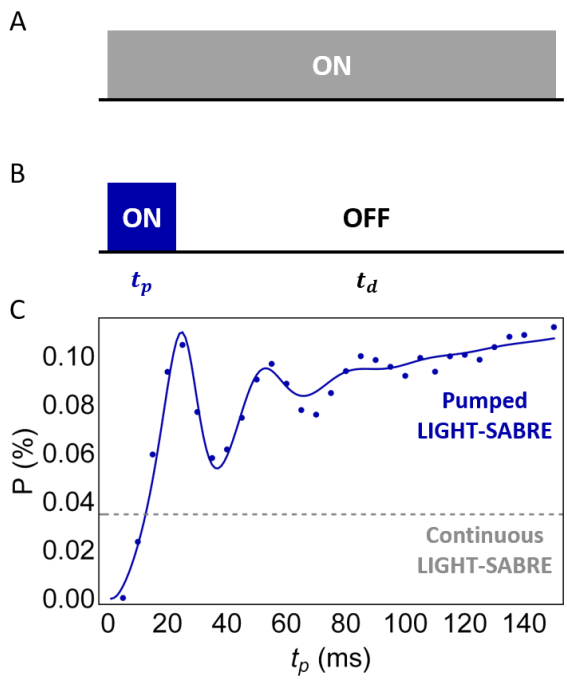

Figure 4: Pumping the matching condition in SABRE. A. The $|S_H^0\beta_L\rangle \rightarrow |T_H^0\alpha_L\rangle$ transition is essentially always 'on' for the entire experiment in the continuous LIGHT-SABRE pulse sequence, which is only periodically interrupted to store the magnetization generated along the irradiation field ($\hat{x}$) along the leading magnetic field ($\hat{z}$). **B.** Only turning this transition on for a time t_p to generate magnetization and then turning it off for a period t_d to permit exchange more efficiently pumps magnetization, which is called the pumped LIGHT-SABRE sequence. **C.** Scanning t_p for a fixed value of $t_d = 400\ ms$ and repeating this sequence for 60 s creates significantly more polarization (blue) than the continuous LIGHT-SABRE sequence (gray). In this case, the transition is driven slightly off-resonance to directly generate magnetization along the leading field ($\hat{z}$). The blue line is the simulation result from the theoretical model developed in this work.

dynamics of the system and was the first step towards decoupling the interplay between coherent and exchange effects in SABRE.

The pumped LIGHT-SABRE and analogous SABRE-SHEATH experiments developed by Shannon Eriksson in the Warren lab[89] showed that driving the system for as little as 5% of the total experiment time could actually generate a larger hyperpolarization than continuously driving the transition. This stood in contrast to what was motivated by framing SABRE in the context of conventional magnetic resonance. As such, it became evident that a new approach to optimizing SABRE would be required. The analytical theoretical framework from which most conventional NMR are motivated[7, 90, 91] assumes that the system itself is static, i.e. molecular parameters do not change with time. However, SABRE requires chemical exchange to catalytically generate hyperpolarization, which introduces time-varying molecular parameters and drives interpretation of the system away from the analytical treatments used in conventional NMR. The theoretical description of coherent dynamics in systems undergoing chemical exchange was originally described by Binsch in 1968[92] as an extension to Redfield's relaxation theory[93]. However, the statistical assumptions required for relaxation are very different than those required for chemical exchange. This realization has guided a significant amount of the theoretical work presented here, which resulted in the complete re-interrogation of the chemical exchange interaction.

This work introduces a more robust approach to the development and optimization of SABRE experiments. Conventional analytical theory is used to guide the construction of new techniques that focus on expanding the scope and capabilities of X-SABRE experiments, but is subject to computational optimization of the system to ensure that the effects of exchange are fairly incorporated. The pairing of analytical and computational theoretical

methods is validated by experimentation. To that end, Chapter 2 will summarize the theoretical basis necessary to facilitate subsequent discussions as well as to introduce notation and conventions to be used throughout this dissertation. Chapter 3 will then address the advancements in the theory of unifying spin dynamics and chemical exchange in SABRE and will introduce the exhaustive SABRE-specific computational models upon which the remainder of the work is based. Chapter 4 details efforts to experimentally unveil coherent hyperpolarization dynamics in SABRE at high magnetic field and builds off of these advancements with demonstrations of the ability to harness coherently driven SABRE in experimental regimes that were previously inaccessible. Chapter 5 explores new directions to expand the capabilities of ultralow field X-SABRE in an effort to develop means to control the dynamics under these conditions and thus optimize hyperpolarization performance. Finally, Chapter 6 will return to the treatments of exchange presented for magnetic resonance in Chapter 3 and introduce the exact form of the exchange interaction that is valid in any physical limit, which will be explored in both for the cases of magnetic resonance as well as the coherent ultrafast spectroscopies.

Chapter 2: Theoretical Basis

Spin angular momentum presents an interesting theoretical predicament in quantum mechanics, as its dynamics and properties are well understood and yet, spin has no convenient interpretation as a parallel to classical mechanics. Angular momentum in classical mechanics is a combination of the rotational momentum of a system about an origin (a planet orbiting a sun) called orbital angular momentum, as well as the rotation of a system about its center of mass (the revolution of a planet) called the spin angular momentum. While it is enticing to project these concepts onto quantum particles, any angular momentum arising from the motion of such particles corresponds to the orbital angular momentum. Additionally, quantum particles have an intrinsic angular momentum that is called spin angular momentum, which was first inferred from high resolution atomic hydrogen spectra[94] and experimentally confirmed in the Stern-Gerlach experiment[95]. However, it was not until Dirac's relativistic treatment of quantum mechanics[96] that this spin angular momentum was accepted on a theoretical basis. Here, the necessary spin physics will be summarized so to facilitate the coming discussions and conventions will be introduced.

2.1 Interactions of spin-1/2 nuclei

We will predominantly treat nuclei with spin $I = 1/2$, as they are the most commonly used nuclei in magnetic resonance as they have sharp spectral features and are readily found in many target compounds. Commonly encountered spin-$1/2$ nuclei are ^{1}H, ^{13}C, ^{15}N, ^{19}F, and ^{31}P. When

discussing multiple different spin-1/2 nuclei, we will use $\boldsymbol{I}$, $\boldsymbol{S}$, and $\boldsymbol{L}$ for various spin-1/2 particles. Nuclear spin is a convenient system to study quantum mechanics, as the spin Hamiltonian may be written down exactly. Before examining this case, let us review the general case. As elements of the Hamiltonian are changed, the resulting eigenstates will be comprised of different linear combinations of basis states. This is called "mixing" of the basis states and indicates which states are coupled to one another. Before examining the different types of couplings that may arise, we will examine a more general case. Conditions where states become mixed are called resonance or matching conditions. Matching conditions indicate the states of a system between which population is allowed to flow and are critical in understanding spectroscopy. To exemplify this, we can analyze a model two-level system consisting of a ground, $|0\rangle$, and excited, $|1\rangle$, state with an energy difference Δ and a coupling rate V (Fig. 5). Throughout this discussion, we will use Dirac notation to delineate states from other vector quantities. The matrix form of this Hamiltonian is then:

$$\hat{\mathcal{H}} = \begin{pmatrix} 0 & V \\ V & \Delta \end{pmatrix} \tag{2.1}$$

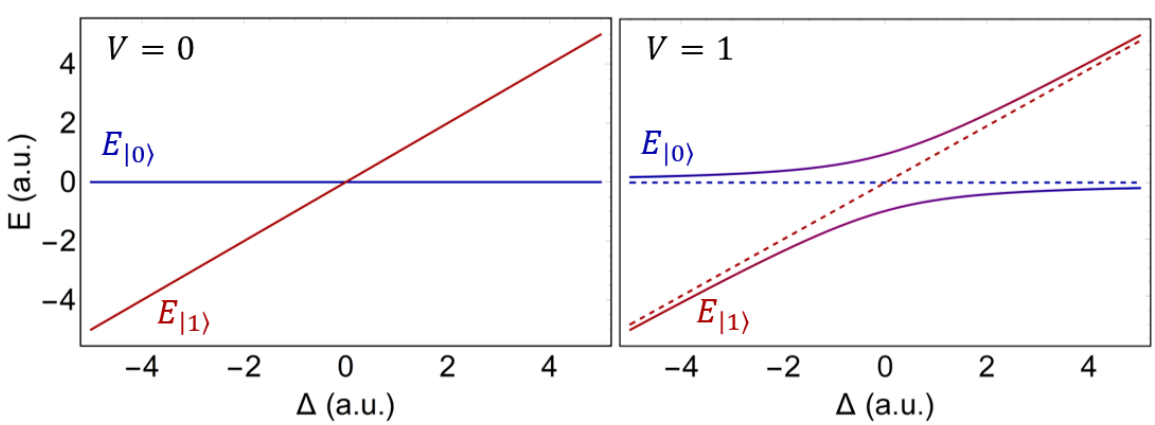

Figure 5: Energy eigenvalues of a two-level system. In the absence of a coupling ($V = 0$), the eigenstates of the system are $|0\rangle$ and $|1\rangle$, and the states do not mix even when $\Delta = 0$ when the states are degenerate. This condition is called a level crossing. However, with a coupling ($V = 1$) the $|0\rangle$ and $|1\rangle$ states mix, leading to the generation of an avoided crossing, or level anti-crossing (LAC). At an avoided crossing, population is allowed to flow between the $|0\rangle$ and $|1\rangle$ states.

The energy eigenvalues of this Hamiltonian are $\left(\Delta \pm \sqrt{4V^2 + \Delta^2}\right)/2$, which may be solved by diagonalizing the Hamiltonian. Plotting these eigenvalues as a function of the energy separation, Δ, yields an important analysis of coupled energy states. In the absence of a coupling, the two states do not mix and populations are locked in these two states. This condition is called a level crossing, as the eigenvalues (the energy) cross without mixing the states. A non-zero coupling permits mixing of the basis states and generates an avoided crossing or, as it is often referred to in the hyperpolarization community, a level anti-crossing (LAC). At an avoided crossing, population is allowed to flow between the basis states, and as such, the analysis of matching conditions is often employed in the construction of spectroscopy experiments. The mixing of the $|0\rangle$ and $|1\rangle$ states is maximized when $\Delta = 0$ for any non-zero coupling, indicated when the diagonal elements of $\hat{\mathcal{H}}$ are degenerate. This condition defines the resonance condition for a given transition.

We may now progress to spin physics as it pertains to nuclear magnetism. In particular, we will treat nuclear spin within a molecule and will restrict discussion to the case where the molecule is in a closed shell electronic configuration where all electrons are paired. Spin is a vector quantity, and as such may be expanded to have the components:

$$\boldsymbol{I} \cdot \boldsymbol{n} = n_x \hat{I}_x + n_y \hat{I}_y + n_z \hat{I}_z$$
$$\hat{I}_x = \frac{1}{2}\begin{pmatrix} 0 & 1 \\ 1 & 0 \end{pmatrix}; \hat{I}_y = \frac{1}{2}\begin{pmatrix} 0 & -i \\ i & 0 \end{pmatrix}; \hat{I}_z = \frac{1}{2}\begin{pmatrix} 1 & 0 \\ 0 & -1 \end{pmatrix}; \tag{2.2}$$

Each of the spin operators used to decompose $\boldsymbol{I}$ may be expressed in terms of the Pauli matrix according to $\hat{I}_i = \hat{\sigma}_i/2$. These are written in the basis $\{(1 \quad 0), (0 \quad 1)\}$, which will gain physical meaning momentarily. The most fundamental interaction for nuclear spins is the interaction with an external magnetic field, called the Zeeman interaction. The nuclear spin $\boldsymbol{I}$

has a magnetic dipole moment $\boldsymbol{\mu}$ that is collinear with and proportional to it, expressed as $\boldsymbol{\mu} = \gamma \boldsymbol{I}$ where γ is the gyromagnetic ratio of the nucleus. The interaction energy of the dipole with the field ($\boldsymbol{B}$) is well known from classical physics as:

$$E = -\boldsymbol{\mu} \cdot \boldsymbol{B} = -\gamma \boldsymbol{I} \cdot \boldsymbol{B} = -\gamma |\boldsymbol{I}||\boldsymbol{B}| \cos(\theta) \tag{2.3}$$

For positive γ, we see that the energy is minimized when the magnetic dipole is parallel to the magnetic field and maximized when anti-parallel the magnetic field. As such, it is convenient to describe the system in terms of an aligned $|\alpha\rangle$ state and an anti-aligned $|\beta\rangle$ state. These states define the basis used above and have the correspondence $\{|\alpha\rangle, |\beta\rangle\} = \{(1 \quad 0), (0 \quad 1)\}$. Using the convention for the leading magnetic field $\boldsymbol{B} = B_0 \boldsymbol{z}$ reduces the energy to the simpler form:

$$E = -\gamma B_0 \hat{I}_z = \omega_0 \hat{I}_z \tag{2.4}$$

We have defined the Larmor frequency $\omega_0 \equiv -\gamma B_0$, and will continue with this sign convention through this work, noting that a positive Larmor frequency corresponds to a *negative* energy.

We may use the operators defined in eq. 2.2 to represent the components of the spin angular momentum when constructing the system Hamiltonian. The Zeeman Hamiltonian can then be written for an N-spin system as:

$$\hat{\mathcal{H}}_Z = \sum_i^N \omega_{0,i} \hat{I}_{iz} \tag{2.5}$$

This Hamiltonian is diagonal in the so-called Zeeman basis, which is constructed of permutations of the $\{|\alpha\rangle, |\beta\rangle\}$ basis set. In conventional NMR spectrometers, the Zeeman interaction has a magnitude on the order of $E_Z/h \approx$ 10-500 MHz, depending on the nucleus

and field. The Zeeman interaction is often the largest interaction for spin-1/2 nuclei, and dictates which nuclei are observed in a magnetic resonance experiment by separating the frequencies of various nuclei to be separated by many MHz at conventional spectrometer fields of $B > 1T$. When constructing this Hamiltonian for an N-spin system, the basis set must span all of the permutations of the different spin states, which is easily constructed by taking the tensor product ($\otimes$) with appropriately-positioned identity matrices ($\hat{E}_n$, n denotes the dimensionality). For instance, the operator $\hat{I}_{1z}$ in a two spin-1/2 system is $\hat{I}_{1z} = \hat{I}_z \otimes \hat{E}_2$, and $\hat{I}_{2z} = \hat{E}_2 \otimes \hat{I}_z$.

In addition to interacting with the magnetic field, spins can interact with each other through couplings. The first of these couplings is the dipolar coupling, which arises between two spins $\boldsymbol{I}$ and $\boldsymbol{S}$, and has a typical magnitude of $E_D/h \approx$ 1-10 kHz. The full dipolar coupling Hamiltonian may be derived from the classical dipolar interaction, making the substitution for the magnetic moment as employed previously, giving:

$$\hat{\mathcal{H}}_D = -\frac{\mu_0 \gamma_I \gamma_S \hbar}{4\pi}\left(\frac{3(\boldsymbol{I}\cdot\boldsymbol{r})(\boldsymbol{S}\cdot\boldsymbol{r})}{r^5} - \frac{\boldsymbol{I}\cdot\boldsymbol{S}}{r^3}\right) \tag{2.6}$$

The vector $\boldsymbol{r}$ connects the two spins

$$\boldsymbol{r} = \begin{pmatrix} r\sin\theta\cos\phi \\ r\sin\theta\sin\phi \\ r\cos\theta \end{pmatrix}, \tag{2.7}$$

θ describes the polar angle, distended from $\hat{z}$, and ϕ describes the azimuthal angle. At high magnetic field, this Hamiltonian can be reduced to its secular component, or those terms which commute with the Zeeman Hamiltonian (i.e., does not change the Zeeman energy). Using the notation $\hat{I}^{\pm} = \hat{I}_x \pm i\hat{I}_y$, this gives:

$$\hat{\mathcal{H}}_D = -\frac{\mu_0 \gamma_I \gamma_S \hbar}{4\pi r^3}(3\cos^2\theta - 1)\left(\hat{I}_z\hat{S}_z - \frac{1}{4}\left(\hat{I}^+\hat{S}^- + \hat{I}^-\hat{S}^+\right)\right)$$
$$= d_{IS}(3\cos^2\theta - 1)\left(\hat{I}_z\hat{S}_z - \frac{1}{4}\left(\hat{I}^+\hat{S}^- + \hat{I}^-\hat{S}^+\right)\right) \tag{2.8}$$

This is one of the few instances where keeping the factor of $\hbar$ is useful, noting that γ is in units of rad s^{-1} T^{-1} by convention. The constants have been collected into the secular dipolar coupling, d_{IS}, which we have defined as:

$$d_{IS} = -\frac{\mu_0 \gamma_I \gamma_S \hbar}{4\pi r^3} \tag{2.9}$$

As an example, the dipolar coupling of two ^{1}H nuclei separated by 2.5Å is $d_{HH} = 7.687\ kHz$. The term $\hat{I}^+\hat{S}^- + \hat{I}^-\hat{S}^+$ only commutes with the Zeeman Hamiltonian if both spins are the same (homonuclear), whereas this term will not commute with the Zeeman Hamiltonian for heteronuclear spins. In this case, the dipolar Hamiltonian reduces to $d_{IS}\hat{I}_z\hat{S}_z$. In the case of a spherical sample of an isotropic liquid, diffusional motion orientationally averages this interaction to zero for nearby spins and is therefore unobservable in the spectrum. However, the isotropic averaging is not present in the solid state and thus the dipolar coupling is observable in a solid-state spectrum. Notably, the dipolar interaction will disappear when $3\cos^2\theta - 1 = 0$, which is at an angle $\theta_m = 54.7°$ called the 'magic angle'. Rotating the sample about this angle at a rate faster than the dipolar coupling essentially induces isotropic averaging, which is the motivation behind magic angle spinning (MAS) NMR experiments. It is important to note that some use the notation $(3\hat{I}_z\hat{S}_z - \hat{I}\cdot\hat{S})/2$ for the form of the coupling, which is the Hermitian form of the coupling (does not use $\hat{I}^{\pm}\hat{S}^{\mp}$).

All terms of the dipolar coupling are present when the condition $\hat{\mathcal{H}}_D \ll \hat{\mathcal{H}}_Z$ is not satisfied as it is at high magnetic field, which is more efficiently written as:

$$\hat{\mathcal{H}}_D = d_{IS}\left(\frac{3(\hat{I}\cdot\boldsymbol{r})(\hat{S}\cdot\boldsymbol{r})}{r^5} - \frac{\hat{I}\cdot\hat{S}}{r^3}\right) = d_{IS}\left(\frac{\hat{I}\cdot(3\boldsymbol{r}\cdot\boldsymbol{r}^T)\cdot\hat{S}}{r^5} - \frac{\hat{I}\cdot\hat{S}}{r^3}\right)$$
$$= d_{IS}\left(\hat{I}\cdot\left(3\boldsymbol{r}\cdot\boldsymbol{r}^T - \hat{E}\right)\cdot\hat{S}\right) = d_{IS}\left(\hat{I}\cdot\ddot{\Omega}\cdot\hat{S}\right) \tag{2.10}$$

Note that identity $\hat{E}$ may be placed anywhere in the expression, such as $\hat{I}\cdot\hat{S} = \hat{I}\cdot\hat{E}\cdot\hat{S}$. This permits us to define the tensor (denoted by an umlaut):

$$\ddot{\Omega} = \begin{pmatrix} 3\sin^2(\theta)\cos^2(\phi) - 1 & 3\sin^2(\theta)\sin(\phi)\cos(\phi) & 3\cos(\theta)\sin(\theta)\cos(\phi) \\ 3\sin^2(\theta)\sin(\phi)\cos(\phi) & 3\sin^2(\theta)\sin^2(\phi) - 1 & 3\cos(\theta)\sin(\theta)\sin(\phi) \\ 3\cos(\theta)\sin(\theta)\cos(\phi) & 3\cos(\theta)\sin(\theta)\sin(\phi) & 3\cos^2(\theta) - 1 \end{pmatrix} \tag{2.11}$$

A tensor is a convenient mathematical tool that describes linear relations between two objects that span the same space. Here, the tensor $\ddot{\Omega}$ determines the rotational dependence of the bilinear interaction between the two spins. We may now directly calculate the tensor product:

$$\hat{I}\cdot\ddot{\Omega}\cdot\hat{S} = \sum_{ij}\hat{I}_i\hat{S}_j\Omega_{ij}$$
$$= \hat{I}_x\hat{S}_x\Omega_{xx} + \hat{I}_x\hat{S}_y\Omega_{xy} + \hat{I}_x\hat{S}_z\Omega_{xz}$$
$$+\hat{I}_y\hat{S}_x\Omega_{yx} + \hat{I}_y\hat{S}_y\Omega_{yy} + \hat{I}_y\hat{S}_z\Omega_{yz}$$
$$+\hat{I}_z\hat{S}_x\Omega_{zx} + \hat{I}_z\hat{S}_y\Omega_{zy} + \hat{I}_z\hat{S}_z\Omega_{zz} \tag{2.12}$$

The first relation greatly simplifies this process, and the notation Ω_{ij} reduces clutter when rearranging this equation. Note that $\ddot{\Omega}$ is a symmetric matrix, meaning that Ω_{ij} and Ω_{ji} will have the same rotational dependence. Typically, eq. 2.12 may be cast in a non-Hermitian form, as was used to show the secular dipolar coupling above, but certain analysis are more convenient by retaining the Hermitian form of the couplings. Together, the above terms form the untruncated dipolar interaction.

The nuclear spin does not only have to interact directly with other nuclear spins but can also have substantial magnetic interactions with electrons in the molecule, which are also

spin-1/2 particles. To approach an understanding of how these interactions arise, we shall use the Pauli description of a massive particle, which can be derived as the non-relativistic limit of the Dirac equation. We may write the entire expression in natural units, which are defined by $\hbar = c = m_e = 1$. The generic form of the Pauli Hamiltonian for a particle with mass m and charge q is given by:

$$\hat{\mathcal{H}} = \frac{1}{2m}\boldsymbol{\sigma} \cdot (\boldsymbol{p} - q\boldsymbol{A})^2 + q\phi, \tag{2.13}$$

where $\boldsymbol{A}$ is the vector potential of the field, ϕ is the scalar potential, and $\boldsymbol{\sigma}$ are the Pauli spin operators corresponding to the spin of the particle. As a brief review of vector calculus, a vector field may be generated by the curl (circulation) of a vector potential, $\nabla \times \boldsymbol{A}$, or may be generated by the gradient of a scalar potential, $\nabla\phi$. Specifically, the magnetic vector potential can be related to a magnetic dipole $\boldsymbol{\mu}$ as:

$$\boldsymbol{A} = \frac{\boldsymbol{\mu} \times \boldsymbol{r}}{r^3} = \nabla \times \left(\frac{\boldsymbol{\mu}}{r}\right) \tag{2.14}$$

The magnetic vector potential is related to $\boldsymbol{B}$ by:

$$\nabla \times \boldsymbol{A} = \boldsymbol{B} \tag{2.15}$$

For reference, the curl of a vector potential can be calculated as

$$\begin{aligned} \nabla \times \boldsymbol{A} &= \begin{pmatrix} \frac{\partial}{\partial x} & \frac{\partial}{\partial y} & \frac{\partial}{\partial z} \end{pmatrix} \times \begin{pmatrix} A_x & A_y & A_z \end{pmatrix} = \begin{vmatrix} \hat{\imath} & \hat{\jmath} & \hat{k} \\ \frac{\partial}{\partial x} & \frac{\partial}{\partial y} & \frac{\partial}{\partial z} \\ A_x & A_y & A_z \end{vmatrix} \\ &= \left(\frac{\partial A_z}{\partial y} - \frac{\partial A_y}{\partial z}\right)\hat{\imath} + \left(\frac{\partial A_x}{\partial z} - \frac{\partial A_z}{\partial x}\right)\hat{\jmath} + \left(\frac{\partial A_y}{\partial x} - \frac{\partial A_x}{\partial y}\right)\hat{k} \end{aligned} \tag{2.16}$$

To make progress, we may expand eq. 2.13 according to the Pauli vector identity:

$$(\boldsymbol{\sigma}\cdot\boldsymbol{a})(\boldsymbol{\sigma}\cdot\boldsymbol{b}) = \boldsymbol{a}\cdot\boldsymbol{b} + i\boldsymbol{\sigma}\cdot(\boldsymbol{a}\times\boldsymbol{b}), \tag{2.17}$$

giving:

$$\begin{aligned}\hat{\mathcal{H}} &= \frac{1}{2m}\boldsymbol{\sigma}\cdot(\boldsymbol{p}-q\boldsymbol{A})^2 + q\phi \\ &= \frac{1}{2m}\Big((\boldsymbol{p}-q\boldsymbol{A})^2 + i\boldsymbol{\sigma}\cdot\big((\boldsymbol{p}-q\boldsymbol{A})\times(\boldsymbol{p}-q\boldsymbol{A})\big)\Big) + q\phi\end{aligned} \tag{2.18}$$

Expanding the $\boldsymbol{\sigma}$-dependent term and using the definition $\boldsymbol{p} = -i\nabla$:

$$\begin{aligned}\hat{\mathcal{H}} &= \frac{1}{2m}\Big((\boldsymbol{p}-q\boldsymbol{A})^2 + i\boldsymbol{\sigma}\cdot\big((\boldsymbol{p}-q\boldsymbol{A})\times(\boldsymbol{p}-q\boldsymbol{A})\big)\Big) + q\phi \\ &= \frac{1}{2m}\big((\boldsymbol{p}-q\boldsymbol{A})^2 - iq\boldsymbol{\sigma}\cdot(\boldsymbol{p}\times\boldsymbol{A}+\boldsymbol{A}\times\boldsymbol{p})\big) + q\phi \\ &= \frac{1}{2m}\big((\boldsymbol{p}-q\boldsymbol{A})^2 - q\boldsymbol{\sigma}\cdot(\nabla\times\boldsymbol{A}+\boldsymbol{A}\times\nabla)\big) + q\phi\end{aligned} \tag{2.19}$$

When the $\boldsymbol{\sigma}$-dependent term is applied to a wavefunction, ψ, we can write:

$$-q\boldsymbol{\sigma}\cdot(\nabla\times\boldsymbol{A}+\boldsymbol{A}\times\nabla)\psi = -q\boldsymbol{\sigma}\cdot(\nabla\times\boldsymbol{A}\psi+\boldsymbol{A}\times\nabla\psi) \tag{2.20}$$

We may use the vector calculus identity

$$\nabla\times\boldsymbol{A}\psi = \psi\nabla\times\boldsymbol{A} - \boldsymbol{A}\times\nabla\psi \tag{2.21}$$

to simplify this expression as:

$$\begin{aligned}\hat{\mathcal{H}} &= \frac{1}{2m}\big((\boldsymbol{p}-q\boldsymbol{A})^2 - q\boldsymbol{\sigma}\cdot(\nabla\times\boldsymbol{A}+\boldsymbol{A}\times\nabla)\big) + q\phi \\ &= \frac{1}{2m}\Big((\boldsymbol{p}-q\boldsymbol{A})^2 - q\boldsymbol{\sigma}\cdot\big(\hat{\nabla}\times\boldsymbol{A}\big)\Big) + q\phi\end{aligned} \tag{2.22}$$

Finally, eq. 2.15 permits us to write the Pauli Hamiltonian as:

$$\hat{\mathcal{H}} = \frac{1}{2m}((\boldsymbol{p}-q\boldsymbol{A})^2 - q\boldsymbol{\sigma}\cdot\boldsymbol{B}) + q\phi \tag{2.23}$$

The term $\boldsymbol{\sigma}\cdot\boldsymbol{B}$ is the Zeeman interaction of the particle with the magnetic field.

To explore electron-nucleus interactions within this framework, we must define specific magnetic vector potentials for the molecular system, which follows the derivation performed by Abragam[1]. To do this, it is often advantageous to recast the problem so that extraneous degrees of freedom are minimized. In electrodynamics, this is called a gauge transformation. We shall use the Coulomb gauge:

$$\nabla \cdot \boldsymbol{A}(\boldsymbol{r}, t) = 0 \tag{2.24}$$

This gauge permits us to write the vector potential for the field produced by the electron k as

$$\boldsymbol{A}_k = \frac{1}{2}(\boldsymbol{B} \times \boldsymbol{r}_k), \tag{2.25}$$

where $\boldsymbol{B}$ is an externally applied field and $\boldsymbol{r}_k$ is the vector to the electron from the gauge origin. We must also consider magnetic vector potential for the electron k generated by the nucleus j as:

$$\boldsymbol{A}_k^{(j)} = \frac{\boldsymbol{\mu}_j \times \boldsymbol{r}_{jk}}{r_{jk}^3} = \nabla \times \left(\frac{\boldsymbol{\mu}_j}{r_{jk}}\right) \tag{2.26}$$

Notice that this construction frames the problem in terms of the electronic degrees of freedom. Furthermore, we can write the magnetic fields in terms of these vector potentials according to $\boldsymbol{B} = \hat{\nabla} \times \boldsymbol{A}$. Then, the Pauli Hamiltonian for a molecule of N electrons and M nuclei is given by:

$$\hat{\mathcal{H}} = \frac{1}{2}\sum_k^N \left(\boldsymbol{p}_k + e\boldsymbol{A}_k + e\sum_j^M \boldsymbol{A}_k^{(j)}\right)^2 + \frac{e}{2}\sum_k^N \boldsymbol{L}_k \cdot \left(\nabla \times \boldsymbol{A}_k + \sum_j^M \nabla \times \boldsymbol{A}_k^{(j)}\right) \tag{2.27}$$

$\boldsymbol{p}_k$, e, $\boldsymbol{L}_k$ are the angular momentum, charge, and spin of the electron, respectively, noting that in natural units $m_e = 1$. We have chosen to drop the electrostatic terms proportional to

the scalar potential ϕ because spin-1/2 nuclei have no magnetic interactions with the electrostatic field at the position of the nucleus[97].

At this juncture, we can expand the above equation and retain effects corresponding to pertinent interactions in magnetic resonance. The first of these is the chemical shift interaction, which arises from the expansion of the first term in the Hamiltonian:

$$\hat{\mathcal{H}}_{CS} = \frac{e^2}{2}\sum_k^N \sum_j^M \boldsymbol{A}_k^{(j)} \cdot \boldsymbol{A}_k = \frac{e^2}{2}\sum_k^N \sum_j^M \frac{1}{r_{jk}^3}\left(\boldsymbol{\mu}_j \times \boldsymbol{r}_{jk}\right) \cdot \left(\boldsymbol{B} \times \boldsymbol{r}_k\right) \tag{2.29}$$

Note, there are two identical terms of the form above that arise in the expansion, but a factor of $1/2$ arises when defining $\boldsymbol{A}_k$ in the Coulomb gauge (eq. 2.25). Using the relation

$$(\boldsymbol{a} \times \boldsymbol{b}) \cdot (\boldsymbol{c} \times \boldsymbol{d}) = (\boldsymbol{a} \cdot \boldsymbol{c})(\boldsymbol{b} \cdot \boldsymbol{d}) - (\boldsymbol{a} \cdot \boldsymbol{d})(\boldsymbol{c} \cdot \boldsymbol{b}), \tag{2.30}$$

we may rewrite eq. 2.29 as:

$$\begin{aligned}
\hat{\mathcal{H}}_{CS} &= \frac{e^2}{2}\sum_k^N \sum_j^M \frac{1}{r_{jk}^3}\left(\boldsymbol{\mu}_j \times \boldsymbol{r}_{jk}\right) \cdot \left(\boldsymbol{B} \times \boldsymbol{r}_k\right) \\
&= \frac{e^2}{2}\sum_k^N \sum_j^M \frac{1}{r_{jk}^3}\Big(\left(\boldsymbol{\mu}_j \cdot \boldsymbol{B}\right)\left(\boldsymbol{r}_{jk} \cdot \boldsymbol{r}_k\right) - \left(\boldsymbol{\mu}_j \cdot \boldsymbol{r}_{jk}\right)\left(\boldsymbol{B} \cdot \boldsymbol{r}_k\right)\Big) \\
&= \frac{e^2}{2}\sum_k^N \sum_j^M \frac{\gamma_j}{r_{jk}^3}\Big(\left(\hat{I}_j \cdot \left(\boldsymbol{r}_{jk} \cdot \boldsymbol{r}_k\right) \cdot \boldsymbol{B}\right) - \left(\hat{I}_j \cdot \left(\boldsymbol{r}_{jk} \cdot \boldsymbol{r}_k^T\right) \cdot \boldsymbol{B}\right)\Big) \\
&= \frac{e^2}{2}\sum_k^N \sum_j^M \frac{\gamma_j}{r_{jk}^3}\left(\hat{I}_j \cdot \ddot{\Lambda}_{jk} \cdot \boldsymbol{B}\right)
\end{aligned} \tag{2.31}$$

We have defined an orientational tensor $\ddot{\Lambda}_{jk}$ as:

$$\ddot{\Lambda}_{jk} = \left(\boldsymbol{r}_{jk} \cdot \boldsymbol{r}_k\right) - \boldsymbol{r}_{jk} \cdot \boldsymbol{r}_k^T \tag{2.32}$$

Unlike the tensor $\ddot{\Omega}$ defined for the dipolar coupling, $\ddot{\Lambda}_{jk}$ survives spherical averaging and is thus observable in conventional liquid state NMR. Note that this interaction is dependent on the coupling to the magnetic field induced on the electron in an external magnetic field, which is distinct from coupling to the magnetic dipole moment of the electron. Typically, we may rewrite $\mathcal{H}_{CS}$ and integrate over the electronic degrees of freedom to give:

$$\hat{\mathcal{H}}_{CS} = -\sum_j \gamma_j \boldsymbol{I}_j \cdot \ddot{\sigma}_j \cdot \boldsymbol{B} \tag{2.33}$$

$\ddot{\sigma}_j$ is the chemical shift tensor. As the chemical shift is dependent on the local electronic environment, it is a powerful indicator of chemical structure and is key in the analysis of NMR spectra of unknown compounds. Furthermore, $\ddot{\sigma}_j$ always acts to oppose the Larmor frequency, and thus we adopt the negative sign in accordance with the convention used to define the Zeeman Hamiltonian. The chemical shift tensor has the components:

$$\ddot{\sigma} = \begin{pmatrix} \sigma_{xx} & \sigma_{xy} & \sigma_{xz} \\ \sigma_{yx} & \sigma_{yy} & \sigma_{yz} \\ \sigma_{zx} & \sigma_{zy} & \sigma_{zz} \end{pmatrix} \tag{2.34}$$

It is often convenient to rotate the reference frame (by a unitary transformation U) of $\ddot{\sigma}$ into the principal axis of the tensor, which then diagonalizes $\ddot{\sigma}$ into:

$$U\ddot{\sigma}U^{-1} = \ddot{\delta} = \begin{pmatrix} \delta_{xx} & 0 & 0 \\ 0 & \delta_{yy} & 0 \\ 0 & 0 & \delta_{zz} \end{pmatrix} \tag{2.35}$$

By convention, $\delta_{xx} \leq \delta_{yy} \leq \delta_{zz}$. As the chemical shift is a tensor quantity, the observed chemical shift δ_0 is dependent on the orientation of the tensor relative to the external magnetic field (assuming $\boldsymbol{B} = B_0\boldsymbol{z}$), which expressed in spherical coordinates is[97]:

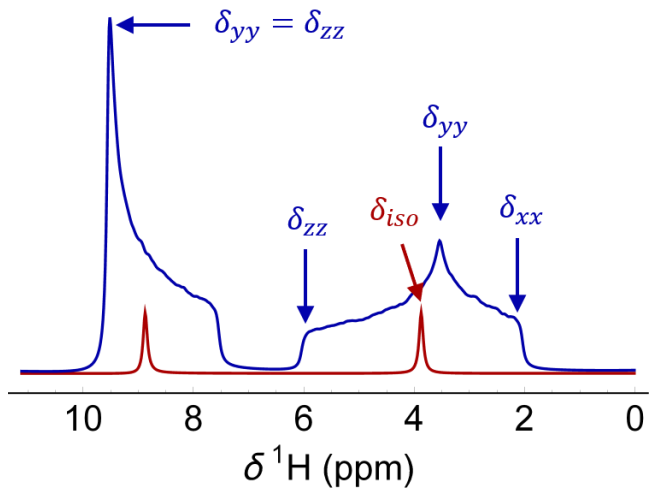

Figure 6: Chemical shift anisotropy in solid state NMR. The blue spectrum is the powder-averaged NMR spectrum of two uncoupled spins. Each spin experiences a different electronic environment and thus has a different chemical shift tensor. The components of the chemical shift tensor can be read directly from the solid state spectrum. The red spectrum shows the isotropic chemical shift of each of these spins, which is what would be observed in the liquid state.

$$\delta_0(\theta,\phi) = \frac{\delta_a}{2}(3\cos^2\theta - 1) - \frac{\delta_a \eta}{2}\cos 2\phi \sin^2\theta + \delta_{iso} \tag{2.36}$$

Here, we have defined the anisotropic chemical shift (δ_a), the chemical shift asymmetry parameter (η), and the isotropic chemical shift (δ_{iso}):

$$\delta_{iso} = \frac{1}{3}(\delta_{xx} + \delta_{yy} + \delta_{zz});\ \delta_a = \delta_{zz} - \delta_{iso};\ \eta = \frac{\delta_{yy} - \delta_{xx}}{\delta_a} \tag{2.37}$$

In the solid-state (powder) sample, where the orientation is fixed for individual molecules but the molecules are randomly oriented to the external field, the NMR spectrum is an average over all of the molecular orientations and results in broad lines. Despite this, the NMR spectrum has a characteristic shape dependent on the chemical shift tensor (Fig. 6) that reflects the different components of $\ddot{\delta}$. In the case of liquid-state NMR, where the orientation of each molecule rapidly changes (ps timescale), the observed chemical shift simply reduces to the isotropic chemical shift. The form of the Hamiltonian in this limit may be reduced to:

$$\hat{\mathcal{H}}_{CS} = -\sum_j \gamma_j \delta_{iso}^{(j)} \hat{I}_{jz} B_0 \tag{2.38}$$

To this point, we have examined the magnetic interactions of a spin-1/2 nucleus with an external magnetic field (Zeeman interaction), the field produced by another spin-1/2 nucleus (the dipolar interaction), and the field induced by the electron orbit (the chemical shift). We will now examine the last pertinent spin interaction, which also arises from electron-nucleus interactions in spin-1/2 nuclei and can be found by expanding the spin-dependent part of the Pauli Hamiltonian:

$$\hat{\mathcal{H}}_{OC} = \frac{e}{2}\sum_k^N \sum_j^M \boldsymbol{L}_k \cdot \left(\nabla \times \boldsymbol{A}_k^{(j)}\right) = \frac{e}{2}\sum_k^N \sum_j^M \boldsymbol{L}_k \cdot \left(\nabla \times \nabla \times \left(\frac{\boldsymbol{\mu}_j}{r_{jk}}\right)\right) \tag{2.39}$$

This term is referred to as the orbital coupling describes a coupling between the electron spin and the nuclear spin. Expanding the term under summation using the curl of a curl identity and rearranging:

$$\begin{aligned}
\hat{\mathcal{H}}_{OC} &= \frac{e}{2}\sum_k^N \sum_j^M \boldsymbol{L}_k \cdot \left(\nabla \times \nabla \times \left(\frac{\boldsymbol{\mu}_j}{r_{jk}}\right)\right) \\
&= \frac{e}{2}\sum_k^N \sum_j^M \frac{1}{r_{jk}} \boldsymbol{L}_k \cdot \left(\nabla\left(\nabla \cdot \boldsymbol{\mu}_j\right) - \boldsymbol{\mu}_j \nabla^2\right) \\
&= \frac{e}{2}\sum_k^N \sum_j^M \frac{1}{r_{jk}} \left((\boldsymbol{L}_k \cdot \nabla)(\boldsymbol{\mu}_j \cdot \nabla) - (\boldsymbol{\mu}_j \cdot \boldsymbol{L}_k)\nabla^2\right) \\
&= \frac{e}{2}\sum_k^N \sum_{\boldsymbol{j}}^M \frac{\gamma_j}{r_{jk}} \boldsymbol{I}_j (\nabla(\boldsymbol{L}_k \cdot \nabla) - \boldsymbol{L}_k \nabla^2)
\end{aligned} \tag{2.40}$$

The divergence of a vector field, $\nabla \cdot \boldsymbol{\alpha}$, generates a scalar field and is calculated as:

$$\nabla \cdot \boldsymbol{\alpha} = \begin{pmatrix} \frac{\partial}{\partial x} & \frac{\partial}{\partial y} & \frac{\partial}{\partial z} \end{pmatrix} \cdot \begin{pmatrix} A_x & A_y & A_z \end{pmatrix} = \frac{\partial A_x}{\partial_x} + \frac{\partial A_y}{\partial_y} + \frac{\partial A_z}{\partial_z} \tag{2.41}$$

Now, we may integrate over the electronic degrees of freedom and rewrite the orbital coupling Hamiltonian as

$$\hat{\mathcal{H}}_{OC} = \sum_j \gamma_j \hat{I}_j \cdot \hat{B}_e, \tag{2.42}$$

where we have defined

$$\hat{B}_e^{(j)} = \sum_k \langle \psi_0 | \frac{\nabla(\boldsymbol{L}_k \cdot \nabla) - \boldsymbol{L}_k \nabla^2}{r_{jk}} | \psi_0 \rangle \tag{2.43}$$

as the field produced by the electron at the position of the nucleus. Note that this expression is formally the first order correction to the energy and integrates over the ground-state electronic wavefunction, $|\psi_0\rangle$. While this term directly results from the Pauli Hamiltonian, the orbital coupling is negligibly small in diamagnetic systems as it is dependent only on one-electron integrals. However, it has a second-order correction to the energy that is observable:

$$\hat{\mathcal{H}}_{OC}^{(2)} = \sum_m \sum_{jl}^{n} \frac{\gamma_j \gamma_l \left\langle \psi_0 \middle| \boldsymbol{I}_j \cdot \hat{B}_e^{(j)} \middle| m \right\rangle \left\langle m \middle| \boldsymbol{I}_l \cdot \hat{B}_e^{(l)} \middle| \psi_0 \right\rangle}{E_0 - E_m} \tag{2.44}$$

In this notation, m indexes over excited electronic states. The scalar coupling is best understood as the perturbation by the nucleus j on the magnetic field generated by the electron ($\gamma_j \boldsymbol{I}_j \cdot \hat{B}_e^{(j)}$) influencing the field at the position of the nucleus l ($\gamma_l \boldsymbol{I}_l \cdot \hat{B}_e^{(l)}$). In short, the electronic spin informs the spin l of the state of j. This interaction scales with the product of the gyromagnetic ratios. Thus, changing γ of one of the nuclei but retaining electronic structure will (to first order) change the J-coupling as the ratio of the two gyromagnetic ratios,

i.e. $J' = (\gamma_l'/\gamma_j)J$. This interaction is bilinear in the orbital coupling interaction for two nuclei i and j and is referred to as the J-coupling coupling interaction. In tensor form, it is:

$$\hat{\mathcal{H}}_J = \boldsymbol{I}_j \cdot J_{jl} \cdot \boldsymbol{I}_l \tag{2.45}$$

The J-coupling is often extremely small (Hz) and thus is mostly restricted to liquid state NMR, where it is not eclipsed by larger magnitude interactions such as the dipolar coupling or chemical shift anisotropy. The orientational averaging of the tensor in the liquid state allows for the substitution of the isotropic scalar coupling constant J_{ij} for the $\boldsymbol{J}_{ij}$ tensor, allowing us to write (changing indices):

$$\hat{\mathcal{H}}_J = 2\pi \sum_{i<j} J_{ij} \hat{I}_i \cdot \hat{I}_j \tag{2.46}$$

The factor of 2π arises as J_{ij} is reported in Hertz. For a J-coupling between two nuclei A and B is separated by n bonds, it is convention to call this the ${}^{n}J_{AB}$ coupling. However, it is often convenient when the resonance frequency difference is much larger than the coupling to reduce the J-coupling Hamiltonian to its secular terms which commute with the Zeeman and chemical shift Hamiltonians. This is always the case for heteronuclear spin pairs at high magnetic field and is often referred to as the weak coupling limit, given by:

$$\hat{\mathcal{H}}_J = 2\pi \sum_{i<j} J_{ij} \hat{I}_{iz} \hat{I}_{jz} \tag{2.47}$$

The Hamiltonian of an isotropic liquid state sample will take the general form:

$$\hat{\mathcal{H}} = \hat{\mathcal{H}}_Z + \hat{\mathcal{H}}_\sigma + \hat{\mathcal{H}}_J = \sum_{i}^{N} (\omega_{0,i} - \delta_i) \hat{I}_{iz} + 2\pi \sum_{i<j} J_{ij} (\boldsymbol{I}_i \cdot \boldsymbol{I}_j) \tag{2.48}$$

Having established the fundamental spin interactions, we may proceed to examine the dynamics of spin systems.

2.2 Quantum dynamics and the density matrix

To this point, we have focused on the energy-level structure of quantum mechanical systems. However, we will require a time-dependent description of these systems, which is the focus of quantum dynamics. It is often advantageous to formulate time-evolution from the perspective of how the dynamics of the system changes with time, which leads to the use of differential equations. As a specific example, $\psi(t)$ is difficult to construct directly for a system with an arbitrary set of parameters but is relatively easy to construct $\partial\psi/\partial t$ for such a case and then solve for the time-evolution.

Before exploring evolution in quantum systems, we examine the differential equation

$$\frac{\partial a(t)}{\partial t} = ka(t), \tag{2.49}$$

where k is a scalar that describes the rate at which $a(t)$, a time-dependent scalar quantity, will change. For instance, if $a(t)$ was a time-dependent position then k would be the rate at which the position is changing over time, or in other words, the velocity. Technically, this equation is only parameterized on one variable, which means that it could be written with a total derivative d/dt, but we will retain the partial derivative for generality. To solve this equation, we will rearrange it such that terms with $a(t)$ are isolated and all other variables are on the other side of the equality, like:

$$\frac{\partial a(t)}{a(t)} = k\partial t \tag{2.50}$$

This is generally referred to as separation of variables and is one of the most common techniques to solve differential equations. Now, we are attempting to solve for $a(t)$. To accomplish this, both sides may be integrated to give:

$$\int_0^t \frac{\partial a(t)}{a(t)} = \int_0^t k\partial t$$
$$\frac{\ln\big(a(t)\big)}{\ln\big(a(0)\big)} = kt \tag{2.51}$$

Exponentiating both sides of the equation isolates $a(t)$:

$$a(t) = e^{kt} a_0 \tag{2.52}$$

Note that $a_0 = a(t = 0)$. When $k \in \mathbb{R}$ (reals) and $k < 0$, $a(t)$ decays exponentially, when $k \in \mathbb{I}$ (imaginaries), $a(t)$ evolves sinusoidally, and when $k \in \mathbb{C}$, $a(t)$ both oscillates and decays. In addition to solving a single differential equation, we may also simultaneously solve systems of differential equations. If in the example above, $a \to \boldsymbol{a}$ (a vector) and $k \to \widehat{K}$ (a real, symmetric matrix, for example), then one may use the same procedure to find the solution of

$$\frac{\partial \boldsymbol{a}(t)}{\partial t} = \widehat{K}\boldsymbol{a}(t) \tag{2.53}$$

to be:

$$\boldsymbol{a}(t) = \exp\big(\widehat{K}t\big)\,\boldsymbol{a}_0 \tag{2.54}$$

If $\widehat{K}$ is diagonal, then each basis state in $\boldsymbol{a}$ evolves independently of one another and has the solution

$$a_i(t) = e^{K_i t} a_{0,i}, \tag{2.55}$$

and it is often convenient to change the basis set of $\boldsymbol{a}$ to be the eigenbasis of $\widehat{K}$.

In direct correspondence to the case described above, the evolution of a quantum mechanical system is governed by the Schrödinger equation

$$\frac{\partial}{\partial t}|\psi\rangle = -i\widehat{\mathcal{H}}|\psi\rangle, \tag{2.56}$$

which is integrable to give the solution:

$$|\psi(t)\rangle = \vec{\mathcal{T}}\exp\left(-i\int_0^t dt'\widehat{\mathcal{H}}(t')\right)|\psi_0\rangle = \exp\left(-i\widehat{\mathcal{H}}t\right)|\psi_0\rangle \tag{2.57}$$

The exponential is the so-called propagator ($\widehat{U}$) of the system, $\vec{\mathcal{T}}$ is the Dyson time-ordering operator, and the second equality holds when the Hamiltonian is time-independent. It states that the evolution of the system will be dictated by the system Hamiltonian. While the Schrödinger equation is perhaps the most prolific equation of quantum mechanics, it is rarely advantageous to interrogate spectroscopy within this formalism. Experiments rarely probe a purely quantum mechanical system, but rather a statistical ensemble of particles that evolve quantum mechanically. Within $|\psi\rangle$, it is not obvious how one handles statistical averaging over an ensemble, as each wavefunction corresponds to a pure quantum state.

To address this, we may introduce the density matrix $\hat{\rho}$, which is a statistical tool developed to describe a single particle or an ensemble of particles. It is defined as

$$\hat{\rho} = \sum_j w_j|\psi_j\rangle\langle\psi_j|, \tag{2.58}$$

where w_j are weights and $|\psi_j\rangle$ are the pure states of the system. Doing so allows us to write a statistical mixed state as a linear combination of pure states, permitting us to perform ensemble averages. In doing so, any interaction between particles in the ensemble are omitted, which will cause problems to be addressed in future chapters. The density matrix is positive

semi-definite (when diagonal, $0 \leq \hat{\rho}_{ii}\ \forall i$) and idempotent ($\hat{\rho}^n = \hat{\rho}$). Furthermore, the elements of the density matrix are more interpretable than those in a wavefunction. For instance, the element $\hat{\rho}_{ii} = c_i^* c_i$ and directly gives the probability of being in the state $|\psi_i\rangle$. As such, the trace of the density matrix is always unity. When the density matrix is written in the Hamiltonian eigenbasis, off-diagonal elements $\hat{\rho}_{ij} = c_i^* c_j$ represent coherences between states. While the idea of coherences is quite abstract, it is easiest to think of a coherence as population in one eigenstate "talking" with population in another eigenstate. In the case of an ensemble, this "talking" is happening simultaneously with all of the particles and defines a macroscopic coherence, which in the case of magnetic resonance manifests as a bulk magnetization perpendicular to the leading field. This will be momentarily elaborated on in greater detail.

The evolution of a density matrix can be found by first taking the definition of $\hat{\rho}$ and inserting the solution of the Schrödinger equation (which will be done in the time-independent Hamiltonian case for legibility):

$$\hat{\rho}(t) = \sum_j w_j \exp\left(-i\hat{\mathcal{H}}t\right) |\psi_{0,j}\rangle\langle\psi_{0,j}| \exp\left(i\hat{\mathcal{H}}t\right) \tag{2.59}$$

Realizing that $\sum_j w_j\, |\psi_{0,j}\rangle\langle\psi_{0,j}| \equiv \hat{\rho}_0$, the initial density matrix, the evolution becomes:

$$\hat{\rho}(t) = \exp\left(-i\hat{\mathcal{H}}t\right) \hat{\rho}_0 \exp\left(i\hat{\mathcal{H}}t\right) \tag{2.60}$$

To find the equation of motion, we may take the time-derivative of the solution:

$$\frac{\partial}{\partial t}\hat{\rho}(t) = -i\hat{\mathcal{H}} \exp\left(-i\hat{\mathcal{H}}t\right) \hat{\rho}_0 \exp\left(i\hat{\mathcal{H}}t\right) + i \exp\left(-i\hat{\mathcal{H}}t\right) \hat{\rho}_0 \exp\left(i\hat{\mathcal{H}}t\right) \hat{\mathcal{H}} \tag{2.61}$$

Using the definition of $\hat{\rho}(t)$ and the commutator, this expression is immediately simplified as

$$\frac{\partial}{\partial t}\hat{\rho}(t) = -i\left[\hat{\mathcal{H}}, \hat{\rho}(t)\right], \tag{2.62}$$

which is known more generally as the Liouville-von Neumann equation. It is a central result of statistical quantum dynamics and will be the foundation of the discussions to follow on coherent dynamics. Thus, it is important that manipulations of this equation are understood.

We begin by identifying the equilibrium density matrix, $\hat{\rho}_0$, for a spin system. The various states of the density matrix will be populated according to Boltzmann statistics, such that:

$$\hat{\rho}_{ii} = \frac{\exp\left(\frac{-\hat{\mathcal{H}}_{ii}}{k_B T}\right)}{\mathrm{Tr}\left[\exp\left(\frac{-\hat{\mathcal{H}}}{k_B T}\right)\right]} = \frac{\exp\left(\frac{-E_i}{k_B T}\right)}{\mathrm{Tr}\left[\exp\left(\frac{-E_i}{k_B T}\right)\right]} \tag{2.63}$$

Importantly, the density matrix thermalizes according to the Hamiltonian eigenbasis. More specifically, the entropy of a density matrix is given by the Von Neumann entropy:

$$S = -\mathrm{Tr}[\rho \ln \rho] \tag{2.64}$$

In the case where $\hat{\rho} \propto \hat{E}$, the identity matrix, S is maximized. In accordance with this, the hypothesis of random phases states that any $\hat{\rho}_{ij} = 0$ at equilibrium in an effort to maximize the entropy of the system. We will use the case of NMR as an example. As the Zeeman interaction is conventionally orders of magnitude larger than any of the other spin interactions for spin-1/2 nuclei in an isotropic liquid, we can assume that only this interaction affects the initial density matrix. Only the population difference, or polarization, between different states is important, as radiation can only interrogate differences in populations in an ensemble. For instance, the thermal polarization of a spin-1/2 nucleus is then:

$$P = \frac{\exp\left(\frac{\gamma B_0}{2k_B T}\right) - \exp\left(\frac{-\gamma B_0}{2k_B T}\right)}{\exp\left(\frac{\gamma B_0}{2k_B T}\right) + \exp\left(\frac{-\gamma B_0}{2k_B T}\right)} = \tanh\left(\frac{\gamma B_0}{2k_B T}\right) \tag{2.65}$$

For the case of a ^{1}H at 1T, $\gamma B_0 \approx 0.02\ cm^{-1}$ (a convenient unit for these calculations) whereas $k_B T \approx 207\ cm^{-1}$ at room temperature, so the polarization is on the order of 10^{-5}. Naturally, this is a factor of 10 smaller for rare nuclei like ^{15}N, which have a gyromagnetic ratio that is ~1/10 that of the ^{1}H. This small spin polarization is the motivation of hyperpolarization methods. However, it is clearer why the common hyperpolarization methods that are available do not often approach polarization in the "brute force" method, as in cooling the system to cryogenic temperatures and relying on the Boltzmann polarization given by eq. 2.65. To achieve a 1% spin polarization on a ^{1}H by thermal methods, one would need a magnetic field of 2.93 kT (the world record is 2.8 kT generated by explosive induction at VNIIEF[98]) or one can cool the sample to 150 mK in a clinical 1.5T magnetic field, but if the goal is to use hyperpolarization methods with clinical research, either method lacks biocompatibility.

In either the hyperpolarized limit or for thermally polarized conditions, the initial density matrix can be written for a single spin system in terms of the spin operator $\hat{I}_z$ as:

$$\hat{\rho}_0 = \frac{1}{2}\hat{E}_2 + \tanh\left(\frac{\gamma B_0}{2k_B T}\right)\hat{I}_z \tag{2.66}$$

For a multi-spin system, one can take the tensor product of the single-spin initial density matrix, but realizing that the polarization $P \ll 1$, only retain terms linear in the polarization. This is known as the high temperature approximation in NMR and is valid under most experimental conditions. However, adding a single field gradient to simple pulse sequences recovers nonlinear terms ($\hat{I}_{1z}\hat{I}_{2z}\cdots$) and is the basis for intermolecular Multiple Quantum Coherences (iMQC)[99-103]. The thermal density matrix can be written for an N-spin system as:

$$\hat{\rho}_0 = \frac{1}{2^N}\hat{E}_{2^N} + 2\sum_i^N \tanh\left(\frac{\gamma_i B_0}{2k_B T}\right)\hat{I}_{iz} \tag{2.67}$$

However, it is important to note that the Liouville-von Neumann equation is linear in the spin density, so the numerical prefactor only contributes a scalar effect. In addition, the term proportional to identity will never evolve, so for brevity, we often only consider the reduced density matrix:

$$\hat{\rho}_0 \approx \sum_i^N \hat{I}_{iz} \tag{2.68}$$

The formalisms of NMR are a convenient method of describing spectroscopy in general, and thus the discussion herein will focus on NMR-specific examples. Optical examples will be introduced in Chapter 3. Before we may proceed to examine the dynamics of a spin system, we must first introduce the experimental geometry. By Lenz' law, a time-varying magnetic fields induces a voltage into a nearby coil. In NMR, our sample generates a time-varying magnetization as the transverse components of the nuclear spin relative to the leading field evolves under the Zeeman Hamiltonian. This evolution is called precession and will be derived explicitly in a moment. However, nuclear spin populations are polarized along the external field and have only a small component of the magnetization vector in the transverse plane as a result of the statistical noise of a macroscopic system. However, we may greatly enhance the observed signal rotating the nuclear spin into the transverse plane and measure the evolving bulk magnetization.

Resonant excitation in any spectroscopy involves the use of an electromagnetic field with a carrier frequency that is the same (or nearly the same) energy as the energy difference between the ground and excited states. When the field is resonant with the transition, there is

efficient power transfer from the field to the system, causing excitation. In magnetic resonance, this pulse is at radiofrequencies, applied along an axis in the *xy*-plane, which causes the spin to rotate into the transverse plane and be available for observation via the inductive coil. If the field is then pulsed quickly, all transitions within the bandwidth of the pulse will be resonantly excited. This is the basis for nearly all pulsed NMR experiments (Fig. 7).

We will begin with the simplest of multi-level spin systems: two coupled spin-1/2 particles that have the same resonance frequency. In the conventional NMR (Pople) notation, this is an A_2 spin system. The letter describes the resonance frequency of the spin and the subscript indicates the number of spins in that system at that frequency. More intricate examples of Pople notation will be described later. The full Hamiltonian during the pulse, which in Fig. 7 is shown with 'x'-phase, for the A_2 system is:

$$\hat{\mathcal{H}}(t) = \omega_0\left(\hat{I}_{1z} + \hat{I}_{2z}\right) + 2\pi J_{12}\boldsymbol{I}_1 \cdot \boldsymbol{I}_2 + \gamma B_x \cos\left(\omega_{rf} t\right)\left(\hat{I}_{1x} + \hat{I}_{2x}\right) \qquad (2.69)$$

The quantity $\gamma B_x = \omega_x$, which is the nutation frequency and is indicative of the pulse power. In the most common case, $\omega_x \gg J_{12}$, and if we are interested in the evolution for times much shorter than $1/J_{12}$ we can write:

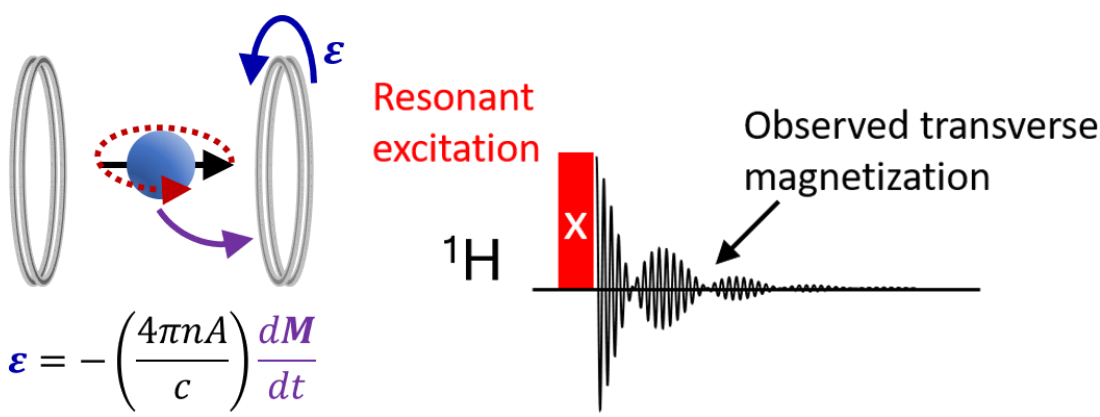

Figure 7: Detection in an NMR experiment. The oscillating magnetization of the sample induces a voltage in a coil proportional to the dM/dt. A resonant pulse is applied to the system, allowing for excitation of the bulk magnetization into the transverse plane of the sample. This magnetization oscillates and is detected by a nearby coil through magnetic induction.

$$\hat{\mathcal{H}}(t) \approx \omega_H\left(\hat{I}_{1z} + \hat{I}_{2z}\right) + \omega_x \cos\left(\omega_{rf} t\right)\left(\hat{I}_{1x} + \hat{I}_{2x}\right) \tag{2.70}$$

This Hamiltonian is time dependent, which complicates interpretation of the dynamics. It is convenient to express the Hamiltonian in a frame where it appears to be time-independent, called the rotating frame transformation, which is defined by a rotation about the z-axis as:

$$\tilde{\psi}(t) \to e^{i\omega_{rf}\hat{I}_z t}\psi(t) \tag{2.71}$$

If we substitute this into the Schrödinger equation, we get:

$$\begin{aligned} i\frac{\partial}{\partial t}\tilde{\psi}(t) &= i\frac{\partial}{\partial t}e^{i\omega_{rf}\hat{I}_z t}\psi(t) = -\omega_{rf}\hat{I}_z\tilde{\psi}(t) + e^{i\omega_{rf}\hat{I}_z t}\mathcal{H}(t)\psi(t) \\ &= -\omega_{rf}\hat{I}_z\tilde{\psi}(t) + e^{i\omega_{rf}\hat{I}_z t}\mathcal{H}(t)e^{-i\omega_{rf}\hat{I}_z t}\tilde{\psi}(t) \\ &= \left[-\omega_{rf}\hat{I}_z + e^{i\omega_{rf}\hat{I}_z t}\mathcal{H}(t)e^{-i\omega_{rf}\hat{I}_z t}\right]\tilde{\psi}(t) \end{aligned} \tag{2.72}$$

Thus, the rotating frame Hamiltonian is given by:

$$\tilde{\mathcal{H}}(t) = -\omega_{rf}\hat{I}_z + e^{i\omega_{rf}\hat{I}_z t}\mathcal{H}(t)e^{-i\omega_{rf}\hat{I}_z t} \tag{2.73}$$

Writing the rotating frame Hamiltonian for just one of the spins:

$$\tilde{\mathcal{H}}(t) = -\omega_{rf}\hat{I}_z + e^{i\omega_{rf}\hat{I}_z t}\begin{Bmatrix} \omega_0\hat{I}_z + \\ \omega_x\left(\dfrac{\hat{I}^+ + \hat{I}^-}{2}\right)\left(\dfrac{e^{i\omega_{rf}t} + e^{-i\omega_{rf}t}}{2}\right) \end{Bmatrix} e^{-i\omega_{rf}\hat{I}_z t} \tag{2.74}$$

Here, we have expanded $\hat{I}_x \equiv \hat{I}^+ + \hat{I}^-$ (for norm-1/2 $\hat{I}^{\pm}$) and used the Euler expansion of $\cos(x)$. At this juncture, it is important to introduce a particularly useful mathematical tool that pertains to cyclically commuting operators, like the spin-1/2 matrices. For any three operators that cyclically commute like

$$\left[\hat{X}, \hat{Y}\right] = i\epsilon_{XYZ}\hat{Z}, \tag{2.75}$$

where ϵ_{XYZ} is the Levi-Civita symbol, these operators have the relation

$$e^{-i\vartheta\hat{X}}\hat{Y}e^{i\vartheta\hat{X}} = \hat{Y}\cos(\vartheta) + \epsilon_{XYZ}\hat{Z}\sin(\vartheta) \tag{2.76}$$

The Zeeman term commutes with the rotating frame transformation and thus can be removed from the terms rotating the Hamiltonian:

$$\widetilde{\mathcal{H}}(t) = (\omega_0 - \omega_{rf})\hat{I}_z + \omega_x e^{i\omega_{rf}\hat{I}_z t}(\hat{I}^+ + \hat{I}^-)e^{-i\omega_{rf}\hat{I}_z t}\left(\frac{e^{i\omega_{rf}t} + e^{-i\omega_{rf}t}}{2}\right) \tag{2.77}$$

It can be found that using the commutation relations above that:

$$e^{-i\vartheta\hat{I}_z}\hat{I}^+e^{i\vartheta\hat{I}_z} = \hat{I}^+e^{i\vartheta};\ e^{-i\vartheta\hat{I}_z}\hat{I}^-e^{i\vartheta\hat{I}_z} = \hat{I}^-e^{-i\vartheta} \tag{2.78}$$

This permits us to write:

$$\begin{aligned}\widetilde{\mathcal{H}}(t) &= (\omega_0 - \omega_{rf})\hat{I}_z + \omega_x(\hat{I}^+e^{-i\omega_{rf}t} + \hat{I}^-e^{i\omega_{rf}t})\left(\frac{e^{i\omega_{rf}t} + e^{-i\omega_{rf}t}}{2}\right) \\ &= (\omega_0 - \omega_{rf})\hat{I}_z + \omega_x\left(\frac{\hat{I}^+ + \hat{I}^-}{2} + \frac{\hat{I}^+e^{-2i\omega_{rf}t} + \hat{I}^-e^{2i\omega_{rf}t}}{2}\right)\end{aligned} \tag{2.79}$$

Here, we can make the approximation that for $\frac{\omega_x}{\omega_{rf}} \ll 1$ that the counter-rotating terms are insignificant and can be ignored, which is called the rotating wave approximation. Thus, the Hamiltonian is given by:

$$\widetilde{\mathcal{H}} \approx \Delta\omega(\hat{I}_{1z} + \hat{I}_{2z}) + \frac{\omega_x}{2}(\hat{I}_{1x} + \hat{I}_{2x}) \tag{2.80}$$

The definition $\Delta\omega = \omega_0 - \omega_{rf}$ is the resonance offset from the pulse carrier frequency. Often, the nutation frequency is simply redefined such that the factor of half is absorbed. Notably, this removes the time-dependence of the Hamiltonian, which makes evaluation of the dynamics significantly easier. Given fully resonant excitation, the Hamiltonian would reduce further to:

$$\widetilde{\mathcal{H}} \approx \omega_x(\hat{I}_{1x} + \hat{I}_{2x}) \tag{2.81}$$

Now we are ready to perform the propagation of the initial density matrix first under the pulse and then under the full Hamiltonian. This can be done by simply substituting the initial density matrix (eq. 2.68) and the Hamiltonian of the pulse (eq. 2.81) into the Liouville-von Neumann equation like:

$$\hat{\rho}(t) = e^{-i\omega_x(\hat{I}_{1x}+\hat{I}_{2x})t}\left(\hat{I}_{1z} + \hat{I}_{2z}\right)e^{i\omega_x(\hat{I}_{1x}+\hat{I}_{2x})t} \tag{2.82}$$

Operators that act on spin 1 will not affect spin 2 unless it is a product operator like $\hat{I}_{1x}\hat{I}_{2x}$. For example, $\hat{I}_{2x}$ will commute with $\hat{I}_{1z}$. This allows us to rearrange this into:

$$\hat{\rho}(t) = e^{-i\omega_x t\hat{I}_{1x}}\hat{I}_{1z}e^{i\omega_x t\hat{I}_{1x}} + e^{-i\omega_x t\hat{I}_{2x}}\hat{I}_{2z}e^{i\omega_x t\hat{I}_{2x}} \tag{2.83}$$

We may simplify the argument of the exponential by defining a pulse angle $\vartheta = \omega_x t$:

$$\hat{\rho}(\vartheta) = e^{-i\vartheta\hat{I}_{1x}}\hat{I}_{1z}e^{i\vartheta\hat{I}_{1x}} + e^{-i\vartheta\hat{I}_{2x}}\hat{I}_{2z}e^{i\vartheta\hat{I}_{2x}} \tag{2.83}$$

Using the commutation relation:

$$\hat{\rho}(\vartheta) = \cos(\vartheta)\left(\hat{I}_{1z} + \hat{I}_{2z}\right) - \sin(\vartheta)\left(\hat{I}_{1y} + \hat{I}_{2y}\right) \tag{2.84}$$

When $\vartheta = \frac{\pi}{2}$, only the transverse components of the spin remain, thus maximizing the signal collected by the coil in placed in the transverse plane of the NMR. This sinusoidal response with respect to the pulse flip angle is called nutation and is also referred to Rabi cycling. Experimentally, this must be calibrated for a certain pulse power, and is often on the order of microseconds for typical powers of what are called 'hard' pulses. A 'hard' pulse uses a large amplitude, so that the Hamiltonian may be approximated as only evolving under the radiofrequency excitation. This implies the existence of 'soft' pulses, which are used in the work here, although there is no official delineation between these limits. By convention, a pulse of $\vartheta = 90°$ (or $\pi/2$) and x-phase is called a 90_x pulse.

In addition to excitation, as described above, it is also of interest to perform inversion of the spins. For instance, setting $\vartheta = \pi$ drives the system from the initial condition of $\hat{I}_{1z} + \hat{I}_{2z}$ to $-(\hat{I}_{1z} + \hat{I}_{2z})$. In other words, it takes the population from $|\alpha\rangle$ and interchanges it with the $|\beta\rangle$ population. As $\vartheta = \omega_x t$, this is often accomplished by simply doubling the pulse length. However, note that if the pulse length is again doubled such that $\vartheta = 2\pi$ that the system is returned to its initial state, which is a characteristic property of quantum dynamics. The ideas that pulses can allow for the interchange of populations will become paramount in the following discussions.

At the point of eq. 2.84 for $\vartheta = \pi/2$, we have rotated the nuclear spin to be in the transverse plane, and thus the macroscopic magnetization of the sample may be detected by inductively coupling it to a nearby coil. It is pertinent to discuss how the NMR signal is collected at this point. NMR frequencies are on the order of ~100 MHz, which is a cycle time of 10 ns. Often, the analog NMR signal detected by the coil is first down-sampled and amplified using a quadrature lock-in amplifier referenced to ω_{rf}. This signal is then integrated over a dwell time (which gives the spectral width) and digitized to give the observed time-domain signal. Thus, it is essentially as if detection is performed in the rotating frame. Thus, we may continue to utilize the rotating frame to describe evolution in the system, as it will be indicative of the signal that is measured in an NMR spectrometer. The J-coupling term in the Hamiltonian commutes with the Zeeman term in the A_2 system, it does not matter in what order interaction the system is evolved. Evolution under the Zeeman Hamiltonian gives:

$$\hat{\rho}(t) = -e^{-i\Delta\omega(\hat{I}_{1z}+\hat{I}_{2z})t}\left(\hat{I}_{1y} + \hat{I}_{2y}\right)e^{i\Delta\omega(\hat{I}_{1z}+\hat{I}_{2z})t} \tag{2.85}$$

Using the same commutation properties of the operators, this can be again propagated to give:

$$\hat{\rho}(t) = -\cos(\Delta\omega t)\left(\hat{I}_{1y} + \hat{I}_{2y}\right) + \sin(\Delta\omega t)\left(\hat{I}_{1x} + \hat{I}_{2x}\right) \tag{2.86}$$

From here, we note that the J-coupling interaction $\boldsymbol{I}_1 \cdot \boldsymbol{I}_2$ commutes with both $\hat{I}_{1y} + \hat{I}_{2y}$ and $\hat{I}_{1x} + \hat{I}_{2x}$ in eq. 2.86, and thus does not appear in the detected signal. However, it does not necessarily mean that the coupling does not exist. For instance, the H_2 molecule has a J-coupling between the two ^1H but this value cannot be extracted from an NMR spectrum of this species. However, the $^1J_{HD}$ coupling is observable as $^1H^2D$ is no longer an A_2 system but an AX system. It is measured to be $^1J_{HD} = 42.8$ Hz, and by eq. 2.44, $^1J_{HH}$ may be approximated to first order as $^1J_{HH} = \frac{\gamma_H}{\gamma_D}\,^1J_{HD} \approx 280\ Hz$.

While the approach for analytically solving $\hat{\rho}(t)$ described above works well in the case where all terms in the Hamiltonian commute at all times, it breaks down in the case where the Hamiltonian does not commute with itself at all times. This does not necessarily mean that $\hat{\mathcal{H}}$ is time-dependent, although that will be a case that we will examine momentarily. The simplest of these cases is off resonance excitation with a soft-pulse, where $\frac{\Delta\omega}{\omega_x} \ll 1$ is no longer valid. Under these conditions, the rotating frame Hamiltonian for a single spin is

$$\hat{\mathcal{H}} = \Delta\omega\hat{I}_z + \omega_x\hat{I}_x \tag{2.87}$$

There are a few approaches to solving $\hat{\rho}(t)$ under this Hamiltonian, which is given exactly as:

$$\hat{\rho}(t) = \exp\left(-i\left(\Delta\omega\hat{I}_z + \omega_x\hat{I}_x\right)t\right)\hat{I}_z\exp\left(i\left(\Delta\omega\hat{I}_z + \omega_x\hat{I}_x\right)t\right) \tag{2.88}$$

The predicament is that the $\Delta\omega\hat{I}_z$ commutes with the initial reduced density matrix $\hat{I}_z$, but as soon as ω_x acts to rotate the initial density matrix away from $\hat{I}_z$, this term will become active. As such, one cannot evolve each component of the Hamiltonian sequentially, as they do not commute. For this case, it is often common to undergo a basis set transformation that makes

the Hamiltonian appear to rotate about an effective field so to reduce the Hamiltonian to a single term. While that approach is useful here, we explore a more general approach that will be a key tool to be used in later chapters. We may first perform the series expansion solution of the density matrix

$$\hat{\rho}(t) = \sum_{n=0}^{\infty} \frac{t^n}{n!} \frac{\partial^n}{\partial t^n} \hat{\rho}(t), \tag{2.89}$$

which is simply the formal definition of the Maclaurin expansion. Each of the higher order time derivatives are given by iteratively substituting the Liouville-von Neumann equation into itself as:

$$\frac{\partial^n}{\partial t^n} \hat{\rho}(t) = i \left[\frac{\partial^{n-1}}{\partial t^{n-1}} \hat{\rho}(t), \hat{\mathcal{H}} \right] \tag{2.90}$$

We will introduce the notation

$$\frac{\partial^n}{\partial t^n} \hat{\rho}(t) = i \left[\frac{\partial^{n-1}}{\partial t^{n-1}} \hat{\rho}(t), \hat{\mathcal{H}} \right] \tag{2.91}$$

for brevity. Substituting this into the series expansion yields:

$$\hat{\rho}(t) = \hat{\rho}_0 + i[\hat{\rho}_0, \hat{\mathcal{H}}]t + i \left[\frac{\partial}{\partial t} \hat{\rho}(t), \hat{\mathcal{H}} \right] \frac{t^2}{2} + \cdots = \sum_n \hat{\rho}^{(n)}(t) \tag{2.91}$$

The notation $\hat{\rho}^{(n)}(t)$ indicates the n-th term in the series expansion. For the moment, we have assumed that $\hat{\mathcal{H}}$ is time-independent. The sequence of terms from the Hamiltonian that must act to generate a desired $\hat{\rho}(t)$ is then known as the spin operator pathway, coherence pathway, or most generally as the Liouville pathway. To exemplify this, we will iteratively expand $\hat{\rho}(t)$ for the case of off-resonant excitation:

$$\hat{\rho}^{(0)} = \hat{I}_z$$

$$\hat{\rho}^{(1)} = i\left[\hat{I}_z, \Delta\omega\hat{I}_z + \omega_x\hat{I}_x\right]t = i\left(\left[\hat{I}_z, \Delta\omega\hat{I}_z\right] + \left[\hat{I}_z, \omega_x\hat{I}_x\right]\right)t = -\hat{I}_y(\omega_x t)$$

$$\hat{\rho}^{(2)} = i\left[-\omega_x\hat{I}_y, \Delta\omega\hat{I}_z + \omega_x\hat{I}_x\right]\frac{t^2}{2} = i\begin{pmatrix}\left[-\omega_x\hat{I}_y, \Delta\omega\hat{I}_z\right] + \\ \left[-\omega_x\hat{I}_y, \omega_x\hat{I}_x\right]\end{pmatrix}\frac{t^2}{2} \tag{2.92}$$

$$= \left(-\omega_x\left(-\Delta\omega\hat{I}_x\right) - \omega_x\left(\omega_x\hat{I}_z\right)\right)\frac{t^2}{2} = \hat{I}_x\left(\frac{\omega_1\Delta\omega t^2}{2}\right) - \hat{I}_z\left(\frac{\omega_x^2 t^2}{2}\right)$$

Naturally, the solutions are only valid for short times unless a large number of terms are calculated. However, this provides analytical insight into the evolution of the system, which can permit the development and interpretation of experiments.

To this point, we have assumed that the Hamiltonian $\widehat{\mathcal{H}}$ has been time-independent for simplicity. When $\widehat{\mathcal{H}}(t)$ changes with time, calculating $\hat{\rho}(t)$ is no longer a simple task, as the propagator is no longer simply $\exp\left(-i\widehat{\mathcal{H}}t\right)$ and is instead given by the time-ordered exponential $\vec{\mathcal{T}}\exp\left(-i\int_0^t dt'\,\widehat{\mathcal{H}}(t')\right)$. However, if we think about $\widehat{\mathcal{H}}(t)$ generating a trajectory between an initial state $\hat{\rho}_1$ and a final state $\hat{\rho}_2$ over some period T, then we should be able to construct a Hamiltonian $\overline{\mathcal{H}}$ that maps $\hat{\rho}_1 \rightarrow \hat{\rho}_2$ in a time-independent fashion (Fig. 8). This is called Average Hamiltonian Theory[2, 91], where the first three terms of the average Hamiltonian are given by:

$$\overline{\mathcal{H}}^{(0)} = \frac{1}{T}\int_0^T dt_1\,\overline{\mathcal{H}}(t_1)$$

$$\overline{\mathcal{H}}^{(1)} = \frac{1}{2iT}\int_0^T dt_1\int_0^{t_1} dt_2\left[\widehat{\mathcal{H}}(t_1), \widehat{\mathcal{H}}(t_2)\right] \tag{2.93}$$

$$\overline{\mathcal{H}}^{(2)} = \frac{-1}{6T}\int_0^T dt_1\int_0^{t_1} dt_2\int_0^{t_2} dt_3\begin{pmatrix}\left[\widehat{\mathcal{H}}(t_1), \left[\widehat{\mathcal{H}}(t_2), \widehat{\mathcal{H}}(t_3)\right]\right] \\ +\left[\left[\mathcal{H}(t_1), \widehat{\mathcal{H}}(t_2)\right], \mathcal{H}(t_3)\right]\end{pmatrix}$$

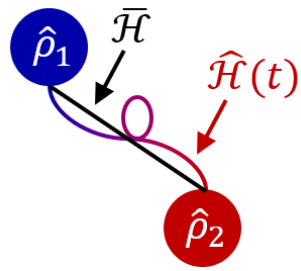

Figure 8: Average Hamiltonian description of system interactions. When $\hat{\mathcal{H}}(t)$ varies with time, the trajectory between any point $\hat{\rho}_1$ and $\hat{\rho}_2$ can be described by a complex pathway. However, there exists an average trajectory between these points given by the average Hamiltonian $\bar{\mathcal{H}}$. Successively higher approximations of $\bar{\mathcal{H}}$ improve the average trajectory and bring the system closer to the final point $\hat{\rho}_2$.

There is an inherent time-ordering of the Hamiltonians such that $t_3 \leq t_2 \leq t_1 \cdots$ that is enforced by $\vec{\mathcal{T}}$. The zeroth order average Hamiltonian $\bar{\mathcal{H}}^{(0)}$ is simply the average of $\hat{\mathcal{H}}(t)$, and $\bar{\mathcal{H}}^{(1)}$ is proportional to the autocorrelation of the Hamiltonian. An ideal case to examine is when the pulse is amplitude modulated, such as by a Gaussian function with a pulse width σ. For the case when $\Delta\omega/\omega_x \ll 1$, we can simplify the rotating frame Hamiltonian to:

$$\hat{\mathcal{H}}(t) = \frac{A_x}{\sigma\sqrt{2\pi}} \exp\left(\frac{-t^2}{2\sigma^2}\right) \hat{I}_x \tag{2.94}$$

A_x is the pulse area in units of rad s^{-1} and, as this pulse is only amplitude modulated, it commutes with itself at all times. Only the $\bar{\mathcal{H}}^{(0)}$ will be non-zero, as all higher order terms are proportional to commutators of $\hat{\mathcal{H}}(t)$ with itself. This gives:

$$\bar{\mathcal{H}}^{(0)} = \frac{1}{T}\int_{-T/2}^{T/2} dt_1 \, \frac{A_x}{\sigma\sqrt{2\pi}} \exp\left(\frac{-t_1^2}{2\sigma^2}\right) \hat{I}_x = \frac{A_x \hat{I}_x}{T} \tag{2.94}$$

Experimentally, the pulse may only be applied to the system for a finite amount of time and is thus only an approximation to a Gaussian. The period $T \geq 6\sigma$ for this to be a relatively robust Gaussian pulse, otherwise truncation of the Gaussian will generate large distortions in the response of the system. Here, we see that the dynamics will only be dependent on the

pulse area, which is equivalently the pulse flip angle. As such, any shape that retains the area will have an identical $\bar{\mathcal{H}}^{(0)}$.

Until this point, we have assumed that evolution in the system was only quantum mechanical, which is generally referred to as coherent evolution where the state at a time $\hat{\rho}(t+\tau)$ is related to the state at a time $\hat{\rho}(t)$ by a unitary transformation. Coherent evolution can take place both microscopically as well as at the ensemble level. In constructing the ensemble averaged density matrix, we ultimately omit any interactions between particles, which leads to solutions of the Liouville-von Neumann equation that do not reflect reality. Exciting the system into a coherence drives it away from its equilibrium state, and so the density matrix must also be allowed to thermalize, or relax, back to its initial state. In magnetic resonance, relaxation is induced by the rotational diffusion of each molecule in the ensemble, which happens on the femtosecond to picosecond timescale. While these scales are much faster than the nanosecond timescale of the Zeeman interaction in most superconducting magnetic fields, it is still dominant enough to cause time-dependent fluctuations of spin interactions that are orientation-dependent, such as the dipolar coupling and chemical shift interaction. As the motion is random, this effect is often referred to as a stochastic interaction. This treatment was first introduced by Redfield in 1957[93]. To include relaxation, we may expand the Hamiltonian to have a time-independent component, where all the coherent dynamics take place, and a time-dependent component which describes the stochastically modulated spin interactions:

$$\hat{\mathcal{H}} = \hat{\mathcal{H}}_0 + \hat{\mathcal{H}}_1(t) \tag{2.95}$$

Substituting this Hamiltonian into the Liouville-von Neumann equation gives:

$$\frac{\partial}{\partial t}\hat{\rho}(t) = -i\left[\hat{\mathcal{H}}_0 + \hat{\mathcal{H}}_1(t), \hat{\rho}(t)\right] \tag{2.96}$$

As is common in these derivations[1, 104-106], we shall boost the reference frame to the interaction representation, using the stationary component of the Hamiltonian, $\hat{\mathcal{H}}_0$, as the reference. This process is mathematically identical to boosting the frame into the rotating frame of the pulse, but instead using $\hat{\mathcal{H}}_0$ to define the reference-frame. For simplicity of notation, hats will be dropped from operators to denote interaction frame. As such, eq. 2.96 becomes:

$$\frac{\partial}{\partial t}\rho(t) = -i[\mathcal{H}_1(t), \rho(t)] \tag{2.97}$$

This partial differential equation may be formally integrated with a Dyson time order operator $\vec{\mathcal{T}}$, which enforces $t' < t$, to give the solution

$$\rho(t) = \rho_0 - i\vec{\mathcal{T}}\int_0^t dt'[\mathcal{H}_1(t'), \rho(t')]. \tag{2.98}$$

Equation 2.98 is then iteratively substituted into the right-hand side of eq. 2.97 to achieve successively higher-order perturbative approximations to the solution, which generates the so-called Dyson series. In the limit where $\|\hat{\mathcal{H}}_1(t)\| \ll \|\hat{\mathcal{H}}_0\|$, which is well within the limit of magnetic resonance, the series can be truncated to second order as higher order terms become negligible under this limit. The equation of motion is then

$$\frac{\partial}{\partial t}\rho(t) = -\vec{\mathcal{T}}\int_0^t dt'\left[\mathcal{H}_1(t), [\mathcal{H}_1(t'), \rho(t')]\right] \tag{2.99}$$

where all terms proportional to the initial density are dropped, as a thermalized spin density commutes with all relaxation mechanisms (it is a fully relaxed state). Here, $\mathcal{H}_1(t)$ is taken to be Hermitian. We will additionally assume that the system has no memory of its prior state, which makes the process Markovian and permits us to make the substitution $\rho(t') \to \rho(t)$:

$$\frac{\partial}{\partial t}\rho(t) = -\vec{\mathcal{T}}\int_0^t dt'\left[\mathcal{H}_1(t),[\mathcal{H}_1(t'),\rho(t)]\right] \tag{2.100}$$

To make further progress, we must introduce the operator expansion of $\mathcal{H}_1(t)$, which is going to be kept as general as possible to begin. This Hamiltonian describes the spin-bath interaction via an operator describing the random motional dynamics of the surrounding spins $\hat{F}_k(t)$, which induce fluctuating local magnetic fields, and the spin-bath coupling operator terms $\hat{A}_k(t)$. The subscript k indexes over all the stochastically modulated spin interactions. As $\hat{A}_k(t)$ are formally quantum mechanical interactions, the operators have well-defined forms. Furthermore, $\hat{A}_k$ are eigenfunctions of $\hat{\mathcal{H}}_0$ and thus can be written

$$A_k(t) = e^{-i\hat{\mathcal{H}}_0 t}\hat{A}_k e^{i\hat{\mathcal{H}}_0 t} = \hat{A}_k e^{-i\omega_k t} \tag{2.101}$$

$\hat{F}_k(t)$ is not a conventionally quantum mechanical interaction, and thus does not have a well-defined operator form. However, it acts at the ensemble-level and thus commutes with ρ. The Hamiltonian is then:

$$\mathcal{H}_1(t) = \sum_k F_k(t)A_k(t) = \sum_k F_k(t)\hat{A}_k e^{-i\omega_k t} \tag{2.102}$$

Substituting this equation back into eq. 2.100, using the commutation of $F_k(t)$, and ensemble averaging gives (dropping formal time-dependence of ρ):

$$\frac{\partial}{\partial t}\rho = -\vec{\mathcal{T}}\sum_{jk}\int_0^t dt'\left[A_j(t),[A_k(t'),\rho]\right]\langle F_j(t)F_k(t')\rangle \tag{2.103}$$

Note that only the stochastic components require the ensemble average. We will now assume that the ensemble-level dynamics are stationary, i.e. the rate of orientational dynamics is time-independent and has no drift. Doing so makes the only important time metric the difference time between t and t'. As such, we make the change of variables $t - t' = \tau$, which gives:

$$\frac{\partial}{\partial t}\rho = -\sum_{jk}\int_0^t d\tau \left[A_j(\tau), \left[\hat{A}_k, \rho\right]\right] \left\langle F_j(\tau)\hat{F}_k\right\rangle \tag{2.104}$$

Note that $\vec{\mathcal{T}}$ is no longer required. We may use the eigenvalue expansion of $\hat{A}_j$ to move the time dependence out of the double commutator as:

$$\frac{\partial}{\partial t}\hat{\sigma} = -\sum_{jk}\left[\hat{A}_j, \left[\hat{A}_k, \rho\right]\right] \int_0^t d\tau \left\langle F_j(\tau)\hat{F}_k\right\rangle e^{-i\omega_j\tau} \tag{2.105}$$

The quantity $\left\langle F_j(\tau)\hat{F}_k\right\rangle$ is the molecular correlation function $g_{jk}(\tau)$, which describes the tumbling of molecules in solution. If we assume that the molecules in solution tumble isotropically with uniform and constant intermolecular forces, we can model the trajectory in 1D as an Einstein random-walk, giving the functional form of the correlation function as:

$$g_{jk}(t) = e^{-|t|/\tau_c}\delta_{jk} \tag{2.106}$$

The parameter τ_c is the correlation time of the molecular tumbling and dictates the rate of relaxation of molecules. We have also imposed δ_{jk}, meaning that each orientationally-modulated interaction is self-correlated. For most liquids at room temperature, τ_c is on the order of a few picoseconds, and given all coherent spin interactions are at most on the nanosecond, we may extend upper limit of integration in equation 2.105 to infinity:

$$\frac{\partial}{\partial t}\rho = -\sum_{k}\left[\hat{A}_k, \left[\hat{A}_k, \rho\right]\right] \int_0^\infty d\tau\, g_k(\tau)e^{-i\omega_k\tau} \tag{2.107}$$

If we neglect the odd-component of the integral, which in NMR is negligible and realize that $g_k(\tau)$ is even, we may extend the lower limit to negative infinity

$$\frac{\partial}{\partial t}\rho = -\frac{1}{2}\sum_{k}\left[\hat{A}_k, \left[\hat{A}_k, \rho\right]\right] \int_{-\infty}^\infty d\tau\, g_k(\tau)e^{-i\omega_k\tau} \tag{2.108}$$

Note that the factor of $1/2$ arises when extending the lower limit of the integral. Now, the integral is the single-point Fourier transform of $g_k(\tau)$, which is often called the spectral density function and is given the notation

$$\frac{1}{2}\int_{-\infty}^{\infty} d\tau\, g_k(\tau)e^{-i\omega_k\tau} = \mathcal{J}_k(\omega_k) \tag{2.109}$$

This gives a relatively simple form for what is often referred to as the relaxation dissipator.

$$\frac{\partial}{\partial t}\rho = -\sum_k \left[\hat{A}_k, \left[\hat{A}_k, \rho\right]\right] \mathcal{J}_k(\omega_k) \tag{2.110}$$

This derivation is somewhat limited in the definition of what the equilibrium state is, as this dissipator will drive the system to unity, which is only achieved in the infinite-temperature limit. For a finite temperature, one often empirically makes the substitution $\hat{\rho} \to \hat{\rho} - \hat{\rho}_0$ to drive the system toward a realistic thermal equilibrium. The transformation from the interaction frame back to the lab frame then gives:

$$\frac{\partial}{\partial t}\hat{\rho} = -i\left[\hat{\mathcal{H}}_0, \hat{\rho}\right] - \sum_k \left[\hat{A}_k, \left[\hat{A}_k, \hat{\rho} - \hat{\rho}_0\right]\right] \mathcal{J}_k(\omega_k), \tag{2.111}$$

where $\hat{\rho}_0$ is the equilibrium density matrix. This is known as the 'master equation' of the Redfield relaxation theory[93], which is the most widely used theory for relaxation processes in magnetic resonance. Interestingly, as $\hat{\rho}_0 \approx \hat{E}$ for hyperpolarization experiments, i.e. when $\hat{\rho}$ largely deviates from $\hat{\rho}_0$, the empirical thermal correction may be dropped.

While the Redfield dissipator formally introduces the method by which relaxation is included in magnetic resonance, it is important to understand the physical interpretation of this equation. The orientational tumbling of molecules in solution has certain frequency components dependent on the correlation time of tumbling given by the spectral density

function $\mathcal{J}_k(\omega_k)$. If these interactions are modulated at a frequency that looks like an NMR transition frequency, the system can undergo that transition. The resulting transition rates that are allowed by each of the stochastically modulated interactions will then drive the system towards the equilibrium state.

2.3 Hyperpolarization methods and parahydrogen

At this juncture, it is pertinent to introduce the concepts of hyperpolarization methods, which aim to overcome the small thermal polarization in NMR by deriving polarization from an external source of spin order. For instance, the electron spin can be thermally polarized to nearly 100%, which has a gyromagnetic ratio ~660x of the proton, at temperatures of a few Kelvin and modest (3T) magnetic fields. Then, the electron spin will interact with nearby protons via the dipolar coupling, however the secular component of dipolar couplings for two unlike spins ($\hat{I}_z\hat{S}_z$) cannot transfer polarization. Even though they are small at high field, the non-secular terms of the dipolar coupling, such as $\hat{I}^{\pm}\hat{S}^{\mp}$, which flips spins in opposite directions, or $\hat{I}^{\pm}\hat{S}^{\pm}$, which flips spins in the same direction, are still active. When the electron spin is irradiated off-resonance by $\Delta\omega_e = \pm\omega_H$, these transitions become partially allowed and polarization flows from the electron to the protons, but only on the timescale of hours. This is known as the DNP solid-effect. In fact, it only works because the electron re-equilibrates with a time-constant of a few microseconds, thus regenerating its unity polarization, whereas the relaxation time of spin-1/2 in a solid at these temperatures is far longer, on the order of tens of minutes to hours[107]. For the reasons previously elaborated, we aim to overcome the limitations of DNP for a faster and cheaper alternative.

In search of an alternate source of spin order, it is at this point that we examine parahydrogen, the singlet spin isomer of dihydrogen. Let us examine the spin wavefunctions for a pair of spin-1/2 nuclei (A_2 system). In fact, it is easiest done by inspection of the A_2 Hamiltonian, which takes the form:

$$\hat{\mathcal{H}} = \begin{array}{c} \\ \langle\alpha\alpha| \\ \langle\alpha\beta| \\ \langle\beta\alpha| \\ \langle\beta\beta| \end{array} \begin{array}{c} \begin{array}{cccc} |\alpha\alpha\rangle & |\alpha\beta\rangle & |\beta\alpha\rangle & |\beta\beta\rangle \end{array} \\ \begin{pmatrix} \frac{J_{12}\pi}{2} - \omega_{0,H} & 0 & 0 & 0 \\ 0 & -\frac{J_{12}\pi}{2} & J_{12}\pi & 0 \\ 0 & J_{12}\pi & -\frac{J_{12}\pi}{2} & 0 \\ 0 & 0 & 0 & \frac{J_{12}\pi}{2} + \omega_{0,H} \end{pmatrix} \end{array} \tag{2.112}$$

The states $|\alpha\alpha\rangle$ and $|\beta\beta\rangle$ are disconnected states in this Hamiltonian, as there is no coupling element between these states and any other state, and are thus eigenstates. However, this is not true for the $|\alpha\beta\rangle$ and $|\beta\alpha\rangle$ states, which are coupled by off-diagonal matrix elements. According to the addition of angular momenta for two spin-1/2 particles, the only two possible total angular momentum (F) states are $F = 1$ (spin-1) and $F = 0$ (spin-0). As both the $|\alpha\alpha\rangle$ and $|\beta\beta\rangle$ states belong to the $F = 1$ manifold, linear combinations of the $|\alpha\beta\rangle$ and $|\beta\alpha\rangle$ states must produce an $F = 1$ and an $F = 0$ state. The states which do this are the spin-1 state $(|\alpha\beta\rangle + |\beta\alpha\rangle)/\sqrt{2}$ and spin-0 state $(|\alpha\beta\rangle - |\beta\alpha\rangle)/\sqrt{2}$. The spin-1 states are together the triplet states, which are delineated from one another by their magnetic moments, $T^+ = |\alpha\alpha\rangle$, $T^0 = (|\alpha\beta\rangle - |\beta\alpha\rangle)/\sqrt{2}$, and $T^- = |\beta\beta\rangle$, and are invariant to permutation. The spin-0 state is the singlet state, $S^0 = (|\alpha\beta\rangle - |\beta\alpha\rangle)/\sqrt{2}$, and is antisymmetric with respect to interchange. We may write the Hamiltonian in this basis as:

$$\hat{\mathcal{H}} = \begin{pmatrix} & |T^+\rangle & |T^0\rangle & |T^-\rangle & |S^0\rangle \\ \langle T^+| & \frac{J_{12}\pi}{2} + \omega_{0,H} & 0 & 0 & 0 \\ \langle T^0| & 0 & \frac{J_{12}\pi}{2} & 0 & 0 \\ \langle T^-| & 0 & 0 & \frac{J_{12}\pi}{2} - \omega_{0,H} & 0 \\ \langle S^0| & 0 & 0 & 0 & -\frac{3J_{12}\pi}{2} \end{pmatrix} \tag{2.113}$$

As this basis diagonalizes the Hamiltonian, it is also an eigenbasis. While the triplet states are magnetized and produce observables in the NMR experiment, the singlet state is NMR silent. The singlet state commutes with the secular dipolar Hamiltonian, $\hat{I}_z\hat{S}_z - \left(\hat{I}^+\hat{S}^- + \hat{I}^-\hat{S}^+\right)/4$, and spin-1/2 pairs that exist in this state are largely immune to relaxation processes, which are dominated by the dipolar interactions.

In the case where the A_2 system is dihydrogen (H_2), the Pauli exclusion principle requires that the total molecular wavefunction is permutation antisymmetric, as ^{1}H is a fermion. The total wavefunction is represented by the product of the wavefunctions of the various degrees of freedom, such that the total wavefunction Ψ is given by:

$$\Psi = \psi_{tr}\psi_{elec}\psi_{vib}\psi_{rot}\psi_{nuc} \tag{2.114}$$

The individual degrees of freedom are given by the translational ψ_{tr}, electronic ψ_{elec}, vibrational ψ_{vib}, rotational ψ_{rot}, and nuclear ψ_{nuc} wavefunctions. However, the only two degrees of freedom of these that will be affected by nuclear permutation are the rotational and nuclear wavefunctions, which then must obey the relation

$$P_{ij}\Psi = P_{ij}\psi_{rot}\psi_{nuc} = -\psi_{rot}\psi_{nuc}, \tag{2.115}$$

where P_{ij} permutes the nuclei. To satisfy the Pauli exclusion principle, this requires that only one of the two degrees of freedom can be in an antisymmetric wavefunction. For instance, if

dihydrogen is in the $|S^0\rangle$ state, it must occupy a symmetric (even) rotational state, which is called parahydrogen (*p*-H_2). Conversely, if dihydrogen occupies any of the triplet states, it must occupy an odd rotational state, which is called orthohydrogen (*o*-H_2).

To calculate the equilibrium fraction of parahydrogen, we must first remind ourselves of the energy levels of a rigid rotor, which are given for the Jth rotational state as:

$$E_J = B_e J(J+1), \tag{2.116}$$

where B_e is the equilibrium rotational constant, inversely proportional to the moment of inertia of the molecule. Importantly, each rotational energy level is (2*J*+1)-fold degenerate. For hydrogen, $B_e = 60.8\ cm^{-1}$. This means that the energy separation between the ground $J = 0$ and first excited $J = 1$ state is $\Delta E_{01} = 2B_e = 121.6\ cm^{-1}$, which is notably far larger than the Zeeman splitting of a proton at a conventional NMR field ($\Delta E_{\alpha\beta} \approx 0.02\ cm^{-1}$) and is on the order of $k_B T \approx 207\ cm^{-1}$. From the Boltzmann distribution, we may calculate the population in any rotational state relative to $J = 0$, N_J/N_0, as:

$$\frac{N_J}{N_0} = (2J+1)\exp\left(\frac{-B_e J(J+1)}{k_B T}\right) \tag{2.117}$$

Using the fractional population in each of the rotational states, we may calculate the parahydrogen enrichment (x_p) as

$$x_p = \frac{N_p}{N_p + N_o} = \frac{1}{Z_J}\sum_{J \in Evens}(2J+1)\exp\left(\frac{-B_e J(J+1)}{k_B T}\right), \tag{2.118}$$

where Z_J is the rotational partition function given by:

$$Z_J = \sum_{J \in Evens}(2J+1)\exp\left(\frac{-B_e J(J+1)}{k_B T}\right) \tag{2.119}$$

$$+ 3 \sum_{J \in Odds} (2J + 1) \exp\left(\frac{-B_e J(J+1)}{k_B T}\right)$$

Note that there is a factor of 3 scaling the odd rotational states to account for the degeneracy of the three triplet states, which are assumed to be approximately degenerate on the scale of the rotational energy.

Using the equations above, it is simple to calculate the parahydrogen and orthohydrogen enrichment as a function of the temperature (Fig. 9). Given the large rotational energy of dihydrogen, thermal cooling can be used to enrich the ground rotational state at even modest temperatures, like at liquid nitrogen (77K), often flowing the sample over a paramagnetic species like iron-(III)-oxide (rust) to relax the spin selection rules and allow for more efficient conversion. This setup is inexpensive (~200 USD), easy to use, and produces approximately 50% enriched *p*-H_2. More elaborate instrumentation can be used, such as the commercial Bruker parahydrogen generator, which operates under the same principles but at a temperature of 40K, generating 90% *p*-H_2.

The following chapters will examine how hyperpolarization is extracted from this non-equilibrium spin order. In particular, SABRE utilizes an organometallic iridium complex to

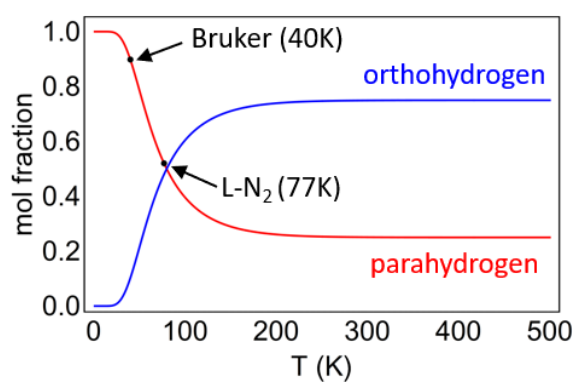

Figure 9: Enrichment of parahydrogen by cooling. Liquid nitrogen (77K) can be used to generate an enrichment of ~50% parahydrogen, whereas the commercial Bruker *p*H_2 generator operates at colder temperatures (40K) and is able to generate ~90% parahydrogen.

break the symmetry of the A_2 spin system of dihydrogen by asymmetrically coupling the two ^{1}H to (at least) one other spin-1/2 nucleus. Under these conditions, $|S_H^0\rangle$ is no longer an eigenstate of the system, and evolution out of this eigenstate permits hyperpolarization of target nuclei. But first, we must examine the theoretical underpinnings of SABRE and unify coherent evolution with chemical exchange.

Chapter 3: Unifying spin dynamics and chemical exchange in SABRE

A hallmark of quantum dynamics is that the state of the system at any time can be related to the state of the system at any other time by a unitary transformation. The dynamics are efficiently represented by use of the density matrix, $\hat{\rho}$, which evolves according to the Liouville-von Neumann (LvN) equation:

$$\frac{\partial}{\partial t}\hat{\rho} = -i\left[\hat{\mathcal{H}}(t), \hat{\rho}\right] \tag{3.1.1}$$

$$\hat{\rho}(t) = \vec{\mathcal{T}} \exp\left(-i\int_0^t dt'\hat{\mathcal{H}}(t')\right)\hat{\rho}_0 \exp\left(i\int_0^t dt'\hat{\mathcal{H}}(t')\right) \tag{3.1.2}$$

This result presents an interesting problem: the solution suggests that if a coherence is established in the system, that it would persist indefinitely. In terms of spectroscopy, this would result in signals that exist for all time after initiating the coherence, which intuitively makes no sense. The discrepancy lies in that the LvN equation has the same form for both single particle (microscopic) and ensemble (macroscopic) systems, as a result of tracing over the individual particles in an ensemble to reduce the density matrix to a tenable size. Doing so omits any interactions between particles that may be present in the system. In all realistic macroscopic systems, the ensemble dynamics induce dissipation of coherences and relax the state of the system back to equilibrium conditions. As such, much effort has been spent developing theoretical frameworks for thermalization in quantum systems. The prevailing theoretical treatment of Redfield relaxation[93] was summarized in Chapter 2.2.

Another interesting instance of ensemble dynamics is chemical exchange, where multiple chemical species in solution that are coupled by molecular or spatial rearrangement. Molecular parameters in the Hamiltonian change ss molecules undergo rearrangement. This change is reflected in the spectrum, where it appears that transitions change as a function of the exchange rate (Fig. 10). Many exchange processes occur on the $\mu s - s$ time scale, which is ideal for detection by NMR. Furthermore, exchange can also induce dissipation of coherences in the ensemble, making it particularly difficult to model the coherent dynamics of such systems in the presence of exchange.

Describing coherent evolution with chemical exchange was first presented by Kaplan[108, 109] and Alexander[110, 111] as an additional term to the Liouville-von Neumann equation.

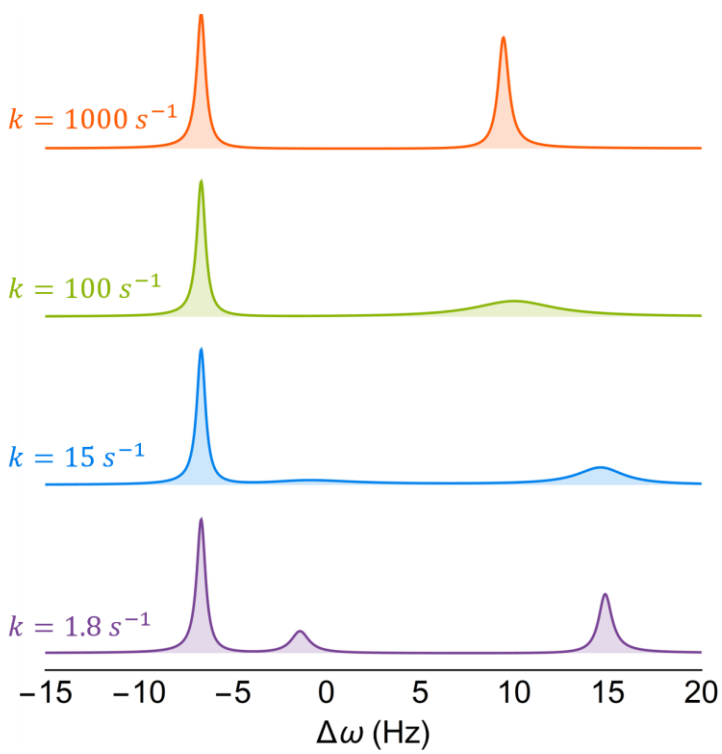

Figure 10: Example spectra with chemical exchange. Chemical exchange initially appears in NMR spectra as a broadening of the peaks caused by the interruptions to the coherent evolution (purple). However, as the exchange rates increase, the individual resonances become extremely broad and subsequently begin to coalesce (blue to green). As the exchange rate becomes larger than the individual coherent interactions in the Hamiltonian, the coalesced peaks will narrow in the fast exchange limit (orange). Simulation: A_3B_6X system parameterized with $\Delta\omega_{AB} = 8\ Hz$, $J_{AB} = 0\ Hz$, $J_{AX} = 5.2\ Hz$, and $J_{BX} = 21\ Hz$.

The form of the exchange interaction was motivated by analysis of the transformations of the density matrix required for a two-site exchange. Binsch[92] later unified Kaplan and Alexander's theory for exchange with Redfield's theory for relaxation, motivating that exchange was simply extension of the relaxation equations derived by Redfield. Binsch's theory could also be recovered in the limit where the coupling between the coherent and exchange degrees of freedom is assumed to be linear. Due to the maturity of NMR in relation to other spectroscopic techniques, and the vast experimental validation of the theoretical predictions, Binsch's theory has been widely accepted in the broader field of spectroscopy. The resultant expression was of the same form of the exchange terms developed by McConnell[112], Kubo[113], and Sack[114] for classical descriptions of magnetic resonance, and the result was simply confirmed by the community.

By motivating that Kaplan and Alexander's exchange term from Redfield theory, Binsch assumed that the ensemble motion for exchange was the same as that for relaxation. The ensemble motion that induces relaxation in magnetic resonance is time-continuous; molecular tumbling in solution generates the necessary dynamics to induce thermalization. In contrast to this, chemical exchange is discontinuous, as the residence time in any particular configuration is different than the time required to perform molecular rearrangement. These discrepancies led to the realization that the theory unifying coherent evolution with chemical exchange was founded on incorrect or incomplete assumptions of the system and required re-interrogation. In SABRE, accurately describing the interplay between the spin dynamics and chemical exchange will be crucial to understanding next steps towards optimizing the scope and performance of hyperpolarization. As such, the fundamental result we derive is directly applied to this problem and culminates in the robust model for SABRE that will be used throughout the rest of this work.

3.1 Quantum Monte Carlo Approach to Chemical Exchange

We will begin in the limit where the molecular rearrangement time is much faster than all other coherent evolution (Fig. 11). In this limit, molecules appear to instantaneously jump between configurations. While most dissipative interactions arise from time-continuous perturbations to the system, chemical exchange involves discrete jumps between molecular configurations. Thus, the most physically rigorous approach for chemical exchange is to undo the ensemble averaging of $\hat{\rho}$ and simulate the dynamics of an ensemble of molecules individually and average the resulting solutions. This is called a quantum Monte Carlo (QMC) simulation method. For the periods between each exchange event, the molecule will evolve according to the LvN equation given in eq. 3.1.2. Then, at randomly sampled intervals proportional to the average lifetime in that configuration, an exchange event is initiated. To accomplish this, the density

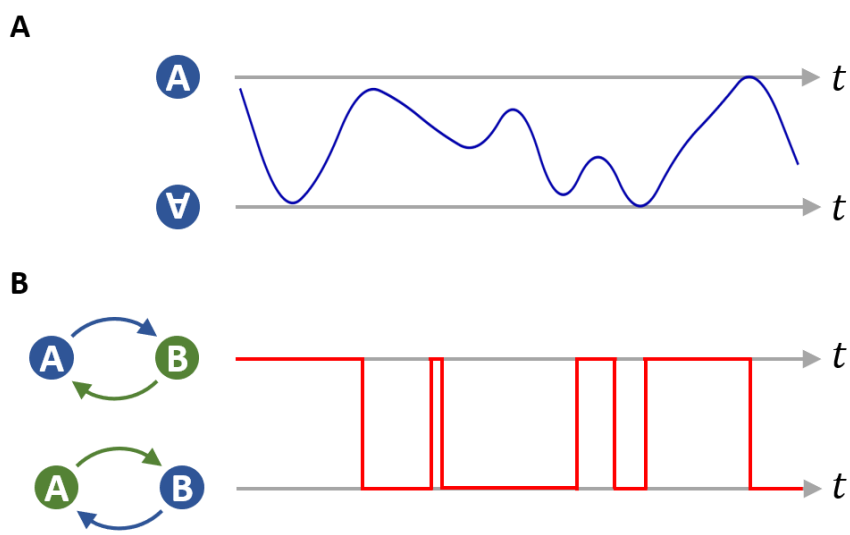

Figure 11: Time-continuous and time-discontinuous ensemble dynamics. A. The rotation of a molecule in solution is a time-continuous process where the trajectory indicates how the molecular orientation is changing over time. This mechanism the basis for relaxation in liquid state NMR where tumbling happens on a ps-timescale. **B.** Exchange between two configurations, where populations are indicated on each site by colors. The trajectory indicates discrete 'jumps' between these configurations that are instantaneous, which is an acceptable approximation in NMR as the reconfiguration time is assumed to be on the order of a femtoseconds.

matrix (for example, $\hat{\rho}_A$) must be projected onto the vector space corresponding to a different configuration ($\hat{\rho}_B$). This can arise in one of a few ways (Fig. 12). In the simplest case, if $\hat{\rho}_A$ and $\hat{\rho}_B$ have the same dimensionality and each of the spins in one configuration directly map to a spin in the other configuration (and no other spins are added), then the density matrix only requires a basis set transformation to rearrange the order of the spins. This is often called a pseudorotation and can be described by a transformation like $\hat{\rho}_B = \hat{R}^\dagger \hat{\rho}_A \hat{R}$, where $\hat{R}$ are unitary "rotation" matrices that permute the basis set. However, $\hat{\rho}_A$ can map onto a configuration where a subset of the spins $\{d\}$ dissociated from the molecule, in which case one must trace over the indices corresponding to each of the dissociated spins ($\hat{\rho}_B = \mathrm{Tr}_{\{d\}}[\hat{\rho}_A]$). Similarly, a subset of spins $\{a\}$ may associate to the molecule, which can be accomplished by taking the tensor product between the associating spins and the density matrix ($\hat{\rho}_B = \hat{\rho}_A \otimes \hat{\rho}_{\{a\}}$).

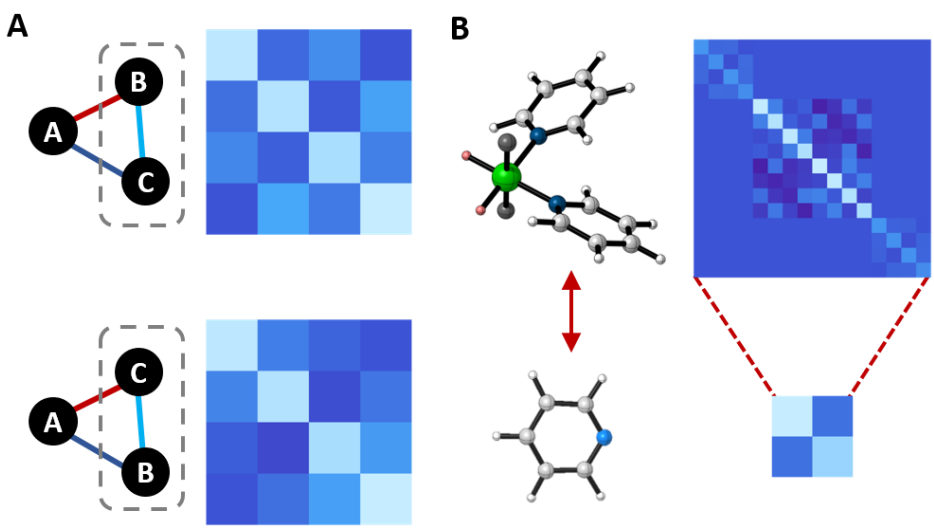

Figure 12: Methods for numerically inducing exchange. A. Exchange that rearranges the molecular geometry but does not change the number of spins can be induced by a basis set transformation, or otherwise called a pseudorotation. In this case, the density matrix of the reduced $\hat{\rho}_{BC}$ subsystems are shown for the two configurations. **B.** Dissociation of a molecule essentially projects that system down onto a different density matrix, and association of that smaller fragment can be accomplished by taking the tensor product ($\otimes$) of the subsystems.

Often, multiple of these mechanisms can be simultaneously present in systems undergoing chemical exchange, as in the case of SABRE. As an illustrative example, we will examine a relatively simple case where the hyperpolarization target and parahydrogen exchange with the iridium catalyst (Fig. 13). In this case, one can numerically implement exchange of the ligand with the QMC sampling and fractionally replenish the parahydrogen during each exchange event. This assumes that there are some number of molecules that all undergo a ligand exchange event at the same time, but that only some fraction of them undergo a parahydrogen exchange. Doing so is possible because the ligand and parahydrogen exchange events are coupled. Fractionally replenishing the parahydrogen essentially "groups" a subset

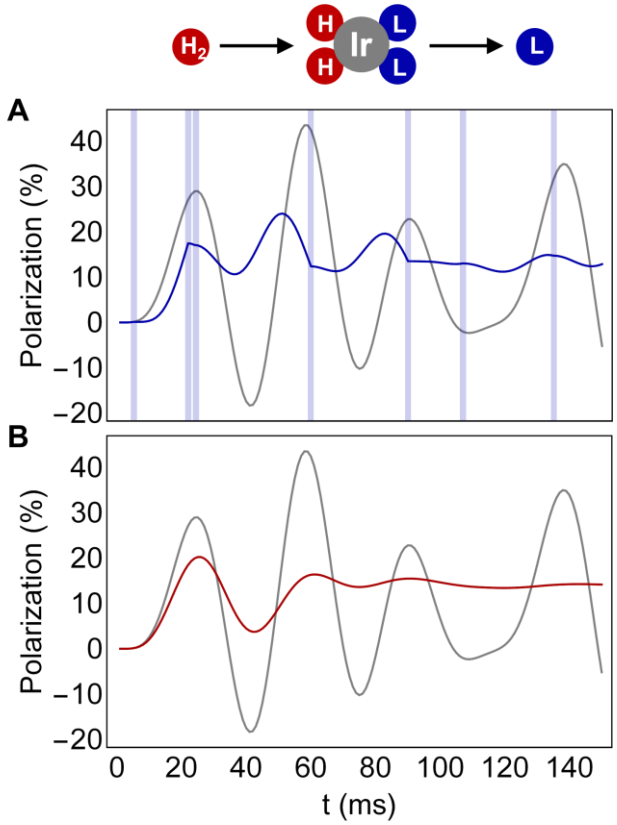

Figure 13: Example QMC simulation of SABRE-SHEATH. For all simulations, the ligand exchange rate was $k_L = 40\ s^{-1}$, the parahydrogen association rate was $k_H = 1\ s^{-1}$, and $B_0 = -0.5\mu T$. **A.** The QMC solution of a single SABRE molecule (blue) is shown overlaid with the fully quantum mechanical solution (gray). The discontinuities observed are when exchange events are sampled, which are demarcated by the vertical lines. **B.** Averaged QMC simulation using $\mathcal{N} = 10{,}000$ molecules. As the SABRE complexes exchange, the evolution loses phase coherence and leads to a decay of the oscillatory structure.

of molecules that undergo ligand exchange simultaneously, and then only permits a fraction of those molecules to undergo parahydrogen exchange. This is only permissible in simulations as there are a macroscopic number of SABRE complexes in the solution. In this example, when exchange is sampled, the density matrix undergoes the transformation

$$\hat{\rho} \rightarrow \left(1 - \frac{k_{a,H}}{k_{d,X}}\right) \mathrm{Tr}_{\{X\}}[\hat{\rho}] \otimes \hat{E} + \frac{k_{a,H}}{k_{d,X}} \hat{\rho}_{pH_2} \otimes \hat{E} \tag{3.2}$$

For simplicity, we will assume an infinite bath of ligand 'X' and parahydrogen. When exchange is initiated, the polarization on the target $\mathrm{Tr}[\hat{\rho} \cdot \hat{S}_z]$ is recorded and used to offset the subsequent polarizations.

While physically rigorous, QMC methods are inherently limited by their slow convergence. For a randomly sampled event like exchange that has a time-independent probability density function (the exchange rate does not change with time), the QMC-sampled variable essentially generates noise in the solution. As such, the solution convergence requires averaging over the noise created by the exchange events, which will disappear at a rate of $\sqrt{1/\mathcal{N}}$. The convergence of the QMC simulation performed in Fig. 13 is shown in Fig. 14.

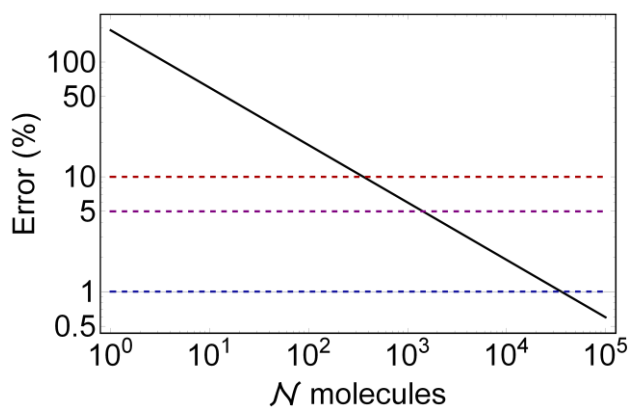

Figure 14: Convergence of QMC simulation. The QMC solution converges very slowly, requiring $\mathcal{N} \approx 50{,}000$ molecules to achieve a solution convergence of less than 1%. As smaller errors are required, an exponentially larger number of iterations are required, making QMC a highly expensive computational technique. The dashed lines are shown to highlight the 10% (red), 5% (purple), and 1% uncertainty points. Simulation: AA'B system (SABRE-SHEATH) at $B = -0.5\ \mu T$, $J_{HH} = -8\ Hz$, and $J_{NH} = -20\ Hz$.

While this convergence is not an issue for the smallest SABRE systems, which only require simulation of a few spin-1/2 nuclei, it makes the simulation of larger, more realistic systems intractable. For instance, it would require over 300 (computer × years) of simulation time to converge a 150 ms simulation of the canonical ^{15}N-pyridine SABRE system, which has 14 coupled spin-1/2 nuclei. With this realization, it became apparent that a different approach to simulating chemical exchange would be required so that realistic SABRE simulations would become tractable.

3.2 Exact Dissipative Master Equation for Magnetic Resonance

While physically robust, QMC models for exchange are rarely used. Instead of performing the ensemble average on the solution, it is common practice to perform the averaging on the equation of motion itself. To accomplish this, the differential equations are perturbatively expanded to provide insight and make progress on actually implementing the interactions. This is the motivation behind quantum master equations, which include the ensemble-level statistical effects in the dynamics. Of key importance is the Dyson expansion of the interaction-frame propagator[115], which casts the Hamiltonian in a reference frame that isolates the time-dependent interactions. This follows similarly to the derivation performed for relaxation in Chapter 2.2. We begin by partitioning the Hamiltonian into a static ($\widehat{\mathcal{H}}_0$) components, corresponding to the coherent interactions, and dynamic ($\widehat{\mathcal{H}}_1(t)$) components, corresponding to the exchange interaction:

$$\frac{\partial}{\partial t}\hat{\rho} = -i\left[\widehat{\mathcal{H}}_0 + \widehat{\mathcal{H}}_1(t), \hat{\rho}\right] \tag{3.3}$$

Importantly, chemical exchange is observable in experiments and thus must correspond to a Hermitian operator, even though it does not result in unitary dynamics. The interaction frame, which isolates the exchange interaction, can be found for an operator $\hat{O}$ as (without hats):

$$O(t) = e^{-i\hat{\mathcal{H}}_0 t}\hat{O}e^{i\hat{\mathcal{H}}_0 t} \tag{3.4}$$

We may write equation 3.3 as:

$$\frac{\partial}{\partial t}\rho = -i[\mathcal{H}_1(t), \rho(t)] \tag{3.5}$$

Integrating equation 3.5 gives:

$$\rho(t) = \rho_0 - i\int_0^t dt_1[\mathcal{H}_1(t_1), \rho(t_1)] \tag{3.6}$$

Equation 3.6 may be iteratively substituted into equation 3.5 to generate the Dyson series:

$$\frac{\partial}{\partial t}\rho = -i\left[\mathcal{H}_1(t), \rho_0 - i\int_0^t dt_1\left[\mathcal{H}_1(t_1), \rho_0 - i\int_0^{t_1} dt_2[\mathcal{H}_1(t_2), \cdots]\right]\right] \tag{3.7}$$

Each of these terms amounts to a perturbative correction to the evolving density matrix. We can write the first four Dyson terms individually as, collecting terms by their power dependence on $\mathcal{H}_1$:

$$\frac{\partial}{\partial t}\rho^{(1)} = -i[\mathcal{H}_1(t), \rho(t)] \tag{3.8.1}$$

$$\frac{\partial}{\partial t}\rho^{(2)} = -\vec{\mathcal{T}}\int_0^t dt_1\ \left[\mathcal{H}_1(t), \left[\mathcal{H}_1^\dagger(t_1), \rho(t_1)\right]\right] \tag{3.8.2}$$

$$\frac{\partial}{\partial t}\rho^{(3)} = i\vec{\mathcal{T}}\iint_0^t dt_n\left[\mathcal{H}_1(t), \left[\mathcal{H}_1^\dagger(t_1), [\mathcal{H}_1(t_2), \rho(t_2)]\right]\right] \tag{3.8.3}$$

$$\frac{\partial}{\partial t}\rho^{(4)} = \vec{\mathcal{T}} \iiint_0^t dt_n \left[\mathcal{H}_1(t), \left[\mathcal{H}_1^\dagger(t_1), \left[\mathcal{H}_1(t_2), \left[\mathcal{H}_1^\dagger(t_3), \rho(t_3)\right]\right]\right]\right] \tag{3.8.4}$$

The symbol $\vec{\mathcal{T}}$ is the Dyson time-ordering operator, which enforces that $t' < t$, and the integral notation,

$$\vec{\mathcal{T}} \iiint_0^t dt_n \cdots = \vec{\mathcal{T}} \int_0^t dt_1 \int_0^{t_1} dt_2 \int_0^{t_2} dt_3 \cdots, \tag{3.9}$$

is used for legibility.

To continue, we will introduce a general form of $\mathcal{H}_1(t)$ as an expansion between the operator $\hat{A}_k$, which is the physical implementation of chemical exchange on the reduced density matrix, and a stochastically modulated operator $\hat{F}_k(t)$, which describes the time evolution of the molecular dynamics for each exchange process (written in the interaction frame):

$$\mathcal{H}_1(t) = \sum_k A_k(t) F_k(t) \tag{3.10}$$

The index corresponds to each exchange process in the system. To make further progress, the equation of motion will be ensemble-averaged. The averaging is restricted to the ensemble motion operators $\hat{F}_k(t)$, as all other operators act only on the reduced density matrix. At this point, we impose that chemical exchange is a stationary process, meaning that the exchange rate is time-independent and that the only time metric that matters is the difference $t - t_1 = \tau$. We may also use this assumption to define $\langle \hat{F}_k(t) \rangle = 0$, as there is no drift to the ensemble motion, i.e. the system is at equilibrium. This forces all odd-order terms in the Dyson expansion to zero and makes the leading order term the second order interaction given in equation 3.8.2, which becomes:

$$\frac{\partial}{\partial t}\rho^{(2)} = -\sum_{jk}\int_0^t d\tau\ \left[A_j(\tau),\left[\hat{A}_k^\dagger,\rho\right]\right]\left\langle F_j(\tau)\hat{F}_k^\dagger\right\rangle \tag{3.11}$$

Here, we have imposed that the exchange dynamics are Markovian, and thus have no memory component. This permits us to write $\rho(t_1) = \rho(t)$ in the PDE, where the formal time-dependence was dropped for legibility. The correlation function, $\left\langle F_j(\tau)\hat{F}_k^\dagger\right\rangle$, describes the time dependence of exchange. We will impose the assumption that each process is only self-correlated, permitting the use of δ_{jk}. Furthermore, its magnitude is proportional to the rate $1/\tau_j$ (where τ_j is the characteristic lifetime in a configuration). Importantly, the time required for the molecule to rearrange is significantly faster than the evolution of the coherent degrees of freedom in the NMR limit, as well as the lifetime in any one configuration (Fig. 11B), and thus the ensemble dynamics can be assumed to be δ correlated in time. This allows the limits of integration to be extended to $\pm\infty$, distributing the resulting factor of $1/2$ into the operators as $\hat{A}_j \to \hat{A}_j/\sqrt{2}$ for brevity, giving:

$$\begin{aligned}\frac{\partial}{\partial t}\rho^{(2)} &= -\frac{1}{2}\sum_{jk}\int_{-\infty}^{\infty} d\tau\ \left[e^{-i\hat{\mathcal{H}}\tau}\hat{A}_j e^{i\hat{\mathcal{H}}\tau},\left[\hat{A}_k^\dagger,\rho\right]\right]\frac{\delta(\tau)\delta_{jk}}{\tau_j} \\ &= -\sum_j \frac{1}{\tau_j}\left[\hat{A}_j,\left[\hat{A}_j^\dagger,\rho\right]\right]\end{aligned} \tag{3.12}$$

To make progress, we may introduce the commutation superoperator $\hat{\hat{O}} = [\hat{O},]$. As such, we may rewrite the double commutator as:

$$\frac{\partial}{\partial t}\rho^{(2)} = -\sum_j \frac{1}{\tau_j}\hat{\hat{A}}_j\hat{\hat{A}}_j^\dagger\rho = -\sum_j \frac{1}{\tau_j}\hat{\hat{A}}_j^2\rho \tag{3.13}$$

The second equality is permitted as $\hat{\hat{A}}_j$ is Hermitian. Now, the squared superoperator $-\hat{\hat{A}}_j^2$ can be identified by inspection as the exchange superoperator $\widehat{K}_j$, which returns the traditional master equation for chemical exchange:

$$\frac{\partial}{\partial t}\hat{\rho} = i[\hat{\rho}, \widehat{\mathcal{H}}] + \sum_j \frac{1}{\tau_j}\widehat{K}_j\hat{\rho} \tag{3.14}$$

It is important to note that this equation is derived not as an extension of Redfield's relaxation theory, as done by Binsch, but under alternate statistical assumptions specific to exchange and in the lowest-order of perturbation theory. In the NMR limit, the exchange rate $1/\tau_j$ can often be on the order of or exceeding dominant couplings and resonance frequency differences. As such, it is not a valid assumption that exchange weakly affects the dynamics and thus can only be included as the lowest-order interaction in perturbation theory.

Corrections to the dynamics can be made by incorporating higher order terms in the perturbative Dyson expansion. As shown previously, all odd-order terms disappear under the assumption that exchange is a stationary process, the next non-zero term is the fourth-order Dyson term:

$$\begin{aligned}\frac{\partial}{\partial t}\rho^{(4)} = \vec{\mathcal{T}}\sum_{ijkl}\int_0^t dt_1\int_0^{t_1} dt_2\int_0^{t_2} dt_3\left[A_i(t),\left[A_j^\dagger(t_1),\left[A_k(t_2),\left[A_l^\dagger(t_3),\rho\right]\right]\right]\right] \\ \times\left\langle F_i(t)F_j^\dagger(t_1)F_k(t_2)F_l^\dagger(t_3)\right\rangle\end{aligned} \tag{3.15}$$

This equation uses the definition of the interaction frame Hamiltonian given in eq. 3.10. We can expand the four-point correlation function into factors of two-point correlators by use of Isserlis' theorem:

$$\langle F_i(t)F_j^\dagger(t_1)F_k(t_2)F_l^\dagger(t_3)\rangle = \langle F_i(t)F_j^\dagger(t_1)\rangle\langle F_k(t_2)F_l^\dagger(t_3)\rangle$$
$$+\langle F_i(t)F_k(t_2)\rangle\langle F_j^\dagger(t_1)F_l^\dagger(t_3)\rangle + \langle F_i(t)F_l^\dagger(t_3)\rangle\langle F_j^\dagger(t_1)F_k(t_2)\rangle \tag{3.16}$$

As previously, the terms within each two-point correlator must correspond to the same exchange process to impose quadratic action of any operator $\hat{A}_k$. However, we shall additionally assume that any non-zero four-point correlator corresponds to a single exchange process (δ_{ijkl}), or in other words, each exchange process is only self-correlated. This makes intuitive sense for two uncoupled exchange processes ($\hat{F}_k$ and $\hat{F}_j$ act independently). Furthermore, $\hat{F}_k$ and $\hat{F}_j$ must be distinguishable, not related by a similarity transform. However, in the case of coupled exchange processes, this assumption is only valid if we redefine the process. If we use the example that $\hat{F}_k$ can only occur if $\hat{F}_j$ has happened, we can rewrite $\hat{F}_k$ as $\hat{F}_{j+k}$ ($\hat{F}_j$ occurs with $\hat{F}_k$) and rewrite $\hat{F}_j$ as $\hat{F}_{j-k}$ ($\hat{F}_j$ occurs without $\hat{F}_k$). This effectively uncouples the processes and permits use of the above assumption. Thinking about this from a mathematical point of view, the matrix $\hat{\mathcal{F}}$ containing all $\hat{F}_j$ must be diagonalized. Under this assumption, all the terms in eq. 3.16 are identical, and in general there will be $(n-1)!! = 3$ identical terms that arise for the $\rho^{(n)}$ term of the Dyson expansion. Furthermore, it will be beneficial to decouple the time-ordered integrals, which is accomplished by dividing the expression by the $(4-1)!$ degenerate time orderings that arise. Thus, we can write:

$$\frac{\partial}{\partial t}\rho^{(4)} = \vec{\mathcal{T}}\sum_{ijkl}\int_0^t dt_1\int_0^{t_1} dt_2\int_0^{t_2} dt_3\left[A_i(t),\left[A_j^\dagger(t_1),\left[A_k(t_2),\left[A_l^\dagger(t_3),\rho\right]\right]\right]\right]$$
$$\times\langle F_i(t)F_j^\dagger(t_1)F_k(t_2)F_l^\dagger(t_3)\rangle \tag{3.17}$$

$$= \sum_{ijkl} \int_0^t dt_1 \left[A_i(t), \left[A_j^\dagger(t_1), \int_0^t dt_2 \int_0^t dt_3 \left[A_k(t_2), \left[A_l^\dagger(t_3), \rho \right] \right] \right] \right]$$

$$\times \frac{3}{3!} \frac{\delta(t - t_1)}{\tau_j} \frac{\delta(t_2 - t_3)}{\tau_j} \delta_{ijkl}$$

Now, we can use the stationary assumption to make the change of variables $t - t_1 = \tau_1$ and $t_2 - t_3 = \tau_2$ to further reduce the expression as:

$$\frac{\partial}{\partial t} \rho^{(4)} = \sum_j \frac{1}{4} \int_{-\infty}^{\infty} d\tau_1 \left[A_j(\tau_1), \left[\hat{A}_j^\dagger, \int_{-\infty}^{\infty} d\tau_2 \left[\hat{A}_j(\tau_2), \left[\hat{A}_j^\dagger, \rho \right] \right] \delta(\tau_2) \right] \right] \delta(\tau_1)$$

$$\times \frac{3}{3!} \frac{1}{\tau_j^2} \int_0^T d\tau_2 \tag{3.18}$$

$$= \sum_j \left[\hat{A}_j, \left[\hat{A}_j^\dagger, \left[\hat{A}_j, \left[\hat{A}_j^\dagger, \rho \right] \right] \right] \right] \frac{T}{2\tau_j^2}$$

Note that we raised the limits of the integrals that act on the commutators to $\pm\infty$ and change the upper integration limit in the final integral to T. Importantly, the factor of ¼ that results from extending the lower limits to infinity is again distributed into each $\hat{A}_j$ for similarity to eq. 3.12. However, the remaining factor of ½ that is in eq. 3.18 results from accounting for degenerate time-orderings. Transforming eq. 3.18 into superoperator form yields:

$$\frac{\partial}{\partial t} \rho^{(4)} = \sum_j \left(-\hat{\hat{A}}_j^2 \right)^2 \frac{T}{2\tau_j^2} \tag{3.19}$$

The numerical coefficient of this term describes the rate of two exchange processes happening during the period T. Using all the assumptions established here, it is possible to completely re-index the Dyson expansion for chemical exchange as:

$$\frac{\partial}{\partial t}\rho = \sum_j \frac{1}{\tau_j} \sum_{n=0}^{\infty} \left(-\hat{\hat{A}}_j^2\right)^{n+1} \frac{1}{n!} \left(\frac{T}{2\tau_j}\right)^n \rho \tag{3.20}$$

Typically, the largest inhibitor to higher-order perturbation theory is the calculation of the powers of the exchange superoperator, $\left(-\hat{\hat{A}}_j^2\right)^n$, particularly as these must be done numerically and are highly computationally expensive. However, the exchange superoperator projects the density matrix onto the same vector space (after removing and adding a ligand) and performing multiple exchange events returns the same density matrix as performing a single exchange event ($\hat{P}^2 = \hat{P}$). This holds when the exchange superoperator is written as a linear combination of exchange pathways, such as when there are multiple indistinguishable binding sites as in the case of SABRE. As such, there is a well-defined relation between all higher order exchange superoperators and the linear exchange superoperator, which is:

$$\left(-\hat{\hat{A}}_j^2\right)^{n+1} \rho = \left(-\hat{\hat{A}}_j^2\right)^n \hat{K}_j \rho = \lambda_n \hat{K}_j \rho, \tag{3.21}$$

where the first equality is given by the definition of the exchange superoperator and higher operator superoperators return a term proportional to $\hat{K}_j$. In fact, the second equality suggests that the higher order superoperators $\left(-\hat{\hat{A}}_j^2\right)^n$ are eigenfunctions of $\hat{K}_j \rho$. For trace-unity exchange superoperators, we find that $\lambda_n = 1$, which permits us to write the relation:

$$\left(-\hat{\hat{A}}_j^2\right)^{n+1} = (-1)^{n+1} \left(\hat{\hat{A}}_j^2\right)^{n+1} = (-1)^{n+1} \left(-\hat{K}_j\right)^{n+1} = (-1)^n \hat{K}_j \tag{3.22}$$

Using this in eq. 3.20 gives:

$$\frac{\partial}{\partial t}\rho = \sum_j \frac{1}{\tau_j} \hat{K}_j \rho \sum_{n=0}^{\infty} \frac{1}{n!} \left(\frac{-T}{2\tau_j}\right)^n \tag{3.23}$$

The n-summation is then the Maclaurin expansion of the exponential, which permits us to write the closed form solution of the infinite-order exchange interaction as:

$$\frac{\partial}{\partial t}\hat{\rho} = i[\hat{\rho}, \hat{\mathcal{H}}] + \sum_j \frac{\hat{K}_j \hat{\rho}}{\tau_j} \exp\left(\frac{-T}{2\tau_j}\right) \tag{3.24}$$

The only difference between the traditional equation of motion for chemical exchange (eq. 3.14) and the exact equation of motion given by eq. 3.24 is the scalar exponential factor that relates the action of all higher-order exchange events to the lowest order term at no additional computational cost. We will refer to this as the exchange generating function. Importantly, as the integration period $T \to dt$, the traditional equation of motion is recovered, which is to be expected as only the lowest-order terms would be present over short times. Even though this result is derived through time-dependent perturbation theory, the closed form solution is not a perturbative result but is the exact result obtained by using a series solution to contract the higher order interactions, which we call the exact Dissipative Master Equation (DMEx)[116]. A summary of the nomenclature used for exchange master equations and what each equation includes is shown in Table 1.

Table 1: Nomenclature and summary of exchange master equations. The model, exchange dissipator, and method of derivation are summarized for each of the master equations discussed in this section.

Model	Dissipator	Derivation method
Traditional	$\sum_j \frac{1}{\tau_j} \hat{K}_j \hat{\rho}$	Analysis of transformation required for exchange
DMEx	$\sum_j \frac{1}{\tau_j} \hat{K}_j \hat{\rho} \exp\left(\frac{-T}{2\tau_j}\right)$	Closed form solution of Dyson series expansion
DMExFR2	$\sum_j \frac{1}{\tau_j} \hat{K}_j \hat{\rho} \exp\left(\frac{-T}{2\tau_j}\right)$	SABRE-specific DMEx model for exchange

3.3 Error analysis of the DMEx and simulating the SABRE system

The master equation treatment of chemical exchange fundamentally differs from the QMC model in that it assumes that exchange provides a continuous perturbation to the system at the level of the ensemble. However, it also differs from the treatments performed by Kaplan[108, 109], Alexander[110, 111], and Binsch[92] as it considers both the lifetime of any one species but also incorporates the instantaneous jump between exchange sites. In limits where the exchange rate is on the order of the coupling, as it is in SABRE, the QMC model permits larger excursions from the average density matrix than is encapsulated in a master equation treatment. To assess the accuracy of this assumption, we can calculate the error in the DMEx simulation relative to the QMC. While the DMEx is an exact equation of motion, it can rarely be analytically integrated. Instead, the DMEx can be numerically solved with the first-order solution:

$$\hat{\rho}(T) = e^{-i\hat{\mathcal{H}}T}\hat{\rho}e^{i\hat{\mathcal{H}}T} + T\sum_{j}\frac{\hat{K}_j e^{-i\hat{\mathcal{H}}T}\hat{\rho}e^{i\hat{\mathcal{H}}T}}{\tau_j}\exp\left(\frac{-T}{2\tau_j}\right) \tag{3.25}$$

This can be found by using the first-order Taylor expansion of eq. 3.24 and replacing the coherent term $i[\hat{\rho},\hat{\mathcal{H}}]T$ with the exact solution. Assessing this intrinsic error requires highly converged QMC solutions, where the convergence is significantly less than the error in the master equation, which can be accomplished using $T = 100\,\mu s$. The DMEx model accumulates a statistically significant error when compared to the QMC solution (Fig. 15), where the black line indicates the convergence error of the QMC solutions (σ_{QMC}) used as the reference simulations. However, the error is only $\langle\sigma_{DMEx} - \sigma_{QMC}\rangle = (0.142 \pm 0.018)\%$ larger than the convergence error of the QMC model. The time required to generate the QMC solution is significantly longer than the time required to integrate the DMEx solution. Thus,

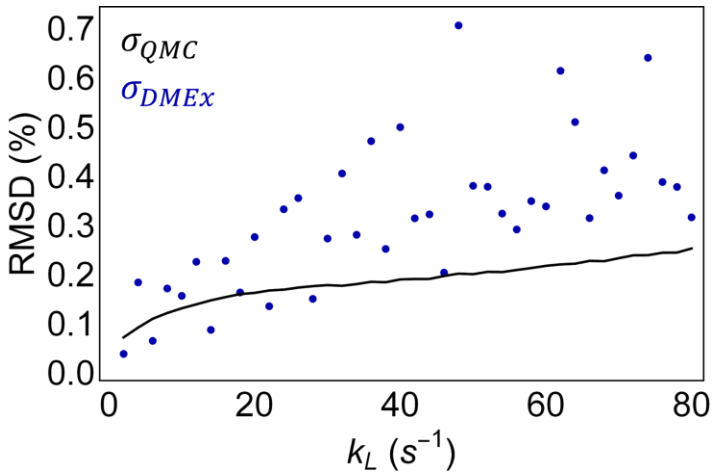

Figure 15: Performance of the DMEx model relative to the QMC. The error in the DMEx (σ_{DMEx}, blue) is shown relative to the convergence error of the QMC solutions used as a ground truth (black). This indicates a small, but significant, error in the DMEx model relative to the QMC. On average, the error is $\langle \sigma_{DMEx} - \sigma_{QMC} \rangle = (0.142 \pm 0.018)\%$. For all simulations, a step size of $T = 100\ \mu s$ was used on a minimal SABRE system.

the assumption that exchange provides a continuous perturbation to the system only generates a negligibly small error in the solution.

The primary application of exchange simulations in this work is as a model for SABRE hyperpolarization dynamics, which was work was done in collaboration with Shannon Eriksson, another graduate student in the Warren lab. As such, much effort went toward constructing a rigorous model that could encapsulate all pertinent interactions that affect hyperpolarization. This is referred to as the DMExFR2 model, which includes free-ligand effects (F), rebinding (R), and relaxation (R). In general, we describe the SABRE system as a combination of ensembles corresponding to each type of species in the system (Fig. 16). By convention, we express the concentrations of each of the ensembles relative to the concentration of the activated iridium complex. The association of a target ligand L from the free-ligand ensemble $\hat{\rho}_L$ onto the iridium catalyst first requires the dissociation of the target. For this pathway, the exchange superoperator can be written as:

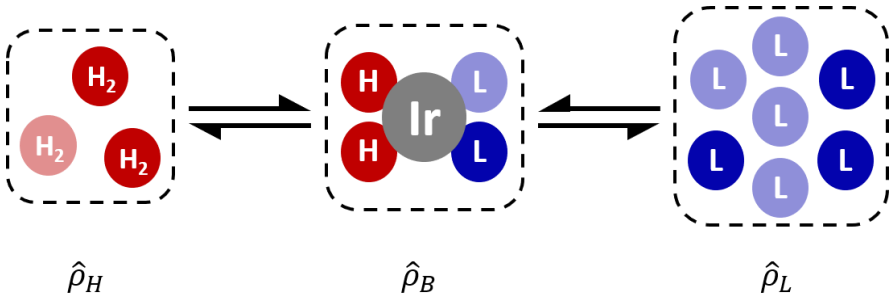

Figure 16: Exchange pathways in SABRE. Hydrogen (H_2) and ligand (L) can reversibly exchange with the iridium catalyst. While there is always a fixed concentration of ligand in the system, the hydrogen is either present at a fixed concentration or is continually replenished. The reversible binding of a molecule that previously interacted with the catalyst is a critical effect limiting the production of hyperpolarization. Each of these species is thought of as a separate ensemble in the system and each can be present in different concentrations.

$$\hat{K}_B^{(L)}(\hat{\rho}_B, \hat{\rho}_L) = \mathrm{Tr}_{\{L\}}[\hat{\rho}_B] \otimes \hat{\rho}_L \tag{3.26}$$

$\mathrm{Tr}_{\{L\}}[\hat{\rho}_B]$ is the partial trace over the ligand basis states, returning a density matrix containing only those nuclei still bound to the complex. This conjugate superoperator that adds the dissociating target into the free-target ensemble is given by:

$$\hat{K}_L^{(L)}(\hat{\rho}_B, \hat{\rho}_L) = \frac{[B]}{[L]} \mathrm{Tr}_{\{B-L\}}[\hat{\rho}_B] \tag{3.27}$$

The factor $[B]/[L]$ scales the bound ensemble to ligand ensemble, and $\mathrm{Tr}_{\{B-L\}}[\hat{\rho}_B]$ traces over the basis states not corresponding to the dissociating ligand. In conjunction with ligand exchange is the exchange of parahydrogen from the hydrogen ensemble $\hat{\rho}_H$, which happens only after a ligand has dissociated from the complex. The exchange superoperator for this pathway is:

$$\hat{K}_B^{(H)}(\hat{\rho}_B, \hat{\rho}_L, \hat{\rho}_H) = \frac{1}{2}\left(\hat{\rho}_H \otimes \mathrm{Tr}_{\{L+H\}}[\hat{\rho}_B] \otimes \hat{\rho}_L + \hat{\rho}_H \otimes \hat{\rho}_L \otimes \mathrm{Tr}_{\{L+H\}}[\hat{\rho}_B]\right) \tag{3.28}$$

By convention, the parahydrogen-derived hydrides are always the first two spins of the bound ensemble. For the case with only one ligand that is bound trans-to a hydride, then only one term in eq. 3.27 is present. The conjugate exchange superoperator is:

$$\widehat{K}_H^{(H)}(\hat{\rho}_B, \hat{\rho}_H) = \frac{[B]}{[H]} \mathrm{Tr}_{\{B-H\}}[\hat{\rho}_B] \tag{3.29}$$

In the case where parahydrogen is continually replenished by bubbling during the experiment, we can assume that $[B] \ll [H]$, which effectively means each parahydrogen that associates with the bound ensemble is a parahydrogen that has not yet bound to an iridium catalyst. When setting the initial state of $\hat{\rho}_H$ to be the parahydrogen singlet, this effectively prevents depletion of the $\hat{\rho}_H$ by exchange. However, this is not a necessary assumption, and analogous exchange superoperators may be derived as above for the case where parahydrogen can reversibly bind from a fixed reservoir. Specific chemical systems may be constructed using combinations of these superoperators and can even include multiple ensembles corresponding to different ligand types.

In addition to exchange, spin relaxation must be included as hyperpolarization is a non-equilibrium state of the system. In the DMExFR2 model, spin relaxation is treated as a boundary value problem where the system is driven towards equilibrium at rate that is either empirically derived or derived from theory. There are two dominant thermalization processes that must be included, which are dephasing (loss of phase coherence), with a rate $1/T_2$, and decoherence (loss of population coherence), with a rate $1/T_1$. Dephasing and decoherence may be included in the dynamics by phenomenologically adding the terms

$$\frac{\partial}{\partial t}\hat{\rho} = \sum_k \frac{\delta_{ij}\hat{\rho}_k - \hat{\rho}}{T_{2,k}} + \frac{\hat{\rho}_{eq,k} - \hat{\rho}}{T_{1,k}} \tag{3.30}$$

to the differential equation. The summation here indexes over the different nuclei. The first term eliminates coherences from the system and the second term drives the system back to its equilibrium conditions. Note that these processes are not related to inhomogeneous broadening of peaks, which is caused by non-uniform magnetic fields.

With all the relevant effects included in the DMExFR2 model, it is possible to assess the performance of the exact master equation relative to the traditional master equation for exchange (Fig. 17). While the solutions converge as the simulation step size $T \rightarrow dt$, as is expected from eq. 3.23, the DMEx model exhibits a faster solution convergence than the traditional equation of motion by approximately a factor of four. Again, it is pertinent to note that this is achieved at no additional computational cost over the traditional implementation. In addition to the superior convergence of the DMEx, it is important for the solution to self-

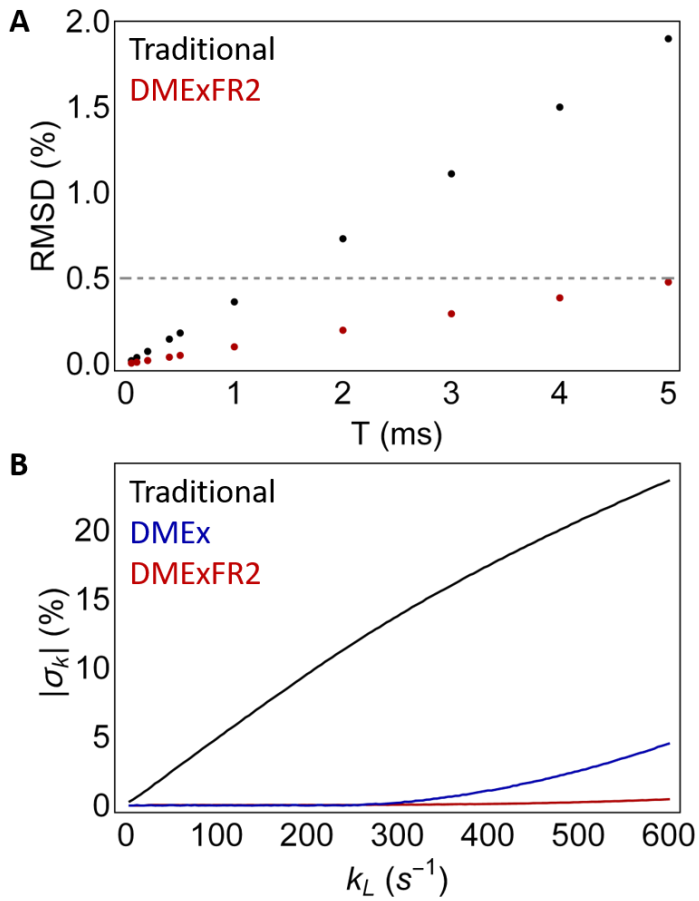

Figure 17: Performance of the SABRE-specific DMExFR2 model. A. The solution convergence of the traditional (black) and DMEx (red) model for $k_L = 20\ s^{-1}$ as a function of simulation step size (T). The gray line indicates the error threshold of 0.5 %, where the DMEx model does not exceed this threshold even for $T = 5\ ms$, which corresponds to $T = 1/10k_L$. **B.** Self-consistency of the DMExFR2 model (red) relative to the traditional implementation (black) and DMEx model (blue) for SABRE without all critical effects. All simulations use $T = 1\ ms$. The self-consistency parameter, σ_k, is the error in the exchange rate predicted by the simulation, using a $T = 10\ \mu s$ simulation as a reference.

consistently predict known exchange rates, as these models are often used in combination with experiment. Here, we have assessed the self-consistency of the DMExFR2 model by introducing the parameter σ_k, which is the relative error in the exchange rate predicted by the model (Fig. 17B). The DMEx models both exhibit superior self-consistency of the solution over the traditional model, which at $T = 1\ ms$ has no regime in which the solution is stable. Surprisingly, the solution self-consistency is improved when including all relevant SABRE interactions. Relative to the traditional implementation, the DMEx model exhibits superior performance in both convergence and accuracy.

Given the superior computational performance of the DMExFR2, we can now determine the importance of using a rigorous model for the SABRE system (Fig. 18). We will first examine the case of coherently pumped SABRE-SHEATH on a (^{15}N-^{13}C)-acetonitrile ligand. Even with a spin system containing only has 5 spin-1/2 nuclei on the target, the coherent dynamics are highly structured, providing an ideal test case for examining the requisite level of theory required to model a SABRE system. In addition to the standard set of exchange pathways included in the generic DMExFR2, one must additionally account for the fact that a hyperpolarization-inactive coligand is used to enhance exchange. This occupies one of the iridium binding sites and thus, there are two isomers of the SABRE-active complex. Therefore, one must account for ligand exchange onto both of these conformations as well as isomerization between the conformations. When fit with a DMExFR2 simulation with every interaction explicitly included, the experimental coherent hyperpolarization dynamics of this system are well reproduced. Furthermore, the extracted exchange rates of the system are self-consistent between experiments at different magnetic fields (Fig. 18C). Importantly, simply removing one of these interactions, such as the coligand exchange pathways, breaks the self-consistency between these data sets. As such, we see that it is critical to include all relevant

exchange pathways for the system when attempting to extract meaningful information from experimental data.

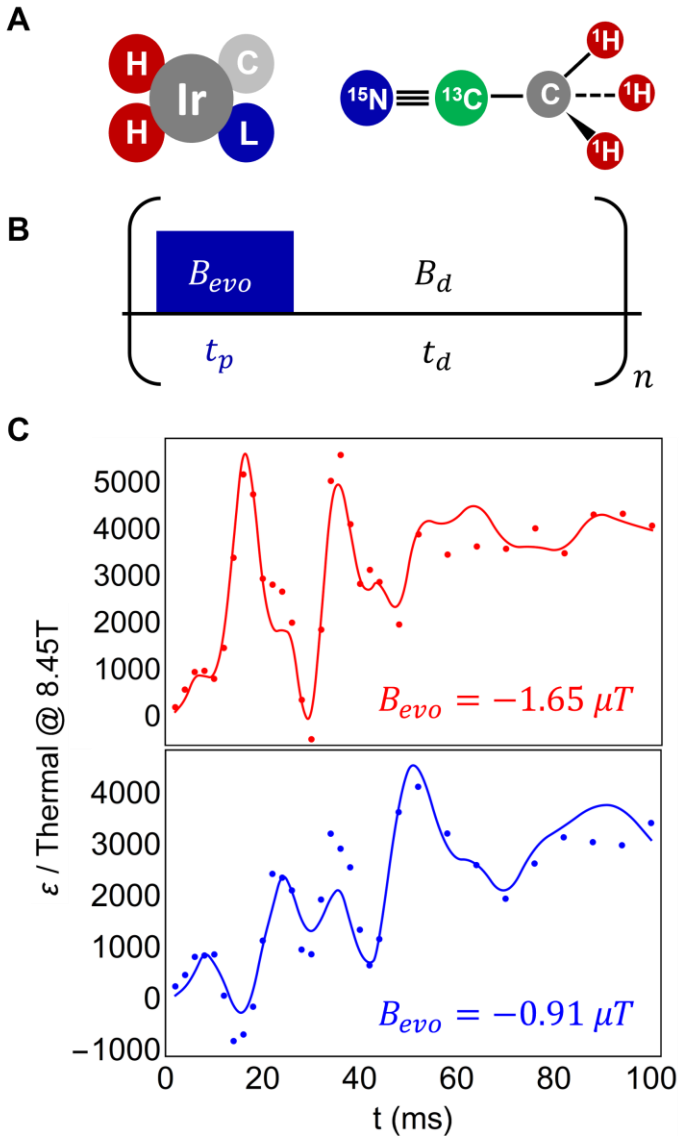

Figure 18: Coherently pumped SABRE-SHEATH of (^{15}N,^{13}C)-acetonitrile. A. Acetonitrile is hyperpolarized by SABRE in the presence of a pyridine coligand (C), and hyperpolarization is monitored either on ^{15}N or ^{13}C. **B.** Coherently-driven X-SABRE hyperpolarization is accomplished by interleaving periods where the magnetic field is resonant with the X-SABRE transition with periods where it is not resonance ($B_d \gg B_{evo}$) to permit exchange. This pulse sequence is repeated for 60s to permit accumulation of hyperpolarization. **C.** Experimental (dots) coherent ^{15}N-SABRE hyperpolarization of (^{15}N,^{13}C)-acetonitrile fit with the DMExFR2 simulation (line). At $B = -1.65\ \mu T$, $k_N = (14.5 \pm 1.8)s^{-1}$ and $k_H = (6.00 \pm 0.75)s^{-1}$. At $B = -0.91\ \mu T$, $k_N = (15.0 \pm 3.3)s^{-1}$ and $k_H = (4.5 \pm 0.98)s^{-1}$. Importantly, the fits produce self-consistent results between the two data sets, as would be expected. Removing even one of the interactions, such as the coligand exchange pathways, breaks this self-consistency and the simulation accrues an error of up to 92% with respect to the full DMExFR2 simulation.

An equally important application of the applications in addition to fitting experimental data is predicting and optimizing the performance of hyperpolarization techniques *in silico*. At short times, on the order of the complex, the coherent dynamics are relatively emphasized. Under these conditions, it is interesting to examine the performance of truncating the model of the canonical X-SABRE system, ^{15}N-pyridine (Fig. 19). Due to the large number of ^{1}H nuclei on each ligand, it has been assumed that truncating all or most of these ^{1}H[117] would be representative of the explicit system. For the first time, the DMExFR2 has the computational efficiency to simulate the full 14-spin iridium-bound system along with the 6-spin free ligand. For brevity, we refer to SABRE systems often with the notation $(P+Q)R$, where P are the number of spin-1/2 nuclei on the iridium complex and Q are the number of spin-1/2 nuclei in the free ligand. $R = \{X, Y\}$ and indicates the binding geometry with one trans-hydride target

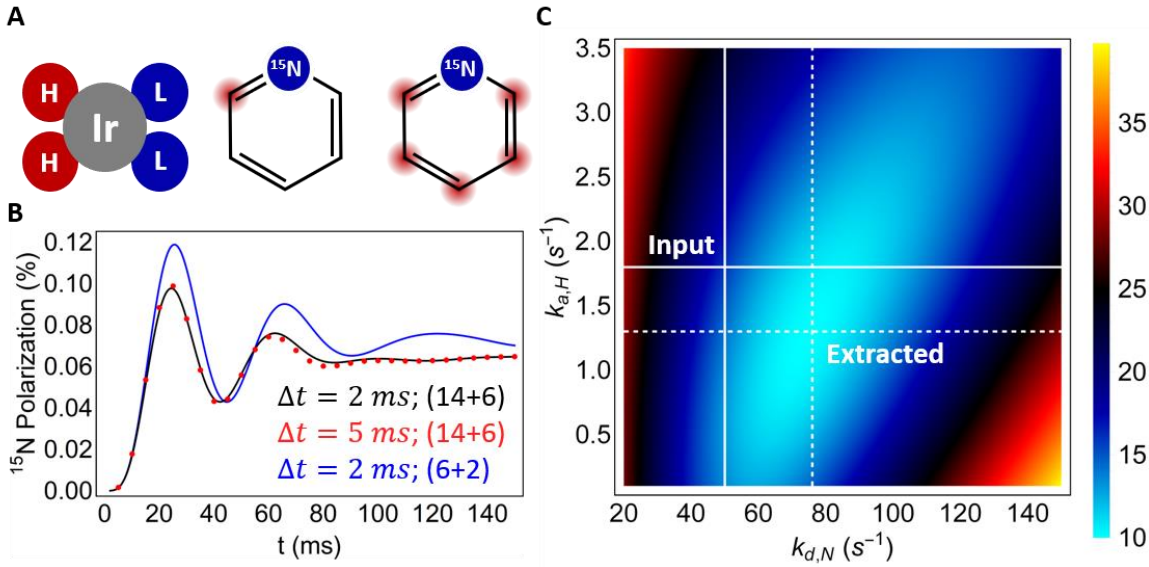

Figure 19: Truncation errors on the order of the average complex lifetime. A. In the ^{15}N-pyridine SABRE system, which has been used to benchmark nearly all of X-SABRE performance, the large number of ^{1}H nuclei on the ligand are often omitted from the theoretical model. The largest approximation in literature utilizes a single ^{1}H, whereas there are five ^{1}H J-coupled to the ^{15}N, indicated by the red markers on the molecular structure. **B.** The hyperpolarization dynamics at times on the order of the complex vary drastically between the explicit model, which is a (14+6)X system, and the approximate (6+2)X model. Even increasing the step size to $\Delta t = 5\ ms$ in the DMExFR2 will still reproduce the actual dynamics. **C.** Fitting the (6+2)X solution to the (14+6)X solution reveals significant artifacts introduced by truncating the spin system, meaning that in silico optimization cannot be judged with any confidence without the full system.

(Y) or two trans-hydride targets (X) As such, the full pyridine system is a (14+6)X spin system, where the largest approximate system reported in literature utilizes only one ^{1}H and is a (6+2)X truncated model. We see that such an approximation dramatically alters the coherent dynamics of the SABRE system, whereas even using a step size that is $\Delta t = 1/4k_N$ in the DMExFR2, where k_N is the ligands exchange rate, reproduces the actual hyperpolarization dynamics well. This highlights that the superior computational performance of the DMEx models can be used to offset the additional time required to model the full system, as doing so is the only way in which reliable simulation results may be obtained.

It is also illustrative to examine the performance of a series of truncated models to predict the hyperpolarization dynamics in SABRE. Here, we will use a SABRE system with a single ^{15}N-pyridine, reflective of a partially ^{15}N-labelled pyridine sample, and compare solutions where ^{1}H are systematically truncated off the ligand. Furthermore, we will examine both the actual hyperpolarized signal predicted by each model as well as the deviation in the predicted dynamics, accessible by scaling the truncated model to the actual result. In the case of SABRE-SHEATH, the Hamiltonian of the system is simply:

$$\hat{\mathcal{H}} = \sum_i \gamma_i B_0 \hat{I}_{iz} + 2\pi \sum_{i<j} J_{ij} \hat{I}_i \cdot \hat{I}_j \tag{3.31}$$

Note that all of the spins in this case are strongly coupled. The only regime when the truncated model predicts a hyperpolarization that is well representative of the actual system is with the (7+5)Y truncation, which still exhibits a $\sigma = 15.8\%$ deviation from the (8+6)Y system (Fig. 20). This system exhibits hyperpolarization dynamics that deviate from the realistic system, despite there only being a single ^{1}H not included in the model that is not even directly J-coupled to the ^{15}N. For every additional truncation of the system, the hyperpolarization

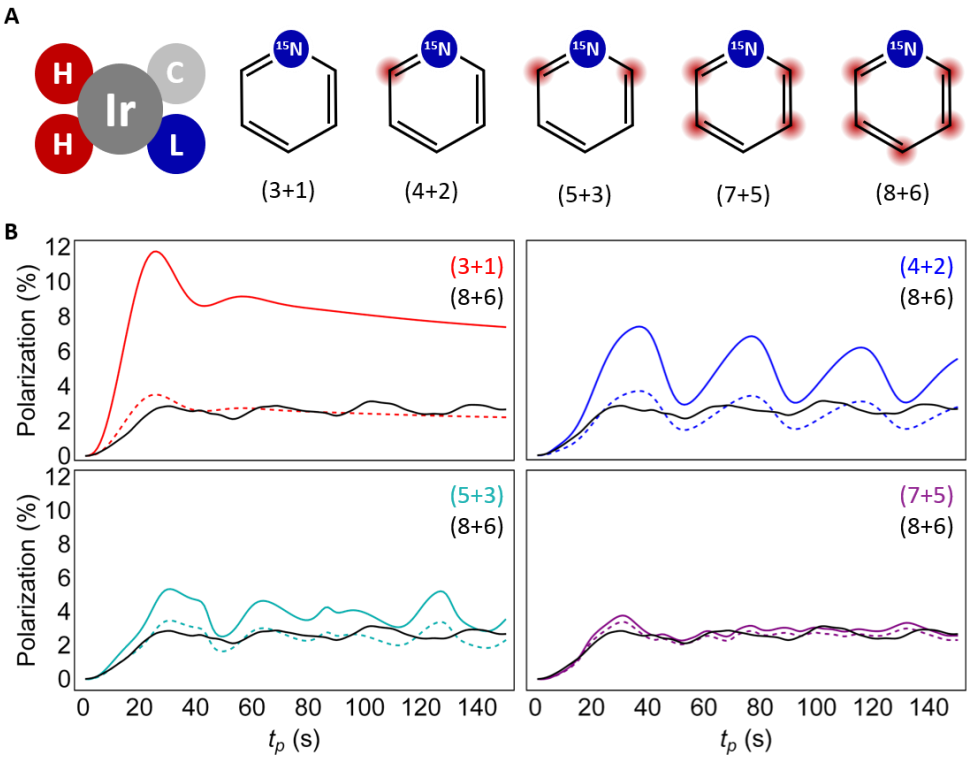

Figure 20: Truncation errors in coherently-driven SABRE-SHEATH experiments. A. Series of truncated ^{15}N-pyridine models as well as the exact (8+6)Y model. **B.** Comparison of the hyperpolarization generated in a coherently-driven SABRE-SHEATH varying the LAC 'ON' time t_p. The solid lines in color are the simulation output, and the dashed lines are the result of fitting the amplitude of the truncated model to the (8+6)Y model. $\tau_N \approx 13\ ms$ for these simulations.

dynamics deteriorate and the predicted hyperpolarized signal deviates from the values predicted from the actual system. By the point where only the ^{15}N is included in the (3+1)Y, the magnitude and structure of the hyperpolarization dynamics differ significantly from the actual system. However, the (3+1)Y truncation highlights an interesting aspect of these simulations, as there are no ancillary ^{1}H in this system and the free-species is represented by a single spin-1/2 nucleus. In comparison to the other truncated models, the additional structure of the hyperpolarization dynamics that persists for times much longer than the average lifetime of the ligand on the complex actually arises from the coherent dynamics of the free ligand. This highlights the critical nature of including all relevant effects when modeling the SABRE system, as next-generation SABRE experiments should be optimized understanding that the evolution of the free species will significantly affect the resultant performance.

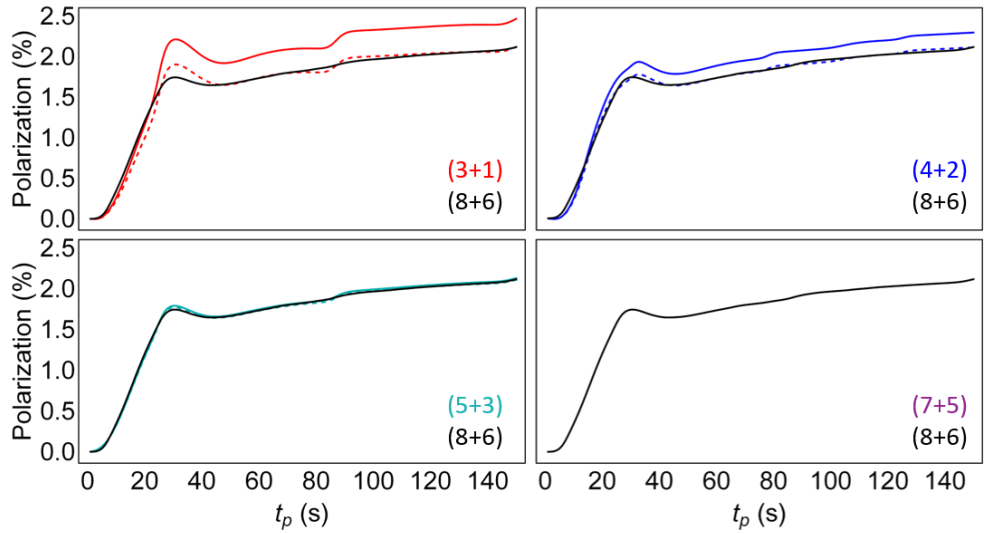

Figure 21: Truncation errors in coherently-driven LIGHT-SABRE experiments. A. Series of truncated ^{15}N-pyridine models as well as the exact (8+6)Y model. **B.** Comparison of the hyperpolarization generated in a coherently-driven LIGHT-SABRE varying the LAC 'ON' time t_p. The solid lines in color are the simulation output, and the dashed lines are the result of fitting the amplitude of the truncated model to the (8+6)Y model. $\tau_N \approx 13\ ms$ for these simulations.

While all ancillary nuclei are strongly coupled in the SABRE-SHEATH limit, examining the case of LIGHT-SABRE provides an interesting comparison to this limit (Fig. 21). As the LIGHT-SABRE experiment is performed at high magnetic field, only the secular components of the heteronuclear J-couplings survive. As such, the Hamiltonian is given by:

$$\hat{\mathcal{H}} = \Delta\omega_N \hat{S}_z + \omega_{1,N}\hat{S}_x + \sum_i \omega_i \hat{I}_{iz} + 2\pi \sum_{i<j} J_{ij}\hat{I}_i \cdot \hat{I}_j + 2\pi \sum_i J_{ij}\hat{I}_{iz}\hat{S}_z \qquad (3.32)$$

In this case, all homonuclear couplings are strongly coupled and the ^{1}H spins are rotated at the frequency of the parahydrogen-derived hydrides. Thus, the first sum only indexes over the ancillary ^{1}H nuclei. Where the SABRE-SHEATH truncated models immediately deteriorate in performance from the explicit (8+6)Y spin system, the LIGHT-SABRE case is more robust to truncation of the ancillary nuclei. In fact, even the (5+3)Y truncated model predicts the hyperpolarization dynamics of the realistic system with only minor deviation. In this case, when the ancillary nuclei are weakly coupled to the target ^{15}N nucleus thus forbidding direct flow of polarization to these nuclei, the impact of truncation is much less than in the case

where the non-secular J-coupling terms can directly convert ^{15}N polarization into spin order on the ancillary ^{1}H.

3.4 Conclusions

The final result that Binsch[92] derived unifying quantum evolution and chemical exchange was correct to lowest order for magnetic resonance, despite having arrived at the result under assumptions that were not reflective of the underlying physics. However, correcting the statistical assumptions upon which the model is built provides access to higher-order exchange interactions that, under many conditions, may be rearranged to give a scalar correction factor to the equation of motion. This has led to the development of an exact master equation treatment for chemical exchange in the superoperator formalisms, called the DMEx[116]. In doing so, a robust and exhaustive theoretical model for SABRE can be constructed to guide the development and optimization of this technique called the DMExFR2. We will utilize the theoretical framework for SABRE developed in this chapter as the fundamental basis for the development and optimization of novel experimental techniques.

Chapter 4: Expanding the scope of heteronuclear SABRE at high field

Extended SABRE (X-SABRE) experiments target the hyperpolarization of spin-1/2 heteronuclei like ^{13}C[43, 46, 118], ^{15}N[44, 47, 49, 51, 52, 87, 119-126], and ^{19}F[84, 127]. These experiments belong to one of two modalities: hyperpolarization at arbitrarily high magnetic fields and hyperpolarization at ultralow magnetic fields. Despite the original demonstration of X-SABRE being at high magnetic field, shown in the LIGHT-SABRE[52] and RF-SABRE[128] experiments, the ultralow-field variant SABRE-SHEATH[51, 87, 123] has become the preeminent X-SABRE hyperpolarization method. This can be attributed to the fact that SABRE-SHEATH routinely generates the largest observed hyperpolarization of the X-SABRE methods and that the ultralow-field matching condition is nearly completely invariant to changes in molecular structure and target heteronucleus. Furthermore, SABRE-SHEATH generates hyperpolarization in both single and multiple ligand environments, whereas LIGHT-SABRE and its variants generate hyperpolarization in systems with a single ligand, which constitute the vast minority of SABRE systems. Unlike SABRE-SHEATH, direct hyperpolarization at the detection field does not require specialized equipment outside of the basic NMR setup and parahydrogen supply, and can be used immediately in conjunction with conventional NMR experiments. Furthermore, high-field methods naturally permit hyperpolarization in the presence of quadrupolar (spin $> 1/2$) nuclei, which act to quench hyperpolarization through the rapid relaxation mechanisms at ultralow magnetic fields[46].

Herein, we will discuss efforts to optimize the hyperpolarization of high-field X-SABRE methods and expand the target scope of these experiments. Importantly, the total hyperpolarization achieved by SABRE-SHEATH is unlikely to be rivaled by high-field techniques. This is because SABRE-SHEATH has the advantage of exposing the entire sample to a homogeneous magnetic field that can be easily varied in any direction, permitting greater flexibility and finer control of the experiment. As highlighted in Table 1, an enormous body of work has been previously developed in the community to pursue high field X-SABRE. In this work, we expand on and improve high-field X-SABRE variants with the DARTH-SABRE[89], ^{1}H-decoupled LIGHT-SABRE[129], and broadband X-SABRE[130] experiments, which were developed to circumvent the limitations of the previous experiments and put high-field and ultralow-field X-SABRE on a similar experimental footing. This progression of experiments provide an avenue to explore X-SABRE hyperpolarization at arbitrarily high

Table 2: Development of high-field X-SABRE experiments. Relative to SABRE-SHEATH, the original LIGHT-SABRE and RF-SABRE experiments have considerable experimental restrictions that limit scope and performance of the technique. Many experiments were developed by the community to augment the original experiments and expand the scope of high field X-SABRE. The DARTH-SABRE, ^{1}H dLIGHT-SABRE (d = decoupled), and broadband X-SABRE experiments (highlighted) were all developed in this work to match the experimental scope of the coherent SHEATH experiment.

	Experiment	Symmetric ligand environments	Asymmetric ligand environments	Coherently pump polarization	Catalytic repolarization	Insensitive to changing target	Multiple targets simultaneously
Ultralow Field	SABRE-SHEATH	✓	✓	✗	✓	✓	✓
	Coherent SHEATH	✓	✓	✓	✓	✓	✓
High Field	LIGHT-SABRE	✓	✗	✗	✓	✗	✗
	RF-SABRE	✓	✗	✗	✓	✗	✗
	INEPT-SABRE	✓	✗	✓	✗	✓	✗
	Re-INEPT-SABRE	✓	✗	✓	✓	✗	✗
	ADAPT-SABRE	✓	✗	✗	✓	✗	✗
	SLIC-SABRE	✓	✗	✗	✓	✗	✗
	DARTH-SABRE	✓	✗	✓	✓	✗	✗
	^{1}H dLIGHT-SABRE	✓	✓	✓	✓	✗	✗
	Broadband X-SABRE	✓	✓	✓	✓	✓	✓

magnetic fields with the same flexibility as SABRE-SHEAH. All of the following results are rigorously grounded in the DMExFR2 theoretical framework discussed in **Chapter 3** and were the used to inform optimization.

4.1 Optimizing the LIGHT-SABRE experiment

The LIGHT-SABRE[52] experiment was the first X-SABRE demonstration in which weak radiofrequency irradiation was used to convert the parahydrogen singlet order into observable magnetization on a ^{15}N-nucleus. This experiment was motivated in the case where the ligand and parahydrogen bind the iridium complex to form an AA'XX spin system, although we will discuss a slightly simpler AA'X system for brevity. Here, we will cast the Hamiltonian in the rotating frame of the pulse and have chosen a rotating frame for the $\hat{I}$-spins such that the Zeeman terms for the hydrides disappear ($\Delta\omega_H = 0$). Then, the Hamiltonian while being irradiated by a radiofrequency pulse on the ^{15}N-channel is:

$$\hat{\mathcal{H}} = \Delta\omega_N \hat{S}_z + \omega_{1,N}\hat{S}_x + 2\pi\left(J_{HH}\hat{I}_1 \cdot \hat{I}_2 + J_{NH}\hat{I}_{1z}\hat{S}_z\right) \tag{4.1}$$

If written in a singlet-triplet basis for the hydrides and the Zeeman basis on the heteronucleus for $\Delta\omega_N = 0$, the pertinent subspace of this Hamiltonian is:

$$\hat{\mathcal{H}} = \begin{pmatrix} & |T_H^0\alpha_N\rangle & |T_H^0\beta_N\rangle & |S_H^0\alpha_N\rangle & |S_H^0\beta_N\rangle \\ \langle T_H^0\alpha_N| & 2\pi J_{HH} & \frac{\omega_{1,N}}{2} & \frac{\pi J_{NH}}{2} & 0 \\ \langle T_H^0\beta_N| & \frac{\omega_{1,N}}{2} & 2\pi J_{HH} & 0 & \frac{-\pi J_{NH}}{2} \\ \langle S_H^0\alpha_N| & \frac{\pi J_{NH}}{2} & 0 & 0 & \frac{\omega_{1,N}}{2} \\ \langle S_H^0\beta_N| & 0 & \frac{-\pi J_{NH}}{2} & \frac{\omega_{1,N}}{2} & 0 \end{pmatrix} \tag{4.2}$$

Under this condition, it is more convenient to recast the basis in terms of magnetization quantized along the radiofrequency field direction by defining the states:

$$|X_N^+\rangle = \frac{|\alpha\rangle + |\beta\rangle}{\sqrt{2}};\ |X_N^-\rangle = \frac{|\alpha\rangle - |\beta\rangle}{\sqrt{2}} \tag{4.3}$$

This basis set diagonalizes the $\hat{S}_x$ operator and gives the hyperpolarization-active subspace:

$$\hat{\mathcal{H}} = \begin{pmatrix} & |T_H^0 X_N^+\rangle & |S_H^0 X_N^-\rangle & |T_H^0 X_N^-\rangle & |S_H^0 X_N^+\rangle \\ \langle T_H^0 X_N^+| & 2\pi J_{HH} + \omega_{1,N} & \frac{\pi J_{NH}}{2} & 0 & 0 \\ \langle S_H^0 X_N^-| & \frac{\pi J_{NH}}{2} & 0 & 0 & 0 \\ \langle T_H^0 X_N^-| & 0 & 0 & 2\pi J_{HH} & \frac{\pi J_{NH}}{2} \\ \langle S_H^0 X_N^+| & 0 & 0 & \frac{\pi J_{NH}}{2} & \omega_{1,N} \end{pmatrix} \tag{4.4}$$

The matching condition for this subspace is given by:

$$\pm\omega_{1,N} \approx 2\pi J_{HH} \tag{4.5}$$

Hyperpolarization may be generated if, for instance, we can excite the transition from the $|S_H^0 X_N^-\rangle \rightarrow |T_H^0 X_N^+\rangle$ states while suppressing the $|S_H^0 X_N^+\rangle \rightarrow |T_H^0 X_N^-\rangle$ transition. Conveniently, one of these transitions is automatically selected for depending on the phase of the pulse, such that a pulse with phase x and with phase $\bar{x}$ generate oppositely-signed magnetization. For instance, the $|S_H^0 X_N^-\rangle \rightarrow |T_H^0 X_N^+\rangle$ transition is optimally excited when $\omega_{1,N} = -2\pi J_{HH}$, giving:

$$\langle S_H^0 X_N^- | \hat{\mathcal{H}} | S_H^0 X_N^- \rangle = \langle T_H^0 X_N^+ | \hat{\mathcal{H}} | T_H^0 X_N^+ \rangle \tag{4.6}$$

For this same condition, the energy separation between the $|S_H^0 X_N^+\rangle$ and $|T_H^0 X_N^-\rangle$ states is $\Delta = 2\pi J_{HH} + \omega_{1,N}$. To gain an understanding of the relative excitation of these subspaces, it is beneficial to examine the quantum dynamics of an arbitrary two-level system, which may be solved exactly, as

$$\hat{\rho}(t) = \exp\left(-i\begin{pmatrix} 0 & V \\ V & \Delta \end{pmatrix} t\right) \cdot \begin{pmatrix} 1 & 0 \\ 0 & 0 \end{pmatrix} \cdot \exp\left(i\begin{pmatrix} 0 & V \\ V & \Delta \end{pmatrix} t\right) \tag{4.7}$$

Equation 4.7 may be solved by hand or with the aid of a numerical programming language, such as Mathematica. From the solution of this equation, we find that the maximum population transfer allowed between the states of a two level system, which we will call Ξ, is given by the magnitude of the on-diagonal terms in $\hat{\rho}(t)$ and is:

$$\Xi = \frac{4V^2}{4V^2 + \Delta^2} \tag{4.8}$$

For $\Delta = 0$, population can be fully inverted between the two states. If we call the subspace containing the $|S_H^0 X_N^-\rangle \rightarrow |T_H^0 X_N^+\rangle$ transition subspace 1, $\Xi_1 = 1$ when $\omega_{1,N} = -2\pi J_{HH}$. However, the other subspace, which we will call subspace 2, is simultaneously excited by the pulse at a diminished magnitude of ($J_{NH} = -25.4; J_{HH} = -9.2; \omega_{1,N} = -J_{HH}$):

$$\Xi_2 = \frac{J_{NH}^2 \pi^2}{J_{NH}^2 \pi^2 + \left(2\pi J_{HH} + \omega_{1,N}\right)^2} \approx 0.72 \tag{4.9}$$

The maximum X-polarization that may be achieved is then given by:

$$P_X = P_S(\Xi_1 - \Xi_2) = P_S\left(1 - \frac{J_{NH}^2 \pi^2}{J_{NH}^2 \pi^2 + \left(2\pi J_{HH} + \omega_{1,N}\right)^2}\right) \tag{4.10}$$

P_S is the initial parahydrogen fraction. This resultant magnetization could then be stored using y-pulses that are selective for the iridium-bound species and are interleaved in the sequence. Experimentally, this approach had been shown to generate signal enhancements on the order of $\varepsilon \approx 150$ for ^{15}N-pyridine[52].

Exchange is occurring continuously throughout the experiment and any ligands to exchange off the bound species before the selective y-pulse is applied are unobserved. As only

the $\hat{S}_z$ spin order is detected at the end of the experiment, it is more beneficial to directly generate z-magnetization, such that the hyperpolarization is stored along $\hat{z}$ when exchange occurs. Directly generating $\hat{S}_z$ spin order essentially increases the efficiency of detecting the hyperpolarization that is generated during the sequence but does not necessarily affect the net magnetization that is generated. This can be accessed for off-resonant excitation and the Hamiltonian then becomes:

$$\hat{\mathcal{H}} = \begin{pmatrix} & |T_H^0\alpha_N\rangle & |T_H^0\beta_N\rangle & |S_H^0\alpha_N\rangle & |S_H^0\beta_N\rangle \\ \langle T_H^0\alpha_N| & 2\pi J_{HH} & \frac{\omega_{1,N}}{2} & \frac{\pi J_{NH}}{2} & 0 \\ \langle T_H^0\beta_N| & \frac{\omega_{1,N}}{2} & \Delta\omega_N + 2\pi J_{HH} & 0 & \frac{-\pi J_{NH}}{2} \\ \langle S_H^0\alpha_N| & \frac{\pi J_{NH}}{2} & 0 & 0 & \frac{\omega_{1,N}}{2} \\ \langle S_H^0\beta_N| & 0 & \frac{-\pi J_{NH}}{2} & \frac{\omega_{1,N}}{2} & \Delta\omega_N \end{pmatrix} \tag{4.11}$$

The matching condition for this transition can be found from the Hamiltonian and is:

$$\pm\Delta\omega_N \approx \omega_{1,N} \approx 2\pi J_{HH} \tag{4.12}$$

For either the on-resonant case or the off-resonant case, it is beneficial to examine the spin operator pathways that connect the initial parahydrogen singlet state, which in operator notation is proportional to $\hat{I}_1 \cdot \hat{I}_2$, to $\hat{S}_z$ magnetization on the target nucleus. As introduced in Chapter 2, the spin operator pathway may be found by performing the Taylor expansion of the density matrix,

$$\begin{aligned} \hat{\rho}(t) &= \hat{\rho}_0 + i[\hat{\rho}_0, \hat{\mathcal{H}}]t + i\left[\frac{\partial\hat{\rho}(t)}{\partial t}, \hat{\mathcal{H}}\right]\frac{t^2}{2} + i\left[\frac{\partial^2\hat{\rho}(t)}{\partial t^2}, \hat{\mathcal{H}}\right]\frac{t^3}{6} + \cdots \\ &= \sum_n \hat{\rho}^{(n)}(t), \end{aligned} \tag{4.13}$$

$$\hat{\mathcal{H}} = \Delta\omega_N \hat{S}_z + \omega_{1,N}\hat{S}_x + J_{HH}\hat{I}_1 \cdot \hat{I}_2 + J_{NH}\hat{I}_{1z}\hat{S}_z$$

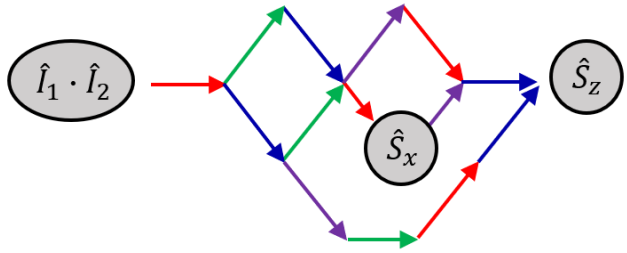

Figure 22: Spin operator pathways for LIGHT-SABRE. To generate magnetization ($\hat{S}_x$ or $\hat{S}_z$) from the parahydrogen singlet ($\hat{I}_1 \cdot \hat{I}_2$), the initial density matrix must sequentially interact with the different terms of the Hamiltonian. The shortest pathways to the magnetized states are shown by each of the arrows, where each arrow corresponds to the density matrix commuting with the representative term of the Hamiltonian.

we may calculate the terms in the expansion until every transition that is accessible by the Hamiltonian is mapped. For efficiency, we have developed a computational formulation of this expansion that performs the expansion for the user, which is described in Appendix B. While writing out the algebraic expressions would be entirely possible, the complexity of the terms and the accrued power dependence obfuscates any use of the technique to interpret the dynamics. However, the states that are accessed by the Hamiltonian may be represented as vertices on a graph and the transitions between these vertices may be represented by directed edges to the graph, where the edge is given a color code based on the term in the Hamiltonian used to generate that transition. This leads to graphs like the one shown in Fig. 22, which maps all the possible transitions by the Hamiltonian given in eq. 4.1 with an initial starting state of $\hat{I}_1 \cdot \hat{I}_2$ through the leading order terms for $\hat{S}_z$. Importantly, the $\hat{I}_{1z}\hat{I}_{2z}$ term commutes with the $\hat{\mathcal{H}}$ given in **eq.** 4.1 at all times, so all meaningful hyperpolarization dynamics arise from the $\hat{I}_{1x}\hat{I}_{2x} + \hat{I}_{1y}\hat{I}_{2y}$ term of the singlet. For the $\Delta\omega_N = 0$ case, there are two pathways that lead to $\hat{S}_x$ that are each linearly dependent on $\omega_{1,N}$, hence why changing the sign of $\omega_{1,N}$ changes the sign of $\hat{S}_x$. The off-resonant case can generate $\hat{S}_z$ spin order and has a quadratic power dependence on $\omega_{1,N}$, meaning that there is no phase-dependence on the pulse (when it is a

constant phase) but acquires a linear dependence on the resonance-offset from the pulse. Each of the steps in the spin operator pathway is optimized at a $\pi/2$ phase rotation under the respective term of the Hamiltonian. For a constant-amplitude irradiation like in LIGHT-SABRE, the pulse sequence parameters are optimized to balance the simultaneous phase evolution under each of the terms. However, this makes the LIGHT-SABRE pulse more sensitive to inhomogeneities in $\omega_{1,N}$ and $\Delta\omega_N$.

In practical limits, the goal is to produce the largest total magnetization. In this case, the pulse amplitude is particularly difficult to control at the sample level, as the sample often extends beyond the active region of the probe coil. As such, $\omega_{1,N}$ varies spatially over the sample. Techniques to compensate for inhomogeneities are well known in conventional magnetic resonance, but were first applied to access the singlet-manifold for pairs of magnetically inequivalent spins by Warren and coworkers in 2014[131]. They examined the case of adiabatically power-ramped pulses, which demonstrated robust performance for storing (and accessing) the singlet state. Adiabatic pulses are generally defined under the condition that the pulse changes slowly with respect to the spin dynamics and can be used to remove various artifacts that are generated by rectangular pulses. For the case of SABRE, the ligand exchanges with a rate on the order of the dominant couplings, meaning that adiabatic pulses can only act on any target spin for its lifetime on the complex. Even after a particular ligand dissociates from the complex, the parahydrogen (AA') nuclei that remain are in a state that is the projection of the system prior to exchange, and essentially provide 'memory' to the coherent dynamics. Thus, even simple alterations to the pulse sequence, such as linearly ramping $\omega_{1,N}$ over hundreds of milliseconds, were shown to compensate for $\omega_{1,N}$ inhomogeneities in LIGHT-SABRE experiments (Fig. 23). As the active region of most NMR

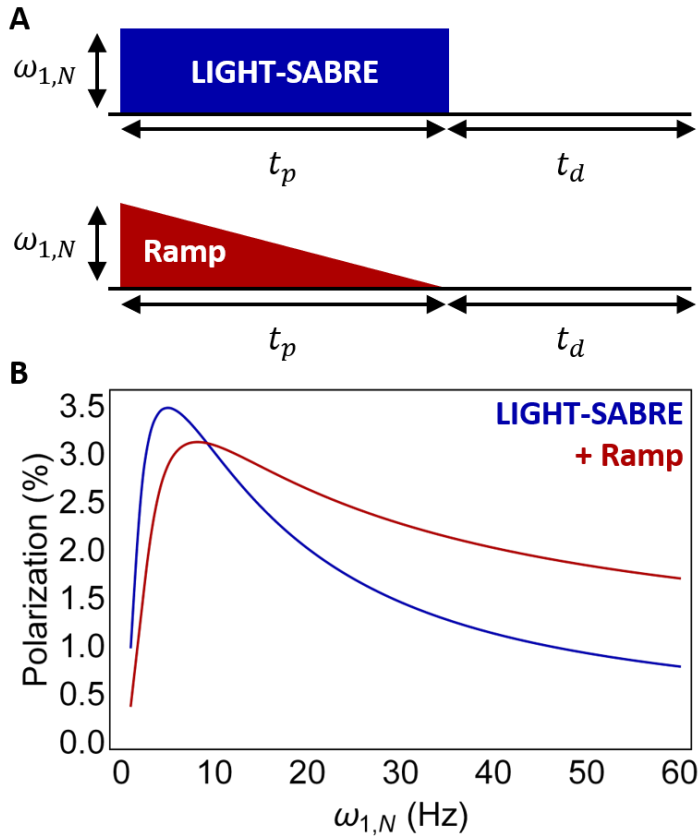

Figure 23: Shaping the LIGHT-SABRE pulse. A. The original LIGHT-SABRE experiment utilizes a constant-amplitude (rectangular) radiofrequency pulse to generate hyperpolarization. Shaping the pulse with a ramped waveform can be used to compensate for experimental inhomogeneities. **B.** Dependence of the SABRE hyperpolarization on the pulse amplitude, $\omega_{1,N}$. For the rectangular pulse, the polarization in optimized at approximately $\omega_{1,N} \approx 2\pi J_{HH}$ and then rapidly decreases with increasing powers. Ramping the pulse down from $\omega_{1,N}$ for the same pulse length makes the experiment less sensitive to B_1 inhomogeneities.

coils only covers a fraction of a standard $500\ \mu L$ SABRE sample, the pulse power will vary anywhere between $\omega_{1,N} \approx 0$ up to the power used in the active region. We will refer to this limit as the quasi-CW limit, where the pulse is essentially a continuous wave irradiation of the system. After the pulse, a delay t_d is used to permit exchange and allow further hyperpolarization to be generated. This pulse sequence may be looped multiple times to accumulate hyperpolarization on the target species. These simulations assume a ligand exchange rate of $k_{d,N} = 50\ s^{-1}$, corresponding to an average lifetime of $\tau_N = 13\ ms$, and a hydride replenishment rate of $k_{a,H} = 2\ s^{-1}$ on a model (4+1)X system at an iridium-to-

substrate ratio of $[Ir]/[S] \approx 1/20$. While the LIGHT-SABRE condition is maximized at approximately $\omega_{1,N} \approx 8\,Hz$, which is approximately the value of the J_{HH} used in the simulation, the performance of the constant-amplitude pulse rapidly degrades with increasing $\omega_{1,N}$. The linearly ramped pulse is predicted to have a much more robust performance in comparison and generates nearly double the polarization at $\omega_{1,N} = 60\,Hz$. For regions outside the active region of the coil, this means that hyperpolarization can still be generated more efficiently than if using a constant-amplitude pulse, which we will refer to as the adiabatic LIGHT-SABRE experiment. A similar experiment was reported by Pravdivtsev *et al.* in 2015 that utilized off-resonant excitation to directly generate $\hat{S}_z$ magnetization and employed a ramped ^{15}N-pulse[128]. However, they only applied the pulses a single time to the system, which does not take advantage of the catalytic nature of SABRE hyperpolarization.

We demonstrated irradiating off-resonance and ramping the LIGHT-SABRE pulse experiment can increase the robustness of the pulse sequence to errors in $\omega_{1,N}$ relative to the constant-amplitude pulse at the same resonance offset (Fig. 24). For these experiments, we utilized using $t_p = 700\,ms$ ramped pulses and $t_d = 500\,ms$ delays between the pulses. While hyperpolarization is generated when the pulse is on-resonance ($\Delta\omega_N = 0$) in the original LIGHT-SABRE experiment, off- resonant excitation can directly generate z-magnetization, which greatly improves performance. Due to the large number of coupled spins in the ^{15}N-pyridine SABRE system, we compare the data to simulations using a truncated (8+3)X model using a ligand exchange rate of $k_{d,N} = 50\,s^{-1}$and hydride exchange rate of $k_{a,H} = 2\,s^{-1}$, which are known from experiment. Importantly, the only parameter that is fit between the experimental data and simulations is the absolute amplitude, indicating excellent agreement

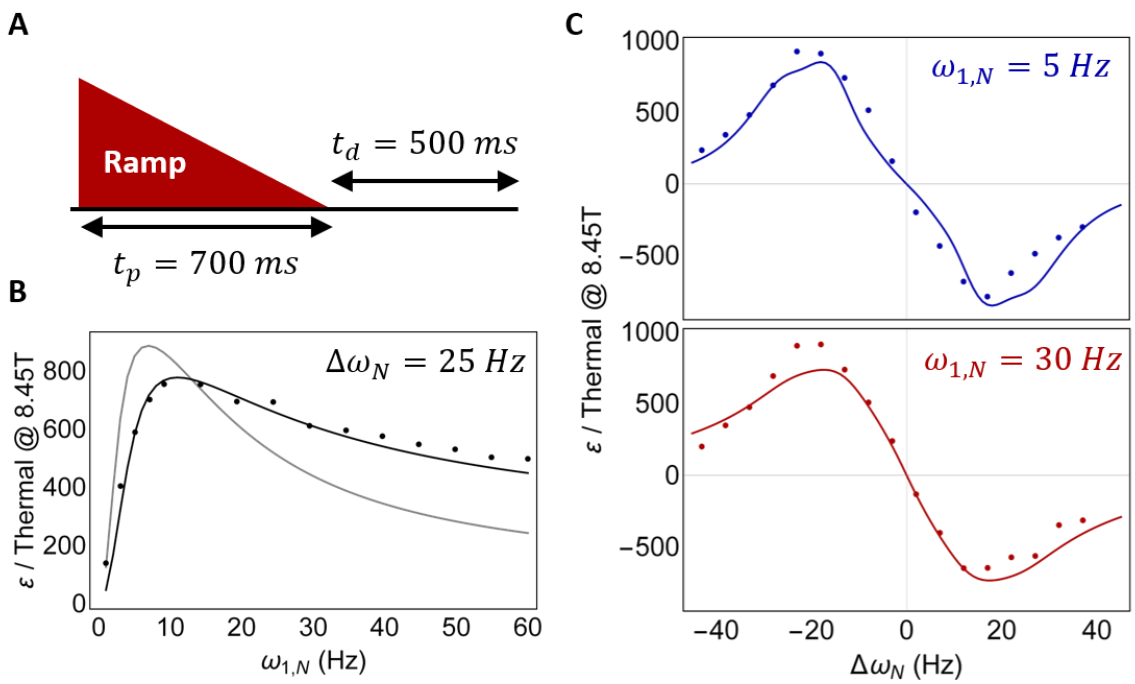

Figure 24: Adiabatic LIGHT-SABRE experiment. A. An adiabatically ramped pulse was applied off-resonance the iridium-bound ^{15}N-pyridine resonance at 8.45T. **B.** The power-dependence of the ramped pulse was measured at $\Delta\omega_N = 25\ Hz$ (experimental data), and compared to simulations using a (8+3)X truncated ^{15}N-pyridine model (black) and compared to the LIGHT-SABRE performance at this offset (gray). **C.** Resonance profiles for the adiabatic LIGHT-SABRE experiment using $\omega_{1,N} = 5\ Hz$ (top) or $\omega_{1,N} = 30\ Hz$ (bottom).

between model and experiment. Signal enhancements up to $\varepsilon \approx 1000\times$ were observed using a parahydrogen enrichment of $[pH_2] \approx 43\%$.

All the original X-SABRE experiments, those developed by the Warren lab as well as others in the field[51, 52, 128, 132], were motivated by analyzing the matching condition to generate SABRE hyperpolarization, akin to the discussion in this section. While identifying this condition is a fundamental for any resonant manipulation of coherent dynamics, the analysis of the quantum mechanics is only partially representative of the underlying spin physics. A complete picture requires incorporating an understanding of the quantum dynamics in tandem with the energy level structure of the system, and as Chapter 3 introduced, accurately incorporating the chemical exchange interaction in these dynamics is essential. Doing so highlights new avenues to develop more robust X-SABRE experiments.

4.2 Unveiling coherently driven hyperpolarization dynamics in SABRE

In the Introduction, we introduced the idea that spurred most of the work in this research: pumping the matching condition provides access to and control over the underlying coherent dynamics in SABRE. The coherent component of the SABRE dynamics had remained elusive to this point, as observable phase coherence is lost to exchange within approximately $3\tau_N$ of the experiment being initiated, on a timescale of tens to hundreds of milliseconds. However, if the matching condition is turned on for a time t_p and then turned off for a time $t_d \gg t_p$ to permit exchange, the coherent dynamics under the pulse are encoded in the resulting hyperpolarization after repeating this sequence for approximately one minute. Performing the same experiment for different values of t_p then provides access to the coherent hyperpolarization dynamics (Fig. 25). The delay t_d is intended to re-initialize the system after each subsequent pulse and thus should be optimized so to permit sufficient ligand and hydride exchange. While the coherent hyperpolarization dynamics are encoded in the polarization after a single pulse, the resulting signals are too low to quantify with any degree of accuracy. As such, this pulse sequence is applied many times so to accumulate large, hyperpolarized signals, and as such, the observed dynamics do not necessarily match the initial dynamics. Even in the case where the delays between pulses are much larger than the lifetime of the complex, the resulting signals from the pulse trains deviate from the initial coherent dynamics (Fig. 25B, top). These deviations are aggravated in the limit when the pulses are on the order of the ligand lifetime of the complex, as multiple pulses are allowed to act on the same complex leading to additional structure to the hyperpolarization dynamics (Fig. 25B, bottom). This highlights the

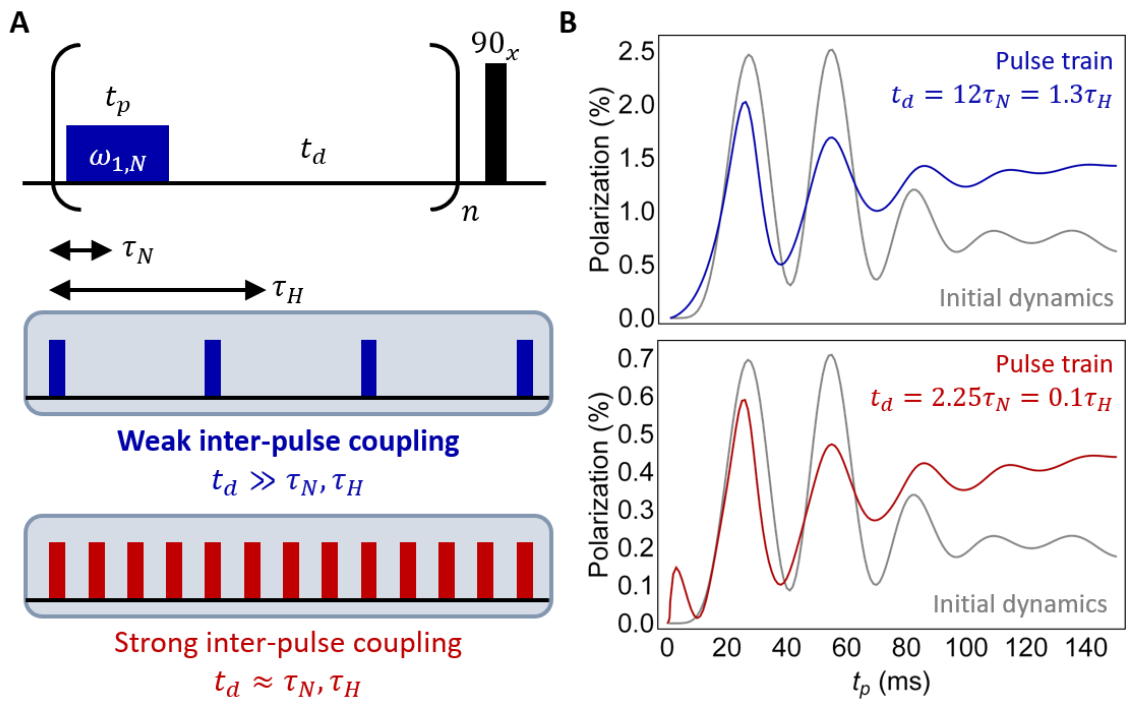

Figure 25: Coherently-driven SABRE hyperpolarization experiment. A. The matching condition is turned on for a time t_p and is followed by a delay t_d permitting exchange of the ligand off the complex. This sequence is repeated n times for approximately 60s to accumulate hyperpolarization on the free species. Depending on the value of t_d, the effects of multiple pulses will either be largely circumvented ($t_d \gg \tau_N$) or generate additional effects from the accumulating action of multiple pulses ($t_d \approx \tau_N$). **B.** The coherent dynamics are encoded in the resulting signal, which may be directly accessed by scanning t_p. The initial coherent dynamics (gray) can deviate largely from the ultimate signal that is encoded at the end of the pulse train and can be further aggravated in the strong inter-pulse coupling limit.

importance of being able to simulate the entire SABRE experiment instead of simply the initial coherent dynamics and emphasizes the benefit of using the DMExFR2 simulations over the more computationally expensive QMC simulations.

The coherent hyperpolarization dynamics in SABRE at high field can be immediately observed using the pumped LIGHT-SABRE variant, which was performed on a ^{15}N-pyridine sample (Fig. 26A). Using a pulse power of $\omega_{1,N} = 32\ Hz$ yields highly visible coherent oscillations in the hyperpolarization as a function of the t_p length. This is far from the matching condition ($\Delta\omega_N \approx \omega_{1,N} \approx J_{HH}$) but is useful in testing the robustness of the DMExFR2 simulations against experiment, which yields a minor $\sigma = 5.8\%$ (RMSD)

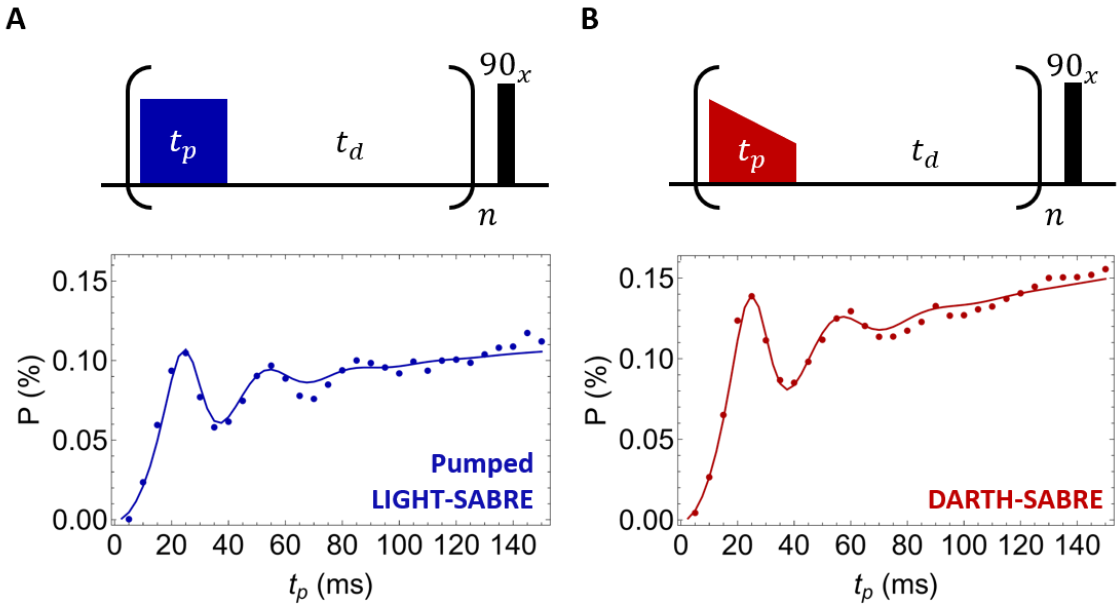

Figure 26: Pumped LIGHT-SABRE and DARTH-SABRE. A. Coherently pumping the LIGHT-SABRE matching condition off-resonance directly generates hyperpolarized $\hat{S}_z$ spin order and increases the efficiency over the original LIGHT-SABRE experiment by more than 2-fold. Furthermore, the experimental results are in excellent agreement with the DMExFR2 simulations. **B.** Shaping the LIGHT-SABRE pulse improves the experimental performance while retaining excellent agreement between experiment and simulation. For both cases, $t_d = 600\ ms$ and the pulse sequence was looped for a total experimental duration of $T = 60\ s$. The DMExFR2 simulations use exchange rates of $k_N = 50\ s^{-1}$ and $k_H = 2\ s^{-1}$, and J-couplings were measured from the ^{1}H spectrum of the iridium hydrides to be $J_{HH} = -8.9\ Hz$, $J_{NH} = -23.6\ Hz$, and (to ortho-^{1}H) $J_{NH'} = -10\ Hz$.

deviation between simulation and experiment. As demonstrated in the previous section, hyperpolarization may be boosted by adiabatically ramping the pulse towards the matching condition, thus compensating for loss to inhomogeneities. This is called the Delayed Adiabatic Ramps Transfer Hyperpolarization for SABRE, or DARTH-SABRE, experiment. Scanning the length of the shaped pulse also provides access to the coherent dynamics under that pulse shape. Furthermore, the t_p scan can identify experimental optima (Fig. 26B). There is excellent agreement between experiment and the DMExFR2 simulation for the case of shaped pulses, yielding a deviation of $\sigma = 3.8\%$. In both cases, the coherent dynamics are damped at a rate commensurate with the exchange rate of the ^{15}N-pyridine on the complex, which from simulation was extracted to be $\ln(2)/k_N \approx 13\ ms$. In other experimental regimes, such as

SABRE-SHEATH, where the matching condition simultaneously permits coherent evolution on both the bound and free species, the decay of the coherent dynamics will not solely be affected by the ligand exchange rate.

The first maximum in the hyperpolarization in Fig. 26 corresponds to inverting the populations between the initial singlet state ($\hat{I}_1 \cdot \hat{I}_2$) and the final magnetized state ($\hat{S}_z$), which may be thought of as a π-pulse for the hyperpolarization dynamics. In terms of conventional magnetic resonance, scanning t_p is analogous to a Rabi-cycling experiment where the hyperpolarization for various flip-angle pulses is measured. The ability to control the flip-angle

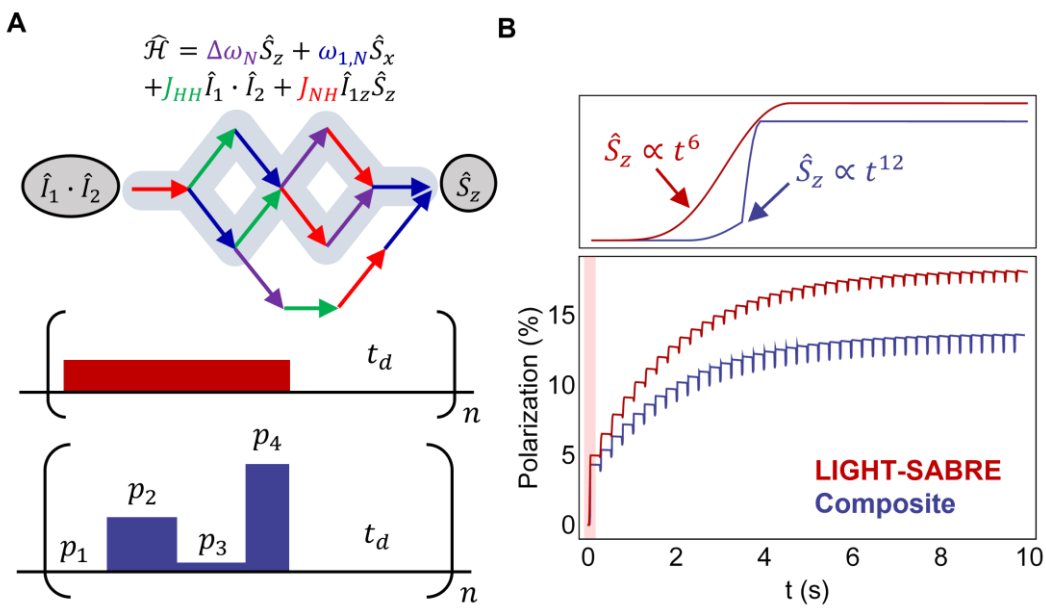

Figure 27: Optimizing the hyperpolarization transfer pulse. A. The spin operator pathway for a LIGHT-SABRE pulse may be used to guide optimization of a composite pulse to be used to generate hyperpolarization more efficiently. This method yielded a pulse shape shown in blue, which selects for the highlighted spin operator pathway, whereas the conventional LIGHT-SABRE pulse simultaneously optimizes all of the Hamiltonian interactions. **B.** While the composite pulse can generate approximately the same polarization as the LIGHT-SABRE pulse over the same time, the rise-time of the hyperpolarization is approximately t^{12} instead of t^6. Even though each step of the spin-operator pathway is optimized, the composite pulse is still outperformed by the LIGHT-SABRE pulse as exchange permits more hyperpolarization to be accumulated over the pulse duration. Simulations used $k_N = 16\ s^{-1}$ and $k_H = 6\ s^{-1}$. The pulse parameters for the periods of the composite pulse are (parameters are zero unless noted) $p_1 = \{t_{p_1} = 17\ ms\}$, $p_2 = \{\omega_{1,N} = 25\ Hz, t_{p_2} = 10\ ms\}$, $p_3 = \{\omega_{1,N} = 3\ Hz, \Delta\omega_N = 16\ Hz, t_{p_3} = 15\ ms\}$, and $p_4 = \{\omega_{1,N} = 45\ Hz, t_{p_4} = 5\ ms\}$. Pulses were all x-phase.

of the hyperpolarization dynamics immediately suggests that there is potential to construct composite or shaped pulses that act on the timescale of the exchange dynamics (Fig. 27). However, the pumped LIGHT-SABRE and DARTH-SABRE data (Fig. 26) indicate that the coherent dynamics can only be efficiently controlled through the first π-pulse due to exchange. While it would be possible to directly optimize a composite pulse shape within the DMExFR2 model, a general structure for the pulse can be motivated from the spin operator pathway for LIGHT-SABRE (Fig. 27A). There are four non-commuting sets of interactions that excite the highlighted pathways, and we may optimize individual pulses p_n to optimize each component of the pathway that join to form the composite pulse. For simplicity, we will use a (6+4)Y type system at a magnetic field where the hydrides are chemically equivalent, such as $0.05\,T$, to simplify the analysis. The conventional optimization of the LIGHT-SABRE pulse essentially looks to simultaneously optimize phase-rotation under each of the terms in the Hamiltonian to generate hyperpolarization. However, each of the individual terms optimizes under different conditions. For instance, the first derivative is proportional to $\hat{I}_{1y}\hat{I}_{2x}\hat{S}_z - \hat{I}_{1x}\hat{I}_{2y}\hat{S}_z$ spin order, which is maximized when the radiofrequency pulse is off. All subsequent spin orders will be scaled by the efficiency of pumping the first derivative, which is generated by phase-rotation under $J_{NH}\hat{I}_{1z}\hat{S}_z$. Selecting the highlighted spin operator pathway in Fig. 27 and sequentially optimizing each of the non-commuting steps in the sequence permits one to generate a composite pulse for coherently exciting X-SABRE hyperpolarization. Despite every step of the spin operator pathway being individually optimized, the performance of the derived composite pulse was worse than the LIGHT-SABRE pulse because the latter will generate polarization proportional to t^6, leading to $\hat{S}_z$ hyperpolarization that will accumulate upon exchange for $t_p < 30\,ms$. The composite pulse approximately generates $\hat{S}_z$ spin order

proportional to t^{12} due to the discontinuous nature of the excitation. This highlights that it will be critical for hyperpolarization to be rapidly generated so to minimize the loss to exchange.

Despite generating lower hyperpolarization, the composite pulse generates hyperpolarization over a significantly larger bandwidth than the LIGHT-SABRE pulse sequence (Fig. 28). The modulations in this resonance profile, which would sometimes prevent hyperpolarization from being generated, may be removed by shifting the phase of the p_2 component of the composite pulse from $x \rightarrow y$, which pre-compensates for evolution under $\Delta\omega_N$ during p_3. Then, hyperpolarization will be generated in at least one of the two spectra acquired with the composite pulse. This is the main idea behind phase cycling techniques, which in combination with expanding the hyperpolarization bandwidth will be treated explicitly in the following section. Importantly, the composite pulse derived here is specific to the molecular parameters that were used to construct the simulation, as all the various powers and times optimized here will change with different molecular parameters like the values of the J_{NH} and J_{HH} couplings. While this can be overcome with further optimization, there are larger intrinsic issues with the general approach that is employed when deriving hyperpolarization from the LIGHT-SABRE matching condition that must be considered.

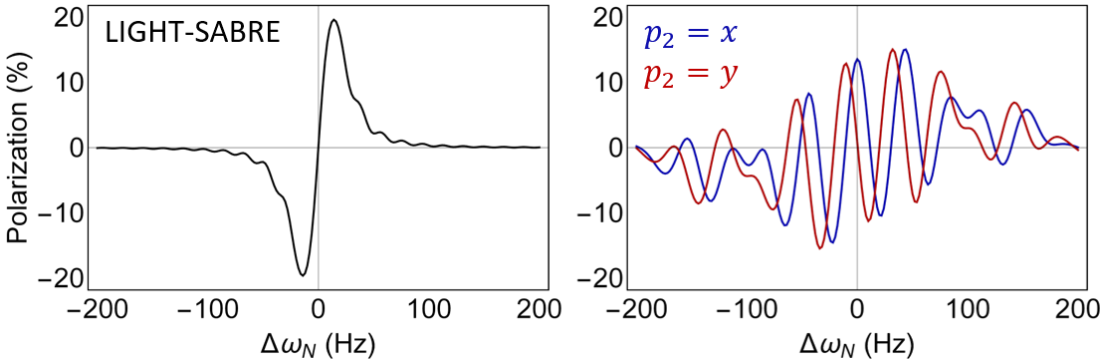

Figure 28: Field profiles for LIGHT-SABRE and composite pulses. The composite pulse can excite a larger bandwidth than the conventional LIGHT-SABRE pulse, although the profile is modulated. This can be compensated for by shifting the p_2 phase to a y-pulse.

While scanning t_p informs on the coherent dynamics of the system, scanning t_d informs on the optimal pumping rate of the system over the course of the experiment. This will depend on a confluence of many factors, such as the efficiency of each individual pulse in generating magnetization, the hydride exchange rate, the ligand to catalyst concentration ratio, and ligand relaxation rates. The dependence on the hydride exchange rate is particularly interesting, as t_d should optimize to shorter values when k_H is high and should optimize to longer values when k_H is slow. In the slow exchange case, the longer delay provides more time for the system to replenish the spin source, thus creating more magnetization. This trend is not observed in the simulations (Fig. 29A), which shows that the dynamics scanning t_d are

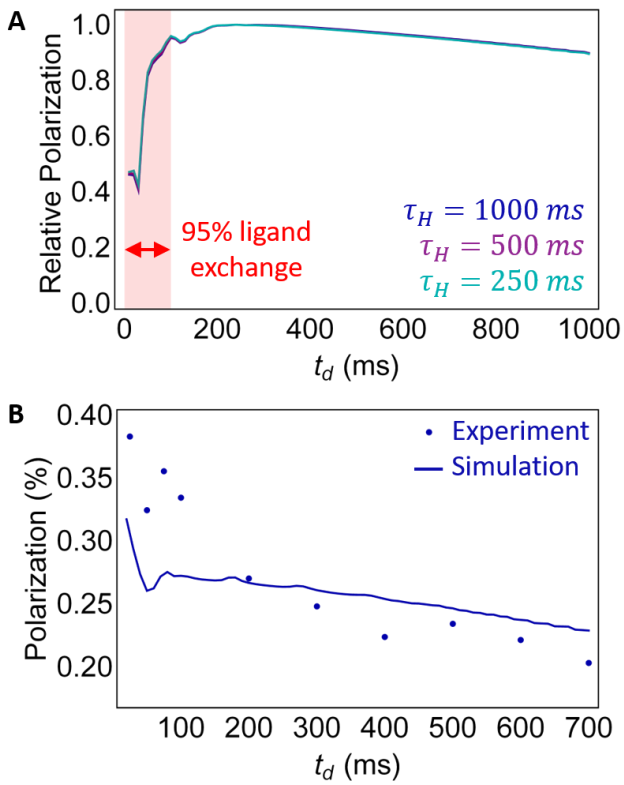

Figure 29: Dependence on t_d for different hydride exchange rates. A. One would expect the optimal value of t_d would decrease as k_H is increased, which should hold for all $t_d \geq 3\tau_N$ when 95% of the ligands have been replenished. However, the predicted dependence on the t_d is nearly completely superimposable even if the average lifetime is iterated from $\tau_H = 250\ ms$ to $\tau_H = 1000\ ms$. Simulations performed at $k_N = 30\ s^{-1}$. **B.** Experimentally scanning t_d using a $t_p = 25\ ms$ DARTH pulse shows significant deviation of the simulation from experiment, in stark contrast to the data collected varying t_p in the same sample.

nearly invariant to altering the k_H. The experimental data scanning t_d grossly deviates from the theoretical prediction (Fig. 29B), which stands in contrast to the excellent agreement shown in the same system when simply varying the parameter t_p in Fig. 26. While scanning t_p yielded results that were entirely expected, the dependence of hyperpolarization on t_d spurred two important questions: why can the simulations not reproduce the t_d dependence and why are the dynamics during t_d invariant to the hydride exchange rate?

The first of these questions is perhaps the most critical, as the development of next generation X-SABRE experiments is predicated on the DMExFR2 model being a robust and exhaustive implementation of the SABRE dynamics. Still, it is puzzling why there is such excellent agreement between experimental data and simulation when scanning one parameter but not the other. This may be unraveled if one considers the actual sample geometry in the high-field magnet probe (Fig. 30). These experiments were performed in a 5mm high-

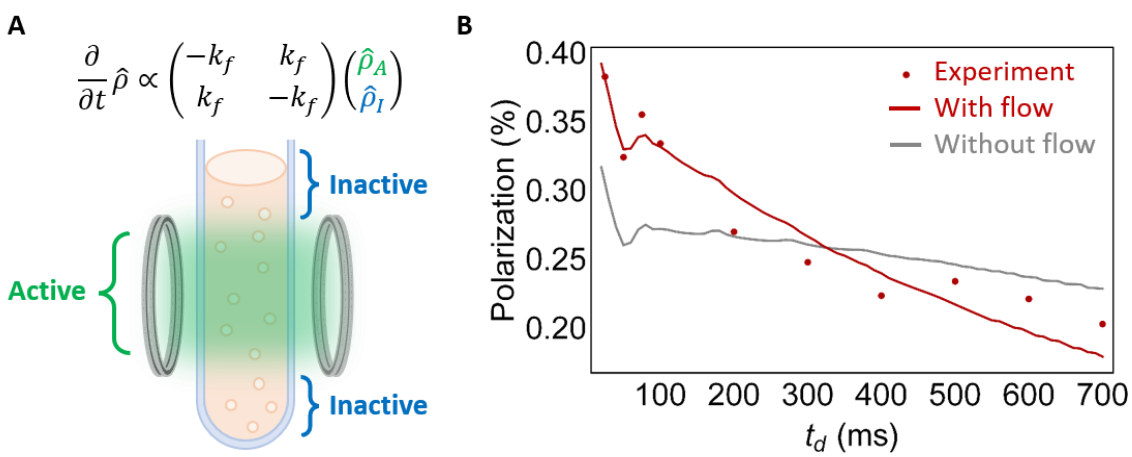

Figure 30: Sample geometry at high-field and flow effects in X-SABRE dynamics. A. The SABRE sample is bubbled within a 5mm high-resolution ^{1}H/^{2}H/^{13}C{^{15}N} probe whereby only a fraction of the sample sits in the active region of the coil. Therefore, the B_1 field (green) only irradiates the fraction of the sample in this region and the sample outside of this volume are essentially hyperpolarization inactive. Bubbling causes population to flow between the active and inactive regions of the sample, which may be included as a two-site pseudo-exchange. **B.** Including flow effects within the DMExFR2 model as a secondary set of exchange pathways and using a ratio of $[A]/[I] = 1/4$ (the relative concentration between the regions) and a flow rate of $k_f = 0.5\ s^{-1}$ recovers the experimental trend. Flow effects were incorporated by Shannon Eriksson.

resolution $^{1}H/^{2}H/^{13}C\{^{15}N\}$ probe where the SABRE sample extends beyond the active volume of the coil. In this case, only the sample in the active volume is irradiated and the sample outside of this region is essentially hyperpolarization inactive. However, parahydrogen is bubbled continuously through the sample during the experiment which leads to a mixing of the populations in these two coil regions. There can be different concentrations of sample in the two regions depending on the sample geometry, which can be represented by the ratio of these concentrations $[A]/[I]$. Then, this mathematically looks like a two-site pseudo-exchange between the active and inactive coil regions, which may be included in the DMExFR2 as additional exchange pathways that obey the same conventions established in Chapter 3 for chemical exchange. Including these effects in the DMExFR2 simulations using the parameters $[A]/[I] = 1/4$ and a flow rate of $k_f = 0.5\ s^{-1}$ recovers the trend observed in the experimental data. Of course, the B_1 field varies continuously between the active and inactive regions of the system but the assumption that we make to model this as an abrupt transition is sufficient to largely recover the flow-dependent effect. Flow effects are not present in SABRE-SHEATH, as it is trivial to build a solenoidal magnet that extends far past the sample.

While flow effects explain the disparity between simulation and experiment when scanning t_d, they do not explain why these dynamics are seemingly invariant to k_H other than uniformly generating more or less hyperpolarization. This suggests that there is a secondary process that counterbalances the addition of parahydrogen such that the optimum value of t_d does not depend on the amount of singlet order in the system. Examining the spin-operator pathway for AA'X or AA'XX' systems provides insight into this problem (Fig. 31A). When starting from singlet order ($\hat{I}_1 \cdot \hat{I}_2$), the transverse terms of the singlet ($\hat{I}_{1x}\hat{I}_{2x} + \hat{I}_{1y}\hat{I}_{2y}$) evolve under the J_{NH} coupling to generate the three-spin $\hat{I}_{1y}\hat{I}_{2x}\hat{S}_z - \hat{I}_{1x}\hat{I}_{2y}\hat{S}_z$ spin order. This order

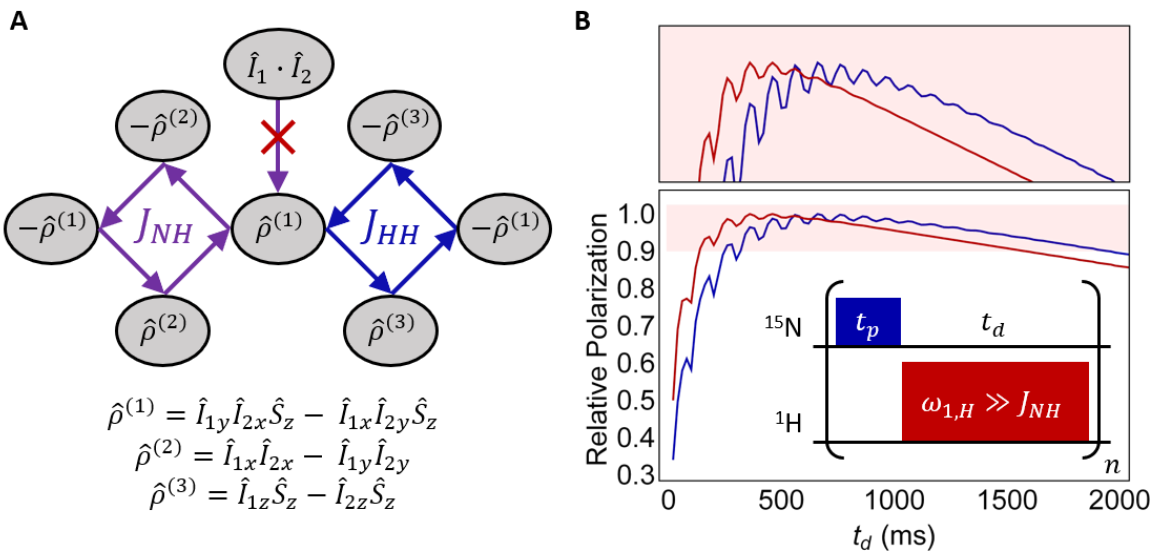

Figure 31: Recovery of k_H-dependent dynamics in the exchange delay. A. Spin operator pathway for AA'X spin systems in the absence of pulses. The J_{NH} coupling transforms the singlet spin order into three-spin $\hat{I}_{1y}\hat{I}_{2x}\hat{S}_z - \hat{I}_{1x}\hat{I}_{2y}\hat{S}_z$ spin order, which we denote as $\hat{\rho}^{(1)}$. This spin order then coherently averages to zero under both the J_{NH} and J_{HH} coupling, consuming the parahydrogen spin order. As $J_{NH} \gg J_{HH} \gg k_H$ under typical conditions, this leads to the k_H independent t_d optimization. Irradiating the ^{1}H channel with a power $\omega_{1,H} \gg J_{NH}$ decouples J_{NH}, effectively locking the $\hat{I}_1 \cdot \hat{I}_2$ spin order. **B.** Continuous wave decoupling the J_{NH} during the exchange delay recovers the expected dependence of t_d on the exchange rate, as the singlet order is preserved. Note that the optimal delay decreases as the hydride exchange rate is increased from $k_H = 1\ s^{-1}$ (blue) to $k_H = 4\ s^{-1}$.

evolves under both the J_{NH} and J_{HH} couplings, which in the presence of chemical exchange generates an average dephasing of this spin order. As $J_{NH} \gg J_{HH} \gg k_H$ under typical conditions, this spin order dephasing is much faster than the singlet order replenishment and thus leads to an optimum t_d that is invariant to k_H in this limit. However, decoupling the J_{NH} coupling by irradiating the ^{1}H channel with a power $\omega_{1,H} \gg J_{NH}$ effectively locks the spin order in $\hat{I}_1 \cdot \hat{I}_2$, which in turn permits t_d to be affected by the hydride exchange rate as one may intuitively expect. It should be noted that $i[\hat{I}_{1z}\hat{I}_{2z}, J_{NH}\hat{I}_{1z}\hat{S}_z] = 0$, preserving the longitudinal term of the singlet at high field.

4.3 Expanding the target scope of high field X-SABRE

The development and benchmarking of high-field X-SABRE has been done exclusively using ^{15}N-pyridine. While it regularly generates large, hyperpolarized signals, pyridine is a poor representative of the larger SABRE target scope. In particular, most SABRE targets require the use of a hyperpolarization-inactive coligand to facilitate exchange with the iridium catalyst, which changes the available exchange pathways that the target experiences that are absent in the pyridine system. Additionally, the parahydrogen-derived hydrides experience different magnetic environments when two different ligands are bound in the equatorial plane of the complex (Fig. 32) . This difference is aggravated at high magnetic field when the individual

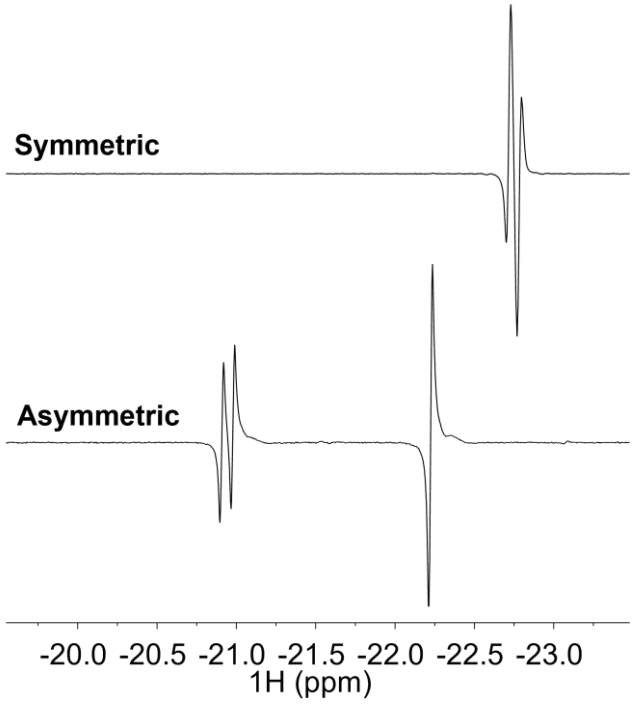

Figure 32: Hydride spectra in symmetric and asymmetric ligand environments. The hydrides in an $[Ir(H)_2(^{15}N\text{-pyridine})_3]^+$ complex (symmetric) are chemically equivalent ($\omega_A = \omega_B$) but inequivalently couple the trans-iridium ^{15}N spins. This permits visualization of the $^2J_{HH}$ and $^2J_{NH}$ couplings in the spectrum. The hydrides in the $[Ir(H)_2(^{15}N\text{-acetonitrile})_x(^{14}N\text{-pyridine})_{3-x}]^+$ complex (asymmetric) show a large splitting between the resonances ($\omega_A \neq \omega_B$) and the same set of couplings is visible in this case.

hydride chemical shifts are no longer identical. Under this condition, the Hamiltonian becomes:

$$\hat{\mathcal{H}} = \frac{\Delta\omega_{HH}}{2}\left(\hat{I}_{1z} - \hat{I}_{2z}\right) + \Delta\omega_N \hat{S}_z + \omega_{1,N}\hat{S}_x + 2\pi\left(J_{HH}\hat{I}_1 \cdot \hat{I}_2 + J_{NH}\hat{I}_{1z}\hat{S}_z\right) \qquad (4.14)$$

We have defined $\Delta\omega_{HH} = (\omega_{0,1} - \omega_{0,2})$ as the frequency difference between the parahydrogen derived hydrides. This is generally referred to as an ABX system in Pople notation. The hyperpolarization active subspace of the Hamiltonian then takes the form:

$$\hat{\mathcal{H}} = \begin{pmatrix} & \left|T_H^0\alpha_N\right\rangle & \left|T_H^0\beta_N\right\rangle & \left|S_H^0\alpha_N\right\rangle & \left|S_H^0\beta_N\right\rangle \\ \left\langle T_H^0\alpha_N\right| & 2\pi J_{HH} & \frac{\omega_{1,N}}{2} & \frac{\Delta\omega_{HH} + \pi J_{NH}}{2} & 0 \\ \left\langle T_H^0\beta_N\right| & \frac{\omega_{1,N}}{2} & \Delta\omega_N + 2\pi J_{HH} & 0 & \frac{\Delta\omega_{HH} - \pi J_{NH}}{2} \\ \left\langle S_H^0\alpha_N\right| & \frac{\Delta\omega_{HH} + \pi J_{NH}}{2} & 0 & 0 & \frac{\omega_{1,N}}{2} \\ \left\langle S_H^0\beta_N\right| & 0 & \frac{\Delta\omega_{HH} - \pi J_{NH}}{2} & \frac{\omega_{1,N}}{2} & \Delta\omega_N \end{pmatrix} \qquad (4.15)$$

For reference, $\Delta\omega_{HH} = 460\ Hz$ at 8.45T while $J_{NH} = -25.4\ Hz$ for the ^{15}N-acetonitrile/^{14}N-pyridine X-SABRE system. Under these conditions, the singlet and triplet manifolds are strongly mixed and the $\hat{I}_{1x}\hat{I}_{2x} + \hat{I}_{1y}\hat{I}_{2y}$ terms of the singlet rapidly accumulate a phase with evolution under the $\Delta\omega_{HH}$ term. This rapid phase-accumulation of the transverse singlet terms prevents hyperpolarization from being generated in ABX spin systems. For this reason, high-field X-SABRE had only ever been pursued on systems that bind the complex in symmetric ligand environments, which do not induce $\Delta\omega_{HH}$, of which there are only a few known examples. Reliance on ligands that bind in symmetric environments dramatically reduces the potential applications of high-field X-SABRE and is thus an interesting experimental limitation to explore.

As the term preventing translation of high-field SABRE methods to asymmetric ligand environments is $\Delta\omega_{HH}$, an approach this problem is to simply remove or reduce the effects of this term. This may be accomplished by concurrently irradiating the $\hat{I}$ and $\hat{S}$-spins, giving:

$$\hat{\mathcal{H}} = \frac{\Delta\omega_{HH}}{2}\left(\hat{I}_{1z} - \hat{I}_{2z}\right) + \omega_{1,H}\left(\hat{I}_{1x} + \hat{I}_{2x}\right) + \Delta\omega_N \hat{S}_z + \omega_{1,N}\hat{S}_x + 2\pi\left(J_{HH}\hat{I}_1 \cdot \hat{I}_2 + J_{NH}\hat{I}_{1z}\hat{S}_z\right) \tag{4.16}$$

If $\omega_{1,H} \gg \Delta\omega_{HH}/2$, we may approximate the Hamiltonian as being simply proportional to the ^{1}H-irradiation terms. Under this condition, the Hamiltonian commutes with the $\hat{I}_1 \cdot \hat{I}_2$ spin order, thus preserving the singlet as it binds a catalyst with an asymmetric ligand environment. However, continuously irradiating on ^{1}H at $\omega_{1,H} \gg \Delta\omega_{HH}/2$ will decouple the hydrides and the target J_{NH} coupling, which means that no polarization may be extracted from the singlet order. Therefore, we must use an intermediate $\omega_{1,H}$ that permits locking the singlet and while not preventing evolution under the J_{NH} coupling.

For $\omega_{1,H} \neq 0$, every state in the ABX system Hamiltonian is connected in a single manifold. As such, this case is far from the limit of a two- or few-level system from which experimental parameters may be immediately derived. Instead, a computational optimization of this Hamiltonian is much more accessible using the DMExFR2 model. As with the other X-SABRE experiments demonstrated here, the matching condition may be driven coherently for a time t_p followed by a delay t_d to permit for exchange of the ligand into solution (Fig. 33A). However, the ^{1}H-irradiation is applied to the system for the entire duration of the experiment to preserve any singlet order that exchanges onto the catalyst during the exchange delay (t_d). Hyperpolarization for this pulse sequence is optimized under the condition where $\omega_{1,H} \approx \Delta\omega_{HH}$ (Fig. 33B), but decreases as $\omega_{1,H}$ is further increased. This is because the ^{1}H-

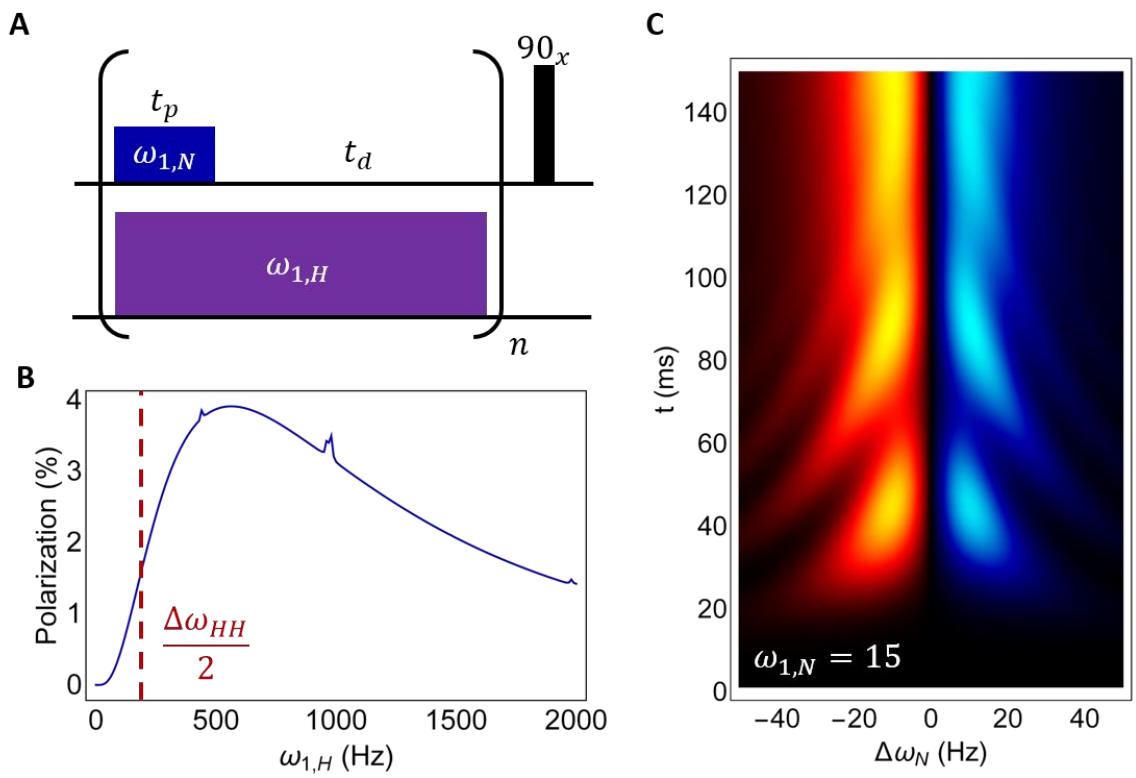

Figure 33: ^{1}H decoupled LIGHT-SABRE. A. Simultaneous irradiation of the ^{1}H and ^{15}N permits the generation of hyperpolarization in ABX spin systems. **B.** Hyperpolarization is efficiently generated using $\omega_{1,H} \gg \Delta\omega_{HH}/2$ (dashed red). As $\omega_{1,H}$ continues to increase, the polarization begins to decrease as the ^{1}H-irradiation is decoupling the J_{NH} interaction. For this simulation, $t_p = 31\ ms$, $t_d = 400\ ms$, $\omega_{1,N} = 15\ Hz$, $k_N = 16\ s^{-1}$, $k_H = 2\ s^{-1}$ were used. **C.** For $\omega_{1,H} \approx \Delta\omega_{HH}$, the matching condition is similar to the case of symmetric ligand environments.

irradiation will act to decouple the J_{NH} interaction, thus preventing spin order from being transferred to the heteronucleus. Conveniently, the matching conditions for ^{15}N-irradiation are similar to the conventional LIGHT-SABRE matching conditions (Fig. 33C). We refer to this as the ^{1}H decoupled LIGHT-SABRE (^{1}H dLIGHT) experiment.

Here, we demonstrated the high-field X-SABRE hyperpolarization in an asymmetric ligand environment for the first time by using ^{1}H decoupling during the entire experimental duration (Fig. 34). Varying $\omega_{1,H}$ shows that hyperpolarization is maximized when the decoupling power is set to $\omega_{1,H} = 1.6\ kHz$, which disagrees with the theoretical prediction. However, this experiment was performed by continuously bubbling parahydrogen through

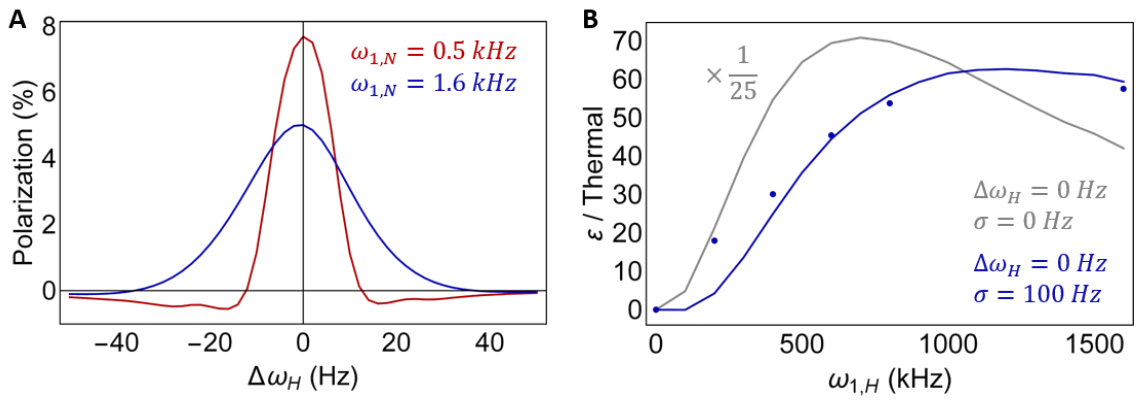

Figure 34: ^{1}H decoupled LIGHT-SABRE performance as function of decoupling. A. While the polarization is larger at $\omega_{1,H} = 0.5\ kHz$, the resonance profile for generating polarization is narrower and has negative features. Increasing the power broadens the profile and minimizes the negative polarizations. **B.** Experimentally, hyperpolarization is recovered for ABX spin systems in the presence of ^{1}H decoupling. The observed power dependence deviates from the theoretical simulation without inhomogeneous broadening (gray). Including Gaussian inhomogeneities with a standard deviation of $\sigma = 100\ Hz$ improves agreement.

the sample, which at 8.45T introduces inhomogeneities due to the large susceptibility difference between parahydrogen gas and methanol. Including Gaussian inhomogeneities in the simulation significantly improves the agreement between the experimental data and theoretical prediction.

Experimentally, we find that it is beneficial to introduce a recoupling period t_R in the ^{1}H dLIGHT experiment that interchanges the $S_H \leftrightarrow T_H^0$ populations as well as invert the $T_H^+ \leftrightarrow T_H^-$ populations with a π_x pulse (Fig. 35A), and find an optimal recoupling time of $t_R = 250\ \mu s$. This corresponds to only approximately $1/4$ of the time required to fully interchange the $S_H \leftrightarrow T_H^0$ states, using $\Delta\omega_{HH} = 460\ Hz$ at 8.45T, but is likely optimized largely due to the broad inhomogeneities arising from the large susceptibility difference between the parahydrogen gas and the solvent. The experimental trend could very likely be fit using a simulation that engineered specific inhomogeneities in the simulation, but this would result in overfitting the data. Still, enhancements of up to $\varepsilon = 101$ were observed on ^{15}N-acetonitrile using this approach (Fig. 35C). Additionally, we showed that ^{15}N-magnetization could be

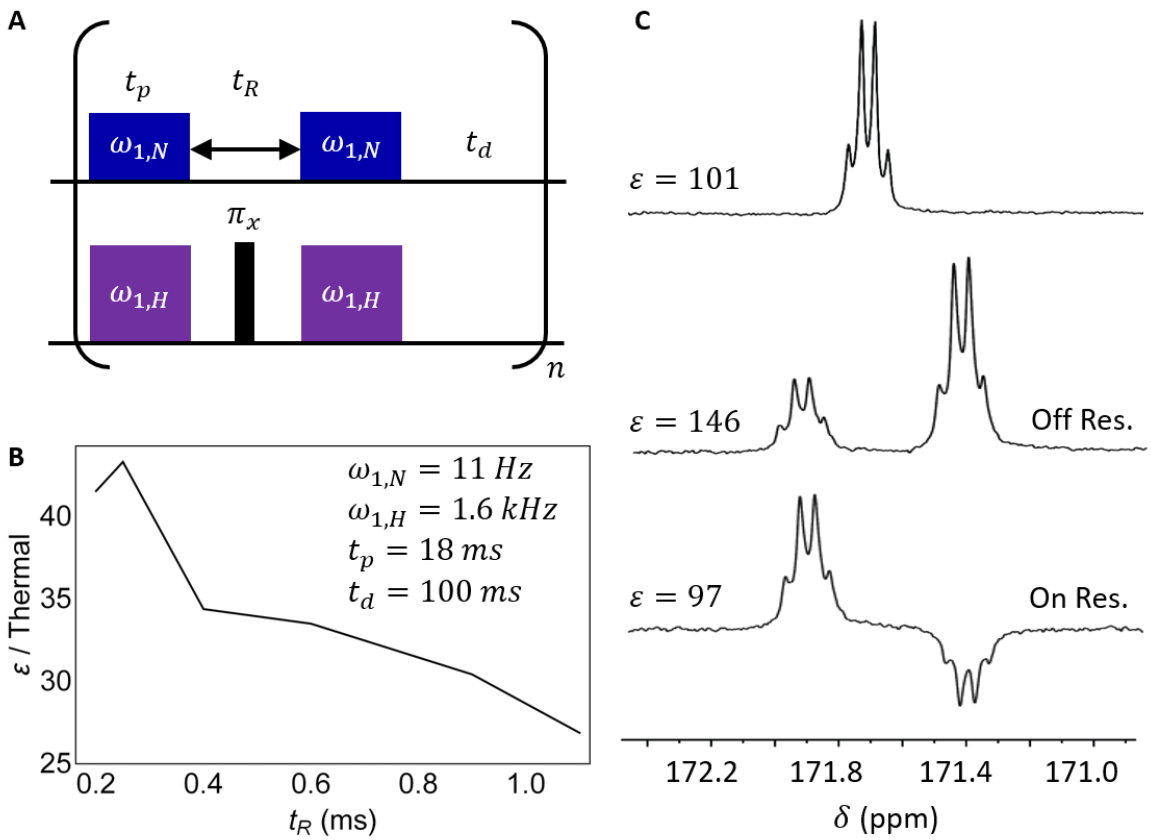

Figure 35: ^{1}H decoupled LIGHT-SABRE results. A. The ^{1}H decoupled/recoupled LIGHT-SABRE variant uses a recoupling time t_R and π_x pulse to interchange the $S_H \leftrightarrow T_H^0$ and $T_H^+ \leftrightarrow T_H^-$ states. **B.** The recoupling time t_R was optimized to $t_R = 0.25\ ms$ using $t_p = 18\ ms$ and $t_d = 100\ ms$. **C.** Optimization of the bubbling yields $\varepsilon = 101$ on ^{15}N-acetontirile. This was extended to the isotopolog (^{15}N,1-^{13}C)-acetonitrile, where magnetization may be pumped when irradiating off-resonance and two-spin, $\hat{N}_z\hat{C}_z$ spin order may be generated when pumping on-resonance. For all these experiments, hyperpolarization was performed using the decoupled/recoupled LIGHT-SABRE variant using the parameters $t_p = 18\ ms$, $t_d = 100\ ms$, $t_R = 0.25\ ms$.

generated on the (^{15}N,1-^{13}C)-acetonitrile isotopolog under the same experimental conditions. Antiphase $\hat{S}_z\hat{L}_z$ spin order on the ^{15}N/^{13}C pair can also be accessed in this system by irradiating on-resonance with the iridium-bound ^{15}N-nucleus, offering opportunities to access hyperpolarized non-Zeeman spin orders at high field. We showed that enhancements of up to $\varepsilon = 146$ could be obtained on (^{15}N,1-^{13}C)-acetonitrile.

Prior to the development of the ^{1}H-decoupled LIGHT-SABRE variants, only a few targets could be hyperpolarized directly at high-field and ^{15}N-pyridine was the only target

reported in the literature[52, 117, 120, 132, 133]. While these experiments broadened the scope of high-field X-SABRE to span the same substrate scope as SABRE-SHEATH, this class of experiments still fundamentally suffered from lack of flexibility when changing between hyperpolarization targets. The matching condition $\Delta\omega_N \approx \omega_{1,N} \approx J_{HH}$ fundamentally incurs a narrow X-SABRE excitation bandwidth limited to match the small value of the J_{HH} coupling. Furthermore, these experiments required $\omega_{1,H} = 1.6\ kHz$ at a magnetic field of 8.45T, meaning that even stronger decoupling power would be required at higher magnetic fields like those used in biomolecular NMR and metabonomics[134-137]. As such, it became evident that an entirely new approach to X-SABRE hyperpolarization at high magnetic field would be required if these techniques were to compete with SABRE-SHEATH.

Perhaps the most fundamental problem with high-field X-SABRE is accessibility to a source of spin order that is not depleted during the exchange delay. For both AA'X and ABX spin systems, hyperpolarization is extracted from the $\hat{I}_{1x}\hat{I}_{2x} + \hat{I}_{1y}\hat{I}_{2y}$ terms of the parahydrogen singlet state. The issue arises in that neither of these terms are an eigenstate of the Hamiltonian during the exchange delay, meaning that they are constantly being converted into other spin-orders that do not facilitate hyperpolarization. However, the $\hat{I}_{1z}\hat{I}_{2z}$ term is an eigenstate of the Hamiltonian even in the presence of pulses. This means that no additional measures need to be taken to isolate this spin order during the X-SABRE process. The only issue arises in that spin order cannot be extracted from this term even in the presence of conventional LIGHT-SABRE type experiments. Thus, it would be beneficial for a new excitation strategy to target extracting hyperpolarization from this source of spin order.

Before designing a suitable experiment that utilizes $\hat{I}_{1z}\hat{I}_{2z}$ spin order, the interactions required to excite this transition should be identified by searching for the relevant spin

operator pathways. To search the spin operator pathways that lead to this transition, we start with the ABX Hamiltonian in the absence of any pulses as

$$\hat{\mathcal{H}} = \frac{\Delta\omega_{HH}}{2}\left(\hat{I}_{1z} - \hat{I}_{2z}\right) + \Delta\omega_N \hat{S}_z + 2\pi\left(J_{HH}\hat{I}_1 \cdot \hat{I}_2 + J_{NH}\hat{I}_{1z}\hat{S}_z\right) \tag{4.17}$$

The AA'X Hamiltonian is recovered in the limit $\Delta\omega_{HH} = 0$. As previously noted, $\hat{I}_{1z}\hat{I}_{2z}$ spin order commutes with **eq. 4.17** at all times. To make progress, let us examine the evolution of $\hat{\rho}(t)$ under an arbitrary sequence of pulses $\hat{U}_1, \hat{U}_2, \cdots$ with delays $\exp\left(-i\hat{\mathcal{H}}t_1\right)$, $\exp\left(-i\hat{\mathcal{H}}t_2\right), \cdots$ interleaved between the pulses. For two pulses and delays, this looks like:

$$\hat{\rho}(t) = e^{-i\hat{\mathcal{H}}t_2}\hat{U}_2 e^{-i\hat{\mathcal{H}}t_1}\hat{U}_1\hat{\rho}_0\hat{U}_1^\dagger e^{i\hat{\mathcal{H}}t_1}\hat{U}_2^\dagger e^{i\hat{\mathcal{H}}t_2} \tag{4.18}$$

If we place

$$\hat{U}_1\hat{U}_1^\dagger = \hat{U}_1\hat{U}_2\hat{U}_2^\dagger\hat{U}_1^\dagger = \hat{E} \tag{4.19}$$

and their conjugates within the sequence, we may write:

$$\hat{\rho}(t) = \left(\hat{U}_1\hat{U}_2\hat{U}_2^\dagger\hat{U}_1^\dagger\right)e^{-i\hat{\mathcal{H}}t_2}\hat{U}_2\left(\hat{U}_1\hat{U}_1^\dagger\right)e^{-i\hat{\mathcal{H}}t_1}\hat{U}_1\hat{\rho}_0 \cdots \tag{4.20}$$

Contracting the terms to the right-hand side and rearranging the parentheses gives:

$$\hat{\rho}(t) = \hat{U}_1\hat{U}_2\left(\hat{U}_1^\dagger\hat{U}_2^\dagger e^{-i\hat{\mathcal{H}}t_2}\hat{U}_2\hat{U}_1\right)\left(\hat{U}_1^\dagger e^{-i\hat{\mathcal{H}}t_1}\hat{U}_1\right)\hat{\rho}_0 \cdots \tag{4.21}$$

Conventionally, we choose $\hat{U}_1\hat{U}_2 = \hat{E}$, which is the case when the pulse flip angles for these pulses sum to 2π to simplify interpretation of the sequence. We may then use the relation

$$\hat{U}_1^\dagger e^{-i\hat{\mathcal{H}}t_1}\hat{U}_1 = e^{-i\left(\hat{U}_1^\dagger\hat{\mathcal{H}}\hat{U}_1\right)t_1} \tag{4.22}$$

to show that evolution through the end of the first period t_1 evolves as if under the Hamiltonian:

$$\widetilde{\mathcal{H}} = \widehat{U}_1^\dagger \widehat{\mathcal{H}} \widehat{U}_1 \tag{4.23}$$

Similarly for the Hamiltonian during the second delay, evolution is dictated by

$$\widetilde{\mathcal{H}} = \widehat{U}_1^\dagger \widehat{U}_2^\dagger \widehat{\mathcal{H}} \widehat{U}_2 \widehat{U}_1, \tag{4.24}$$

where the time-ordering of the pulses acting on $\widehat{\mathcal{H}}$ is reversed from the time-ordering that the pulses are applied to the system. This is called the toggling-frame Hamiltonian, which was derived in the development of Average Hamiltonian Theory and facilitates interpretation of complex pulse sequences. Thus, evolution may happen under terms in the Hamiltonian as well as rotations generated by pulses. For instance, if a ^{1}H 90_y pulse was applied to the system, the toggling frame Hamiltonian during the subsequent delay period t_1 would be

$$\begin{aligned}\widetilde{\mathcal{H}} &= e^{\frac{-i\pi}{2}(\hat{I}_{1y}+\hat{I}_{2y})} \begin{pmatrix} \frac{\Delta\omega_{HH}}{2}\left(\hat{I}_{1z} - \hat{I}_{2z}\right) \\ +2\pi J_{HH}\hat{I}_1 \cdot \hat{I}_2 \\ +2\pi J_{NH}\hat{I}_{1z}\hat{S}_z + \Delta\omega_N \hat{S}_z \end{pmatrix} e^{\frac{i\pi}{2}(\hat{I}_{1y}+\hat{I}_{2y})} \\ &= \frac{\Delta\omega_{HH}}{2}\left(\hat{I}_{1x} - \hat{I}_{2x}\right) + 2\pi J_{HH}\hat{I}_1 \cdot \hat{I}_2 + 2\pi J_{NH}\hat{I}_{1x}\hat{S}_z + \Delta\omega_N \hat{S}_z\end{aligned} \tag{4.25}$$

Note that we have formally used time-reversal to cast the rotation in the conventional form. We see that the form of the toggling-frame Hamiltonian now contains a term like $\hat{I}_{1x}\hat{S}_z$, which is not a conventional term in the J-coupling. Thus, we may search for the spin operator pathways that lead to magnetization using not only the terms of the Hamiltonian but also terms that are generated by evolution under pulses. Often, multiple toggling frame Hamiltonians can be generated to lead to an average Hamiltonian that has the desired properties without any extraneous terms, which is the method we will employ here.

There are multiple, identical spin operator pathways that excite the $\hat{I}_{1z}\hat{I}_{2z} \rightarrow \hat{S}_z$ transition and all do so in three interactions with various toggling frame Hamiltonians. For

simplicity, we will choose one of these pathways and work out the Taylor series expansion explicitly. The first term in the expansion utilizes the J_{NH} coupling to generate a coherence between the hydrides and target nucleus, and is given by:

$$\rho^{(1)}(t) = i\left[\hat{I}_{1z}\hat{I}_{2z}, 2\pi J_{NH}\hat{I}_{1y}\hat{S}_y\right]t = \hat{I}_{1x}\hat{I}_{2z}\hat{S}_y(2\pi J_{NH}t) \tag{4.26}$$

$\hat{I}_{1y}\hat{S}_y$ is one of the non-secular J-coupling terms and can be generated using simultaneous ^{1}H and ^{15}N pulses. The next term utilizes the J_{HH} coupling to remove $\hat{I}_2$ from the coherence:

$$\rho^{(2)}(t) = i\left[\hat{I}_{1x}\hat{I}_{2z}\hat{S}_y, 2\pi J_{HH}\hat{I}_1 \cdot \hat{I}_2\right](\pi J_{NH}t^2) = \hat{I}_{1y}\hat{S}_y\left(\frac{\pi^2 J_{NH}J_{HH}t^2}{2}\right) \tag{4.27}$$

A phase-shifted form of the J_{NH} is all that is required to generate $\hat{S}_z$ magnetization:

$$\rho^{(3)}(t) = i\left[\hat{I}_{1y}\hat{S}_y, 2\pi J_{NH}\hat{I}_{1y}\hat{S}_x\right]\left(\frac{\pi^2 J_{NH}J_{HH}t^3}{6}\right) = \hat{S}_z\left(\frac{\pi^3 J_{NH}^2 J_{HH}t^3}{12}\right) \tag{4.28}$$

The term $\hat{I}_{1y}\hat{S}_x$ is not a naturally-occurring form of the J-coupling, so we must introduce this term in the toggling-frame Hamiltonian. The power-dependence of this coherence pathway is completely independent of any pulse parameters, meaning that hyperpolarization may be generated if the Hamiltonian takes on the form dictated by this pathway. Various other phases of the J_{NH} coupling may be used to obtain the same result.

Here, we have assumed that no phase is accumulated by $\Delta\omega_N$ terms in the spin operator pathway. If $\Delta\omega_N$ were permitted to act after the second interaction, then the third term in the expansion would be:

$$\rho^{(3)}(t) = i\left[\hat{I}_{1y}\hat{S}_y, \Delta\omega_N\hat{S}_z\right]\left(\frac{\pi^2 J_{NH}J_{HH}t^3}{6}\right) = -\hat{I}_{1y}\hat{S}_x\left(\frac{\pi^2 \Delta\omega_N J_{NH}J_{HH}t^3}{6}\right) \tag{4.29}$$

This term would then commute with the $J_{NH}\hat{I}_{1y}\hat{S}_x$ term that was originally used in eq. 4.28, thus not giving hyperpolarization. However, if the same sequence was applied but the form of the second J_{NH} coupling was shifted to $\hat{I}_{1y}\hat{S}_y$, as it was in the first step, then hyperpolarization could be generated in the fourth term of the expansion as:

$$\begin{aligned}\rho^{(4)}(t) &= -i\left[\hat{I}_{1y}\hat{S}_x, 2\pi J_{NH}\hat{I}_{1y}\hat{S}_y\right]\left(\frac{\pi^2\Delta\omega_N J_{NH}J_{HH}t^3}{6}\right) \\ &= \hat{S}_z\left(\frac{\pi^3\Delta\omega_N J_{NH}^2 J_{HH}t^4}{12}\right)\end{aligned} \tag{4.30}$$

In cycling the excitation phase between these two combinations of J_{NH} couplings, we may compensate for the resonance offset of the heteronucleus. A similar treatment may be used to compensate for phase-accumulation on the $\hat{I}$-spins, which leads to a four-step phase cycle that removes dependence on the chemical shifts of all spins.

The coherence pathway described above can be excited if the phase of the J_{NH} coupling can be selectively generated, which is accomplished by the pulse sequence shown in Fig. 36. Only the solid-color pulses in Fig. 36 are required to generate the desired J_{NH} coupling, and the remaining dashed-outline pulses may be included to refocus off-resonant evolution. For this pulse sequence, the relevant toggling-frame terms are listed below. To make it clear which pulses to which we are referring, we will always refer to them in the notation ^{1}H/^{15}N. Let us examine the pulse sequence to generate a J_{NH} coupling of the form $\hat{I}_y\hat{S}_z$. The first set of $90_{\bar{x}}/90_y$ dictate the phase of the toggling-frame J_{NH} coupling according to the phase of the pulse used on each nucleus. More specifically, the toggling frame Hamiltonian during the 2τ period after the first pulses is given by:

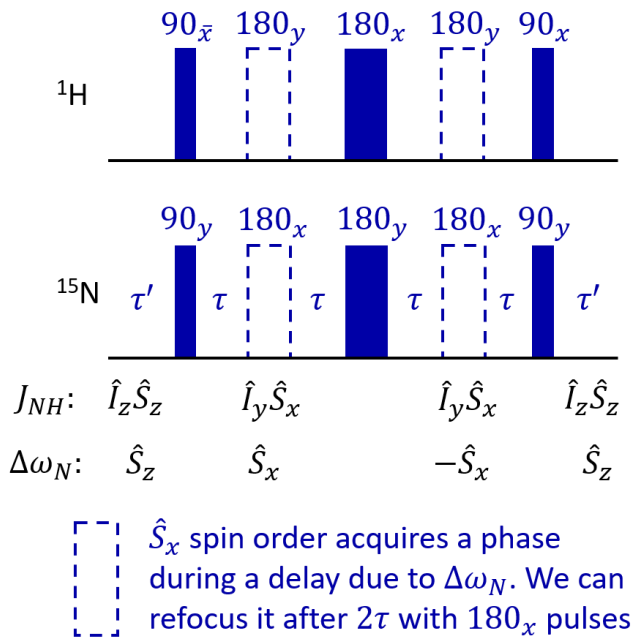

Figure 36: Excitation block for broadband X-SABRE. The phase of the non-secular J_{NH} couplings required to generate X-SABRE hyperpolarization from the $\hat{I}_{1z}\hat{I}_{2z}$ term is essentially determined by the first $90_{\bar{x}}$ and 90_y pulses in this block, but this converts the resonance offset term into one proportional to $\hat{S}_x$. The central 180_x and 180_y pulses are used to invert the phase of the $\hat{S}_x$ term, which is then removed from the average Hamiltonian. The final pulse halts evolution under the non-secular J_{NH} coupling. The dashed pulses may be added to compensate for the phase evolution under the resonance offset terms during 2τ, and are employed in practice.

$$\tilde{\mathcal{H}}^{(A)} = e^{\frac{-i\pi}{2}(\hat{S}_y-\hat{I}_{1x}-\hat{I}_{2x})}\begin{pmatrix} \frac{\Delta\omega_{HH}}{2}(\hat{I}_{1z}-\hat{I}_{2z}) \\ +2\pi J_{HH}\hat{I}_1\cdot\hat{I}_2 \\ +2\pi J_{NH}\hat{I}_{1z}\hat{S}_z+\Delta\omega_N\hat{S}_z \end{pmatrix} e^{\frac{i\pi}{2}(\hat{S}_y-\hat{I}_{1x}-\hat{I}_{2x})}$$

$$= \frac{\Delta\omega_{HH}}{2} e^{\frac{i\pi}{2}(\hat{I}_{1x}+\hat{I}_{2x})}(\hat{I}_{1z}-\hat{I}_{2z})e^{\frac{-i\pi}{2}(\hat{I}_{1x}+\hat{I}_{2x})} + \Delta\omega_N e^{\frac{-i\pi}{2}\hat{S}_y}\hat{S}_z e^{\frac{i\pi}{2}\hat{S}_y} \qquad (4.31)$$

$$+2\pi J_{HH}\hat{I}_1\cdot\hat{I}_2 + 2\pi J_{NH} e^{\frac{i\pi}{2}\hat{I}_{1x}}\hat{I}_{1z}e^{\frac{-i\pi}{2}\hat{I}_{1x}}e^{\frac{-i\pi}{2}\hat{S}_y}\hat{S}_z e^{\frac{i\pi}{2}\hat{S}_y}$$

$$= \frac{\Delta\omega_{HH}}{2}(\hat{I}_{1y}-\hat{I}_{2y}) + \Delta\omega_N\hat{S}_x + 2\pi J_{HH}\hat{I}_1\cdot\hat{I}_2 + 2\pi J_{NH}\hat{I}_{1y}\hat{S}_x$$

We have called this toggling-frame Hamiltonian $\tilde{\mathcal{H}}^{(A)}$. Again, the $\hat{I}_1\cdot\hat{I}_2$ is unaffected by rotations as it is a zero-rank tensor (dot product), and thus invariant to rotations. For simplicity, we will consider the case where the optional $180_y/180_x$ pulses are not used, as it makes the result more followable and generates the same result. While the Hamiltonian in eq.

4.31 contains terms proportional to $J_{NH}\hat{I}_{1y}\hat{S}_x$, it converts the resonance offsets of the spins into unwanted terms that look like pulses. To suppress these terms, we must generate a second toggling-frame Hamiltonian such that the average Hamiltonian does not evolve under these interactions. This is accomplished by using a pair of $180_x/180_y$ pulses, which for the period 2τ after these pulses gives a toggling-frame Hamiltonian:

$$\begin{aligned}\tilde{\mathcal{H}}^{(B)} &= \frac{\Delta\omega_{HH}}{2} e^{\frac{i\pi}{2}(\hat{I}_{1x}+\hat{I}_{2x})} e^{-i\pi(\hat{I}_{1x}+\hat{I}_{2x})}\left(\hat{I}_{1z}-\hat{I}_{2z}\right) e^{i\pi(\hat{I}_{1x}+\hat{I}_{2x})} e^{\frac{-i\pi}{2}(\hat{I}_{1x}+\hat{I}_{2x})} \\ &\quad +\Delta\omega_N e^{\frac{-i\pi}{2}\hat{S}_y} e^{-i\pi\hat{S}_y}\hat{S}_z e^{i\pi\hat{S}_y} e^{\frac{i\pi}{2}\hat{S}_y} + 2\pi J_{HH}\hat{I}_1\cdot\hat{I}_2 \\ &\quad +2\pi J_{NH} e^{\frac{i\pi}{2}\hat{I}_{1x}} e^{-i\pi\hat{I}_{1x}}\hat{I}_{1z} e^{i\pi\hat{I}_{1x}} e^{\frac{-i\pi}{2}\hat{I}_{1x}} e^{\frac{-i\pi}{2}\hat{S}_y} e^{-i\pi\hat{S}_y}\hat{S}_z e^{i\pi\hat{S}_y} e^{\frac{i\pi}{2}\hat{S}_y} \\ &= \frac{-\Delta\omega_{HH}}{2}\left(\hat{I}_{1y}-\hat{I}_{2y}\right) - \Delta\omega_N\hat{S}_x + 2\pi J_{HH}\hat{I}_1\cdot\hat{I}_2 + 2\pi J_{NH}\hat{I}_{1y}\hat{S}_x\end{aligned} \tag{4.32}$$

In using the $180_x/180_y$ pulses, the single-spin terms have changed sign but leaves the sign of the J_{NH} coupling intact. The final $90_x/90_y$ pulses return the conventional form of the J_{NH} coupling and stop evolution under the non-secular form. At this point, may calculate the zeroth order average Hamiltonian of this sequence as:

$$\begin{aligned}\bar{\mathcal{H}}^{(0)} &= \frac{1}{T}\int_0^T dt'\,\hat{\mathcal{H}}(t') = \frac{1}{4\tau}\left(2\tilde{\mathcal{H}}^{(A)}\tau + 2\tilde{\mathcal{H}}^{(B)}\tau\right) \\ &= 2\pi\left(J_{HH}\hat{I}_1\cdot\hat{I}_2 + J_{NH}\hat{I}_{1y}\hat{S}_x\right)\end{aligned} \tag{4.33}$$

This Hamiltonian no longer contains any dependence on $\Delta\omega_N$ or $\Delta\omega_{HH}$, meaning that this form of the interactions will be present anywhere within the bandwidth of the pulses.

The desired coherence pathway is excited by joining two, phase-shifted excitation blocks separated by a delay τ_{HH} that permits evolution under the J_{HH} coupling (Fig. 37A). A pulse sequence that generates $\hat{I}_{1y}\hat{S}_y + \hat{I}_{1y}\hat{S}_x$ in $\bar{\mathcal{H}}^{(0)}$ is called a $yy + yx$ sequence. We have

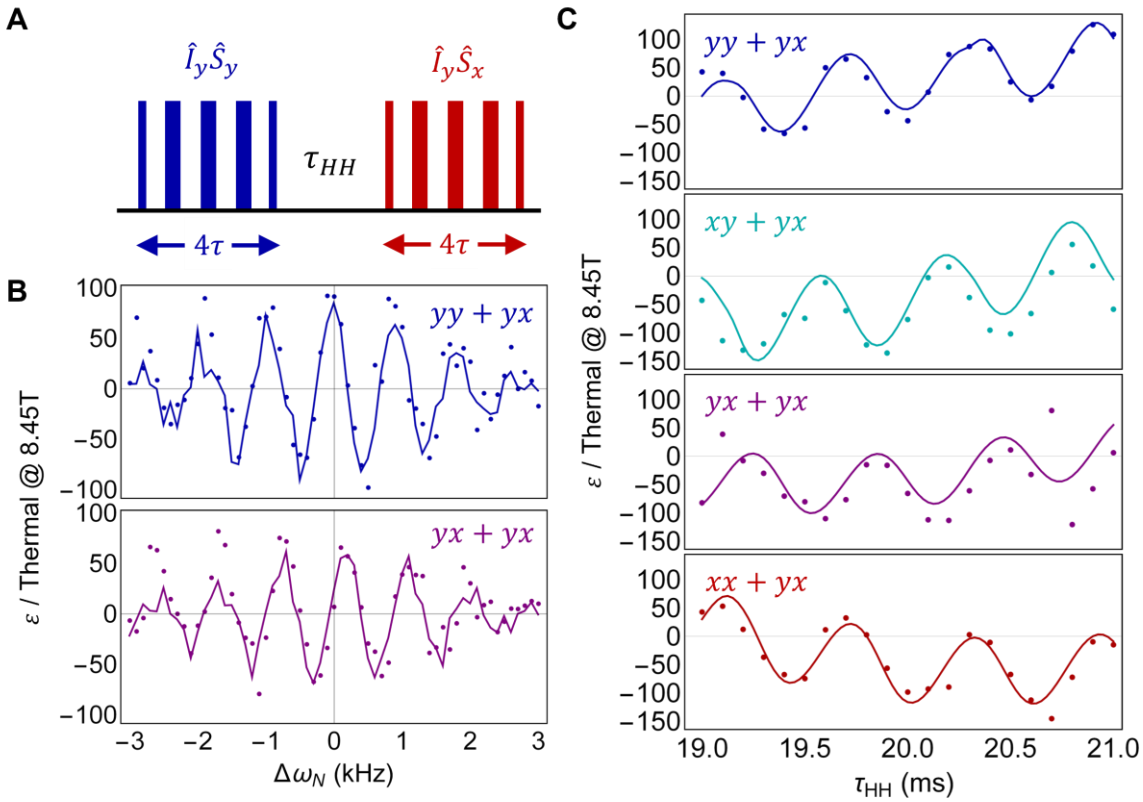

Figure 37: Broadband X-SABRE hyperpolarization at high field on ^{15}N-acetonitrile. A. Utilizing two phase-coherent excitation blocks separated by a delay τ_{HH} generates broadband X-SABRE hyperpolarization at an arbitrarily high magnetic field. **B.** Using $\tau_{HH} = 21\ ms$ and $\tau = 3\ ms$, hyperpolarization may be generated over a 6 kHz bandwidth with $\omega_{1,N} = 2.5\ kHz$ (90_ϕ) and $\omega_{1,N} = 5\ kHz$ (180_ϕ) pulses. Phase cycling between $yy + yx$ and $yx + yx$ excitation blocks phase-shifts the resonance offset profiles by $\pi/2$ such that hyperpolarization is always generated. **C.** The four steps of the phase cycle significantly reduce the sensitivity to τ_{HH}. This circumvents the need to finely optimize the τ_{HH} delay. Data were fit to DMExFR2 simulations using the parameters $k_N = 16\ s^{-1}$, $k_H = 2\ s^{-1}$, and $[Ir]/[S] \approx 1/20$ for the ^{15}N-acetontirile system. Sample was ^{15}N-acetonitrile (191 mM), ^{14}N-pyridine (25 mM), and [Ir(IMes)(COD)]Cl (3.7 mM).

demonstrated that this approach can generate hyperpolarization from the $\hat{I}_{1z}\hat{I}_{2z}$ spin order in ABX systems using the ^{15}N-acetontrile/^{14}N-pyridine X-SABRE system (Fig. 37B). Cycling the excitation phase to $yx + yx$ and co-adding the resulting spectra compensates for $\pi/2$ phase shifts induced by the resonance offset and permits X-SABRE hyperpolarization to be generated continuously over a 6 kHz bandwidth. Phase shifts of π induced by the resonance offset can be still hyperpolarized by the $yy + yx$ sequence but generate negatively-signed hyperpolarized signals. Note that the actual structure of the resonance-offset profile is much

more structured than the data shown in Fig. 37B, and the modulation observed is a difference frequency from a multiple of the actual modulation frequency. This pulse sequence excites a coherence in the first excitation block that evolves under the Zeeman interactions for both ^{1}H and ^{15}N spins during τ_{HH}. As such, hyperpolarization is strongly dependent on the exact value of τ_{HH}. Similar to how shifting the excitation phase from $yy + yx \rightarrow yx + yx$ compensates for the ^{15}N-phase accumulation in the $\Delta\omega_N$ profile, a four step phase-cycle where the first excitation block is cycled through the phases $yy, yx, xy,$ and xx while keeping the phase of the second excitation fixed fully compensates for Zeeman evolution during τ_{HH} (Fig. 37C).

Much of conventional magnetic resonance is predicated on the idea that coherences can be established such that population is transferred between coupled nuclei, which is the basis for much of multidimensional spectroscopy as well as polarization-transfer experiments like the INEPT (Insensitive Nuclei Enabled by Polarization Transfer) pulse sequence[132]. The broadband X-SABRE experiment takes a similar approach, even though it uses non-secular J_{NH} couplings that are generated in the toggling frame. Evolution of the initial $\hat{I}_{1z}\hat{I}_{2z}$ state under a coupling of the form $\hat{I}_{1y}\hat{S}_y$ is:

$$\begin{gathered}\hat{\rho}(t) = e^{-2\pi i J_{NH}\hat{I}_{1y}\hat{S}_y t}\hat{I}_{1z}\hat{I}_{2z}e^{2\pi i J_{NH}\hat{I}_{1y}\hat{S}_y t} \\ \hat{\rho}(t) = \hat{I}_{1z}\hat{I}_{2z}\cos(\pi J_{NH}t) + \hat{I}_{1x}\hat{I}_{2z}\hat{S}_y\sin(\pi J_{NH}t)\end{gathered} \tag{4.34}$$

Maximizing the conversion to $\hat{I}_{1x}\hat{I}_{2z}\hat{S}_y$ spin order requires $\pi J_{NH}t = \pi/2$ over the course of the first excitation block where $t = 4\tau$. Therefore, we predict that the signal would be maximized at $\tau = 1/8J_{NH} \approx 5\ ms$ for this system ($J_{NH} = -25\ Hz$). However, the $\hat{I}_{1x}\hat{I}_{2z}\hat{S}_y$ spin order is a three-spin coherence that is not preserved during exchange, and thus in the limit where $k_N \approx J_{NH}$, the optimum value of τ is difficult to predict from first principles.

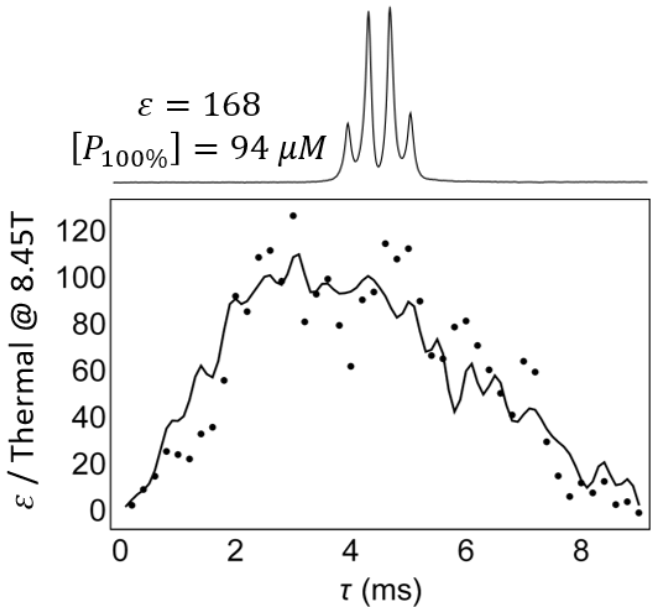

Figure 38: Evolution time under J_{NH} couplings. The evolution time τ determines the degree to which the non-secular J_{NH} couplings can generate evolution in the system. If a $\pi/2$ phase accumulation is desired under this term, then $\tau = 1/(8J_{NH}) \approx 5\ ms$. However, exchange leads to a loss of phase coherence and means that the optimum value of τ is found at shorter times than expected. In this case, the optimum value was found to be $\tau \approx 3\ ms$ (data) in rigorous accordance with the DMExFR2 simulation (black). Under these conditions, we were able to achieve a maximum enhancement of $\varepsilon = 168$, corresponding to a $[P_{100\%}] = 94\ \mu M$. Data were acquired with at a $yy + yx$ sequence on a ^{15}N-acetonitrile (191 mM), ^{14}N-pyridine (25 mM), and [Ir(IMes)(COD)]Cl (3.7 mM) sample using $\tau_{HH} = 21\ ms$

However, the DMExFR2 simulations can readily predict where τ is optimized as a function of the various sequence parameters (Fig. 38). We find that hyperpolarization is optimized at $\tau \approx 3\ ms$ for ^{15}N-acetontrile, which has an exchange rate of $k_N = 16\ s^{-1}$ at room temperature. Under the optimal conditions, we were able to observe signal enhancements up to $\varepsilon = 168$. There are many important effects that are not dependent on the signal enhancement but on the magnetization of the sample, such as dipolar field effects and radiation damping. As such, it is important to also report the absolute signal intensity. The largest signals here correspond to a concentration of 100% polarized ^{15}N-acetontrile of $[P_{100\%}] = 94\ \mu M$, which is also referred to as a molar polarization. For reference, the signal of neat ^{15}N-acetonitrile at 8.45T has a molar polarization of $[P_{100\%}] = 55\ \mu M$, corresponding

to a hyperpolarized signal nearly twice that of the neat solution. Also, it should be emphasized that the molar fraction of parahydrogen used in this experiment was $x_{pH_2} = 43\%$, meaning that the hyperpolarization could be tripled if $x_{pH_2} = 90\%$ were used.

The phase-coherent excitation method discussed here recovers the ability to generate X-SABRE hyperpolarization in ABX spin systems while greatly reducing power dissipation of the pulse sequence relative to ^{1}H decoupled LIGHT-SABRE and does so over a large, 6 kHz bandwidth. However, the large excitation bandwidth and the ability to phase-cycle permits further progress towards the terminal high-field X-SABRE applications like hyperpolarized biomolecular NMR and metabonomics. Towards this, we have shown that the broadband X-SABRE experiment can simultaneously hyperpolarize multiple targets with no additional modification to the pulse sequence (Fig. 39A). In a two-component ^{15}N-acetonitrile and ^{15}N-pyridine system, we chose an excitation frequency between the free-species resonances of each of the targets and used the four-step phase cycle to compensate for the resonance offset of each target. The hyperpolarized multicomponent spectrum is obtained by calculating the root-mean-square (RMS) of the spectra from the steps of the phase cycle, which show large enhancement on both targets. Scanning the τ delay and measuring the RMS enhancement between the four-steps of the phase cycle indicates that both targets hyperpolarize nearly equally (Fig. 39B). Expanding the system to a mixture of ^{15}N-pyridine, ^{15}N-nicotinamide, ^{15}N-benzylamine, and $^{15}N_2$-imidazole permits investigation of co-polarization in a regime where the chemical shift dispersion is significantly larger than in the ^{15}N-acetonitrile/^{15}N-pyridine system. At the cost of slightly increased power dissipation, the pulse bandwidth could be increased to excite the entire ^{15}N-spectrum more equally. However, sweeping the excitation frequency over a 7 kHz bandwidth with 1 kHz spacings between each step and acquiring the

broadband X-SABRE spectrum at each frequency rapidly provides access to the entire hyperpolarized spectrum (Fig. 39C). Co-adding the resulting spectra yields high SNR spectra, with SNR ranging from ≈20-850, that are readily interpretable (Fig. 39D). This spectrum is a composite of 28 individual X-SABRE spectra, meaning that comparison of the reported

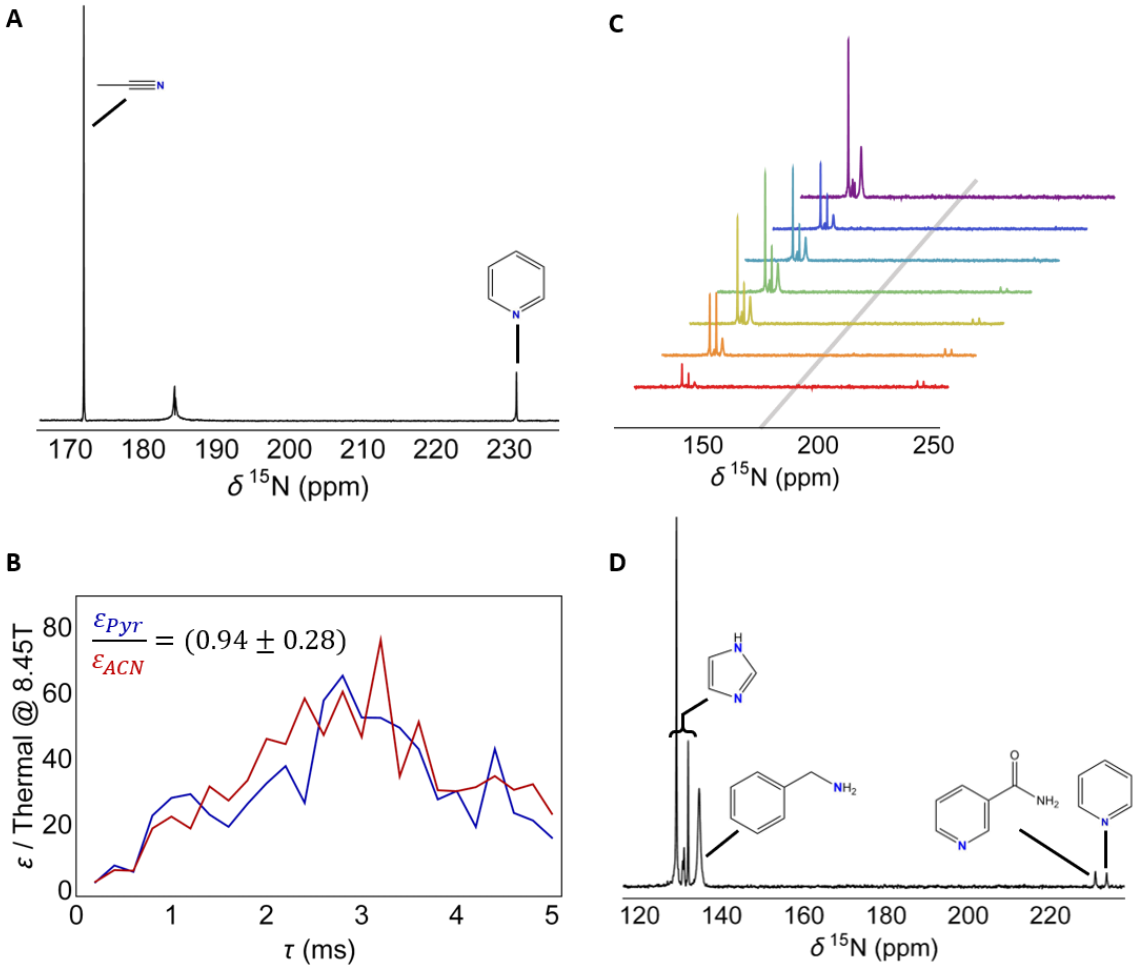

Figure 39: Simultaneous hyperpolarization of multiple targets at high field. A. Choosing an excitation frequency central to the ^{15}N-acetontrile (191 mM) and ^{15}N-pyridine (50 mM) resonances and phase cycling the broadband X-SABRE sequence permits simultaneous hyperpolarization of multiple targets, which are delineated by the respective molecular structure. **B.** Scanning τ demonstrates that both targets hyperpolarize nearly equally. **C.** For systems with a larger chemical shift dispersion, the broadband X-SABRE experiment may be iterated by scanning the excitation frequency. Here, we show a scan over 7 kHz in 1 kHz increments in a four-component sample with ^{15}N-pyridine, ^{15}N-nicotinamide, ^{15}N-benzylamine and $^{15}N_2$-imidazole. **D.** Co-adding these spectra generates high SNR ^{15}N-spectra of multiple targets. For all spectra, ^{1}H-decoupling was used during acquisition to narrow lines and simplify visual analysis. The signal-to-noise of the individual components are $^{15}N_2$-imidazole (184 mM): 856, ^{15}N-benzylamine (125 mM): 146, ^{15}N-nicotinamide (59 mM): 24, and ^{15}N-pyridine (53 mM): 20.

SNRs must be scaled down by $1/\sqrt{N} \approx 1/5.3$ to be compared to the SNR of single-shot spectra, as is conventionally reported in hyperpolarization literature. Again, no additional changes to the broadband X-SABRE pulse sequence were required to generate simultaneous hyperpolarization of multiple targets at high field. Collecting these 28 hyperpolarized spectra to generate the spectrum in Fig. 39D requires 14 minutes of acquisition time, which is orders of magnitude faster than collecting a comparable spectrum using thermal polarization.

It is worth noting that phase-coherent pulse sequences may also be designed to extract spin order from the $\hat{I}_{1x}\hat{I}_{2x} + \hat{I}_{1y}\hat{I}_{2y}$ terms of the singlet that is preserved in symmetric ligand environments (Fig. 40). Under these conditions, the required form of the J_{NH} couplings are $\hat{I}_{1z}\hat{S}_x$ and $\hat{I}_{1z}\hat{S}_y$, which are pseudosecular couplings where one of the two spins is quantized along the leading field and the other is quantized in an orthogonal direction. These J-couplings will excite the coherence pathway according to:

$$\begin{aligned} \rho^{(1)}(t) &= i\left[\hat{I}_{1x}\hat{I}_{2x} + \hat{I}_{1y}\hat{I}_{2y}, 2\pi J_{NH}\hat{I}_{1z}\hat{S}_x\right]t \\ &= \left(\hat{I}_{1x}\hat{I}_{2y}\hat{S}_x - \hat{I}_{1y}\hat{I}_{2x}\hat{S}_x\right)(2\pi J_{NH}t) \end{aligned} \tag{4.35}$$

Note that the $\hat{I}_{1z}\hat{I}_{2z}$ term may be neglected as it commutes with these pseudosecular J_{NH} couplings. The second derivative is accessed by evolving under the J_{HH} coupling:

$$\begin{aligned} \rho^{(2)}(t) &= i\left[\hat{I}_{1x}\hat{I}_{2y}\hat{S}_x - \hat{I}_{1y}\hat{I}_{2x}\hat{S}_x, 2\pi J_{HH}\hat{I}_1 \cdot \hat{I}_2\right]\left(\frac{2\pi J_{NH}t^2}{2}\right) \\ &= \left(\hat{I}_{1z}\hat{S}_x - \hat{I}_{2z}\hat{S}_x\right)(\pi^2 J_{HH}J_{NH}t^2) \end{aligned} \tag{4.36}$$

Finally, this spin order is converted into magnetization by evolution under a phase-shifted form of the pseudosecular J_{NH} coupling used to initiate excitation:

$$\rho^{(3)}(t) = i\left[\hat{I}_{1z}\hat{S}_x - \hat{I}_{2z}\hat{S}_x, -2\pi J_{NH}\hat{I}_{1z}\hat{S}_y\right]\left(\frac{\pi^2 J_{HH} J_{NH} t^3}{3}\right)$$
$$= \left(\frac{1}{4}\hat{S}_z - \hat{I}_{1z}\hat{I}_{2z}\hat{S}_z\right)\left(\frac{2\pi^3 J_{HH} J_{NH}^2 t^2}{3}\right) \tag{4.37}$$

For simplicity, we have treated the AA'X spin system case, and hyperpolarization flows similarly in the AA'XX' case. Note that the sign of the second pseudosecular J_{NH} coupling was chosen to be negative in this case, which may be changed by choice of pulse phase.

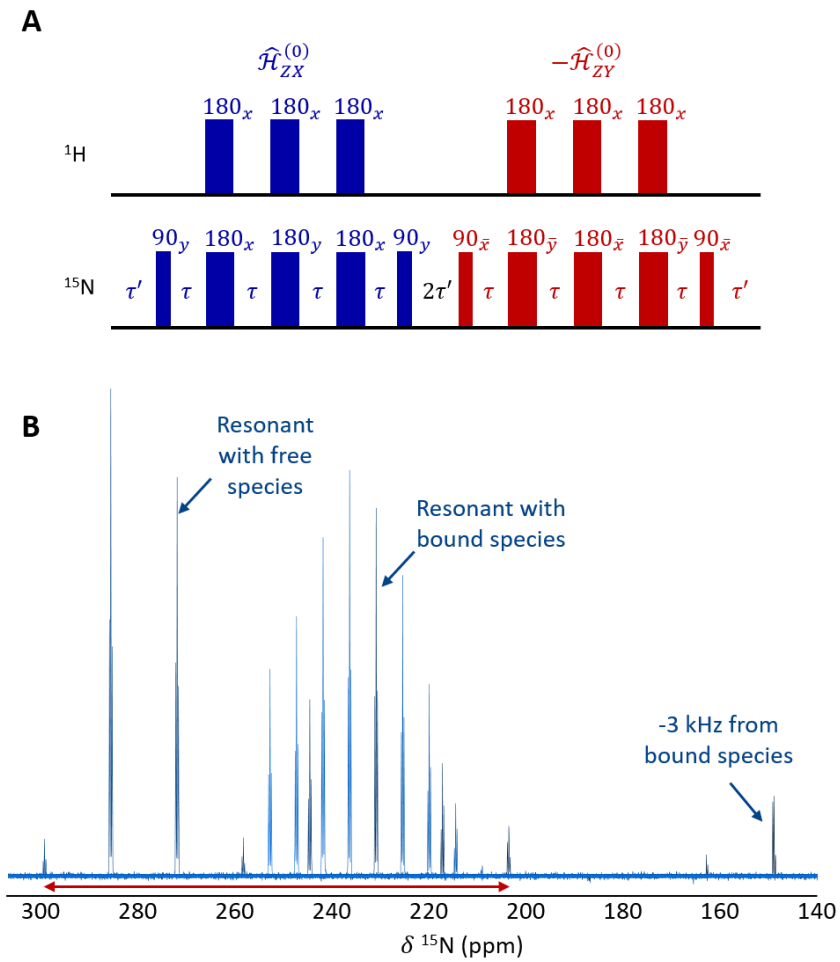

Figure 40: Broadband hyperpolarization in symmetric ligand environments. A. Pseudosecular J_{NH} couplings may be generated in the toggling-frame average Hamiltonian to extract hyperpolarization from the $\hat{I}_{1x}\hat{I}_{2x} + \hat{I}_{1y}\hat{I}_{2y}$ terms of the singlet. **B.** Hyperpolarization is observed on ^{15}N-pyridine over a 3.65 kHz region when using $\omega_1 = 2.5/5\ kHz$ pulses. The pulse sequence parameters were $\tau = 5.1\ ms$ and $\tau' = 0.1\ ms$, and $t_d = 400\ ms$ delays were used between application of the sequence. The maximum enhancement observed in this case was $\varepsilon = 164$ at 8.45T. Sample composition was ^{15}N-pyridine (75 mM) and [IrIMes(COD)]Cl (3.3 mM).

We have demonstrated the ability to expand the scope of high-field X-SABRE experiments to include both asymmetric as well as the original symmetric ligand environments. Furthermore, we showed that efficient pulse-sequence design permits broadband, phase-coherent hyperpolarization of single targets as well as multicomponent systems. By extracting hyperpolarization from the $\hat{I}_{1z}\hat{I}_{2z}$ term of the singlet, we avoid needing to spin-lock the parahydrogen in the initial state during the exchange delay and reduce power dissipation.

4.4 Optimizing X-SABRE hyperpolarization at high field

The previous sections of this chapter introduced new methods for broadening the scope of X-SABRE at high magnetic field and demonstrated robust agreement between simulation and theory. Due to exchange and related effects, is nearly impossible to report a certain set of pulse sequence parameters that will generate large hyperpolarization across the substrate scope. While this space would be impossible to search experimentally, it is entirely feasible to explore the X-SABRE parameter space computationally. Herein, we will present illustrative examples on optimizing high-field X-SABRE experiments that could be used as a more general optimization strategy.

There are a few characteristics that are critical to understand when simulating X-SABRE systems, as they will vastly alter how optimization should be pursued. To exemplify these characteristics, we have simulated the hyperpolarization dynamics of a model (4+1)X system under the coherently pumped LIGHT-SABRE experiment (Fig. 41A). Perhaps the most critical point to note is that the hyperpolarization dynamics under a single pulse do not predict the sequence-level behavior of the experiment (Fig. 41B). Simply changing the ligand

exchange rate dramatically affects the performance of the experiment. For $k_N = 16\ s^{-1}$, multiple applications of the pulse sequence lead to an accumulation of hyperpolarization on

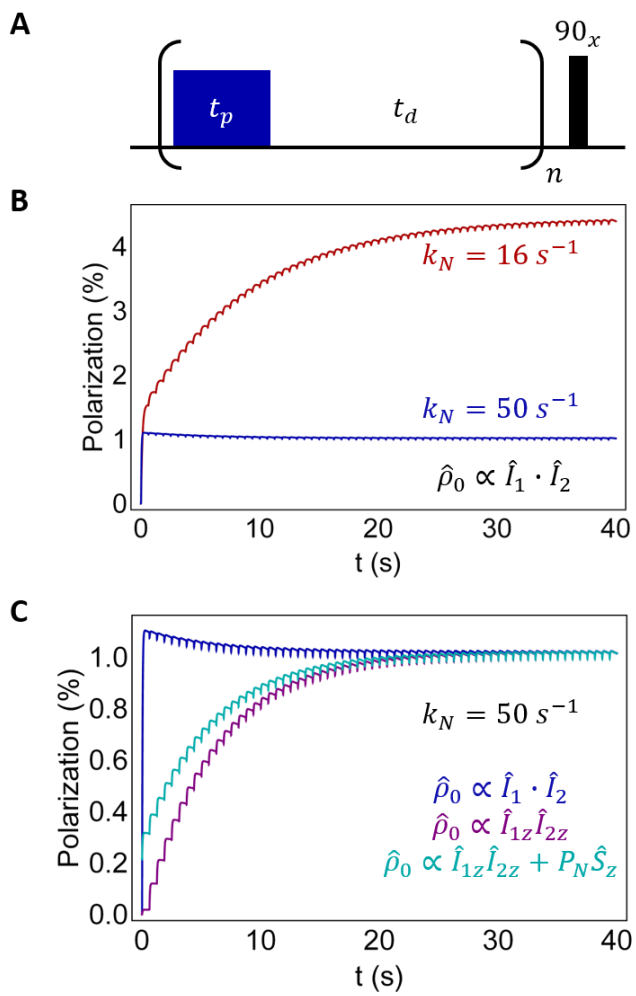

Figure 41: Optimizing high-field X-SABRE hyperpolarization. A. Calculations were performed on a model (4+1)X system using the pumped LIGHT-SABRE pulse sequence, and all simulations used the parameters $t_p = 25\ ms$, $t_d = 600\ ms$, $\omega_{1,N} = 32\ Hz$, $\Delta\omega_N = 20\ Hz$ and $[Ir]/[S] = 1/20$. **B.** Hyperpolarization generated during the same pumped LIGHT-SABRE experiment for two different exchange rates using an initial state proportional to $\hat{I}_1 \cdot \hat{I}_2$. In the case of slower exchange, hyperpolarization may be catalytically generated under the pulse sequence, leading to an accumulation of hyperpolarization in solution. For the fast exchange rate, only the first pulse effectively generates hyperpolarization and each subsequent pulse simply maintains this polarization, although a small loss is observed. **C.** The final hyperpolarization that is measured at the end of an experiment is invariant to the initial condition used, so long as all other parameters remain constant. For instance, changing the initial state from $\hat{I}_1 \cdot \hat{I}_2$ (blue) to $\hat{I}_{1z}\hat{I}_{2z}$ (purple) leads to a dramatic change in the time evolution but results in the same polarization. Similarly, using an initial state that would result after a separate LIGHT-SABRE experiment that used $t_p = 10$ ms still leads to the same final polarization.

the free species, generating the characteristic exponential 'build-up' curve associated with SABRE experiments. Increasing the exchange rate to $k_N = 50\ s^{-1}$ dramatically alters the pulse sequence efficiency, as this corresponds to an average lifetime that is approximately half the $t_p = 25\ ms$ pulse used to excite the hyperpolarization. At this exchange rate, only the first pulse effectively generates hyperpolarization, and the subsequent train of pulses simply maintains this hyperpolarization with a small loss. Even though the resulting hyperpolarization is $P{\sim}1\%$ for this case, the sequence-level dynamics highlight that the efficiency of this pulse sequence is dramatically worse for more rapidly exchanging ligands.

The other important characteristic to note when optimizing X-SABRE experiments is that the final polarization is completely invariant to the initial conditions of the experiment, so long as the pulse train is applied for long enough as to permit the asymptotic convergence of hyperpolarization (Fig. 41C). Starting the system from the parahydrogen singlet state, proportional to $\hat{I}_1 \cdot \hat{I}_2$ (noting this is identical to the simulation shown in Fig. 41B) permits large generation of hyperpolarization under the first pulse with a small loss of polarization during the rest of the pulse train. As discussed previously in Fig. 31, this inefficiency during the rest of the pulse sequence is an artifact of the initial singlet state not commuting with the Hamiltonian, leading to an ultimate loss of phase coherence of the transverse terms of the singlet ($\hat{I}_{1x}\hat{I}_{2x} + \hat{I}_{1y}\hat{I}_{2y}$). Starting the system from the time-averaged initial state, which is simply proportional to $\hat{I}_{1z}\hat{I}_{2z}$ spin order, generates vastly different sequence-level hyperpolarization dynamics but converges to the same final hyperpolarization. Testing the invariance to the initial condition may be exacerbated by starting the simulation with an initial condition that has some hyperpolarization on the free-species ($P_N\hat{S}_z$), such as if two different hyperpolarization experiments were carried out sequentially, which is how the initial state was

set in this example. Even when there is a hyperpolarized target that binds the complex at the beginning of the experiment, the final hyperpolarization converges to the same as if the system had been initialized with purely singlet spin order. The invariance of the final hyperpolarization to the initial condition is a result of a finite memory that the system retains over the course of the experiment and highlights an important limitation to optimization. As such, this should be considered when developing optimization schemes that optimize sequence-level hyperpolarization.

The most robust method by which a $\mathcal{N}$-parameter phase-space may be optimized is to index the space on a $\mathcal{N}$-dimensional grid and calculate the hyperpolarization obtained for each of the positions on the grid. This is shown for a $\{\Delta\omega_N, t_p\}$ slice of the phase space in the case of the coherently-pumped LIGHT-SABRE experiment (Fig. 42A). Importantly, the grid optimization must be calculated at the specific exchange rates that are used in the simulations, as the parameter-space will optimize at different conditions as a function of the exchange rates. A pulse sequence such as the coherently pumped LIGHT-SABRE experiment depends parametrically on $t_p, t_d, \omega_{1,N}$, and $\Delta\omega_N$ for any one set of exchange parameters, of which there are k_N, k_H, and $[Ir]/[S]$. As such, this parameter space is $\mathcal{N} = 7$ dimensional for any given system. The $[Ir]/[S]$ is set experimentally and the exchange rates are intrinsic to the system at a given temperature, so it is often advantageous to optimize the pulse sequence parameter dimensions for a subset of exchange parameters. Even still, this only reduces the grid dimensionality to $\mathcal{N} = 4$. For instance, in just the two-dimensional slice of the parameter space shown in Fig. 42A contains 1,300 simulations and requires approximately 30 minutes of computational time to calculate on a minimal (4+1)X spin system. Instead of calculating the

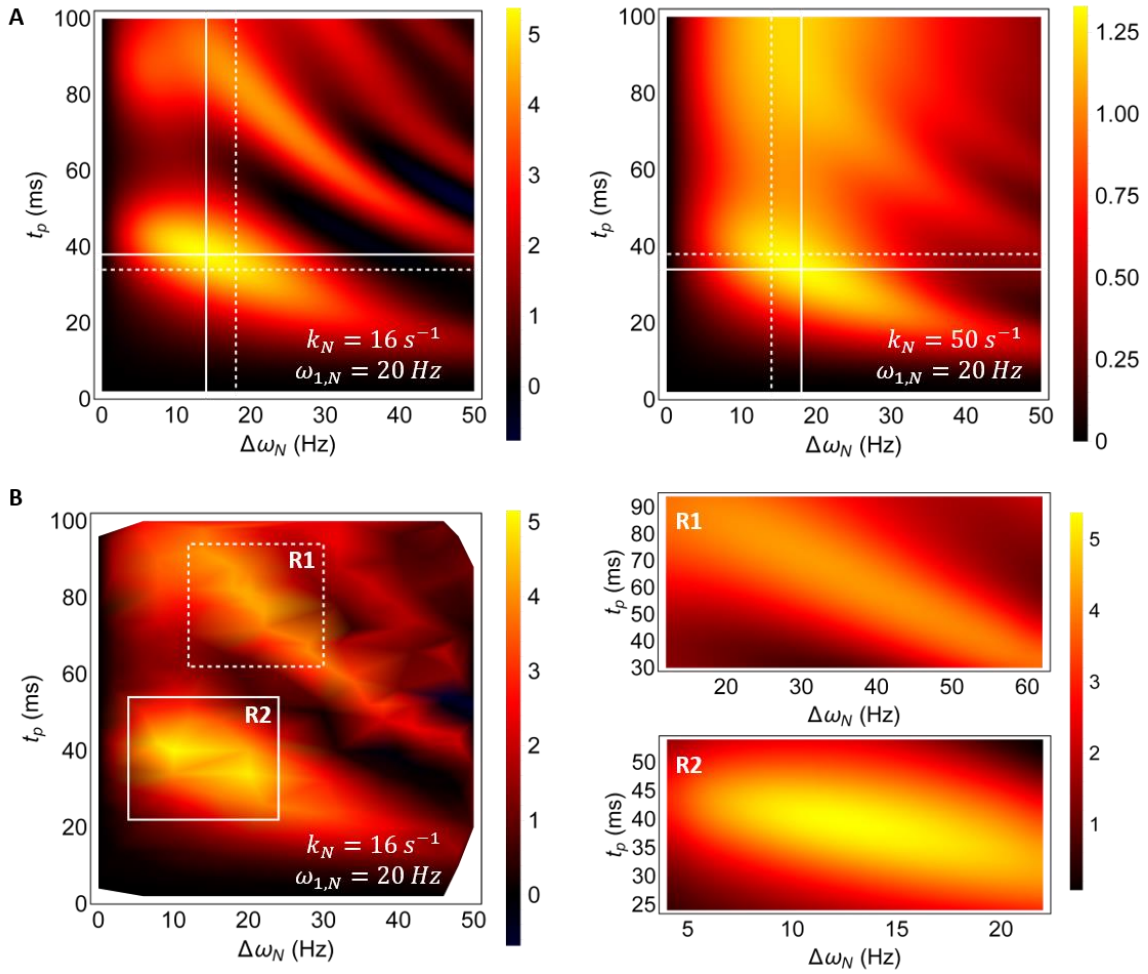

Figure 42: Projections of pulse sequence phase-spaces for pumped LIGHT-SABRE. A. Optimizing the $\{\Delta\omega_N, t_p\}$ phase-space by explicitly calculating a grid varying the parameters will find the optimal conditions to generate hyperpolarization so long as the grid is permitted to span a space that contains the optimal condition. For each plot, the solid lines indicate the position of the maximum for that exchange rate, and the dashed lines indicate that position of the maximum for the other rate. However, this method becomes computationally expensive when three or more parameters are co-optimized. **B.** A 10% random sampling of the grid before exhaustive optimization can eliminate large regions of the phase space. The maxima may be found by grid-optimizing around regions of interest. This circumvents having to exhaustively search the entire parameter phase-space. All simulations use a (4+1)X model.

entire space by brute force, large regions of the space may be neglected by randomly sampling the space at a fractional rate, which was done at a 10% sampling rate as an example (Fig. 42B). Subsequently optimizing around local maxima with a narrower grid can yield the optimum sequence parameters but at a greatly reduced computational expense. Depending on the experiment and the number of parameters being co-optimized, additional iterations of

randomly sampling areas of the phase space closer to the local maxima can reduce computational time. It should be noted that with an approximately 3-fold decrease in the average lifetime that the maximum polarization decreases by a factor of approximately 4.

In addition to initially down-sampling the pulse sequence parameter phase-space, other parameters such as the hydride exchange rate k_H very weakly affect the pulse sequence optimization other than scaling the resulting hyperpolarization (Fig. 43). Increasing the exchange rate by a factor of four only results in a $\Delta t_p = 2\ ms$ change in the optimum pulse length and no additional change in the optimal pulse power. The one parameter that the k_H directly affects is the t_d parameter (Fig. 31), but very weakly after $t_d \gg k_N^{-1}$. As such, it is often acceptable to fix the value of k_H in the initial optimization of pulse sequence parameters and then sample this rate as the optimization enters final stages of optimization, which we refer to as the fine-graining stage. It should be noted that in the traditional 'bubbling' SABRE setup, this parameter is highly coupled to the bubbling rate of the system, which is often controlled qualitatively by use of a needle valve, as well as the diffusion of parahydrogen in

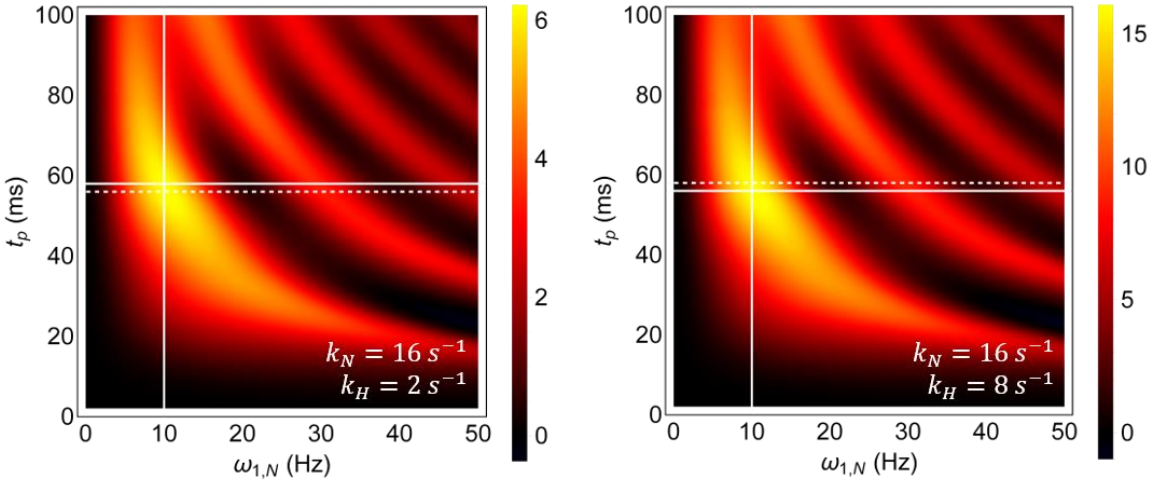

Figure 43: Parameter elimination during optimization. Certain parameters, such as k_H which does not vary greatly for most SABRE experiments, often have a weak dependence on the optimization other than resulting in a scaling factor. As such, these parameters may often be neglected when initially optimizing pulse sequence parameters.

the solution. As such, this parameter is perhaps the most difficult to experimentally control, so fine-grain optimization of the k_H is often not required.

In addition to optimizing how singlet order is converted into magnetization, it is also important to consider the mechanisms for how the singlet order is being preserved when spin order is not being transferred (Fig. 44). Previously, we noted that evolution under the J_{NH} and

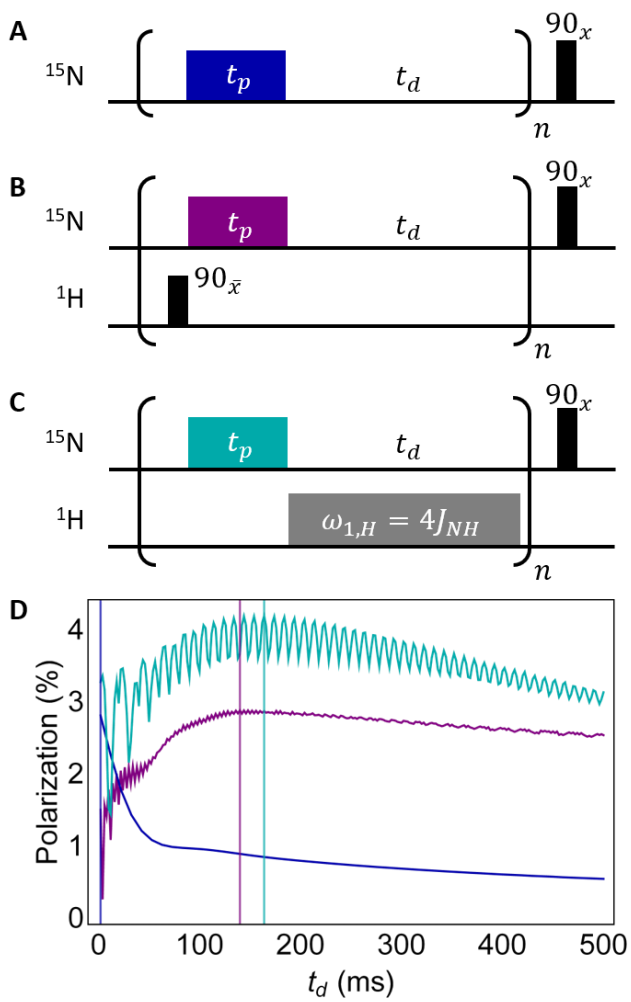

Figure 44: Effects of spin order conservation on sequence optimization. A. The exchange delay of the pumped LIGHT-SABRE sequence allows conversion of $\hat{I}_1 \cdot \hat{I}_2 \rightarrow \hat{I}_{1z}\hat{I}_{2z}$, whereas **B.** the SLIC-SABRE experiment converts the $\hat{I}_{1z}\hat{I}_{2z} \rightarrow \hat{I}_{1y}\hat{I}_{2y}$ spin order and **C.** a ^{1}H decoupled LIGHT-SABRE variant preserves $\hat{I}_1 \cdot \hat{I}_2$ by decoupling J_{NH}. **D.** For a constant set of pulse parameters ($t_p = 50\ ms$, $\omega_{1,N} = 8\ Hz$, and $\Delta\omega_N = 20\ Hz$), optimization of each of these sequences and resulting performance is vastly different depending on the method by which spin order is preserved. Vertical lines indicate positions of the maximum hyperpolarized signal. For all simulations, $k_N = 50\ s^{-1}$, $k_H = 2\ s^{-1}$, and $[Ir]/[S] = 1/20$.

J_{HH} couplings essentially reduce the parahydrogen spin order from $\hat{I}_1 \cdot \hat{I}_2 \rightarrow \hat{I}_{1z}\hat{I}_{2z}$, and proposed that ^{1}H decoupling by simply irradiating the $\hat{I}$-spins could preserve the transverse terms of the singlet. Knecht and coworkers introduced the SLIC-SABRE (SLIC = Spin Lock Induced Crossing) method that appends a $\pi/2$ pulse on the ^{1}H nuclei that converts $\hat{I}_{1z}\hat{I}_{2z} \rightarrow \hat{I}_{1y}\hat{I}_{2y}$ (if an $\bar{x}$-phase pulse is used), which can be converted into hyperpolarized $\hat{S}_z$ spin order under a subsequent SLIC pulse[120]. Even when all the parameters of the spin-order transferring pulse are kept constant, the dependence of hyperpolarization on other parameters that should be consistent between different experiments, such as the inter-pulse delay time t_d, dramatically changes when compared to the original LIGHT-SABRE experiment. In the case of LIGHT-SABRE, the optimal hyperpolarization is achieved when no delay is used, as in that case it is more advantageous to continually hyperpolarize the system, which essentially does not permit the loss of spin order by continually using it as parahydrogen exchanges with the catalyst. In this limit, coherently pumping the system reduces the ultimate hyperpolarization, but continually irradiating the matching condition is entirely possible as the power-dissipation of the LIGHT-SABRE experiment is minimal (microwatts). However, the SLIC-SABRE experiment can generate comparable hyperpolarization by adding a $90_{\bar{x}}$ pulse on the ^{1}H channel and optimizes at a condition consistent with a coherently-pumped experiment ($t_d \gg k_N^{-1}$). Finally, decoupling the J_{NH} by irradiating at a power of $\omega_{1,H} = 4J_{NH} = 100\ Hz$ during the exchange delay preserves $\hat{I}_1 \cdot \hat{I}_2$ spin order and leads to the largest generation of hyperpolarization for the three experiments. Furthermore, this experiment also optimizes in a coherent pumping regime. The fine structure observed in these simulations is a direct result of the irradiation on the ^{1}H channel.

While the model (4+1)X system is representative of the ^{15}N-pyridine system that was used to develop and benchmark many of the high field X-SABRE experiments to date, there are only a few X-SABRE systems that readily hyperpolarize without a coligand. As such, it is much more pertinent to discuss optimization using a high field (3+1)Y ABX spin system. For comparisons sake, we will begin with a system that use the chemical shift difference between the two hydrides $\Delta\omega_{HH} = 460\ Hz$, which is the experimental value in a ^{15}N-acetonitrile/^{14}N-pyridine system at 8.45T, and utilizes the same couplings as the (4+1)X system we have been using, $J_{HH} = -9\ Hz$ and $J_{NH} = -25\ Hz$. These couplings are nearly the same for the ^{15}N-pyridine and ^{15}N-acetonitrile X-SABRE systems. We will examine the ^{1}H decoupled LIGHT-SABRE (Fig. 33) experiment as an example for a direct analogy to the previous discussion (Fig. 45). At a pulse power of $\omega_{1,N} = 8\ Hz$ and resonance offset of $\Delta\omega_N = 20\ Hz$, the pulse (t_p) and exchange delay (t_d) length optimize to approximately $t_p \approx t_d \approx 40\ ms$, which is preserved when $k_N = 16\ s^{-1}$ is increased to $k_N = 50\ s^{-1}$. Interestingly, there is a structure at $t_p + t_d \approx 36\ ms$ that likely results from an accumulating pulse effect because this feature

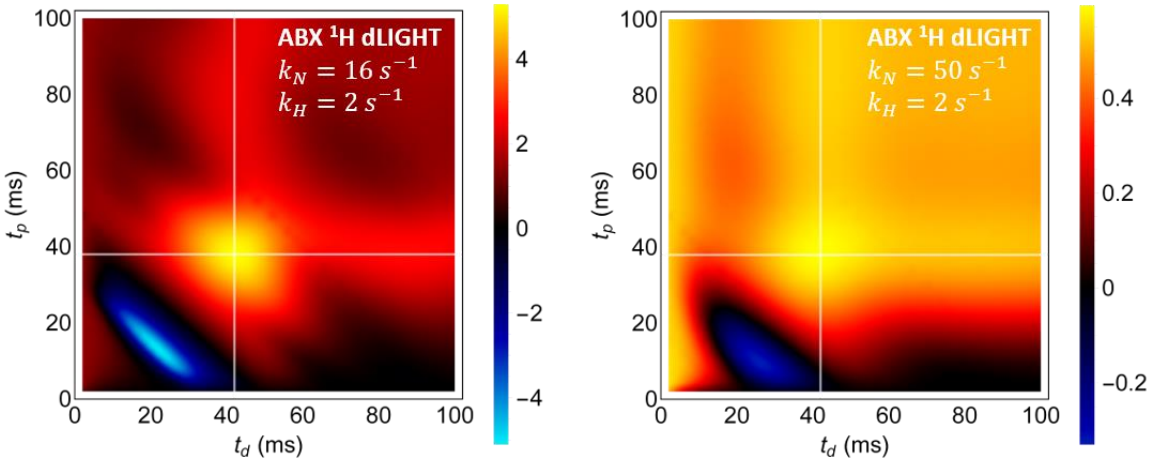

Figure 45: Pulse and exchange delay optimization of ^{1}H dLIGHT in an ABX system. The pulse and exchange delay lengths co-optimize to approximately the same length of $t_p \approx t_d \approx 40\ ms$. In this regime, many pulses are coupled together over the lifetime of a single parahydrogen, suggesting a low conversion efficiency per pulse. Crosshairs indicate position of the maximum. Color bars indicate percent polarization (P%).

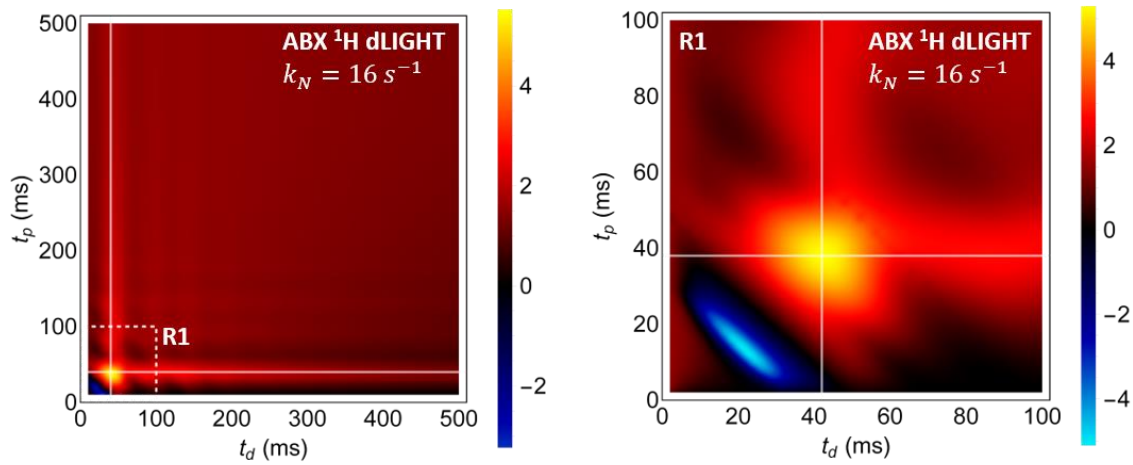

Figure 46: Structured features in the $\{t_p, t_d\}$ space. When the pulse and exchange delay lengths are on the order of the dominant couplings and pulse sequence powers, which often appear when $t_p + t_d \leq 100\ ms$ for typical experiments, fine structures appear that should be sampled at an increased frequency. Other regions of phase space are significantly less structured, and as such do not require such fine sampling. Color bars indicate percent polarization (P%).

is disproportionatley smaller for $k_N = 50\ s^{-1}$, where a given complex is exposed to fewer pulses. As ^{1}H decoupling is used for the entire duration of the pulse sequence, there are no pulse artifacts that appear in the $\{t_p, t_d\}$ phase space. Comparing these two exchange rates used in Fig. 45 is interesting, as it highlights that hyperpolarization decreases by a factor of approximately 10 with an approximately 3-fold decrease in the average lifetime. Importantly, while most of the $\{t_p, t_d\}$ phase space is unstructured, fine details will emerge when these sequence parameters are on the order of the couplings and pulse powers (Fig. 46). As such, it is often advantageous to increase the sampling rate of the simulations in this regime.

In general, we find two modes in which LIGHT-SABRE variants optimize (Fig. 47). When the exchange rate is slow enough to permit a π-pulse in the hyperpolarization dynamics (a maximum polarization), then the dynamics can optimize in a regime where the system is coherently pulsed. In the coherently pumped limit, we find an optimum at a pulse length of $t_p \approx 40\ ms$ and $\Delta\omega_N = 20\ Hz$. However, as the exchange rate increases such that the average lifetime of the complex is less than the π-pulse length, the solution will tend to

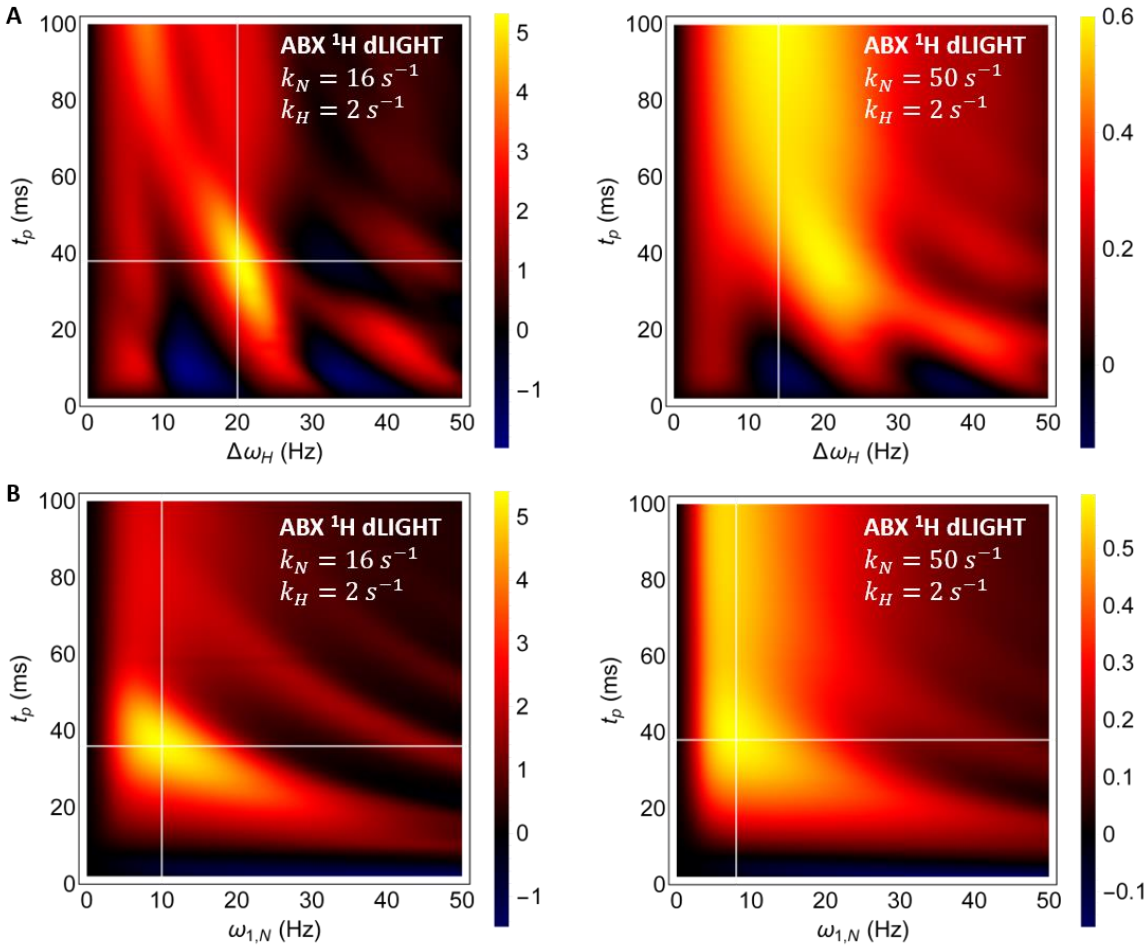

Figure 47: Two optimization modes of LIGHT-SABRE sequences at $t_d = 42\ ms$. When the k_N is slow relative to the coherent evolution, the pulse sequence optimizes to a coherent pumping regime. In this regime, the $\{\Delta\omega_N, t_p\}$ phase space becomes highly structured and deviates from a simple nutation pattern as seen at longer delay lengths. As the ligand exchange rate increases, structure is lost and the solution optimizes to a pseudo-continuous regime where the pulse length is much longer than the average lifetime. Color bars indicate percent polarization (P%).

optimize to a regime where the irradiation may be applied continuously. In the continuously pumped limit, the $\Delta\omega_N$ also decreases so to avoid generating unnecessary phase rotation under this term. Similar effects are observed when exploring the $\{\omega_{1,N}, t_p\}$ phase space (Fig. 47B). This shifting to a continuously pumped limit suggests that the ^{1}H dLIGHT pulse sequence is inefficient when the exchange rate increases, as evidenced by the large decrease in the hyperpolarization.

With the above points in mind, we may now pursue optimization of the experimental phase space. We shall use the ^{1}H dLIGHT sequence as an example, establishing $\omega_{1,H} = 1.6\ kHz$ for $\Delta\omega_{HH} = 460\ Hz$ and if ^{1}H excitation is on resonance ($\Delta\omega_{H} = 0$). Furthermore, we will perform optimization assuming a fixed $k_H = 2\ s^{-1}$ and shall explore optimization for the two exchange rates that we have previously used, $k_N = 16\ s^{-1}$ and $k_N = 50\ s^{-1}$. Under these conditions, there are 4 optimizable parameters ($\omega_{1,N}, \Delta\omega_N, t_p, t_d$), and given the various examples listed above, this phase space may be indexed on a grid consisting of the ranges $\omega_{1,N} = \Delta\omega_N = [1,15,\Delta1]Hz$, and $\{t_p, t_d\} = \{[2,100,\Delta2],[110,500,\Delta10]\}$. In the notation $[a,b,\Delta c]$, the range extends from a to b in steps of Δc, and $\{,\}$ joins two of these ranges together. This results in a grid with 1,822,500 data points, which would require 67 days to fully calculate on the computer that was used to run these simulations (Intel i5-10400 CPU 12 core @ 4.0 GHz, 12 GB RAM). Loaiza and Warren[138] reported on a computational method for pulse shaping that follows a so-called evolutionary strategy[139], whereby a large-dimensional grid is sparsely sampled and the top 5% of simulations that minimize a cost function are then used as starting points for subsequent generations (Fig. 48). Each subsequent generation takes the starting point and perturbs the parameters in each optimization dimension. This strategy may be iterated multiple times to find optimal pulse sequence solutions, and the size of the perturbation may be adjusted to focus on specific regions of phase space. After three generations, the resulting hyperpolarization from the ^{1}H dLIGHT pulse sequence was increased by approximately 50% for both the cases of $k_N = 16\ s^{-1}$ and $k_N = 50\ s^{-1}$.

Interestingly, both cases optimized to conditions where the ^{15}N-channel was essentially continuously irradiating the bound species. Furthermore, the optimum solutions indicate that

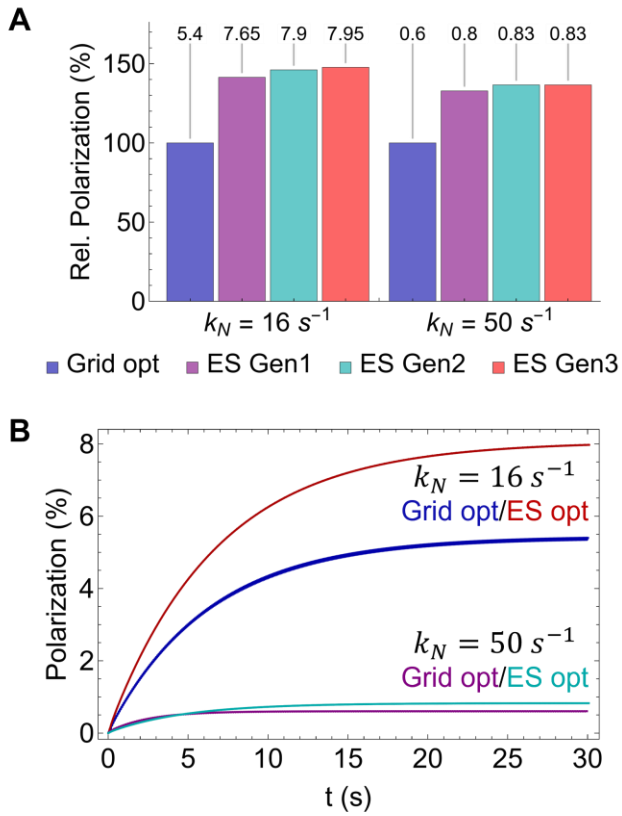

Figure 48: Evolutionary strategy for high-field X-SABRE optimization. A. The polarization resulting from the evolutionary strategy (ES) relative to the grid optimization results shown previously in this section show that the resulting hyperpolarization may be increased by approximately 50% in just three generations of the evolutionary strategy. Final polarizations indicated above bars. **B.** The rate at which polarization is pumped is not necessarily correlated with the final polarization. For $k_N = 16\ s^{-1}$, the higher pumping rate is accompanied by a larger polarization, whereas for $k_N = 50\ s^{-1}$ the higher polarization results from a lower pumping rate. This emphasizes the need to run the simulation for long enough that the polarization converges.

the initial buildup rate does not necessarily yield the largest hyperpolarization (Fig. 48B). While this is the case for $k_N = 16\ s^{-1}$, the optimum solution for the case of $k_N = 50\ s^{-1}$ generates hyperpolarization more slowly than the grid optimized solution, but ultimately yields larger signal. This stresses the importance of optimizing the solution using simulations that permit the convergence of the hyperpolarization.

An interesting feature of this optimization is that level anti-crossing (LAC) condition $\Delta\omega_N \approx \omega_{1,N} \approx J_{HH}$ does not actually predict where the optimum hyperpolarization is achieved when exchange is considered (Fig. 49). At slow exchange rates, the requisite pulse

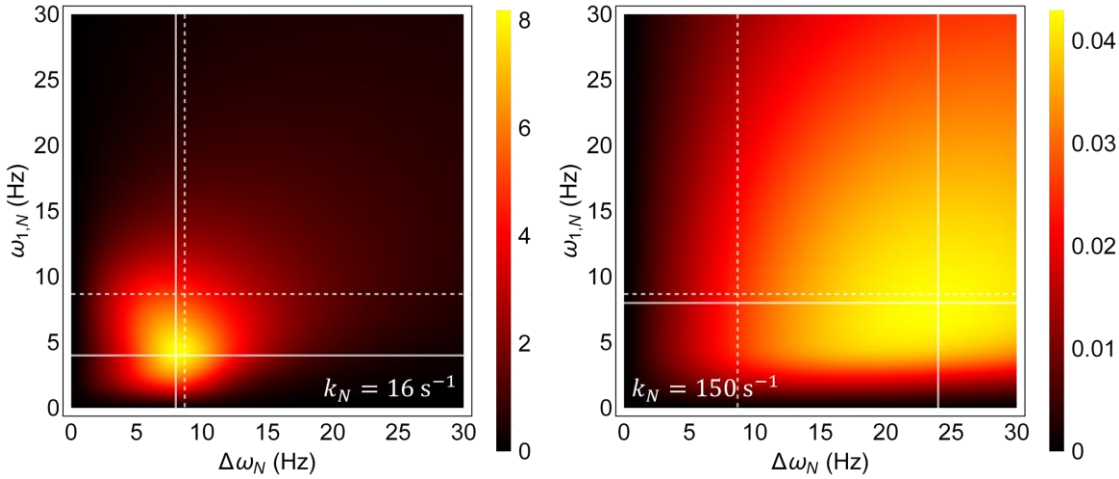

Figure 49: Optimum hyperpolarization after continuous irradiation for 20s. For both slow and fast ligand exchange, hyperpolarization in a ^{1}H dLIGHT experiment is optimized (solid lines) at conditions that are far from the LAC condition (dashed lines). In these simulations, $k_H = 2\ s^{-1}$. Color bars indicate percent polarization (P%).

power is approximately half of what is required to generate hyperpolarization while the resonance offset optimizes at approximately $\Delta\omega_N \approx J_{HH}$. For fast exchange, the resonance offset is approximately double the expected value and $\omega_{1,N} \approx J_{HH}$. While the LAC condition is useful to gain an intuition of the regimes where hyperpolarization will be generated, it is insufficient in predicting the optimum hyperpolarization.

While pen-and-paper theory can provide insight on the development of new X-SABRE experiments, optimization of hyperpolarization should be done through use of the DMExFR2 simulations. We have shown illustrative examples of optimizing the high-field X-SABRE signal that can be extended to exploring optimization with other high-field experiments as well as to next-generation ultralow field experiments. Grid optimization is perhaps the most accurate method for optimization, but it exponentially scales with the number of pulse sequence parameters. Evolutionary strategy in conjunction with grid optimization accelerates the process and is a robust method to finding the global optimum. Computational optimization of X-SABRE experiments motivated by pencil-and-paper theory is a key step in considering the effects of exchange when designing new experiments.

4.5 Outlook and conclusions

There are a few interesting extensions of this work that will be interesting to explore. The first pertains to current efforts for increasing the polarization and scale of X-SABRE experiments, which will be critical for preclinical and clinical applications. As mentioned previously, perhaps the most difficult parameter to control is the parahydrogen replenishment rate, k_H, as conventional X-SABRE systems use a setup where *p*-H_2 gas is continuously bubbled through the sample. This constrains the amount of parahydrogen that may be dissolved into solution. The concentration limits may be circumvented by either increasing the pressure of parahydrogen in a conventional solution or generating a supercritical state with CO_2 or Xe gas where the molar fraction of *p*-H_2 can be as high as 20%. However, such a system would have a fixed amount of the parahydrogen singlet state that would not be replenished by bubbling (Fig. 50). One of the significant hurdles associated with such an experimental geometry is that at the lab field ($100\mu T - 200\mu T$), the transverse terms of the singlet ($\hat{I}_{1x}\hat{I}_{2x} + \hat{I}_{1y}\hat{I}_{2y}$) are

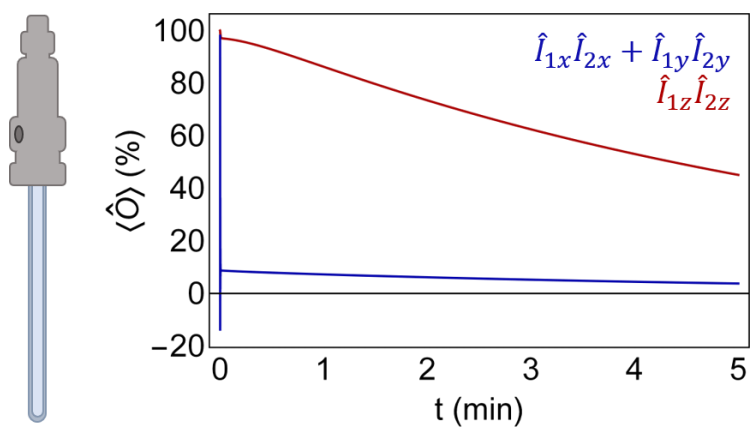

Figure 50: Spin order while loading a supercritical X-SABRE sample. It requires approximately 5 minutes to pump the high-pressure NMR tube to 160 bar for a supercritical CO_2 or Xe experiment. During this time, the catalyst facilitates the destruction of the transverse terms of the singlet order (blue), rapidly leading to an attenuation of the singlet. However, the $\hat{I}_{1z}\hat{I}_{2z}$ term of the singlet is largely preserved during this time, and can be used in lieu of the transverse terms in the broadband X-SABRE experiment.

not preserved due to evolution under the J_{NH} coupling. The $\hat{I}_{1z}\hat{I}_{2z}$ term is preserved at this field and is available to use for expeirmentation even after the 5 minutes required to pressurize this system. Importantly, the system only retains approximately 10% of the initial transverse spin order over this period. We may target hyperpolarization with the broadband X-SABRE experiment on this sample. Experiments may be applied sequentially without having to reload new samples as only a small amount of this spin order is converted into magnetization with each pulse sequence.

Consecutive broadband X-SABRE experiments may be easily simulated using the DMExFR2 to computationally interrogate the potential for this application. We find that it is possible to generate generate hyperpolarization using consectuve broadband X-SABRE experiments (Fig. 51A), and shows good agreement to the single-shot variant of this expeirment. Here, we show a scan of the τ delay using $\tau_{HH} = 21\ ms$ using $\Delta\tau = 0.25\ ms$ step sizes, where the multiplexed curve is calculated by consecutively increasing the τ delay and the single shot curve coincides with separate simulations that all share the same initial state. Even at the maximum spin-order consuption of this expeirment, which coincides with the conditions yielding the largest signal, the resultant hyperpolarization only decreases from $P \approx 4\%$ to $P \approx 1\%$ after $\mathcal{N} = 40$ experiments have been repeated.

Importantly, this effect will be strongly dependent on the exchange rate of the parahydrogen with the catalyst as well as the concentrations of the relevant species. Keeping $[Ir]/[pH_2] = 1/500$, we may calculate $\langle \hat{I}_{1z}\hat{I}_{2z} \rangle$ after 5 minutes at the lab field while varying the hydride exchange rate (Fig. 52). In all of these simulations, we have assumed a free parahydrogen $T_{1,f} = 20\ s$ and $T_{S,f} = 3600\ s$, and bound parahydrogen $T_{1,b} = 5\ s$ and that relaxation of the singlet state on the bound species negligible. When bound to the catalyst, the

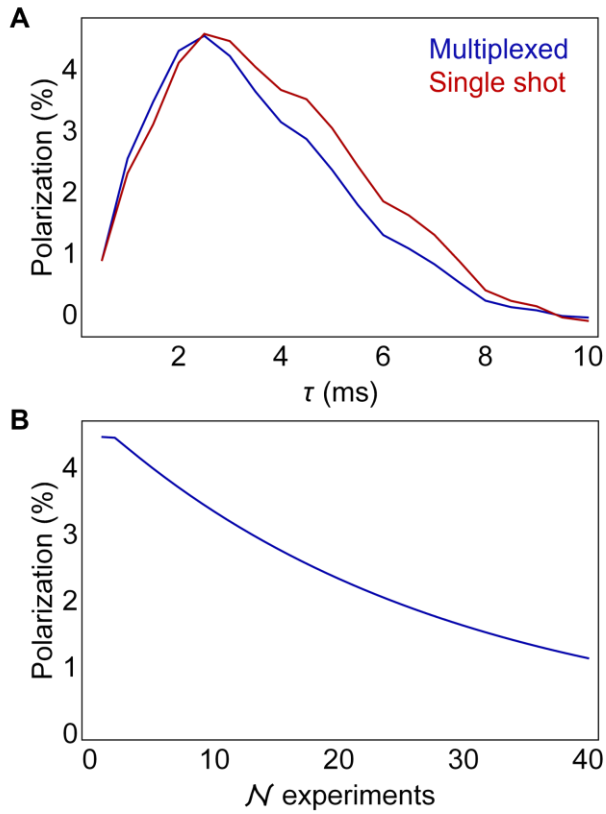

Figure 51: Multiplexed X-SABRE. A. Running a high-pressure SABRE experiment in multiplexed mode (blue) differs only slightly from the single-shot version of this experiment (red). $[Ir]/[pH_2] = 1/500$ and $[Ir]/[S] = 1/20$ in a model (3+1)Y system using $k_H = 2\ s^{-1}$. **B.** A broadband X-SABRE experiment using $\tau = 3\ ms$ may be run in multiplexed mode as a test of the longevity of the signal. This delay maximizes the signal, and subsequently maximizes consumption of spin order. Even after 40 experiments, the hyperpolarization is greater than $P = 1\%$, making this a promising technique for parameter identification for the high pressure and supercritical SABRE experiments.

singlet spin order is unlocked into spin order that relaxes more rapidly to equilibrium. Hence, there is a strong dependence on the hydride exchange rate on the preservation of the $\hat{I}_{1z}\hat{I}_{2z}$ spin order during the 5 minutes of loading time. While conventional X-SABRE experiments usually exhibit polarization levels consistent $k_H = 1 - 6\ s^{-1}$, these experiments are inherently diffusion limited. In a supercritical expeirment, where the parahydrogen is much larger than in a conventional experiment, we expect k_H to increase. Spin order can be preserved by simply cooling the system while being pressurized, thus decreasing the hydride exchange rate.

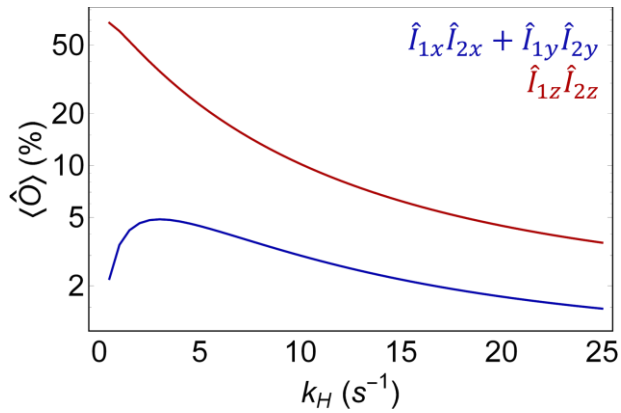

Figure 52: Spin order preservation after 5 minutes at the lab field. For all simulations, $[Ir]/[pH_2] = 1/500$ and $[Ir]/[S] = 1/20$ in a model (3+1)Y system using $k_N = 100\ s^{-1}$. The fraction of preserved spin order is strongly dependent on the hydride exchange rate, decreasing with an increase in the exchange rate. This effect is largely independent of the ligand exchange rate.

Another extension of the work presented here is the ability to hyperpolarize rapdily exchanging targets. Of the various techniques introduced here, hyperpolarization in the broadband X-SABRE experiment scales the fastest at t^3. Decreasing the overall sequence length ($T = 8\tau + \tau_{HH} + 10t_p$) permits access to faster exchange rates (Fig. 53), with enhancements of $\varepsilon \approx 10$ at exchange rates as fast as $k_N \approx 500\ s^{-1}$. Hyperpolarization at such fast exchange rates will be critical in expanding the applications of X-SABRE to a broader substrate scope as well as to improve compatibility with the supercritical X-SABRE experiments, which often have to be run at elevated temperatures. In comparison, hyperpolarization in the ^{1}H dLIGHT experiment scales as t^6, meaning that performance is attenuated at fast exchange rates. However, the two experiments do perform comparably when the exchange rate is in the regime of $50\ s^{-1} < k_N < 150\ s^{-1}$. All of the simulations in Fig. 53 have assumed hydride exchange rates of $k_H = 2\ s^{-1}$.

Here, we have extended the scope of high field X-SABRE to be comparable to that of the widely used SABRE-SHEATH method. We demonstrated the ability to coherently drive the X-SABRE level anti-crossing condition, which permitted us to experimentally

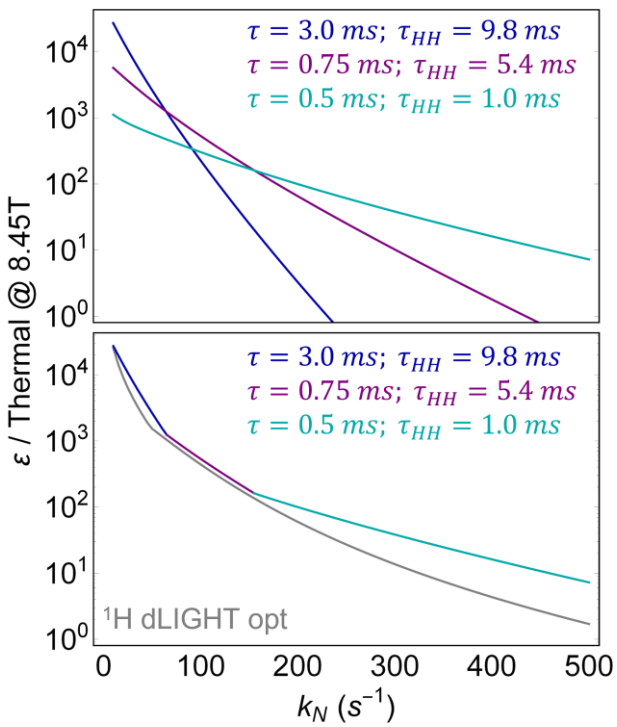

Figure 53: Broadband X-SABRE and ^{1}H dLIGHT in the fast exchange limit. Top. Decreasing the total length of the broadband X-SABRE pulse sequence ($T = 8\tau + \tau_{HH} + 10t_p$) makes the sequence less sensitive to the exchange rate. **Bottom.** Compared to the ^{1}H dLIGHT experiment, the broadband X-SABRE experiment exhibits superior performance at fast exchange rates and similar performance at slow exchange rates. For the ^{1}H dLIGHT simulations, $\omega_{1,H} = 1.6\ kHz$ and irradiation was continuously applied for 20 s. All simulations were run on a truncated (3+1)Y system using the ^{15}N-acetonitrile parameters at 8.45T.

ground the DMExFR2 model under high field conditions. Using this model, we then sought to expand the scope of high field X-SABRE by targeting asymmetric ligand environments for hyperpolarization, which form the vast majority of X-SABRE systems. The ^{1}H decoupled LIGHT-SABRE variants spin lock the transverse components of the singlet state using strong irradiation at the center-frequency of the parahydrogen-derived hydrides. *In silico* exploration of this system facilitated the development of the broadband X-SABRE experiment, which expanded the capabilities and bandwidth of high-field X-SABRE experiments. This permitted the first demonstration of simultaneous hyperpolarization of multiple targets at high field. Finally, we showed illustrative examples to describe optimization procedures that would permit robust optimization of X-SABRE pulse sequences.

Chapter 5: Expanding the capabilities of X-SABRE at ultralow field

While the developments of high field X-SABRE are supported by decades of experimental and theoretical techniques, it was only recently that spin physics at ultralow magnetic fields became interesting and accessible[89, 140-142]. Relative to experiments at high magnetic field, ultralow magnetic fields are simple to generate with nearly arbitrary control over the amplitude and waveform in any direction. This provides an enormous amount of experimental flexibility and broadens the opportunities to control the underlying spin dynamics. The ultralow field X-SABRE experiment SABRE-SHEATH utilizes static microTesla magnetic fields to generate the necessary matching conditions to transfer hyperpolarization to heteronuclei. Much of the work in this chapter was done in collaboration with Christian Tanner and Clark Eriksson, who worked in the Warren lab as undergraduate researchers, and followed from the pioneering coherently pumped ultralow field X-SABRE experiments performed by Shannon Eriksson and Xiaoqing Li. Herein, we will explore various routes to expanding the capabilities of ultralow field X-SABRE by shaping the magnetic field in various ways.

It is beneficial to review the underlying mechanism for SABRE-SHEATH, as this will inform the following discussion. At ultralow magnetic field, the chemical shift Hamiltonian becomes negligible and frequency differences are controlled directly by the Zeeman interaction. Many of the following results will be discussed using a model (3+1)Y ^{15}N -SABRE system, which at ultralow field has the Hamiltonian:

$$\hat{\mathcal{H}} = \omega_H\left(\hat{I}_{1z} + \hat{I}_{2z}\right) + \omega_N \hat{S}_z + 2\pi\left(J_{HH}\hat{I}_1 \cdot \hat{I}_2 + J_{NH}\hat{I}_1 \cdot \hat{S}\right) \tag{5.1}$$

This Hamiltonian contains two orthogonal 3×3 subspaces that dictate hyperpolarization and two disconnected eigen states proportional to unity. We will focus on one of the orthogonal hyperpolarization-active subspaces for this discussion, which in the $\mathbb{ST} \otimes \mathbb{Z}$ basis set (singlet-triplet on the hydrides, Zeeman on the heteronucleus) is given by (all constants in rad s^{-1}):

$$\hat{\mathcal{H}} = \begin{pmatrix} & |T_H^+\beta_N\rangle & |T_H^0\alpha_N\rangle & |S_H\alpha_N\rangle \\ \langle T_H^+\beta_N| & \omega_H - \omega_N & \frac{J_{NH}}{2\sqrt{2}} & -\frac{J_{NH}}{2\sqrt{2}} \\ \langle T_H^0\alpha_N| & \frac{J_{NH}}{2\sqrt{2}} & \frac{J_{NH}}{4} & \frac{J_{NH}}{4} \\ \langle S_H\alpha_N| & -\frac{J_{NH}}{2\sqrt{2}} & \frac{J_{NH}}{4} & \frac{J_{NH}}{4} - J_{HH} \end{pmatrix} \tag{5.2}$$

This Hamiltonian suggest hyperpolarization is transferred from $|S_H\alpha_N\rangle$ to $|T_H^+\beta_N\rangle$ when the matching condition $\omega_H - \omega_N \approx J_{NH}/4 - J_{HH}$ is met. Converting the frequency difference into a magnetic field via $\omega_H - \omega_N = (\gamma_H - \gamma_N)B_0$ yields a matching condition given by $B_0 = J_{NH}/4 - J_{HH} \approx 0.04\mu T$. These magnetic fields are a small fraction of the Earth's magnetic field ($B_{Earth} \approx 50\ \mu T$ in North Carolina), but in practice for most magnetic resonance labs, it is the stray fields of nearby superconducting magnets that must be removed, which are often larger than the Earth's magnetic field. This may be accomplished by using a μ-metal shield, which is a ferromagnetic alloy with a high magnetic permeability that when saturated acts as a magnetic waveguide and can reduce the external magnetic field by a factor of approximately $1/1000$. The internal magnetic field may be tuned using a solenoid electromagnet, which depending on the configuration and current can generate extremely homogeneous magnetic fields.

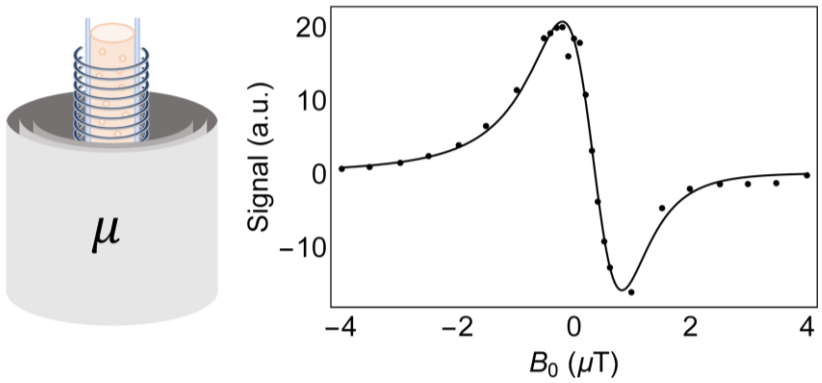

Figure 54: The SABRE-SHEATH experiment. A solenoid is placed inside a μ-metal shield to generate controllable microTesla magnetic fields. Scanning the magnetic field in the microTesla regime yields the SABRE-SHEATH field profile. Similar to the profile in LIGHT-SABRE, this profile is anti-symmetric about the center frequency, which under these conditions is when $B_0 = 0\ \mu T$.

Experimentally, it is common practice to scan the field produced by the solenoid to generate a SABRE-SHEATH profile (Fig. 54). The field profile gives the field that maximizes the hyperpolarization, which is often near $B_0 \approx 1\ \mu T$, as well as the residual field of the magnetic shield. Importantly, this magnetic field is about an order or magnitude larger than the field predicted by the level anti-crossing condition. The LAC predicts the magnetic field as if the couplings to the $|T_H^0 \alpha_N\rangle$ state do not exist, and approximates this three-level system as a two-level system. Hence, the actual magnetic field that optimizes hyperpolarization is much larger than the field predicted by the LAC condition.

As previously mentioned, the SABRE-SHEATH experiment has several distinct advantages over high field X-SABRE methods. Firstly, hyperpolarization can nearly always be achieved at $B_0 \approx 1\ \mu T$ for any substrate, meaning that it was easy to rapidly assess a broad scope of X-SABRE targets without needing to reoptimize the experiment. Secondly, this experiment was used to demonstrate large heteronuclear polarizations in under a minute, orders of magnitude faster than dDNP. We showed that pumping the SABRE-SHEATH field between an evolution field ($B_0 \approx 1\ \mu T$) and a delay field ($B_d \approx 50\ \mu T$) could unveil the coherent hyperpolarization dynamics at ultralow field, which spurred the work in the previous

chapter at pumping the X-SABRE dynamics at high field[89]. Since then, there have been several avenues that have been pursued to further optimize the ultralow field X-SABRE experiment. Herein, some of these advances will be described and future directions will be discussed.

5.1 Pumping heteronuclear singlets

As mentioned previously, we demonstrated the possibility to coherently drive X-SABRE hyperpolarized magnetization[89]. While direct $\hat{S}_z$ magnetization was the original target spin state for this sequence, X-SABRE has also been shown to generate hyperpolarized singlet states ($\hat{S}_1 \cdot \hat{S}_2$) between pairs of nuclei, such as $^{13}C_2$ and $^{15}N_2$ spin pairs. However, the existence of more exotic spin states such as singlets between heteronuclei ($\hat{S} \cdot \hat{L}$) had only been once reported between ^{1}H and ^{13}C[143]. Furthermore, control of population in and out of this state had yet to be coherently manipulated. Introducing another spin $\hat{L}$ on the hyperpolarization target, and writing the Hamiltonian in a $\mathbb{ST} \otimes \mathbb{ST}$ basis set (singlet-triplet on the hydrides and the heteronuclear spin pair) gives a hyperpolarization active subspace (rad s^{-1}) for the model ^{15}N,^{13}C-acetonitrile system:

$$\hat{\mathcal{H}} = \begin{pmatrix} & |T_H^+ T_{NC}^0\rangle & |T_H^0 T_{NC}^+\rangle & |T_H^+ S_{NC}\rangle & |S_H T_{NC}^+\rangle \\ \langle T_H^+ T_{NC}^0| & \omega_H & \Sigma J_{NH} & \frac{\Delta\omega_{NC}}{2} - \Delta J_{NC} & -\Sigma J_{NC} \\ \langle T_H^0 T_{NC}^+| & \Sigma J_{NC} & \frac{\Sigma\omega_{NC}}{2} & -\Delta J_{NC} & \Sigma J_{NC} \\ \langle T_H^+ S_{NC}| & \frac{\Delta\omega_{NC}}{2} - \Delta J_{NC} & -\Delta J_{NC} & \omega_H - J_{NC} & \Delta J_{NC} \\ \langle S_H T_{NC}^+| & -\Sigma J_{NC} & \Sigma J_{NC} & \Delta J_{NC} & \frac{\Sigma\omega_{NC}}{2} - J_{HH} \end{pmatrix} \quad (5.3)$$

We have defined $\Delta\omega_{NC} = \omega_N - \omega_C$, $\Sigma\omega_{NC} = \omega_N + \omega_C$, $\Delta J_{NC} = (J_{NH} - J_{CH})/4$, and $\Sigma J_{NC} = (J_{NH} + J_{CH})/4$ for brevity. Note that hyperpolarized spin order may be transferred

from $S_H \leftrightarrow S_{NC}$ when $\omega_H - \Sigma\omega_{NC} \approx J_{NC} - J_{HH}$. At non-zero magnetic fields, the transitions out of the singlet state are amplified by $\Delta\omega_{NC}$, but the $\hat{S} \cdot \hat{L}$ singlet spin order is preserved at zero magnetic field ($\omega_N = \omega_C$), as the Hamiltonian subspace simplifies to:

$$\hat{\mathcal{H}} = \begin{pmatrix} & |T_H^+ T_{NC}^0\rangle & |T_H^0 T_{NC}^+\rangle & |T_H^+ S_{NC}\rangle & |S_H T_{NC}^+\rangle \\ \langle T_H^+ T_{NC}^0| & 0 & \Sigma J_{NH} & -\Delta J_{NC} & -\Sigma J_{NC} \\ \langle T_H^0 T_{NC}^+| & \Sigma J_{NC} & 0 & -\Delta J_{NC} & \Sigma J_{NC} \\ \langle T_H^+ S_{NC}| & -\Delta J_{NC} & -\Delta J_{NC} & -J_{NC} & \Delta J_{NC} \\ \langle S_H T_{NC}^+| & -\Sigma J_{NC} & \Sigma J_{NC} & \Delta J_{NC} & -J_{HH} \end{pmatrix} \tag{5.4}$$

There is still a non-zero transition dipole moment between $S_H \leftrightarrow S_{NC}$ spin orders, which permits evolution of the parahydrogen singlet into a singlet between the heteronuclei. At zero magnetic field, another Hamiltonian subspace equally pumps T_{NC}^- spin order simultaneously with this space pumping T_{NC}^+, meaning that no magnetization is generated. Note that this Hamiltonian subspace has no experimentally tunable parameters.

In an effort to extract the coherent hyperpolarization dynamics of heteronuclear singlet states, we experimentally showed that $\hat{S} \cdot \hat{L}$ order could be coherently generated in a coherently pumped SABRE-SHEATH variant that utilizes a zero-field pulse of time t_p interleaved with high magnetic fields (Fig. 55)[140]. In the previous coherently pumped SABRE-SHEATH experiment, the pumped spin order ($\hat{S}_z$) is an eigenstate of delay field B_d, and thus it does not evolve during the inter-pulse delay. In this case, the 'delay' field halts coherent evolution out of the parahydrogen singlet state but also permits evolution of the transverse terms of the $\hat{S} \cdot \hat{L}$ spin order according to

$$\begin{aligned} \langle \hat{S} \cdot \hat{L} \rangle(t) \approx & \left(\hat{S}_x \hat{L}_x + \hat{S}_y \hat{L}_y\right) \cos(\Delta\omega_{NC} t) \\ & + \left(\hat{S}_y \hat{L}_x - \hat{S}_x \hat{L}_y\right) \sin(\Delta\omega_{NC} t) + \hat{S}_z \hat{L}_z \end{aligned} \tag{5.5}$$

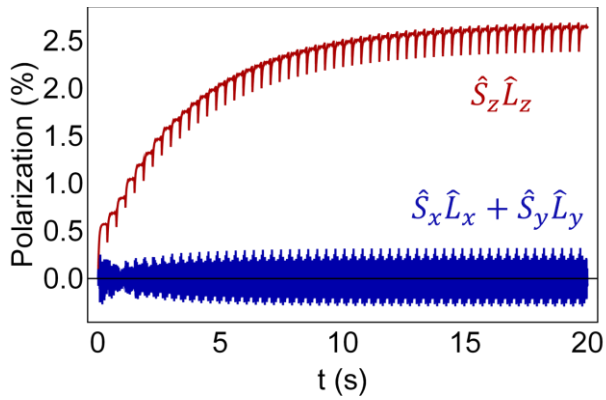

Figure 55: Spin order preservation of heteronuclear singlet. While the longitudinal $\hat{S}_z\hat{L}_z$ terms are preserved at the delay field and may be coherently pumped, the transverse terms of the heteronuclear singlet ($\hat{S}_x\hat{L}_x + \hat{S}_y\hat{L}_y$) lose phase coherence over the course of the experiment due to chemical exchange and do not accumulate hyperpolarized spin order.

As the magnetic field in a SABRE-SHEATH can be very homogeneous, loss of phase coherence due to fluctuating $\Delta\omega_{NC}$ is less of a concern than it would be at high magnetic field. However, the combination of multiple applications of the zero-field pulse generating $\hat{S}\cdot\hat{L}$ spin order and exchange with the catalyst causes the transverse terms of this singlet lose phase coherence, and the system only preserves longitudinal $\hat{S}_z\hat{L}_z$ spin order (Fig. 55). Even so, large signal enhancements were observed for (^{15}N,1-^{13}C)-acetonitrile (Fig. 56). As in the previous coherently pumped X-SABRE experiments, the oscillations arise from the coherent driving of

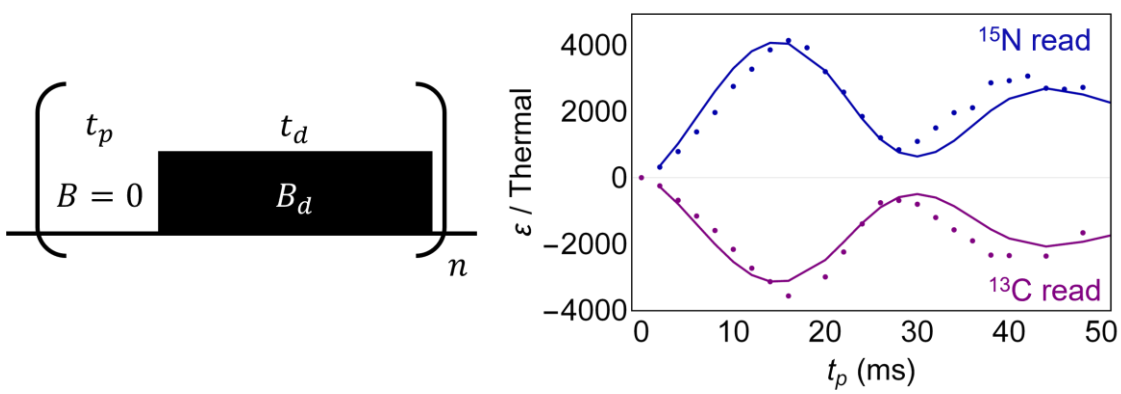

Figure 56: Coherently pumping heteronuclear singlets. A zero-field pulse is applied to the system to coherently drive production of $\hat{S}\cdot\hat{L}$ spin order followed by a high field $B_d = -22.5\ \mu T$ that acts to halt coherent flow of hyperpolarized spin order. Repeating this sequence for an experiment time of 60 seconds permits the coherent hyperpolarization dynamics to be read out in the final signal as a function of t_p. The DMExFR2 simulations (solid lines) were run on a (7+5)Y system parameterized on the (^{15}N,1-^{13}C)-acetonitrile parameters using $k_N = 24\ s^{-1}$, $k_H = 6\ s^{-1}$, and $[Ir]/[S] = 1/20$. The experimental data was collected and analyzed by Christian Tanner.

the system. Furthermore, as the heteronulcear singlet is a two-spin order, it may be detected on both the ^{15}N and ^{13}C channels at high magnetic field.

Conveniently, $\hat{S}_z\hat{L}_z$ spin order is an eigenstate of high magnetic field and is detectable in a conventional NMR spectrometer so long as $\omega_S \neq \omega_L$ or if there are inequivalent J-couplings out of the spin pair. This spin order gives rise to anti-phase NMR peaks, which integrate to zero (Fig. 57). However, an asymmetric integration of the NMR spectrum yields signals proportional to the preserved $\hat{S}_z\hat{L}_z$ spin order of the heteronuclear singlet. This is different than a magnitude transform off the spectrum, which will take the modulus of $s(\omega)$ and then integrate the signal. This ensures that noise, which is randomly distributed, does not contribute to the integration. Note that given the opposite gyromagnetic ratios of ^{15}N and ^{13}C that the signals are also oppositely signed. Furthermore, these operations are algebraically orthogonal, which means that they may be applied to the same NMR spectrum to quantify linear combinations of $\hat{S}_z$ and $\hat{S}_z\hat{L}_z$ in the final hyperpolarized signal.

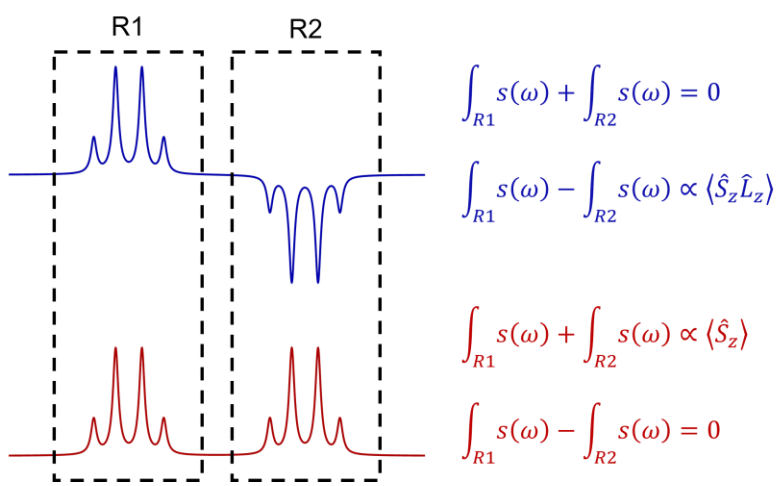

Figure 57: Data analysis for heteronuclear singlet spectra. The NMR spectrum of the ^{15}N spin in (^{15}N,^{13}C)-acetonitrile is shown with polarized $\hat{S}_z\hat{L}_z$ spin order (blue) and $\hat{S}_z$ spin order (red). Dividing the spectrum into two regions, delineated by the spin state of the ^{13}C nucleus, permits an easy interpretation of the spectrum in quantifying the expectation values of magnetization and $\hat{S}_z\hat{L}_z$ spin order. Symmetric integration (normal) will yield a signal proportional to the magnetization, as is conventional in magnetic resonance. Asymmetric integration yields the signal proportional to the $\hat{S}_z\hat{L}_z$ spin order created upon pumping the heteronulcear singlet.

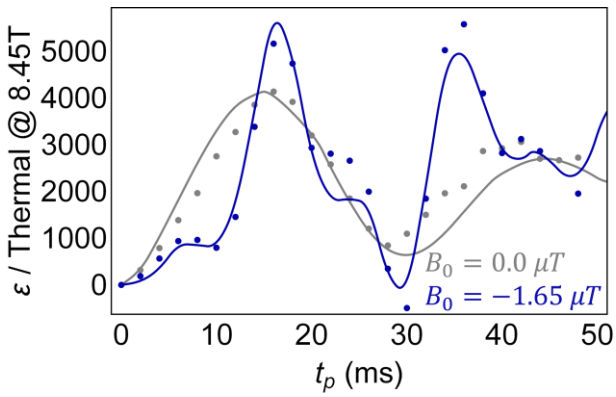

Figure 58: Coherent hyperpolarization dynamics in (^{15}N,^{13}C)-acetonitrile. The coherent hyperpolarization dynamics of the heteronuclear singlet $\hat{S} \cdot \hat{L}$ at zero field are relatively unstructured. The ^{15}N magnetization ($\hat{S}_z$) dynamics at a non-zero field of $B_0 = -1.65\ \mu T$ are much more structured and result in complex dynamics in the coherent SABRE-SHEATH experiment. The experimental data was collected and analyzed by Christian Tanner.

The (^{15}N,1-^{13}C)-acetonitrile system highlighted two interesting points of controlling the coherent hyperpolarization dynamics in X-SABRE. Firstly, while the hyperpolarization dynamics at zero magnetic field are relatively unstructured, the dynamics of this system become extremely structured and complicated at any non-zero field (Fig. 58). This is despite there only being 5 coupled spin-1/2 nuclei in the free-species, which correspond to the two target nuclei (^{15}N, ^{13}C), and the three ^{1}H of the methyl group. Secondly, the Hamiltonian contains a variety of parameters that cannot be experimentally controlled, such as the form of the Hamiltonian at zero magnetic field (eq. 5.4). However, the ability to control the coherent degrees of freedom allows us to manipulate the system in ways similar to conventional NMR at high field. As such, the following sections will examine new methods in approaching ultralow field X-SABRE in an effort to govern the spin dynamics of these systems more finely.

5.2 Ultralow field shaping for control of coherent X-SABRE dynamics

The work done controlling the coherent hyperpolarization dynamics at ultralow magnetic fields[89, 140] essentially introduced the ability to selectively generate evolution of the

hyperpolarization by a specified 'flip angle', in analogy with conventional magnetic resonance. When hyperpolarization is maximized, one essentially permits a full phase-inversion between the initial ($\hat{I}_1 \cdot \hat{I}_2$) and final ($\hat{S}_z$ or $\hat{S} \cdot \hat{L}$) states, corresponding to a π-pulse in the hyperpolarization dynamics. The ability to control the evolution of this inversion permits opportunities to translate techniques from conventional magnetic resonance to further control different aspects of the hyperpolarization dynamics. An interesting application to this problem is highlighted by the zero-field Hamiltonian shown in eq. 5.4, which contains no manipulatable parameters. The only method to control evolution in this Hamiltonian is to reintroduce a magnetic field to halt evolution between certain target states.

Conventional SABRE-SHEATH is performed using a static microTesla magnetic field of $B_0 \approx 1\ \mu T$. However, if the magnetic field is allowed to have both a static component $\langle B_0 \rangle$ and a time-varying component $B(t)$ that is cyclic with a period T and is defined as having $\langle B(t) \rangle = 0$, then the Hamiltonian of a minimal (3+1)Y AA'B ^{15}N SABRE-SHEATH system becomes:

$$\begin{aligned} \hat{\mathcal{H}}(t) = \gamma_H\big(\langle B_0 \rangle + B(t)\big)\big(\hat{I}_{1z} + \hat{I}_{2z}\big) + \gamma_N\big(\langle B_0 \rangle + B(t)\big)\hat{S}_z \\ +2\pi\big(J_{HH}\hat{I}_1 \cdot \hat{I}_2 + J_{NH}\hat{I}_1 \cdot \hat{S}\big) \end{aligned} \tag{5.6}$$

We may rearrange this Hamiltonian such that the first term is proportional to the total spin angular momentum in the z-direction:

$$\begin{aligned} \hat{\mathcal{H}}(t) = \gamma_H\big(\langle B_0 \rangle + B(t)\big)\big(\hat{I}_{1z} + \hat{I}_{2z} + \hat{S}_z\big) + (\gamma_N - \gamma_H)\big(\langle B_0 \rangle + B(t)\big)\hat{S}_z \\ +2\pi\big(J_{HH}\hat{I}_1 \cdot \hat{I}_2 + J_{NH}\hat{I}_1 \cdot \hat{S}\big) \end{aligned} \tag{5.7}$$

The term $\hat{I}_{1z} + \hat{I}_{2z} + \hat{S}_z$ commutes with the rest of the Hamiltonian as well as the target state, $\hat{S}_z$, and thus may be dropped for brevity in the following analysis. Defining $\Delta\gamma_{NH} = \gamma_N - \gamma_H$ gives the Hamiltonian:

$$\hat{\mathcal{H}}(t) = \Delta\gamma_{NH}\big(\langle B_0\rangle + B(t)\big)\hat{S}_z + 2\pi\big(J_{HH}\hat{I}_1 \cdot \hat{I}_2 + J_{NH}\hat{I}_1 \cdot \hat{S}\big) \tag{5.8}$$

Note that $B(t) = 0$ returns the SABRE-SHEATH Hamiltonian in the form with the total z-angular momentum dropped. To assess the dynamics of this time-dependent Hamiltonian, we will again employ average Hamiltonian theory. When the period T is much faster than any other term in the Hamiltonian at any time, only the lowest-order average Hamiltonian $\bar{\mathcal{H}}^{(0)}$ gives:

$$\begin{aligned} \bar{\mathcal{H}}^{(0)} &= \frac{1}{T}\int_0^T dt'\, \hat{\mathcal{H}}(t') \\ &= \Delta\gamma_{NH}\langle B_0\rangle\hat{S}_z + 2\pi\big(J_{HH}\hat{I}_1 \cdot \hat{I}_2 + J_{NH}\hat{I}_1 \cdot \hat{S}\big) \end{aligned} \tag{5.9}$$

This Hamiltonian is identical to the SABRE-SHEATH Hamiltonian when the total z-angular momentum is dropped. Perhaps the simplest implementation of this is when $B(t)$ is a square wave with an amplitude B. For this condition, $T \ll (\Delta\gamma_{NH}B)^{-1}$ for the above assumptions to hold. While the effective magnetic field is simply $\langle B_0\rangle$, the instantaneous magnetic field for this case is $\langle B_0\rangle \pm B$. This is important as nuclear spin relaxation in the liquid state is determined by picosecond rotational dynamics, thus only the instantaneous magnetic field will dictate relaxation rates. Using this method permits experimental control over the relaxation rate of various nuclei, which can be important when attempting to maximize the hyperpolarized signal.

There is an experimental limit on how rapidly a square wave may be generated in an electromagnet that is coupled to the maximum magnitude of the magnetic field produced by the solenoid. For a solenoid of length ℓ, area A, number of turns of wire N, resistance R, with a voltage across the solenoid V, the magnetic field produced is approximately:

$$B = \frac{\mu_0 N V}{\ell R} \tag{5.10}$$

Coupled to this magnetic field is the inductance of the coil:

$$L = \frac{\mu_0 N^2 A}{\ell} \tag{5.11}$$

The risetime of this coil is then proportional to:

$$\tau_R = \frac{R}{L} = \frac{R\ell}{\mu_0 N^2 A} \tag{5.12}$$

While the magnetic field of the solenoid is linearly proportional to the number of loops of wire used to wrap the solenoid, the inductance is quadratically proportional to N. As such, real coils have a finite risetime of the square wave. However, for $\tau_R \ll T \ll (\Delta\gamma_{NH} B)^{-1}$, all the assumptions made to this point are adequate. Typically, there are several experimental factors

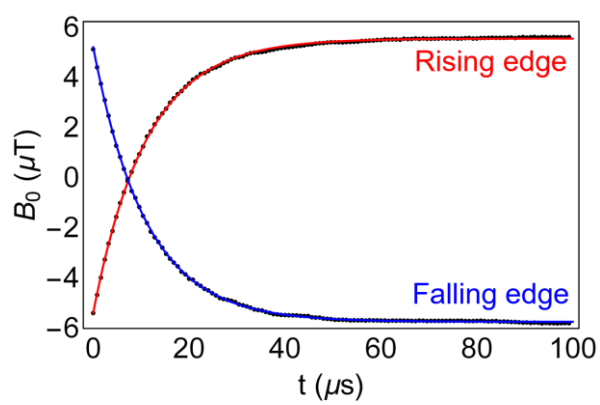

Figure 59: Calibration of field and risetime of an electromagnet. Rising and falling edges of a bipolar square wave oscillating at 5 kHz ($T = 100\ \mu s$). For this magnet, $\tau_R \approx 11\ \mu s$ by measuring the voltage-drop across a known resistor and $B/I \approx 600\ \mu T/A$. The magnetic field produced by this coil can be shaped on timescales much faster than $(\Delta\gamma_{NH} B)^{-1}$.

that arise when constructing an electromagnet, so many of these parameters are simply measured (Fig. 59). Even with the finite risetimes, it is entirely possible to build electromagnets that satisfy $\tau_R \ll T \ll (\Delta\gamma_{NH}B)^{-1}$, meaning that the magnetic field may be shaped faster than the coherent dynamics of the system evolve. Naturally a square-wave is a composition of many different frequency components, and waveform distortion may be avoided by using a sinusoidal waveform with a single frequency component.

The idea of utilizing a shaped magnetic field was experimentally validated by comparing the hyperpolarization of ^{15}N-pyridine using a SABRE-SHEATH field of $B_0 = -1.1\ \mu T$ to a square-wave excitation of the hyperpolarization using $\langle B_0 \rangle = -1.1\ \mu T$, $B \approx 20\ \mu T$, and a period of $T = 133\ \mu s$ (Fig. 60). Under these conditions, $|(\Delta\gamma_{NH}B)^{-1}| = 1066\ \mu s$ and the limit $T \ll (\Delta\gamma_{NH}B)^{-1}$ is satisfied. Under these conditions, there is negligible difference in the hyperpolarization signal between when the magnetic field is either

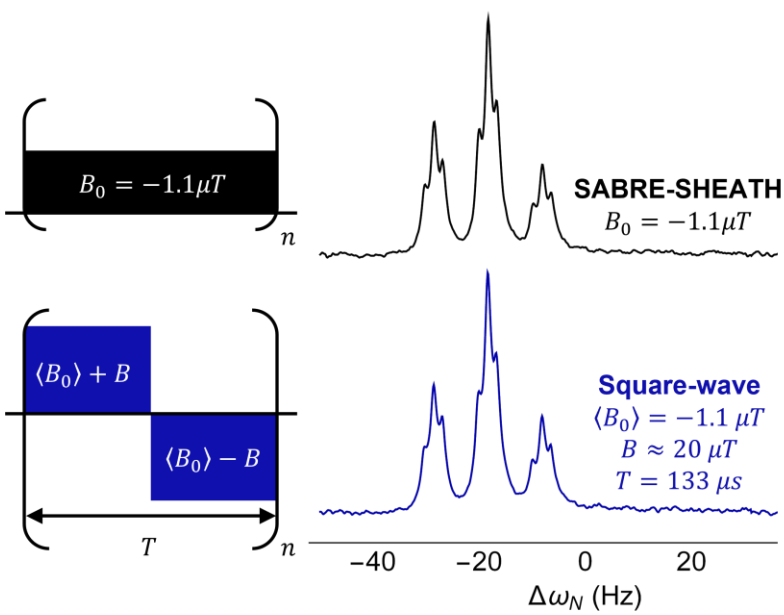

Figure 60: Initial experiments using square-wave excitation of SABRE-SHEATH. Top. SABRE-SHEATH hyperpolarization ^{15}N-pyridine using $B_0 = -1.1\ \mu T$ for an experimental duration of 60 s. **Bottom.** Square-wave excitation of SABRE-SHEATH using $\langle B_0 \rangle = -1.1\ \mu T$, $B \approx 20\ \mu T$, and a square wave period of $T = 133\ \mu s$ (7.5 kHz). The signal obtained using this experiment is nearly identical to the signal obtained by SABRE-SHEATH. $[Ir]/[S] = 0.14$ for these experiments.

instantaneously or on-average at the optimal field condition but varying the magnitude of the field can be varied to control the T_1 of the system, and potentially increase polarization.

While the coherent hyperpolarization dynamics present for SABRE-SHEATH are preserved by using a rapid square-wave excitation, the dynamics become very interesting when the condition $T \ll (\Delta\gamma_{NH}B)^{-1}$ is not met. We will no longer restrict the period T, complicating the convergence of the average Hamiltonian. To circumvent having to calculate high-order terms in the Magnus expansion, we will use a toggling frame to accelerate the average Hamiltonian convergence. For flexibility, we will define

$$\Delta\gamma_{NH}B(t) \equiv \Delta\omega_{NH}w(t), \tag{5.13}$$

where $w(t)$ is generalized waveform that is periodic over T, is amplitude-normalized (maximum amplitude of one), and has a zero-average. We may additionally assume that the waveform is antisymmetric about $T/2$, which will simplify the following analysis. This lets us define a toggling frame using the time-varying component of the magnetic field as the reference frame, which is defined by the transformation:

$$\mathcal{H}(t) = \exp\left(-i\Delta\omega_{NH}\hat{S}_z\int_0^t dt'w(t')\right)\widehat{\mathcal{H}}\exp\left(i\Delta\omega_{NH}\hat{S}_z\int_0^t dt'w(t')\right) \tag{5.14}$$

For brevity, we will introduce the notation

$$\Theta(t) = \Delta\omega_{NH}\int_0^t dt'w(t') \tag{5.15}$$

As the time-varying flip angle of the toggling frame, which simplifies eq. 5.14 to:

$$\mathcal{H}(t) = \exp\left(-i\hat{S}_z\Theta(t)\right)\widehat{\mathcal{H}}\exp\left(i\hat{S}_z\Theta(t)\right) \tag{5.16}$$

Remembering that formally, the rotating frame transformation is applied to the evolving density matrix, which at the end of a period T is given by:

$$\hat{\rho}(T) = e^{i\hat{S}_z\Theta(T)} \exp\left(-i\int_0^T dt\,\mathcal{H}(t)\right)\hat{\rho}_0 \exp\left(i\int_0^T dt\,\mathcal{H}(t)\right)e^{-i\hat{S}_z\Theta(T)} \tag{5.17}$$

Typically, we aim to design sequences and toggling frames such that

$$e^{i\hat{S}_z\Theta(T)} = \hat{E}, \tag{5.18}$$

to simplify analysis of the average Hamiltonian, but this does not necessarily need to be the case. The toggling frame Hamiltonian is then given explicitly by:

$$\begin{aligned}\mathcal{H}(t) = \langle\Delta\omega_{NH}\rangle\hat{S}_z + 2\pi\left(J_{HH}\hat{I}_1\cdot\hat{I}_2 + J_{NH}\hat{I}_{1z}\hat{S}_z\right)\\ +2\pi J_{NH}\begin{pmatrix}\cos\left(\Theta(t)\right)\left(\hat{I}_{1x}\hat{S}_x + \hat{I}_{1y}\hat{S}_y\right)\\ +\sin\left(\Theta(t)\right)\left(\hat{I}_{1y}\hat{S}_x - \hat{I}_{1x}\hat{S}_y\right)\end{pmatrix}\end{aligned} \tag{5.19}$$

We have used the definition $\langle\Delta\omega_{NH}\rangle \equiv \Delta\gamma_{NH}\langle B_0\rangle$. Let us examine the form of $\Theta(t)$ for the case described here when $w(t)$ is center antisymmetric with a zero-mean. If we now define $w(t)$ with the form

$$w(t) = \begin{cases} w_1(t) & 0 < t \leq T/2 \\ w_2(t) & T/2 < t \leq T \end{cases} \tag{5.20}$$

where $w_2(t) = -w_1(T/2 - t)$ and generates the anti-symmetry about $T/2$, then we may define $\Theta(t)$ as a piecewise time-dependent function as:

$$\Theta(t) = \Delta\omega_{NH}\begin{cases}\displaystyle\int_0^t dt' w_1(t') & 0 < t \leq T/2 \\ \displaystyle\int_0^{T/2} dt' w_1(t') + \int_0^{t-T/2} dt' w_2\left(t' + \frac{T}{2}\right) & T/2 < t \leq T\end{cases} \tag{5.21}$$

Utilizing a center-antisymmetric waveform ensures that at the end of the period T that $\Theta(T) = 0$ and thus eq. 5.18 is satisfied. Using the square-wave for example:

$$w(t) = \begin{cases} 1 & 0 < t \leq T/2 \\ -1 & T/2 < t \leq T \end{cases}$$
$$\Theta(t) = \Delta\omega_{NH} \begin{cases} t & 0 < t \leq T/2 \\ T - t & T/2 < t \leq T \end{cases} \tag{5.22}$$

Similarly with a sawtooth waveform:

$$w(t) = \begin{cases} \frac{2t}{T} & 0 < t \leq T/2 \\ \frac{2t}{T} - 1 & T/2 < t \leq T \end{cases}$$
$$\Theta(t) = \Delta\omega_{NH} \begin{cases} \frac{t^2}{T} & 0 < t \leq T/2 \\ \frac{t^2}{T} - t & T/2 < t \leq T \end{cases} \tag{5.23}$$

Using the square wave as an example, we may calculate the toggling frame Hamiltonian in a piecewise time-dependent form as:

$$\mathcal{H}(t) = \Delta\omega_{NH}\hat{S}_z + 2\pi\left(J_{HH}\hat{I}_1 \cdot \hat{I}_2 + J_{NH}\hat{I}_{1z}\hat{S}_z\right)$$
$$+2\pi J_{NH} \begin{cases} \begin{pmatrix} \cos(\Delta\omega_{NH}t)\left(\hat{I}_{1x}\hat{S}_x + \hat{I}_{1y}\hat{S}_y\right) \\ +\sin(\Delta\omega_{NH}t)\left(\hat{I}_{1x}\hat{S}_y - \hat{I}_{1y}\hat{S}_x\right) \end{pmatrix} & 0 < t \leq T/2 \\ \begin{pmatrix} \cos\left(\Delta\omega_{NH}(T-t)\right)\left(\hat{I}_{1x}\hat{S}_x + \hat{I}_{1y}\hat{S}_y\right) \\ +\sin\left(\Delta\omega_{NH}(T-t)\right)\left(\hat{I}_{1x}\hat{S}_y - \hat{I}_{1y}\hat{S}_x\right) \end{pmatrix} & T/2 < t \leq T \end{cases} \tag{5.24}$$

Note that when $w(t)$ is antisymmetric about $T/2$ that the first period from $0 < t \leq T/2$ corresponds to a positive-sense rotation of the Hamiltonian on a given trajectory and the second period from $T/2 < t \leq T$ corresponds to a negative-sense rotation along the same trajectory. As such, this lets us simply integrate from $0 < t \leq T/2$, as the integration from $T/2 < t \leq T$ will have the same average. As such, $\bar{\mathcal{H}}^{(0)}$ is given by:

$$\bar{\mathcal{H}}^{(0)} = \frac{1}{T/2}\int_0^{T/2} dt'\, \mathcal{H}(t') \tag{5.25}$$

$$= \Delta\omega_{NH}\hat{S}_z + 2\pi\left(J_{HH}\hat{I}_1 \cdot \hat{I}_2 + J_{NH}\hat{I}_{1z}\hat{S}_z\right)$$

$$+ \frac{2\pi J_{NH}}{T/2}\int_0^{\frac{T}{2}} dt' \begin{pmatrix} \cos(\Delta\omega_{NH}t')\left(\hat{I}_{1x}\hat{S}_x + \hat{I}_{1y}\hat{S}_y\right) \\ + \sin(\Delta\omega_{NH}t')\left(\hat{I}_{1x}\hat{S}_y - \hat{I}_{1y}\hat{S}_x\right) \end{pmatrix}$$

$$= \Delta\omega_{NH}\hat{S}_z + 2\pi\left(J_{HH}\hat{I}_1 \cdot \hat{I}_2 + J_{NH}\hat{I}_{1z}\hat{S}_z\right)$$

$$+2\pi J_{NH}\begin{pmatrix} \frac{\sin(\Delta\omega_{NH}T/2)}{\Delta\omega_{NH}T/2}\left(\hat{I}_{1x}\hat{S}_x + \hat{I}_{1y}\hat{S}_y\right) + \\ \frac{1-\cos(\Delta\omega_{NH}T/2)}{\Delta\omega_{NH}T/2}\left(\hat{I}_{1x}\hat{S}_y - \hat{I}_{1y}\hat{S}_x\right) \end{pmatrix}$$

Equation 5.25 shows that the phase and magnitude of the transverse terms of the J_{NH} coupling may be controlled by altering the period of the square wave (Fig. 61). Note that as $T \to 0$ that the SABRE-SHEATH Hamiltonian is recovered, as is expected in the limit discussed previously. However, as T increases, the amplitude of the J_{NH} terms can be selectively decreased and the relative phase of the J_{NH} coupling may be controlled, and when $\Delta\omega_{NH}T/2$ is integer-valued, these terms average fully to zero. Similarly, the sawtooth gives:

$$\bar{\mathcal{H}}^{(0)} = \Delta\omega_{NH}\hat{S}_z + 2\pi\left(J_{HH}\hat{I}_1 \cdot \hat{I}_2 + J_{NH}\hat{I}_{1z}\hat{S}_z\right)$$

$$+2\pi J_{NH}\begin{pmatrix} \frac{C_F\left(2\sqrt{\Delta\omega_{NH}T}\right)}{2\sqrt{\Delta\omega_{NH}T}}\left(\hat{I}_{1x}\hat{S}_x + \hat{I}_{1y}\hat{S}_y\right) + \\ \frac{S_F\left(2\sqrt{\Delta\omega_{NH}T}\right)}{2\sqrt{\Delta\omega_{NH}T}}\left(\hat{I}_{1x}\hat{S}_y - \hat{I}_{1y}\hat{S}_x\right) \end{pmatrix} \tag{5.26}$$

The functions $C_F(t)$ and $S_F(t)$ are the Fresnel integrals, which are defined by:

$$C_F(z) = \int_0^z dt \cos\left(\frac{\pi t^2}{2}\right) \tag{5.27}$$

$$S_F(z) = \int_0^z dt \sin\left(\frac{\pi t^2}{2}\right) \tag{5.28}$$

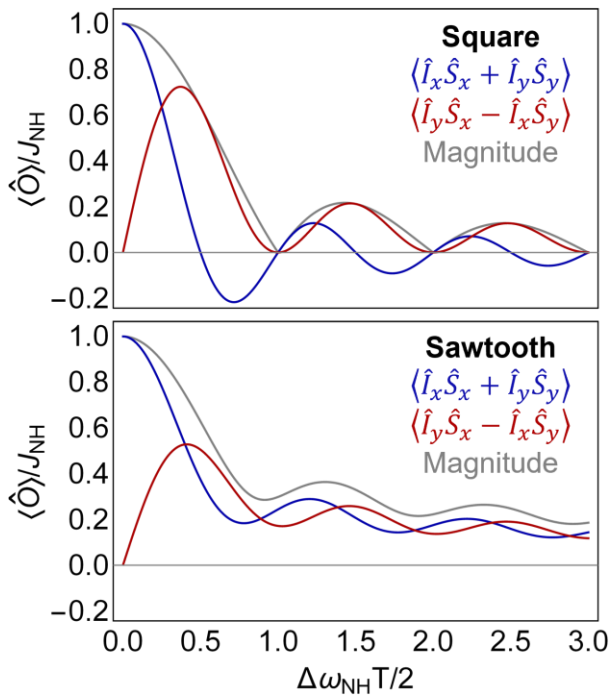

Figure 61: Operator magnitudes under different waveforms. For square-wave excitation, the $\hat{I}_x\hat{S}_x + \hat{I}_y\hat{S}_y$ term of the J_{NH} coupling can be fully converted into a $\hat{I}_y\hat{S}_x - \hat{I}_x\hat{S}_y$ term. When $\Delta\omega_{NH}T/2$ is an integer value, these terms fully average to zero. When a sawtooth waveform is used, the $\hat{I}_x\hat{S}_x + \hat{I}_y\hat{S}_y$ term cannot be fully converted into a $\hat{I}_y\hat{S}_x - \hat{I}_x\hat{S}_y$, meaning that there are also no nodes where the transverse terms of the J_{NH} coupling average to zero.

Importantly, while the transverse terms of the J_{NH} coupling may be fully averaged to zero in the case of the square wave, this is not the case in the sawtooth wave. Let us examine the case of $\Delta\omega_{NH}T/2 = 1/2$ as an example, which corresponds to a π phase rotation of the transverse coupling terms trajectory, or $\hat{I}_x\hat{S}_x + \hat{I}_y\hat{S}_y \rightarrow -(\hat{I}_x\hat{S}_x + \hat{I}_y\hat{S}_y)$. For the square wave, the $\hat{I}_x\hat{S}_x + \hat{I}_y\hat{S}_y$ spend an equivalent amount of time being positively-valued for every point on the trajectory as they do being negatively valued, meaning that on average the $\hat{I}_x\hat{S}_x + \hat{I}_y\hat{S}_y$ terms average to zero, thus leading to the presence of nodes. However, while a sawtooth wave that satisfies $\Delta\omega_{NH}T/2 = 1/2$ makes the same transformation, the $\hat{I}_x\hat{S}_x + \hat{I}_y\hat{S}_y$ terms spend more time in the positively-valued region of the trajectory than they do in the negatively-valued region of the trajectory. As such, there is an incomplete averaging of the terms and $\hat{I}_x\hat{S}_x +$

$\hat{I}_y\hat{S}_y$ has a non-zero value at $\Delta\omega_{NH}T/2 = 1/2$. By extension, this also means that the nodes that appear when using a square wave that are not present when using a sawtooth waveform.

Using a longer square-wave period T also showed promising results for generating hyperpolarization (Fig. 72). Here, we used the conditions where $\Delta\omega_{NH}T/2 \approx 1$ (but not equal), which according to eq. 5.26 attenuates the magnitude of the transverse terms of the J_{NH} coupling. Even still, nearly identical hyperpolarization was observed as compared to the comparable signal obtained by SABRE-SHEATH. These experiments were performed on ^{15}N-pyridine as the hyperpolarization target and are in the process of being extended[144].

The opportunity to generate phase-coherent J-couplings for X-SABRE excitation opens the possibility to control the coherent hyperpolarization dynamics using methods derived from conventional high field NMR, as was done with the broadband X-SABRE experiments[130] in Chapter 4. We will introduce the notation

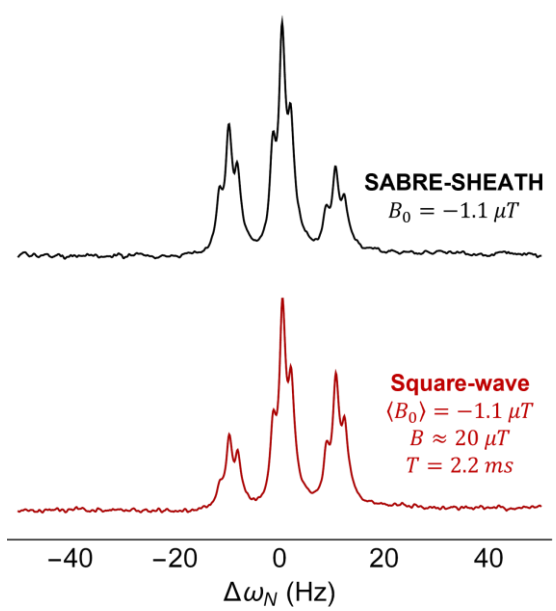

Figure 62: J_{NH} attenuation for SABRE-SHEATH. Using a square-wave excitation parameterized for $\Delta\omega_{NH}T/2 \approx 1$ (red) reduces the magnitude of the J_{NH} coupling but still generates nearly identical X-SABRE hyperpolarization to conventional SABRE-SHEATH (black). Notably, if $\Delta\omega_{NH}T/2 = 1$ then there would be no hyperpolarization.

$$M_0 = \frac{\sin(\Delta\omega_{NH}T/2)}{\Delta\omega_{NH}T/2}; N_0 = \frac{1-\cos(\Delta\omega_{NH}T/2)}{\Delta\omega_{NH}T/2} \tag{5.29}$$

to delineate the two phases of the transverse J_{NH} coupling terms. Perhaps the simplest means by which phase-coherent excitation may be performed at ultralow magnetic field is to combine the use of M_0 and N_0. We may look again to the Taylor series expansion of the density matrix to identify spin operator pathways by which $\hat{S}_z$ spin order is produced. For the SABRE-SHEATH case, there are a large number of terms that arise, which may clutter analysis. However, a graphical representation of this process aids in the interpretation of the results, as previously demonstrated. We find that magnetization is generated in SABRE-SHEATH after four commutations with the Hamiltonian in the order $J_{NH} \rightarrow J_{HH} \rightarrow \Delta\omega_{NH} \rightarrow J_{NH}$ or in the order $J_{NH} \rightarrow \Delta\omega_{NH} \rightarrow J_{HH} \rightarrow J_{NH}$ as these pathways commute (Fig. 63). However, two of the steps in this spin operator pathway, namely evolution under J_{NH} and $\Delta\omega_{NH}$, may be concatenated by instead permitting evolution under the operator that results from the commutation of these two terms, which is $i[\hat{S}_z, \hat{I}_{1x}\hat{S}_x + \hat{I}_{1y}\hat{S}_y] = \hat{I}_{1x}\hat{S}_y - \hat{I}_{1y}\hat{S}_x$. As such, $\hat{S}_z$

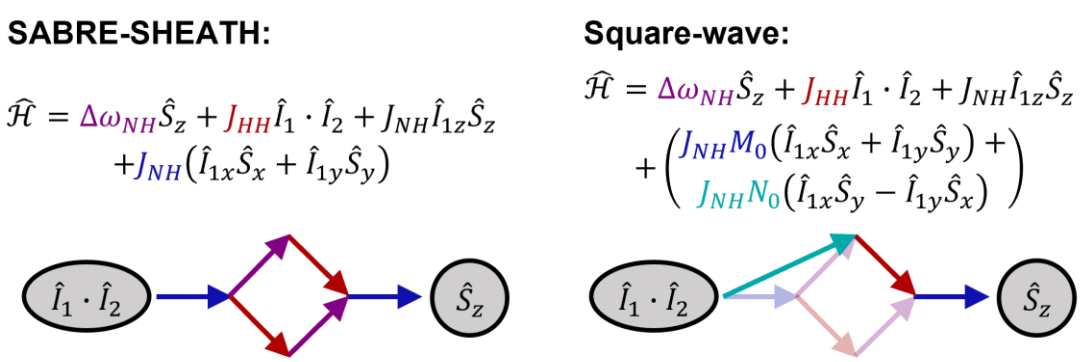

Figure 63: Spin operator pathways for SABRE-SHEATH and square-wave excitation. $\hat{S}_z$ spin order is produced in the fourth derivative with the SABRE-SHEATH Hamiltonian following the diagrammatic spin operator pathway shown here. The evolution under J_{NH} and $\Delta\omega_{NH}$ may be concatenated by evolving under a single operator that results from the commutation of the J_{NH} and $\Delta\omega_{NH}$ term $i[\hat{S}_z, \hat{I}_{1x}\hat{S}_x + \hat{I}_y\hat{S}_y] = \hat{I}_{1x}\hat{S}_y - \hat{I}_{1y}\hat{S}_x$, or in other words the N_0 term that arises from the square wave at $\Delta\omega_{NH}T/2 = 1/2$. The spin operator pathway for the square wave-excitation can generate $\hat{S}_z$ spin order in the third derivative by using a combination of the M_0 and N_0 terms generated by square-wave excitation.

spin order may be generated by exciting the $J_{NH}N_0 \rightarrow J_{HH} \rightarrow J_{NH}M_0$ coherence pathway. Perhaps the simplest way to generate excitation of this sequence is to apply a square wave that selects for only the $N_0(\hat{I}_y\hat{S}_x - \hat{I}_x\hat{S}_y)$ term ($\Delta\omega_{NH}T/2 = 1/2$) and then turn off the magnetic field to permit evolution under M_0 to select for the $\hat{I}_{1x}\hat{S}_x + \hat{I}_{1y}\hat{S}_y$, noting that J_{HH} acts at all time as $\hat{I}_1 \cdot \hat{I}_2$ is a zero-rank tensor. While this experiment could theoretically generate hyperpolarization at zero magnetic field, as the coherence pathway is not dependent on $\Delta\omega_{NH}$, repeated application of this sequence would essentially generate a train of $N_0 \rightarrow M_0 \rightarrow N_0 \rightarrow \cdots$ and the reverse time-ordering of the phase-shifted terms will prohibit generation of magnetization at zero field. As such, a non-zero field must be introduced to break this symmetry and pump a specific sign of magnetization.

Here we examined the performance of this experiment using the DMExFR2 simulations. All of the following simulations were calculated on a truncated (3+1)Y ^{15}N-acetonitrile system using $k_N = 24\ s^{-1}$, $k_H = 9\ s^{-1}$, and $[Ir]/[S] = 1/20$. We find that

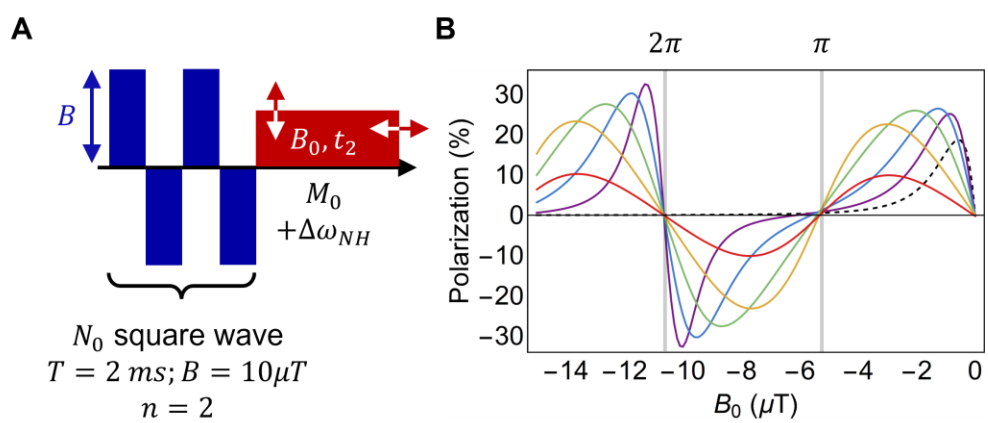

Figure 64: Phase coherent excitation of ultralow field X-SABRE. A. A N_0 square wave selectively generates $\hat{I}_{1y}\hat{S}_x - \hat{I}_{1x}\hat{S}_y$ repeated twice ($n = 2$) followed by a static magnetic field that generates the conventional $\hat{I}_{1x}\hat{S}_x + \hat{I}_{1y}\hat{S}_y$ J_{NH} term permits phase-coherent generation of X-SABRE hyperpolarization. The average magnetic field $\langle B_0 \rangle = 0\ \mu T$. **B.** The offset field B_0 generates the necessary symmetry breaking to pump magnetization with this pulse sequence compared to the SABRE-SHEATH field profile (black). The number of N_0 loops was varied between $n = 1$ (purple), $n = 2$ (blue), $n = 4$ (green), $n = 8$ (yellow), and $n = 16$ (red). Hyperpolarization recurs at evolution flip angles centered at $\Delta\omega_{NH}t_2 = 2\pi$ in a fashion similar to two-state SABRE.

phase-coherent generation of X-SABRE hyperpolarization is possible using this pulse sequence (Fig. 64). Scanning the offset field of the M_0 portion of the sequence (red) shows that hyperpolarization is generated at ultralow magnetic fields, similar to SABRE-SHEATH, and also recurs when the phase evolution is offset from $\Delta\omega_{NH}t_2 = 2\pi m$ in a fashion similar to the Two-State SABRE experiment[145]. Under these conditions, $e^{i\hat{S}_z\Theta(T)} \neq \hat{E}$ except for conditions when $\Delta\gamma_{NH}B_0t_2 \approx 2\pi$, giving rise to refocused sidebands. Interestingly, the field required to generate hyperpolarization is approximately 40% larger each time the number of loops of the N_0 square wave is doubled. This may be interpreted as a phase-evolution matching between the N_0 and M_0 portions of this experiment. Using the exact parameters for the simulations calculated here, we find that the attenuation factor during N_0 portion is:

$$J_{NH}N_0 \approx 0.67J_{NH} \tag{5.30}$$

Thus, doubling the evolution time permitted under $\hat{I}_{1y}\hat{S}_x - \hat{I}_{1x}\hat{S}_y$ term requires only approximately 40% more phase evolution under $\Delta\omega_{NH}$ to refocus the coupling.

As n is increased, the field profile noticeably broadens, making hyperpolarization naturally less sensitive to field inhomogeneities (Fig. 65). This was tested by comparing the performance of $n = 1$ and $n = 4$ N_0 square waves in both homogeneous and inhomogeneous magnetic fields. While hyperpolarization in the $n = 1$ case is notably larger than that obtained by the $n = 4$ case, the narrower resonances make this experiment more susceptible to field inhomogeneities. Even $0.05B_0$ static inhomogeneities greatly reduce the performance of the resonance near $B_0 = -32\ \mu T$. In comparison, the sequence using $n = 4$ loops of the square wave is significantly less sensitive to field inhomogeneities. It should be mentioned that while a 5% inhomogeneity seems easily obtainable, it is relatively easy to build solenoids that have

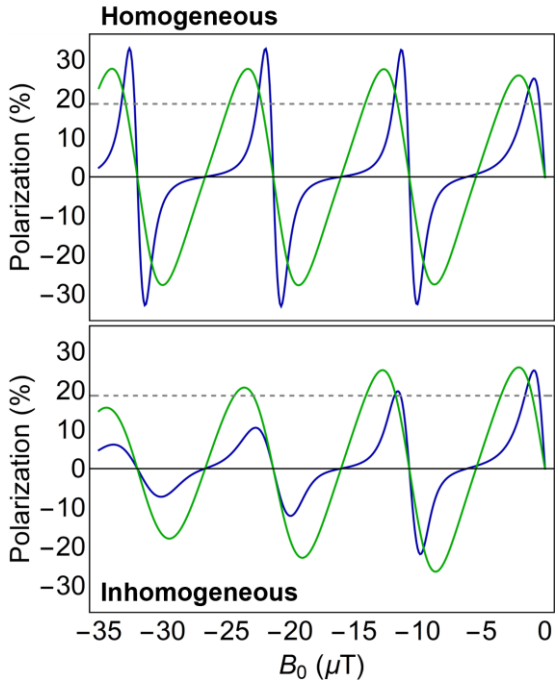

Figure 65: Hyperpolarization using phase coherent excitation in an inhomogeneous field. Gray line indicates maximum SABRE-SHEATH signal. A $n = 1$ (blue) and $n = 4$ (green) N_0 square wave was applied in either a homogeneous magnetic field (top) or using $B_{inhom} = 0.05B_0$ static inhomogeneity. While the performance from the using $n = 1$ rapidly deteriorates with inhomogeneities, the $n = 4$ sequence is more robust to these inhomogeneities.

extremely high homogeneities. There have been multiple demonstrations[144, 145] of cycling $\Delta\omega_{NH}$ many times without any deterioration in signal.

In addition to the sensitivity to the magnetic field, it is also interesting to examine the performance of these pulse sequences to variations in the exchange rate (Fig. 66). In the limit of slow exchange, $n = 1$ loops of the N_0 square wave maximizes hyperpolarization at the sideband centered at $\Delta\omega_{NH}t_2 = 2\pi$ and the performance falls off as n is increased. However, in the limit of fast exchange, hyperpolarization is maximized when $n = 2$ loops are used despite this being a pulse sequence that is twice as long. In this limit, more phase evolution under the $\hat{I}_{1y}\hat{S}_x - \hat{I}_{1x}\hat{S}_y$ term is required over a single application of the square wave, which results in the sequence optimizing at a larger n. However, this sequence does not perform significantly better than SABRE-SHEATH in the limit of fast exchange, although the cycle

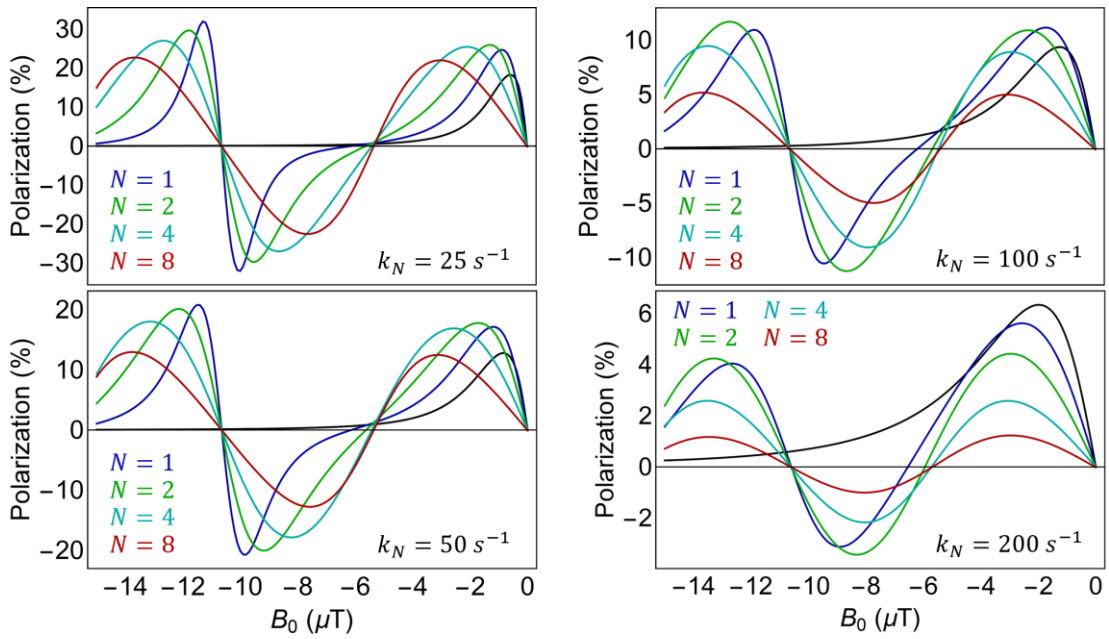

Figure 66: Exchange rate dependence for the phase-coherent sequence. For all simulations, the number of loops was varied (indicated by color) and the field profile was calculated using $t_2 = 2\ ms$ delays between each application of the N_0 loops. For the N_0 square wave, $B = 10\ \mu T$ and $T = 2\ ms$. The SABRE-SHEATH profile for each exchange rate is also shown for reference.

time of the pulse sequence may be decreased by increasing the magnetic field strengths and hence decreasing the square wave periods to facilitate more rapid exchanging ligands (Fig. 67). It is critical to note that the large hyperpolarization that is being predicted by the simulations is due to the fact that pure parahydrogen is assumed in these calculations and is rapidly exchanging with the SABRE system ($k_H = 9\ s^{-1}$). While these conditions are unlikely in conventional X-SABRE experiments, they are potentially feasible in a supercritical X- SABRE experiment where the parahydrogen fraction can exceed 10%. Still, these simulations indicate that developing phase-coherent excitation schemes for ultralow field X-SABRE is entirely possible.

In addition to center-antisymmetric waveforms, it is also interesting to explore the dynamics when the waveform is not center-antisymmetric. For this case, we will remove the constraint that $\langle B(t) \rangle = 0$ and will instead define $\langle B(t) \rangle = \delta B_0$, which will be represented

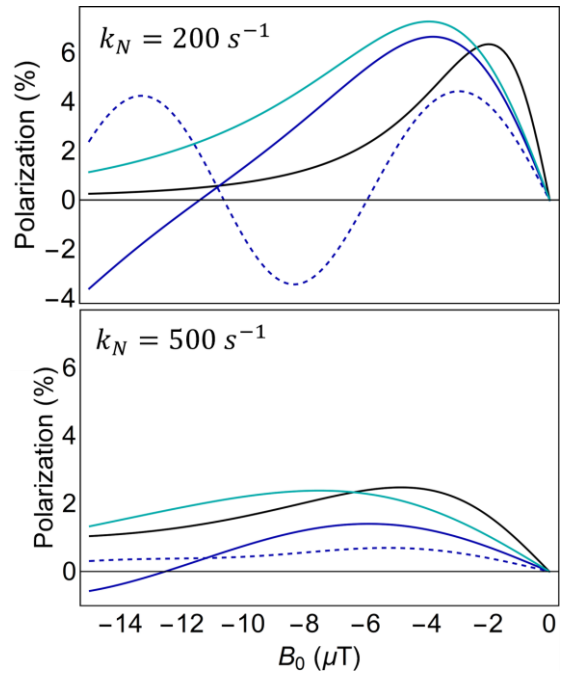

Figure 67: Reoptimizing phase-coherent ultralow field sequence for fast exchange. The cycle time of the experiment may be decreased by increasing the magnetic field of the square wave. Here, we show hyperpolarization using $T = 2\ ms$ periods (dashed blue), $T = 1\ ms$ periods (blue), and $T = 0.5\ ms$ periods (cyan) for an $n = 2$ N_0-selective square wave. The SABRE-SHEATH hyperpolarization under these conditions is shown in black.

by $\delta\omega_{NH}$ when converted to a frequency. This case is best discussed with an illustrative example using an asymmetrically timed square-wave defined as:

$$w(t) = \begin{cases} -1 & 0 < t \leq \tau_1 \\ +1 & \tau_1 < t \leq T \end{cases}$$
$$\Theta(t) = (\Delta\omega_{NH} + \delta\omega_{NH}) \begin{cases} -t & 0 < t \leq \tau_1 \\ t - 2\tau_1 & \tau_1 < t \leq T \end{cases} \tag{5.31}$$

It will be beneficial to introduce the notation $T - \tau_1 = \tau_2$. The toggling frame Hamiltonian is then given by:

$$\bar{\mathcal{H}}^{(0)} = \hat{U}^\dagger \frac{1}{T} \int_0^T dt'\, \mathcal{H}(t')\, \hat{U} = \hat{U}^\dagger \frac{1}{T} \left(\int_0^{\tau_1} dt'\, \mathcal{H}(t') + \int_{\tau_1}^T dt'\, \mathcal{H}(t') \right) \hat{U}$$
$$= (\Delta\omega_{NH} + \delta\omega_{NH}) \hat{S}_z + 2\pi \left(J_{HH} \hat{I}_1 \cdot \hat{I}_2 + J_{NH} \hat{I}_{1z} \hat{S}_z \right) \tag{5.32}$$

$$+\frac{2\pi J_{NH}}{T}\int_0^{\tau_1} dt' \begin{pmatrix} \cos(-\Delta\omega_{NH}t')\,\hat{U}^\dagger\big(\hat{I}_{1x}\hat{S}_x+\hat{I}_{1y}\hat{S}_y\big)\hat{U} \\ +\sin(-\Delta\omega_{NH}t')\,\hat{U}^\dagger\big(\hat{I}_{1x}\hat{S}_y-\hat{I}_{1y}\hat{S}_x\big)\hat{U} \end{pmatrix}$$

$$+\frac{2\pi J_{NH}}{T}\int_{\tau_1}^{T} dt' \begin{pmatrix} \cos\big(\Delta\omega_{NH}(t'-2\tau_1)\big)\,\hat{U}^\dagger\big(\hat{I}_{1x}\hat{S}_x+\hat{I}_{1y}\hat{S}_y\big)\hat{U} \\ +\sin\big(\Delta\omega_{NH}(t'-2\tau_1)\big)\,\hat{U}^\dagger\big(\hat{I}_{1x}\hat{S}_y-\hat{I}_{1y}\hat{S}_x\big)\hat{U} \end{pmatrix}$$

$$=(\Delta\omega_{NH}+\delta\omega_{NH})\hat{S}_z+2\pi\big(J_{HH}\hat{I}_1\cdot\hat{I}_2+J_{NH}\hat{I}_{1z}\hat{S}_z\big)$$

$$+2\pi J_{NH}\begin{pmatrix} \dfrac{\sin(\Delta\omega_{NH}\tau_1)}{\Delta\omega_{NH}T}+ \\ \dfrac{\sin\big(\Delta\omega_{NH}(\tau_2-\tau_1)\big)+\sin(\Delta\omega_{NH}\tau_1)}{\Delta\omega_{NH}T} \end{pmatrix}\hat{U}^\dagger\begin{pmatrix} \hat{I}_{1x}\hat{S}_x \\ +\hat{I}_{1y}\hat{S}_y \end{pmatrix}\hat{U}$$

$$+2\pi J_{NH}\begin{pmatrix} \dfrac{\cos(\Delta\omega_{NH}\tau_1)-1}{\Delta\omega_{NH}T}- \\ \dfrac{\cos\big(\Delta\omega_{NH}(\tau_2-\tau_1)\big)-\cos(\Delta\omega_{NH}\tau_1)}{\Delta\omega_{NH}T} \end{pmatrix}\hat{U}^\dagger\begin{pmatrix} \hat{I}_{1x}\hat{S}_y \\ -\hat{I}_{1y}\hat{S}_x \end{pmatrix}\hat{U}$$

In the limit when $\tau_2=\tau_1$, the center-antisymmetric square wave solution is recovered. Importantly, notice the additional factor of $\delta\omega_{NH}$ that is appended to the Zeeman term to account for the non-zero field average of the square wave. To analyze this result, we may define an asymmetry parameter

$$\eta=\frac{(\tau_2-\tau_1)}{T}, \tag{5.33}$$

which indicates the relative degree of waveform asymmetry and is analogous to the duty cycle. Calculating the magnitude of the transverse J_{NH} coupling terms given by equation 5.32 highlights an interesting feature of the asymmetrically-timed square wave: the nodes that are present for the symmetrically-timed square wave disappear at certain values of η (Fig. 68).

In the limit where $\Delta\omega_{NH}T/2\ll 1$, the phase and magnitude of the transverse J_{NH} coupling terms can be preserved, but the $\delta\omega_{NH}$ term will still be present. Importantly, the $\Delta\omega_{NH}$ term controlled by the static magnetic field will act to counter-balance $\delta\omega_{NH}$ such that

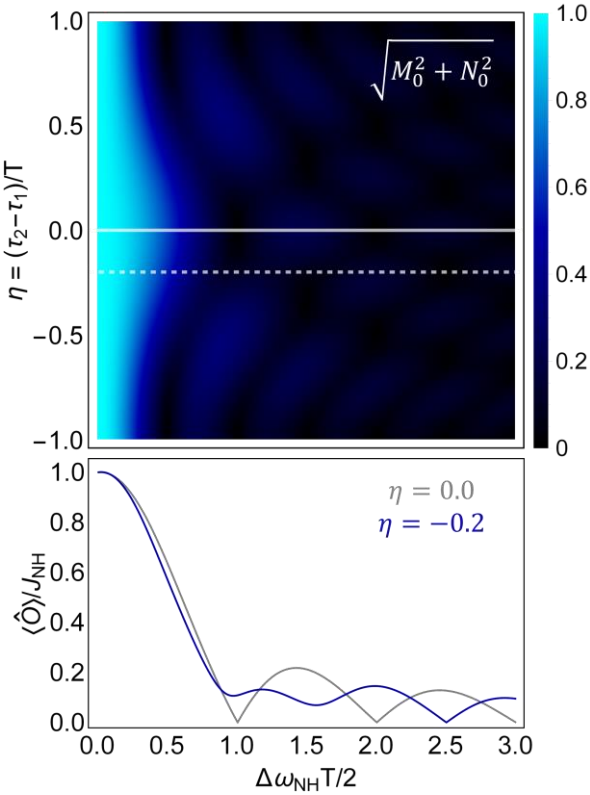

Figure 68: Magnitude of transverse J_{NH} coupling terms using an asymmetric square wave. While the magnitude of the transverse J_{NH} terms is invariant to the sign of η, the sign of N_0 is dependent on η. At certain values of η, the regular nodal structure observed at $\eta = 0.0$ (the symmetrically-timed square wave) disappear. However, this sequence does still have nodes that appear for non-zero values of η at $\Delta\omega_{NH}T/2 = |1/2\eta|$.

the center of the X-SABRE resonance is still at approximately zero (average) field. This was demonstrated experimentally using $\eta = 0.3$ and $\eta = 0.4$ asymmetrically-timed square waves and comparing to the traditional SABRE-SHEATH resonance (Fig. 69). For these experiments, $\Delta\omega_{NH}T/2 = 0.04$, meaning that the magnitude and phase of the transverse J_{NH} couplings were preserved to high fidelity. We found that shifts in the center of the X-SABRE resonance could be readily observed and even generated signals using $\eta = 0.4$ that were approximately 7% larger than the largest SABRE-SHEATH signal. This could lead to the ability to generate ultralow field X-SABRE hyperpolarization without a μ-metal shield if the residual field $\delta B \approx -B_{Earth}$. Conveniently, the Earth's magnetic field is relatively homogeneous, and one would only have to compensate for transverse components of the

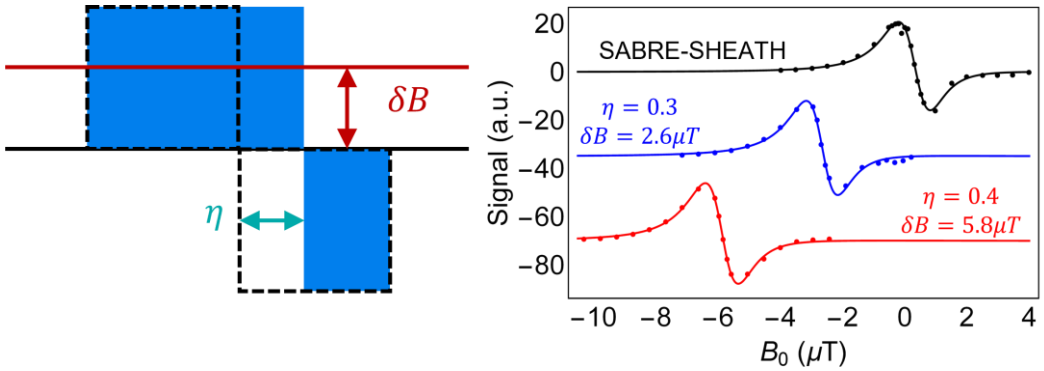

Figure 69: Shifting the X-SABRE resonance with asymmetrically-timed square waves. The residual field generated by an asymmetrically timed square-wave sequence shown here will cause the center of the X-SABRE resonance to shift such that δB is opposed. This could potentially permit hyperpolarization without a μ-metal shield, which is a considerable fraction of the cost of a SABRE-SHEATH experimental apparatus.

field either by aligning the sample orthogonally to these components or using additional electromagnets to actively shield the sample.

Following from the Two-State SABRE experiment[145], the condition $\Delta\omega_{NH} \neq -\delta\omega_{NH}$ is not required for hyperpolarization to be generated. Hyperpolarization may be recovered at sidebands that appear at $\Delta\omega_{NH} = \pm n\delta\omega_{NH}$ (Fig. 70A). While $\Delta\omega_{NH}T/2 \approx 0.05$, there is insufficient phase-evolution of the couplings under δB over the period of the square wave for the magnetic fields that were sampled to generate large hyperpolarization sidebands and only the central resonance where the magnetic field opposes δB is visible. However, increasing $\Delta\omega_{NH}T/2 \approx 0.5$ generates large hyperpolarization sidebands that both give more hyperpolarization and are narrower than the central resonance. The former case would then be expected to show sidebands at a field approximately $(0.5/0.05) \times 21.3\mu T \approx 213\mu T$. For sidebands, hyperpolarization is obtained at $2\pi n \pm \epsilon$ phase evolution of the couplings, which on average attenuates the coupling magnitude by a factor of $\epsilon/2\pi$. Hence, these features often generate more hyperpolarization and are narrower. Heteronuclear couplings will acquire phase evolution differently under δB depending on the $\Delta\gamma$ of the two nuclei (Fig. 70B). For instance,

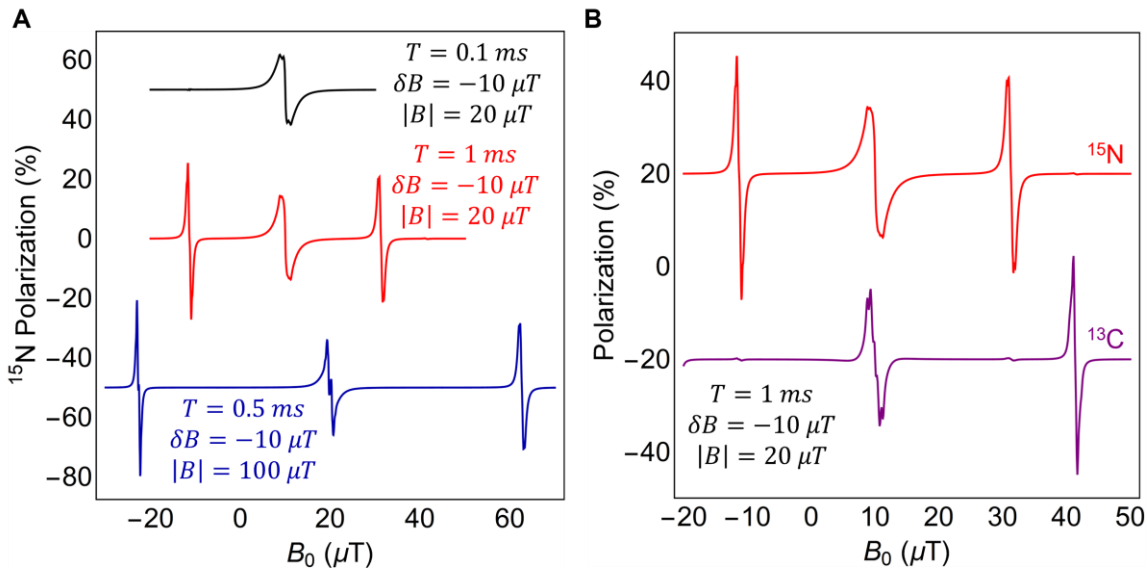

Figure 70: Selective excitation of heteronuclei with asymmetrically-timed square waves. A. When $\Delta\omega_{NH}T/2 \approx 0.05$ (black), there is insufficient phase evolution of the couplings over the field range used to generate hyperpolarization sidebands. However, increasing $\Delta\omega_{NH}T/2 \approx 0.5$ (red) permits sufficient phase evolution of the couplings to generate hyperpolarization sidebands at $\Delta\omega_{NH} = \mp n\delta\omega_{NH}$. Note that the central resonance at $B_0 \approx 10\ \mu T$ does not substantially change position, meaning that the impact of $\bar{\mathcal{H}}^{(1)}$ terms proportional to $(\hat{I}_{1z} - \hat{S}_z)$ is small. However, further increasing $\Delta\omega_{NH}T/2 \approx 1.2$ does generate a shift from the expected field of the center resonance. **B.** The phase evolution under the asymmetrically-timed square wave is different depending on $\delta\gamma_{XH}$ for the different heteronuclei. For instance, the ^{13}C sidebands are centered at a field that is a factor of $\Delta\gamma_{NH}/\Delta\gamma_{CH}$ larger than the field that refocuses the ^{15}N sidebands. This permits selective decoupling of different heteronuclei depending on the chosen magnetic field while retaining the ability to hyperpolarize other heteronuclei.

^{13}C sidebands are refocused at a magnetic field that is $\Delta\gamma_{NH}/\Delta\gamma_{CH}$ larger than the field required to generate a ^{15}N sideband. This essentially permits one to selectively decouple certain heteronuclear J-couplings while retaining the ability to hyperpolarize other heteronuclei.

An interesting extension of this problem is hyperpolarization in the presence of quadrupolar (spin greater than 1/2) nuclei, which suffer from strong quadrupolar relaxation and act as polarization sinks[43, 46]. For instance, hyperpolarizing partially ^{15}N-labelled compounds where the various nitrogens are J-coupled is not possible at ultralow magnetic fields. Here, we simulate a (^{15}N,^{14}N)-diazirine with a $T_{1,Q} = 2\ ms$ (Fig. 71). Hyperpolarization is quenched for SABRE-SHEATH due to spin polarization transfer to the quadrupole, but

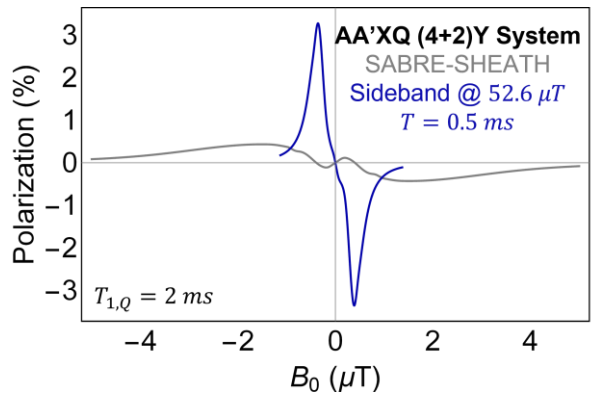

Figure 71: Recovery of hyperpolarization in AA'XQ spin system. The presence of quadrupolar nuclei (Q) quenches hyperpolarization in SABRE-SHEATH (gray). However, hyperpolarization at sidebands generated by asymmetrically-timed square waves can be used to decouple the quadrupolar nucleus, allowing for large enhancement of the hyperpolarization signal. Here, we show a sideband centered at 52.6 μT generating approximately 6× larger polarization.

may be recovered by hyperpolarizing using a sideband generated by an asymmetrically-timed square wave. In this case, $T = 0.5\,ms$ was used to generate a signal enhancement of approximately 6-fold at a sideband centered at $B_0 = 52.6\,\mu T$. It is important to note that the asymmetrically-timed square wave does not decouple the secular $J_{NQ}\hat{S}_z\hat{Q}_z$ term, meaning that spin order may be extracted during the spin operator pathway but cannot be converted into longitudinal quadrupolar magnetization. Fully decoupling the J_{NQ} coupling would be required to fully optimize this problem, but attenuating the non-secular coupling terms already generates a large improvement.

There are many potential avenues to take with this research. As the transformations from the input waveform to the toggling-frame Hamiltonian are easily inverted by taking the necessary derivatives, one could think about engineering a certain response from the system to derive the necessary waveform. This does assume that only the $\bar{\mathcal{H}}^{(0)}$ term acts, which we have shown is sufficient under many conditions. In addition to reverse-engineering waveforms that accomplish desired effects, this problem can also be computationally optimized using something like the evolutionary strategy[138] that was discussed in the previous chapter for

sequence-level high-field X-SABRE optimization. In any case, we have demonstrated that shaping the ultralow magnetic field is a powerful method to control the hyperpolarization dynamics in X-SABRE.

5.3 X-SABRE with transverse fields

To this point, all demonstrations manipulating ultralow field X-SABRE were done using a single magnetic field in the $\hat{z}$ direction. The issue using transverse magnetic fields under these conditions is that irradiation of the target heteronucleus can readily randomize the targeted $\hat{S}_z$ magnetization. One method to circumvent this is to raise the $\hat{z}$ field to $B_0 \approx 50\ \mu T$, where the frequency difference $\Delta\omega_{NH} \approx 2.3\ kHz$, and then use low-power resonant excitation to selectively manipulate certain spins, namely the ^{1}H spins. However, this method establishes an upper limit on the ω_x nutation frequency that may be used to retain selective excitation, which in turn limits how rapidly transverse pulses can be applied. For instance, if the limit was set at $B_0/B_x = 10$ to retain selective excitation, which is approximately where the excitation edges of a rectangular pulse are negligible, then the highest nutation frequency for ^{1}H would be $\omega_x = 213\ Hz$ at $B_0 = 50\ \mu T$, corresponding to a 2.3 ms π-pulse. While this is not an issue for ligands that exchange slowly, it does become problematic when trying to treat rapid exchange when average lifetimes can be on the order of a few milliseconds. Clark Eriksson performed the pioneering simulations for this problem, which will be expanded on here.

Ultralow field X-SABRE exists in a convenient experimental regime that is not obtainable at high field: the magnetic fields may be rapidly shaped in any direction. The use of resonant excitation at high field is required because of the large difference in magnitude

between the leading and transverse fields. In this regime, it is entirely possible to gate the B_0 field off and instead apply a static B_x field. For a pair of heteronuclear spins magnetized along B_0, this would transform the system as:

$$\begin{aligned}\rho(t) &= e^{-i(\gamma_H \hat{I}_x + \gamma_N \hat{S}_x)B_x t}\left(\hat{I}_{z,0} + \hat{S}_{z,0}\right)e^{i(\gamma_H \hat{I}_x + \gamma_N \hat{S}_x)B_x t} \\ &= \cos(\gamma_H B_x t)\,\hat{I}_z - \sin(\gamma_H B_x t)\,\hat{I}_y \\ &\quad + \cos(\gamma_N B_x t)\,\hat{S}_z - \sin(\gamma_N B_x t)\,\hat{S}_y\end{aligned} \tag{5.34}$$

Note that the flip angle $\theta = \gamma B t$ is $\gamma_N/\gamma_H = 1/10$ as large for ^{15}N as it is for ^{1}H. Thus, a 180° pulse on ^{1}H is only approximately an 18° pulse on ^{15}N, which preserves approximately 95% of the projection of the system on $\hat{S}_z$. Then, using a second B_x pulse while reversing the field direction will undo this evolution and recover both $\hat{I}_z$ and $\hat{S}_z$, but the projection of $\hat{I}_z$ over this period is $\langle \hat{I}_z \rangle = 0$ while $\langle \hat{S}_z \rangle \approx 0.97\hat{S}_{z,0}$. Using this method, pulse sequences may be designed using transverse fields to manipulate the spin Hamiltonian and potentially optimize hyperpolarization and expand the scope of ultralow field X-SABRE.

As a first step towards exploring new potential pulse sequences that use transverse excitation, 'virtual' ^{1}H selective pulses that only contained the pulse (B_x) terms as an extension of the δ-pulse limit used at high field. He found that a pulse sequence where π-pulses were interleaved between short, 2 ms periods of B_0 significantly amplified the performance of ultralow field X-SABRE by a factor of up to 5-fold over the conventional SABRE-SHEATH. Translating this ideal experiment into one that could be done experimentally is made easy by using a center-symmetric phase-cycle of B_x pulses (Fig. 72). As discussed previously, using two π-pulses of opposite phase ($x\bar{x}$) will reverse flip-angle errors on ^{15}N and make the sequence selective for ^{1}H on average. However, using the phase cycle $x\bar{x}\bar{x}x$ compensates for

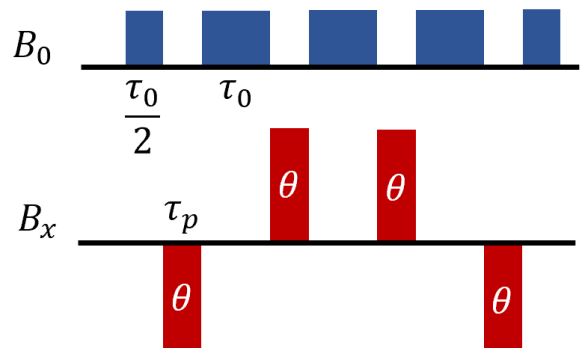

Figure 72: Adapting virtual ^{1}H π pulses to an experimental pulse sequence. A pulse sequence that uses an $x\bar{x}\bar{x}x$ phase cycle of the B_x pulses will approximate a train of ^{1}H π pulses while retaining $\hat{S}_z$ spin order. Because this sequence is center-symmetric, this naturally forces $\bar{\mathcal{H}}^{(2n+1)}$ terms to zero by time-ordering anti-symmetry and facilitates analysis of this sequence.

both flip angle errors on ^{15}N and maintains the average projection of $\hat{S}$ along only $\hat{z}$, $\langle\hat{S}\rangle \propto \hat{S}_{z,0}$. Choosing the cycle of the pulse sequence such that the field terms are symmetric about $T/2$ will naturally force $\bar{\mathcal{H}}^{(2n+1)}$ terms to zero.

To understand the effect of the π-pulse train on the hyperpolarization dynamics, we will again look to average Hamiltonian theory. First, we will choose a toggling frame that facilitates this analysis, and will explore the problem using the model (3+1)Y AA'B X-SABRE system. We will use the variable τ_0 to denote time spent evolving under the B_0 field, and will use τ_p to denote the pulse length of the B_x field. The time-dependent Hamiltonian can be written in a piecewise time-independent form that has nine different periods. However, the toggling frame Hamiltonian may have one of three values during any period:

$$\hat{\mathcal{H}}(t) = J_{HH}\hat{I}_1 \cdot \hat{I}_2 + J_{NH}\hat{I}_1 \cdot \hat{S} + \begin{cases} \hat{\mathcal{H}}_Z = \omega_H(\hat{I}_{1z} + \hat{I}_{2z}) + \omega_N\hat{S}_z \\ \pm\hat{\mathcal{H}}_X = \pm(\Omega_H(\hat{I}_{1x} + \hat{I}_{2x}) + \Omega_N\hat{S}_x) \end{cases} \tag{5.35}$$

We have used the notation Ω_n to denote the nutation frequency (about B_x) and ω_n to denote the Larmor frequency (about B_z). The toggling frame will be chosen as the transverse field

terms, which is convenient to use as these terms are periodic on T. Using the phases shown in Fig. 72 gives the toggling frame Hamiltonians (using $\widetilde{\mathcal{H}}_j$ to denote the jth period):

$$\widetilde{\mathcal{H}}_1 = J_{HH}\hat{I}_1 \cdot \hat{I}_2 + J_{NH}\hat{I}_1 \cdot \hat{S} + \omega_H\left(\hat{I}_{1z} + \hat{I}_{2z}\right) + \omega_N\hat{S}_z \tag{5.36}$$

$$\widetilde{\mathcal{H}}_2 = J_{HH}\hat{I}_1 \cdot \hat{I}_2 + J_{NH}\hat{I}_{1x}\hat{S}_x + J_{NH}\begin{pmatrix}\left(\hat{I}_{1y}\hat{S}_y + \hat{I}_{1z}\hat{S}_z\right)\cos(\Delta\Omega_{NH}t_2) \\ +\left(\hat{I}_{1z}\hat{S}_y - \hat{I}_{1y}\hat{S}_z\right)\sin(\Delta\Omega_{NH}t_2)\end{pmatrix} \tag{5.37}$$

$$\begin{aligned}\widetilde{\mathcal{H}}_3 &= J_{HH}\hat{I}_1 \cdot \hat{I}_2 + J_{NH}\hat{I}_{1x}\hat{S}_x + J_{NH}\begin{pmatrix}\left(\hat{I}_{1y}\hat{S}_y + \hat{I}_{1z}\hat{S}_z\right)\cos\left(\Delta\Omega_{NH}\tau_p\right) \\ +\left(\hat{I}_{1z}\hat{S}_y - \hat{I}_{1y}\hat{S}_z\right)\sin\left(\Delta\Omega_{NH}\tau_p\right)\end{pmatrix} \\ &+\omega_H\begin{pmatrix}\left(\hat{I}_{1z} + \hat{I}_{2z}\right)\cos\left(\Omega_H\tau_p\right) \\ +\left(\hat{I}_{1y} + \hat{I}_{2y}\right)\sin\left(\Omega_H\tau_p\right)\end{pmatrix} + \omega_N\begin{pmatrix}\hat{S}_z\cos\left(\Omega_N\tau_p\right) \\ +\hat{S}_y\sin\left(\Omega_N\tau_p\right)\end{pmatrix}\end{aligned} \tag{5.38}$$

$$\begin{aligned}\widehat{\mathcal{H}}_4 &= J_{HH}\hat{I}_1 \cdot \hat{I}_2 + J_{NH}\hat{I}_{1x}\hat{S}_x \\ &+J_{NH}\begin{pmatrix}\left(\hat{I}_{1y}\hat{S}_y + \hat{I}_{1z}\hat{S}_z\right)\cos\left(\Delta\Omega_{NH}\left(\tau_p - t_4\right)\right) \\ +\left(\hat{I}_{1z}\hat{S}_y - \hat{I}_{1y}\hat{S}_z\right)\sin\left(\Delta\Omega_{NH}\left(\tau_p - t_4\right)\right)\end{pmatrix}\end{aligned} \tag{5.39}$$

We have defined $\Delta\Omega_{NH} = \Omega_N - \Omega_H$, and when calculating the multiple stages of evolution for $\widetilde{\mathcal{H}}_4$, reducing the expression with product-to-sum identities after evolution under both the $\hat{I}_x$ and $\hat{S}_x$ terms made evaluation of this expression significantly easier. The total angular momentum in the x-direction ($\hat{I}_{1x} + \hat{I}_{2x} + \hat{S}_x$) was not removed from the definition of the reference frame because there are terms that are dependent on the difference $\Delta\Omega_{NH}$ as well the nutation frequency the individual spin Ω_n. Importantly, $\widetilde{\mathcal{H}}_4(\tau_p) = J_{HH}\hat{I}_1 \cdot \hat{I}_2 + J_{NH}\hat{I}_1 \cdot \hat{S}$, as is to be expected if the pulses were taken in the δ-pulse limit. From this point, the remaining toggling frame Hamiltonians are relatively easy to calculate, the first two pulses generate no net rotation and the second two pulses generate the opposite-signed rotations of the first two. The remaining toggling frame Hamiltonians are:

$$\widetilde{\mathcal{H}}_5 = J_{HH}\hat{I}_1 \cdot \hat{I}_2 + J_{NH}\hat{I}_1 \cdot \hat{S} + \omega_H\left(\hat{I}_{1z} + \hat{I}_{2z}\right) + \omega_N\hat{S}_z \tag{5.40}$$

$$\widetilde{\mathcal{H}}_6 = J_{HH}\hat{I}_1 \cdot \hat{I}_2 + J_{NH}\hat{I}_{1x}\hat{S}_x + J_{NH}\begin{pmatrix} \left(\hat{I}_{1y}\hat{S}_y + \hat{I}_{1z}\hat{S}_z\right)\cos(\Delta\Omega_{NH}t_6) \\ -\left(\hat{I}_{1z}\hat{S}_y - \hat{I}_{1y}\hat{S}_z\right)\sin(\Delta\Omega_{NH}t_6) \end{pmatrix} \tag{5.41}$$

$$\begin{aligned} \widetilde{\mathcal{H}}_7 &= J_{HH}\hat{I}_1 \cdot \hat{I}_2 + J_{NH}\hat{I}_{1x}\hat{S}_x + J_{NH}\begin{pmatrix} \left(\hat{I}_{1y}\hat{S}_y + \hat{I}_{1z}\hat{S}_z\right)\cos\left(\Delta\Omega_{NH}\tau_p\right) \\ -\left(\hat{I}_{1z}\hat{S}_y - \hat{I}_{1y}\hat{S}_z\right)\sin\left(\Delta\Omega_{NH}\tau_p\right) \end{pmatrix} \\ &+\omega_H\begin{pmatrix} \left(\hat{I}_{1z} + \hat{I}_{2z}\right)\cos\left(\Omega_H\tau_p\right) \\ -\left(\hat{I}_{1y} + \hat{I}_{2y}\right)\sin\left(\Omega_H\tau_p\right) \end{pmatrix} + \omega_N\begin{pmatrix} \hat{S}_z\cos\left(\Omega_N\tau_p\right) \\ -\hat{S}_y\sin\left(\Omega_N\tau_p\right) \end{pmatrix} \end{aligned} \tag{5.42}$$

$$\begin{aligned} \widetilde{\mathcal{H}}_8 &= J_{HH}\hat{I}_1 \cdot \hat{I}_2 + J_{NH}\hat{I}_{1x}\hat{S}_x \\ &+J_{NH}\begin{pmatrix} \left(\hat{I}_{1y}\hat{S}_y + \hat{I}_{1z}\hat{S}_z\right)\cos\left(\Delta\Omega_{NH}\left(\tau_p - t_8\right)\right) \\ -\left(\hat{I}_{1z}\hat{S}_y - \hat{I}_{1y}\hat{S}_z\right)\sin\left(\Delta\Omega_{NH}\left(\tau_p - t_8\right)\right) \end{pmatrix} \end{aligned} \tag{5.43}$$

$$\widetilde{\mathcal{H}}_9 = J_{HH}\hat{I}_1 \cdot \hat{I}_2 + J_{NH}\hat{I}_1 \cdot \hat{S} + \omega_H\left(\hat{I}_{1z} + \hat{I}_{2z}\right) + \omega_N\hat{S}_z \tag{5.44}$$

Note that the durations of $\widetilde{\mathcal{H}}_1$ and $\widetilde{\mathcal{H}}_9$ are $\tau_0/2$ and not τ_0, while the duration of all other $\widetilde{\mathcal{H}}_{2j+1}$ terms is τ_0 and the duration of the $\widetilde{\mathcal{H}}_{2j}$ terms is τ_p.

We may now calculate the zeroth order average Hamiltonian of this sequence, noting that because the $J_{HH}\hat{I}_1 \cdot \hat{I}_2$ and $J_{NH}\hat{I}_{1x}\hat{S}_x$ terms appear in every term unmodulated by the toggling frame, that these terms may be simply removed from the time-averaging. This gives:

$$\begin{aligned} \overline{\mathcal{H}}^{(0)} &= J_{HH}\hat{I}_1 \cdot \hat{I}_2 + J_{NH}\hat{I}_{1x}\hat{S}_x \\ &+J_{NH}\left(\frac{\sin\left(\Delta\Omega_{NH}\tau_p\right)}{\Delta\Omega_{NH}\left(\tau_p + \tau_0\right)} + \frac{\tau_0\left(\cos\left(\Delta\Omega_{NH}\tau_p\right) + 1\right)}{2\left(\tau_p + \tau_0\right)}\right)\left(\hat{I}_{1y}\hat{S}_y + \hat{I}_{1z}\hat{S}_z\right) \\ &+\frac{\tau_0\left(\cos\left(\Delta\Omega_{NH}\tau_p\right) + 1\right)}{2\left(\tau_p + \tau_0\right)}\omega_H\left(\hat{I}_{1z} + \hat{I}_{2z}\right) + \frac{\tau_0\left(\cos\left(\Delta\Omega_{NH}\tau_p\right) + 1\right)}{2\left(\tau_p + \tau_0\right)}\omega_N\hat{S}_z \end{aligned} \tag{5.45}$$

We introduce the notation

$$M_0 = \frac{\sin(\Delta\Omega_{NH}\tau_p)}{\Delta\Omega_{NH}(\tau_p + \tau_0)} + \frac{\tau_0(\cos(\Delta\Omega_{NH}\tau_p) + 1)}{2(\tau_p + t_0)} \tag{5.46}$$

$$A_X = \frac{\tau_0(\cos(\Delta\Omega_{NH}\tau_p) + 1)}{2(\tau_p + \tau_0)} \tag{5.47}$$

to simplify the form of this equation:

$$\begin{aligned}\bar{\mathcal{H}}^{(0)} = J_{HH}\hat{I}_1 \cdot \hat{I}_2 + J_{NH}\left(\hat{I}_{1x}\hat{S}_x + M_0(\hat{I}_{1y}\hat{S}_y + \hat{I}_{1z}\hat{S}_z)\right) \\ + A_H\omega_H(\hat{I}_{1z} + \hat{I}_{2z}) + A_N\omega_N\hat{S}_z\end{aligned} \tag{5.48}$$

Now, we see that the zeroth order average Hamiltonian is nearly identical to the traditional SABRE-SHEATH Hamiltonian but offers additional experimental control over the J_{NH} coupling as well as the resonance frequencies of each of the spins, similar to the square-wave excitation explored previously. One of the major differences that is present is that expanding non-secular components of the J_{NH} coupling gives:

$$\hat{I}_{1x}\hat{S}_x + M_0\hat{I}_{1y}\hat{S}_y = \frac{1 + M_0}{4}(\hat{I}_1^+\hat{S}^- + \hat{I}_1^-\hat{S}^+) + \frac{1 - M_0}{4}(\hat{I}_1^+\hat{S}^+ + \hat{I}_1^-\hat{S}^-) \tag{5.49}$$

In addition to the typical zero-quantum terms ($\hat{I}_1^+\hat{S}^- + \hat{I}_1^-\hat{S}^+$), this Hamiltonian also has double-quantum interactions ($\hat{I}_1^+\hat{S}^+ + \hat{I}_1^-\hat{S}^-$), which opens opportunities to design pulse sequences that take advantage of the differential phase-relationship for these terms.

The dependence of M_0 on the evolution angle θ_{NH} between the hydrides and nitrogen is interesting to compare to a square-wave excitation where the field was oscillated in the x-direction (Fig. 73), which the case when $\tau_0 = 0$ in the above equations. While the square wave solution shows attenuation of the M_0 term with an increasing θ_{NH}, the $(\hat{\mathcal{H}}_z, \pm\theta_x)$-pulse train described by this experiment can recover the magnitude of these terms depending on the ratio of τ_0/τ_p. Furthermore, there is very little to no phase-inversion of the M_0 term when $\tau_p \leq$

τ_0, which permits M_0 to be less sensitive to inhomogeneities when $\theta_{NH} \approx \pi$, where the square wave solution changes sign and generates a zero-average.

Using the condition that was found in the original simulations by Clark Eriksson, when $\theta_H = \pi$, $\theta_{NH} = (1 - \gamma_N/\gamma_H)\pi \approx 1.1\pi$, and $M_0 \approx 0$ for this case. $A_H = 0$ and $A_N \approx 0.65$, meaning that any phase rotation caused by evolution with B_0 must be accumulated using only the ^{15}N-spin. The Hamiltonian under this condition is:

$$\bar{\mathcal{H}}^{(0)} \approx J_{HH}\hat{I}_1 \cdot \hat{I}_2 + J_{NH}\hat{I}_{1x}\hat{S}_x + A_N\omega_N\hat{S}_z \tag{5.50}$$

The simulated field profile using the $(\hat{\mathcal{H}}_z, \pm\pi_x)$ pulse sequence (Fig. 74) shows that the optimum hyperpolarization is obtained at a magnetic field that is approximately a factor of 10 larger than the field required to generate the phase shift required for the SABRE-SHEATH experiment. The resultant hyperpolarization is significantly larger for this sequence than for a

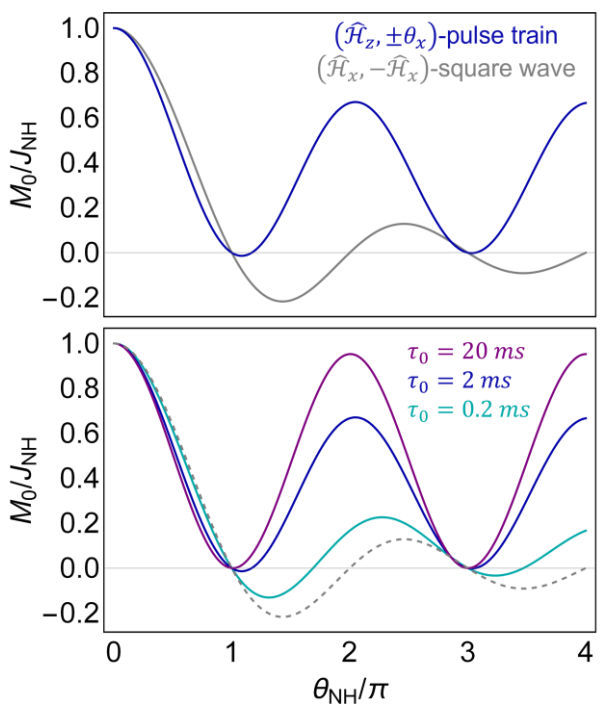

Figure 73: Dependence of M_0 on θ_{NH} compared to a square-wave solution. Top. While the square wave ($\tau_0 = 0$ solution, gray) attenuates the magnitude of J_{NH} with an increasing period, the $(\hat{\mathcal{H}}_z, \pm\theta_x)$-pulse train can refocus J_{NH}. **Bottom.** The degree to which the J_{NH} coupling terms may be refocused is dependent on the ratio of τ_0/τ_p. For these simulations, $\tau_p = 1\ ms$.

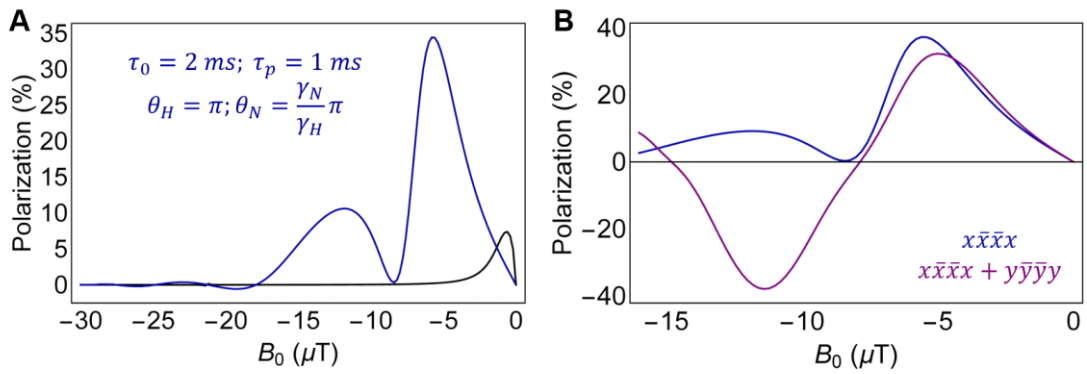

Figure 74: Ultralow field X-SABRE profile of the ^{1}H π-pulse train. A. In comparison to the SABRE-SHEATH solution on the same system, the $(\widehat{\mathcal{H}}_z, \pm\pi_x)$-pulse train can generate significantly larger hyperpolarization. The field which optimizes B_0 is also significantly larger than the SABRE-SHEATH field, due to the attenuation of the $\Delta\omega_{NH}$ terms by the pulse sequence. **B.** Appending a $y\bar{y}\bar{y}y$ phase cycle to the $x\bar{x}\bar{x}x$ sequence generates larger hyperpolarization at large B_0, as this sequence can refocus the $\hat{S}_x$ spin order generated at large B_0. A model (3+1)Y X-SABRE system using $k_N = 16\ s^{-1}$, $k_H = 2\ s^{-1}$, and $[Ir]/[S] = 1/20$ was used for all simulations.

SABRE-SHEATH experiment using identical parameters. Unlike the SABRE-SHEATH experiment, this field profile appears to have regular structure that is not present in the typical SABRE-SHEATH profile, which is likely to appear as higher order terms in the average Hamiltonian become more prominent with increasing B_0. For instance, evolution of the fractionally excited $\hat{S}_y$ spin order under B_0 would lead to $\hat{S}_x$, which commutes with the B_x field and is thus not refocused by the pulse sequence. As such, one may imagine performing additional phase-cycling using combinations of x- and y-pulses. For instance, a $y\bar{y}\bar{y}y$ pulse sequence has an identical $\bar{\mathcal{H}}^{(0)}$ as eq. 5.48 with just the $\hat{I}_{1x}\hat{S}_x \leftrightarrow \hat{I}_{1y}\hat{S}_y$ terms interchanged. Figure 74B shows that doing so improves the hyperpolarization at high B_0, where the conversion of $\hat{S}_y \rightarrow \hat{S}_x$ is more efficient. This suggests that phase-cycling schemes are a potential option to improve hyperpolarization when using transverse fields.

As the B_x field is not selective for ^{1}H, it is crucial that inhomogeneities will not dramatically affect the hyperpolarization performance (Fig. 75). All simulations were run at $\tau_0/\tau_p = 2$. Relative B_x inhomogeneities of $\pm 20\%$ show very little impact in the field profile

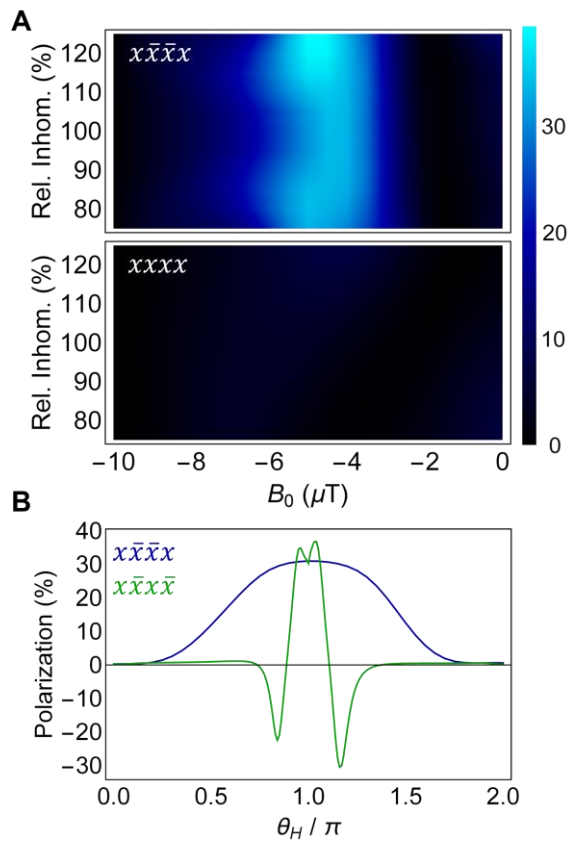

Figure 75: Robustness to field inhomogeneity. A. The B_0 profile is relatively insensitive to inhomogeneities in B_x for the $x\bar{x}\bar{x}x$ phase cycle. The $xxxx$ phase cycle, which continuously nutates both $\hat{I}$ and $\hat{S}$, generates a small fraction of the hyperpolarization that the $x\bar{x}\bar{x}x$ phase cycle does, largely because there is no component of $\bar{\mathcal{H}}^{(0)}$ that generates nutation. **B.** The $x\bar{x}\bar{x}x$ phase cycle is robust to errors in the flip angle, showing hyperpolarization that exceeds the SABRE-SHEATH signal for the region that is covered by approximately $\pi/2 < \theta_H < 3\pi/2$. In comparison, the $x\bar{x}x\bar{x}$ phase cycle is significantly more sensitive to the pulse flip angle as it does not fully eliminate unwanted terms from the average Hamiltonian. Color bar in units of polarization (P%).

when a $x\bar{x}\bar{x}x$ phase cycle is used. When all $xxxx$ pulses are used, we observe a large attenuation of the hyperpolarization. This arises as the pulse sequence no longer compensates for the non-selectivity of the pulses and permits nutation of both $\hat{I}$ and $\hat{S}$. An interesting extension of this problem is to examine a $x\bar{x}x\bar{x}$ phase cycle, which is essentially just the average Hamiltonian of the first half of the pulse sequence, which adds the pseudosecular terms $\hat{I}_{1z}\hat{S}_y - \hat{I}_{1y}\hat{S}_z$ as well as the terms $\hat{I}_{1y} + \hat{I}_{2y}$ and $\hat{S}_y$:

$$\bar{\mathcal{H}}^{(0)} = J_{HH}\hat{I}_1 \cdot \hat{I}_2 + J_{NH}\hat{I}_{1x}\hat{S}_x + J_{NH}M_0\left(\hat{I}_{1y}\hat{S}_y + \hat{I}_{1z}\hat{S}_z\right) + A_H\omega_H\left(\hat{I}_{1z} + \hat{I}_{2z}\right) \qquad (5.51)$$

$$+A_N\omega_N\hat{S}_z + J_{NH}\left(\frac{1-\cos(\Delta\Omega_{NH}\tau_p)}{\Delta\Omega_{NH}(\tau_p+\tau_0)} + \frac{\tau_0\sin(\Delta\Omega_{NH}\tau_p)}{2(\tau_p+\tau_0)}\right)(\hat{I}_{1z}\hat{S}_y - \hat{I}_{1y}\hat{S}_z)$$

$$+\frac{\tau_0\sin(\Omega_H\tau_p)}{2(\tau_p+\tau_0)}\omega_H(\hat{I}_{1y}+\hat{I}_{2y}) + \frac{\tau_0\sin(\Omega_N\tau_p)}{2(\tau_p+\tau_0)}\omega_N\hat{S}_y$$

Notice that the performance of the $x\bar{x}x\bar{x}$ pulse sequence deteriorates even for small deviations from $\theta_H = \pi$, while the $x\bar{x}\bar{x}x$ pulse sequence is robust to changes in θ_H. Notably, the values of θ_H that generate enhanced hyperpolarization over the SABRE-SHEATH experiment spans the range of approximately $\pi/2 < \theta_H < 3\pi/2$, meaning that this experiment can be readily implemented with little to no concern for B_x inhomogeneities. This is convenient because building transverse electromagnets with the homogeneity comparable to that of a solenoid is significantly more difficult due to the available geometries for these magnets.

In addition to being robust to experimental inhomogeneities, it is critical that this experiment permit hyperpolarization over a broad range of exchange rates to facilitate the diverse X-SABRE substrate scope (Fig. 76). Even when the exchange rate is $k_N = 500\ s^{-1}$, the $(\hat{\mathcal{H}}_z, \pm\pi_x)$ pulse sequence shows a five-fold improvement over SABRE-SHEATH and

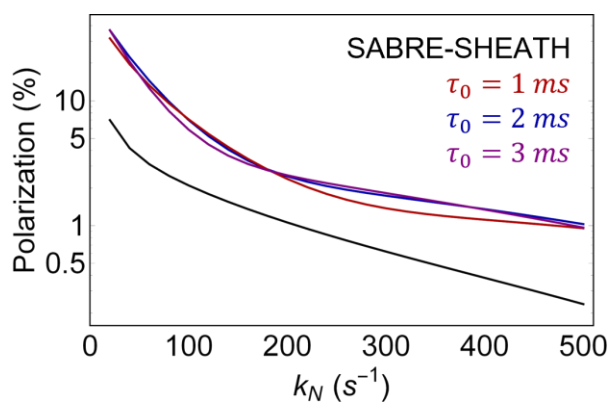

Figure 76: Hyperpolarization of rapidly exchanging targets with the ^{1}H π-pulse train. Relative to SABRE-SHEATH, the $(\hat{\mathcal{H}}_z, \pm\pi_x)$-pulse train can generate 3- to 5-fold improvement in the hyperpolarization in both the rapid and slow exchange regimes. In particular, the predicted hyperpolarization from this experiment when $k_N = 500\ s^{-1}$ is still $P{\sim}1\%$. For these simulations $\tau_p = 1\ ms$ and τ_0 was varied between $\tau_0 = 1 - 3\ ms$.

predicts a polarization of $P{\sim}1\%$, which is consistent over a range of exchange rates. The rapid exchange case is very interesting, as the system only experiences maximally 1 cycle of the pulse sequence on average. However, phase evolution of $\hat{S}_z$ under the field interactions is unaffected by exchange at ultralow field due to the absence of the chemical shift interaction.

We have demonstrated a new direction for manipulating the ultralow field X-SABRE Hamiltonian using a phase-cycled train of transverse field pulses. We have shown the average Hamiltonian interpretation of such pulse sequences and have discussed methods to overcome spin selectivity at ultralow magnetic field. Employing a simple $x\bar{x}\bar{x}x$ phase cycle significantly improves the performance of X-SABRE hyperpolarization under these conditions, we show that the experiment is highly robust to field inhomogeneities. Furthermore, this experiment shows an approximate 3- to 5-fold improvement over a broad range of exchange rates, yielding $P{\sim}1\%$ for a $k_N = 500\ s^{-1}$. While the results shown here are certainly promising, this is an ideal candidate for computational optimization of the pulse sequence, and it may be interesting to augment the field shaping techniques of the previous section with those presented here.

5.4 Conclusions and outlook on ultralow field X-SABRE

Ultralow field X-SABRE is an exciting experimental regime due to the relatively under-explored spin physics. With the ability to rapidly manipulate the field in any direction comes exciting new possibilities for controlling the coherent hyperpolarization dynamics of X-SABRE. We have demonstrated that pulsing between a zero-field and a high field can access the coherent dynamics of non-magnetized states and demonstrated this with a ^{15}N,^{13}C heteronuclear singlets. Expanding on the ideas of pulsing the B_0 field led to the development

of using shaped waveforms to control the phase and magnitude of the heteronulcear J_{NH} coupling. We introduced a generalized average Hamiltonian formalism to explore the spin interactions using shaped waveforms and applied this idea to show that hyperpolarization in the presence of nearby quadrupolar nuclei could be recovered using an asymmetrically-timed waveform. Finally, we introduced a new avenue for generating hyperpolarization at ultralow field combining multiple orthogonal fields, discussing the issues with nuclear spin selectivity under these experimental conditions.

There are many directions in which ultralow field X-SABRE research may be taken, including such things as optimization of the field waveforms to boost hyperpolarization and coupling zero to ultralow field (ZULF) spectroscopy to X-SABRE as a means for direct in-shield monitoring. While both of these endeavors are being pursued in the Warren lab currently, another interesting direction is actually revisiting one that has already been explored: using heterogeneous catalysts to perform X-SABRE hyperpolarization. Perhaps the most critical step to bridge X-SABRE to preclinical research is the ability to hyperpolarize an X-SABRE solution and then rapidly remove the catalyst prior to injection of a hyperpolarized bolus. Previously, the Goodson and Chekmenev labs[121] explored the use of iridium catalysts fixed to a functionalized $40 - 60\ \mu m$ SiO_2 bead (approximately the size of a grain of sand) and showed that hyperpolarization could be performed at ultralow magnetic field. This allowed simple filtration to remove the iridium catalyst from solution, and offers an economic way to translate X-SABRE into the preclinical setting. However, the initial demonstrations using heterogeneous catalysts were only capable of generating a small fraction of the hyperpolarization as the conventional homogeneous catalyst, and, since then, this problem has not been revisited.

Perhaps one of the most common misconceptions in liquid state magnetic resonance is that dipolar couplings between spins may be neglected. These couplings are still present but are (mostly) averaged away due to the picosecond-timescale rotational tumbling of small molecules in solution. Dipolar effects may be exaggerated by field gradients at high magnetic field, when the symmetry of the sample no longer permits a spherical averaging. This realization led to the intermolecular Multiple Quantum Coherence (iMQC)[100, 146-151] work done by the Warren lab. Similarly, dipolar couplings can be recovered if the rotational correlation time of the molecule is too slow to permit orientational averaging on the timescale of the coupling, which is likely one of the consequences of tethering the iridium catalyst to a SiO_2 bead, which will have an estimated rotational correlation time with a lower limit of tens of milliseconds. In the original experiments, it was assumed that the dipolar couplings would average away and that hyperpolarization would be optimized at $B_0 \approx \pm 0.5\ \mu T$. However, let us briefly examine what would happen if the dipolar couplings no longer average away at ultralow field.

We will begin with the full form of the Hamiltonian, which is given by (rad s^{-1}):

$$\hat{\mathcal{H}} = \omega_H\left(\hat{I}_{1z} + \hat{I}_{2z}\right) + \omega_N \hat{S}_z + J_{HH}\hat{I}_1 \cdot \hat{I}_2 + J_{NH}\hat{I}_1 \cdot \hat{S} + \sum_{i<j} d_{ij}\hat{I} \cdot \ddot{\Omega} \cdot \hat{S} \qquad (5.52)$$

The tensor $\ddot{\Omega}$ was previously defined as:

$$\ddot{\Omega} = 3\boldsymbol{r} \cdot \boldsymbol{r}^T - \hat{E}; \boldsymbol{r} = \begin{pmatrix} \sin(\theta)\cos(\phi) \\ \sin(\theta)\sin(\phi) \\ \cos(\theta) \end{pmatrix} \qquad (5.52)$$

The full dipolar Hamiltonian is written out explicitly in Chapter 2.1. Assuming that the tether to the SiO_2 bead does not permit free-tumbling in solution, the dipolar interaction does not necessarily average away although it may be attenuated if the tether is sufficiently flexible.

Under this condition, it is pertinent to search for coherence pathways that permit the excitation from $\hat{I}_1 \cdot \hat{I}_2 \rightarrow \pm\hat{S}_z$ spin order that survive the tumbling of the SiO_2 bead. This is dependent on the relative orientations of the various nuclei in the complex. Firstly, the first four time-derivatives of the Hamiltonian given by equation 5.52 (neglecting the J-coupling terms) were calculated computationally using the spin operator pathway algorithm described in the Appendix. This yielded 2,176 transitions, of which 156 pathways lead to positive magnetization ($+\hat{S}_z$) and another 156 lead to negative magnetization ($-\hat{S}_z$). Of each 156 pathways, 84 pathways arise in the third derivative and are proportional to only dipolar coupling terms. Naturally, inverting the time-ordering of any two of these three couplings will result in the opposite-signed magnetization, and as such, no net magnetization is expected to be produced from these couplings after spherical averaging. The remaining 72 pathways produce magnetization in the fourth derivative and are proportional to three dipolar coupling terms and a single interaction with the magnetic field. This interaction with the field breaks the symmetry of the terms and can potentially permit magnetization to survive averaging.

The potential for dipolar couplings to survive the orientational averaging when tethered to the SiO_2 bead was tested for the iridium complex using the geometry depicted in Fig. 77A. For this system, the third- and fourth-order dependences of $\hat{S}_z$ were calculated and sampled over 2.5M orientations of the complex, which was performed by setting the r_{NH} vector as the molecular reference frame and randomly sampling the Euler angles α, β, and γ of that reference frame. While the third-order dependences of $\hat{S}_z$ do not survive orientational averaging, the fourth-order dependences of $\hat{S}_z$ survive the orientational averaging of the SiO_2 bead and indicate that hyperpolarization could realistically be generated by evolution under the dipolar Hamiltonian instead of the J-coupling Hamiltonian.

Simulations of the model (3+1)Y X-SABRE system were performed using the same parameters described in Fig. 77 and assumed that only the subsystems bound to the SiO_2 bead exhibited dipolar interactions. Furthermore, we assumed that the iridium catalyst was tethered to the bead using a flexible tether that permitted isotropic attenuation of the dipolar coupling by a factor of 10. Even still, X-SABRE hyperpolarization is observed at fields of $B_0 = \pm 50\ \mu T$ in accordance with the predicted behavior from perturbation theory (Fig. 78). These simulations assumed isotropic rotational constants for the SiO2 beads of $\tau_c = 50\ ms$, which is perhaps at the lower limit of the correlation time but we have assumed that there is turbulent fluid flow in the sample tube due to bubbling parahydrogen. This correlation time would be expected to increase if the sample were assumed in a high-pressure mode, where there is no bubbling to disturb the sample. It is also important to note that in the absence of experimental parameters, which may only be inferred from prior knowledge, the exact field dependence or hyperpolarization cannot be accurately predicted. However, these simulations do suggest that this is an interesting endeavor. The process outlined here for the case of heterogeneous

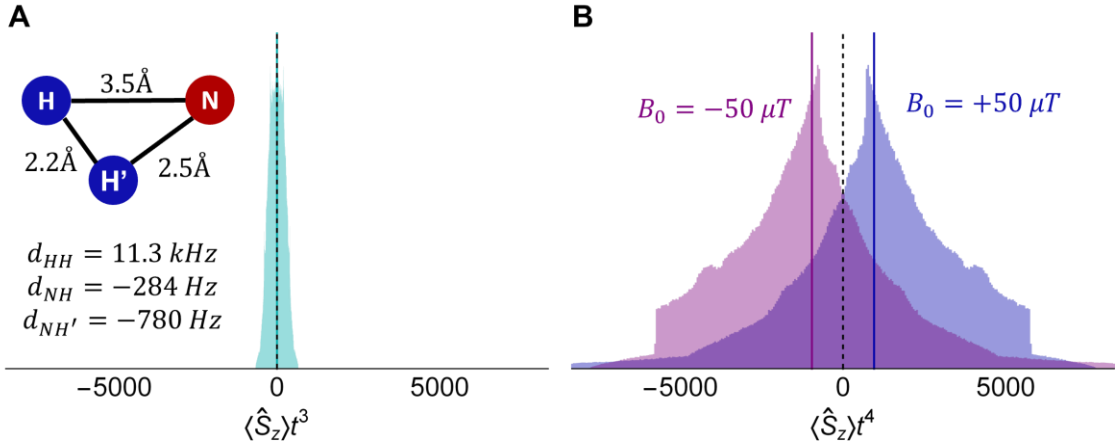

Figure 77: Orientational averaging of the dipolar Hamiltonian in a SiO_2 bead system. A. There are no terms present to break the symmetry of the third-order dependence of the hyperpolarized $\hat{S}_z$ spin order and thus, the average $\langle \hat{S}_z \rangle \approx 0$ for these terms. **B.** The field-dependent fourth-order dependences have the requisite ability to break the symmetry of the spin operator pathways pumping $\hat{S}_z$ and thus can generate net magnetization, which is indicated by the vertical solid lines for both the $B_0 = \pm\ 50\ \mu T$ cases. These assume a rigid tether to the SiO_2 beads.

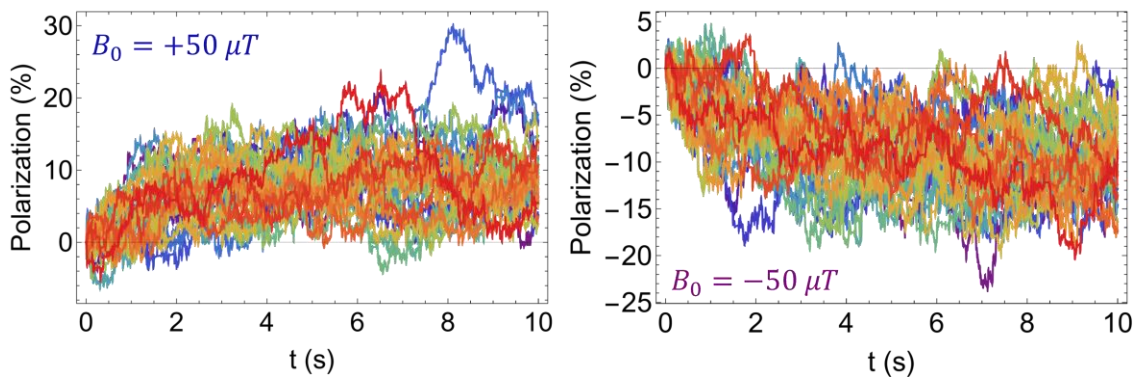

Figure 78: Hyperpolarization on an isotropically rotating SiO_2 bead with a $\tau_c = 50\ ms$. X-SABRE hyperpolarization is generated at both $B_0 = \pm 50\ \mu T$ on an isotropically rotating SiO_2 bead with a 50 ms rotational correlation time. For each field, 32 different random trajectories were sampled and, on average, hyperpolarization is generated through the dipolar couplings. An isotropic attenuation of the dipolar couplings of 1/10 was assumed, as well as using $k_N = 16\ s^{-1}$ and $k_H = 2\ s^{-1}$ for a sample of $[Ir]/[S] = 1/20$.

catalyst in SABRE is highly indicative of the future development of next generation X-SABRE experiments: a combination of pencil-and-paper theory confirmed and optimized by simulation has already shown and will continue to be an ideal way to pursue optimization of this system.

Chapter 6: A generalized Lindblad master equation for chemical exchange

In Chapter 3, we demonstrated that exact master equations for chemical exchange could be derived in the magnetic resonance limit, when the time required to jump between exchange sites is taken as $\tau_c = 0$, i.e., that the jump between configurations is instantaneous. While this is a valid approximation for exchange caused by molecular rearrangement in NMR ($\mu s - s$), it is not obvious that this approximation holds for applications such as site hopping[152, 153], where a molecule exchanges between discrete sites and transport between these sites is diffusion assisted. Furthermore, chemical exchange is not unique to NMR spectroscopy, and is often investigated on ultrafast timescales with two-dimensional infrared spectroscopy (2DIR)[154, 155]. Demonstrations of hydrogen bond formation and protein side chain conformational dynamics are among the many applications investigated by 2DIR, as these chemical processes are all on the fs-ps timescale[156]. Under these conditions, the instantaneous jump limit is no longer valid.

Here, we extend our exact master equation treatment of chemical exchange to the fully generalized case, which is valid in any experimental limit. While the DMEx was constructed within a formalism convenient and familiar to most in magnetic resonance, other fields utilize the more general Lindblad formalism[157-159] to describe dissipative dynamics as it is valid when the density matrix is far-from equilibrium, unlike most NMR applications. This formalism will be used to assess the chemical exchange interaction in both the optical and NMR limits, and

provides convenient access to previously unexplored exchange effects, such as the interactions arising from a finite jump time between exchange sites. As optics is not the core focus of this work, 2DIR will be summarized before exploring the exchange effects.

6.1 Lindblad equation for exchange in the instantaneous jump limit

While the superoperator formalism used for the DMEx provides arbitrary flexibility in the definition of the exchange superoperator $\widehat{K}_j$, this construction is mostly pertinent to magnetic resonance. To broaden the scope of exact master equations for chemical exchange, we will explore the Lindblad equation as a formalism for chemical exchange in other forms of spectroscopy that use vastly different timescales. The Lindblad equation is the most general equation of motion that describes both coherent and dissipative dynamics while preserving the trace of $\hat{\rho}$ for any initial condition. We will first treat the Lindblad equation in the limit where the rearrangement time is significantly faster than all other degrees of freedom in the system, as is the case in magnetic resonance, providing a direct corollary to the DMEx. This will be referred to as the instantaneous jump limit, or IJL. Using this treatment, we will find a significantly more diverse set of exact master equations that may be constructed that are not compatible with the DMEx formalism. In the following sections, we will expand this treatment to the case where the jump time can no longer be neglected.

As this treatment seeks to broaden the generality of the treatment of exchange, we will first establish the foundational assumptions upon which this derivation will be pursued:

(1) Chemical exchange is a Hermitian, multiparticle coupling, and therefore has a corresponding Hamiltonian $\widehat{\mathcal{H}}_1(t)$. The components of $\widehat{\mathcal{H}}_1(t)$ that either interact

with the density matrix or dictate the molecular dynamics are treated quantum mechanically and have associated operators.

(2) The system is Markovian and memoryless. This permits us to make the substitution $\hat{\rho}(t_n) \rightarrow \hat{\rho}(t)$ in the equation of motion, where $t > t_n$ by time-ordering.

(3) To satisfy the Hermiticity requirement, the system is at a steady state equilibrium. The steady state requires that the molecular dynamics are stationary. In essence, for any exchange event from site $A \rightarrow B$, a corresponding particle must exchange from site $B \rightarrow A$ to retain the steady state.

(4) Any exchange processes is only self-correlated, which may be accomplished by simply diagonalizing the basis set of $\{k\}$ exchange processes. Given the Hermiticity requirement and the steady state, there will always exist a basis that diagonalizes $\{k\}$.

(5) We will assume that the jump time to exchange between sites, τ_c, is significantly faster than any other degree of freedom in the system.

Throughout the derivation, we will identify the various assumptions used at each point and will delineate from equations by using the notation 'assumption (n)'. While these are the only fundamental assumptions that must be established, there are additional, physical restrictions that must be imposed throughout the derivation to obtain an equation of motion for exchange.

The Lindblad equation is motivated from the Dyson expansion, as in the DMEx, but requires a quantum mechanical treatment of the ensemble-level dynamics, which is valid under

assumption (1). As such, we may begin with the assumption that exchange is Markovian (2) and that the ensemble dynamics are stationary (3), which permits us to write the leading order term as (in the interaction frame):

$$\frac{\partial}{\partial t}\rho^{(2)} = -\vec{\mathcal{T}}\int_0^t dt_1\ \left[\mathcal{H}_1(t),\left[\mathcal{H}_1^\dagger(t_1),\rho\right]\right] \tag{6.1}$$

The stochastic Hamiltonian may then be expanded as:

$$\mathcal{H}_1(t) = \sum_k A_k(t)\otimes F_k(t) \tag{6.2}$$

The operator A_k is the again operator inducing exchange on the reduced density matrix and $\hat{F}_k$ describes the molecular dynamics, and the tensor product ($\otimes$) between these degrees of freedom formally permits a quantum mechanical treatment of the ensemble. As both $\hat{A}_k$ and $\hat{F}_k$ are Hermitian, we drop the conjugate transposes for brevity. Using this in eq. 6.1:

$$\frac{\partial}{\partial t}\rho^{(2)} = -\vec{\mathcal{T}}\sum_{jk}\int_0^t dt_1\begin{pmatrix} A_j(t)\otimes F_j(t)A_k(t_1)\otimes F_k(t_1)\rho \\ -A_j(t)\otimes F_j(t)\rho A_k(t_1)\otimes F_k(t_1) \\ -A_k(t_1)\otimes F_k(t_1)\rho A_j(t)\otimes F_j(t) \\ +\rho A_k(t_1)\otimes F_k(t_1)A_j(t)\otimes F_j(t)\end{pmatrix} \tag{6.3}$$

We may now isolate the ensemble degrees of freedom in the density matrix

$$\rho = \rho\otimes\rho_B, \tag{6.4}$$

where ρ_B is acted on by the $\hat{F}_k$ operators. Using this definition, as well as the fact that the $[A_k,\rho_B] = [F_k,\rho] = 0$, permits us to rearrange eq. 6.3 and trace over the ensemble as:

$$\frac{\partial}{\partial t}\rho_A^{(2)} = -\vec{\mathcal{T}}\sum_{jk}\int_0^t dt_1\begin{pmatrix} A_j(t)A_k(t_1)\rho\langle F_j(t)F_k(t_1)\rho_B\rangle \\ -A_j(t)\rho A_k(t_1)\langle F_j(t)\rho_B F_k(t_1)\rangle \\ -A_k(t_1)\rho A_j(t)\langle F_k(t_1)\rho_B F_j(t)\rangle \\ +\rho A_k(t_1)A_j(t)\langle\rho_B F_k(t_1)F_j(t)\rangle\end{pmatrix} \tag{6.5}$$

Firstly, we will expand the three-point correlation function according to Isserlis' theorem[160], which for the first term would give:

$$\begin{aligned}\langle F_j(t)F_k(t_1)\rho_B\rangle &= \langle F_j(t)F_k(t_1)\rangle\langle\rho_B\rangle \\ &+\langle F_j(t)\rho_B\rangle\langle F_k(t_1)\rangle + \langle F_k(t_1)\rho_B\rangle\langle F_j(t)\rangle\end{aligned} \tag{6.6}$$

As the dynamics are assumed to be stationary and realizing that $\langle\rho_B\rangle = \hat{E}$ (unity), the only non-zero three-point correlator is proportional to $\langle F_j(t)F_k(t_1)\rangle$. Furthermore, the stationary assumption allows us to make the change of variables $t - t_1 = \tau$ to give:

$$\frac{\partial}{\partial t}\rho_A^{(2)} = \vec{\mathcal{T}}\sum_{jk}\int_t^0 d\tau\begin{pmatrix} A_j(\tau)\hat{A}_k\rho\langle F_j(\tau)\hat{F}_k\rangle - A_j(\tau)\rho\hat{A}_k\langle F_j(\tau)\hat{F}_k\rangle \\ +\rho\hat{A}_k A_j(\tau)\langle\hat{F}_k F_j(\tau)\rangle - \hat{A}_k\rho A_j(\tau)\langle\hat{F}_k F_j(\tau)\rangle\end{pmatrix} \tag{6.7}$$

Inverting the limits of integration gives:

$$\frac{\partial}{\partial t}\rho^{(2)} = \vec{\mathcal{T}}\sum_{jk}\int_0^t d\tau\begin{pmatrix} A_j(\tau)\rho\hat{A}_k\langle F_j(\tau)\hat{F}_k\rangle - A_j(\tau)\hat{A}_k\rho\langle F_j(\tau)\hat{F}_k\rangle \\ +\hat{A}_k\rho A_j(\tau)\langle\hat{F}_k F_j(\tau)\rangle - \rho\hat{A}_k A_j(\tau)\langle\hat{F}_k F_j(\tau)\rangle\end{pmatrix} \tag{6.8}$$

In the limit where the jump, or correlation, time is much faster than the other degrees of freedom in the system, given by assumption (5), we may take the correlation functions as:

$$\langle F_j(t)\hat{F}_k\rangle = \delta_{jk}\frac{g_k(t)}{\tau_k} = \delta_{jk}\frac{\delta(t)}{\tau_c\tau_k} \tag{6.9}$$

Additionally, we will retain the assumption that exchange processes are only self-correlated (4). Doing so gives:

$$\frac{\partial}{\partial t}\rho^{(2)} = \vec{\mathcal{T}}\sum_{k}\int_0^t d\tau\begin{pmatrix} A_k(\tau)\rho\hat{A}_k - A_k(\tau)\hat{A}_k\rho \\ +\hat{A}_k\rho A_k(\tau) - \rho\hat{A}_k A_k(\tau)\end{pmatrix}\frac{\delta(\tau)}{\tau_k} \tag{6.10}$$

Note, that $\langle F_j(\tau)\hat{F}_k\rangle = \langle\hat{F}_k F_j(\tau)\rangle$ using the cyclic permutation of matrices under a trace. As the correlation function is even and decays infinitely fast, we may extend the integration limits to $\pm\infty$, acquiring a factor of ½, and gives:

$$\frac{\partial}{\partial t}\hat{\rho}^{(2)} = i[\hat{\rho}, \hat{\mathcal{H}}] + \sum_k \frac{1}{\tau_k}\left(\hat{A}_k\hat{\rho}\hat{A}_k^\dagger - \frac{1}{2}\{\hat{A}_k\hat{A}_k^\dagger, \hat{\rho}\}\right) \tag{6.11}$$

We used the hermiticity of $\hat{A}_k$ (permitting us to write $\hat{A}_k = \hat{A}_k^\dagger$) and the definition of the anticommutator $\{\hat{A}, \hat{B}\} = \hat{A}\hat{B} + \hat{B}\hat{A}$ to cast the equation into the traditional Lindblad form. The quantity in parentheses is referred to as the 'Lindbladian dissipator', or simply as the 'Lindbladian', and it will become convenient to write it in the shorthand $\hat{\mathcal{L}}_k\hat{\rho}$. In comparison with the DMEx, the Lindbladian is a traceless quantity whereas the exchange superoperator $\hat{K}$ is a projection, and thus is trace unity. This equation will be referred to as the Lindblad Master Equation, or LME.

While the Lindblad equation formally only uses the leading-order term from the Dyson expansion, it is possible to extend this treatment to all higher order terms as done with the DMEx. This yields a similar re-summation of the entire Dyson series as observed in the derivation of the DMEx. We now write the re-summation of the series, as the result may be confirmed using the same transformations employed in the derivation of the DMEx:

$$\frac{\partial}{\partial t}\hat{\rho} = i[\hat{\rho}, \hat{\mathcal{H}}] + \left\{\sum_{n=0}^{\infty}\left(\sum_k \frac{\hat{\mathcal{L}}_k}{\tau_k}\right)^{n+1}\frac{1}{n!}\left(\frac{T}{2}\right)^n\right\}\hat{\rho} \tag{6.12}$$

There are several types of exchanging systems that may be described within this framework. Exchange processes can either be distinguishable, meaning that different chemical processes are unique regardless of frame, or indistinguishable, where the processes become identical under a similarity transformation. Dissociation of the ligand from the SABRE complex and association of the parahydrogen are distinguishable processes, whereas something like the clockwise and anticlockwise rotations of a methyl group are

indistinguishable. For the case of exchange between distinguishable molecular processes, the following substitution

$$\left(\sum_k \frac{\hat{\mathcal{L}}_k}{\tau_k}\right)^n = \sum_k \left(\frac{\hat{\mathcal{L}}_k}{\tau_k}\right)^n \tag{6.13}$$

is possible because in higher order correlators, like $\langle \hat{F}_i(t)\hat{F}_j^\dagger(t_1)\hat{F}_k(t_2)\hat{F}_l^\dagger(t_3)\rangle$ that arises from the fourth-order term in the expansion, it is assumed that exchange processes are only self-correlated, and thus δ_{ijkl} is imposed. However, in the case of exchange between indistinguishable ensembles, any one molecular rearrangement appears identical to all of the other processes ($\hat{F}_j = \hat{F}_k$) while still exchanging populations between different configurations. This permutation invariance requires δ_{ijkl} to be bifurcated into $\delta_{ij}\delta_{kl}$, where $i = j$ and $k = l$ is still imposed such that the quadratic action of the $\hat{A}_k$ operators enforces an exchange event, and eq. 6.13 is no longer valid. For indistinguishable molecular processes, $\|\hat{F}_j\| = \|\hat{F}_k\|$, meaning that all exchange processes have the same characteristic lifetime τ.

Systems that have indistinguishable processes often have an intrinsic symmetry that permits classification. The set of all exchange operators $\{\hat{A}_k\}$ that map the exchange pathways of the system correspond to the group $\mathcal{G}^h$ of the system, where h denotes the symmetry order of the group. The identity operation $\hat{E}$ is also included in these groups as the 'no exchange' operation. For example, for a system that exchanges between three configurations, where each configuration is a permutational isomer of any other configuration, that system is said to have three-fold permutation symmetry. For this system, there exists a group $\mathcal{G}^3$ that contains all the exchange operators that map the exchange pathways in that system. $\hat{A}_k$ is called an element of the group ($\hat{A}_k \in \mathcal{G}^h$). If the property $[\hat{A}_j, \hat{A}_k] = 0$ for all $j \neq k$ holds, indicating that elements

may be applied to the system in any order and have it produce the same result, then the group is considered to be an Abelian group. The permutation group $\mathcal{G}^2$ is an Abelian group. Higher order permutation groups that can be written in terms of a 'forward' ($\hat{R}$) and 'backward' ($\hat{R}^{-1}$) pseudorotation, which essentially casts them as a $\mathcal{G}^2$ group ($\mathcal{G}^{h>2} \rightarrow \tilde{\mathcal{G}}^2 = \{\hat{E}, \hat{R}, \hat{R}^{-1}\}$), are also Abelian. Groups that do not obey this relation, i.e. $[\hat{A}_j, \hat{A}_k] \neq 0$, are called non-Abelian groups (Fig. 79).

While the computationally-expensive step in evaluating eq. 6.13 is calculating the higher-order Lindblad dissipators, it is still impossible to complete the summation by brute force. However, this equation can be rearranged if the Lindbladian has the property:

$$\hat{\mathcal{L}}^{n+1}\hat{\rho} = \hat{\mathcal{L}}^{n}\hat{\mathcal{L}}\hat{\rho} = \lambda_n \hat{\mathcal{L}}\hat{\rho} \tag{6.14}$$

where λ_n is a constant. This states that the dissipator $\hat{\mathcal{L}}\hat{\rho}$ is an eigenfunction of $\hat{\mathcal{L}}^n$ with an eigenvalue λ_n, and we will identify the systems that obey this eigenequation in Chapter 6.3.

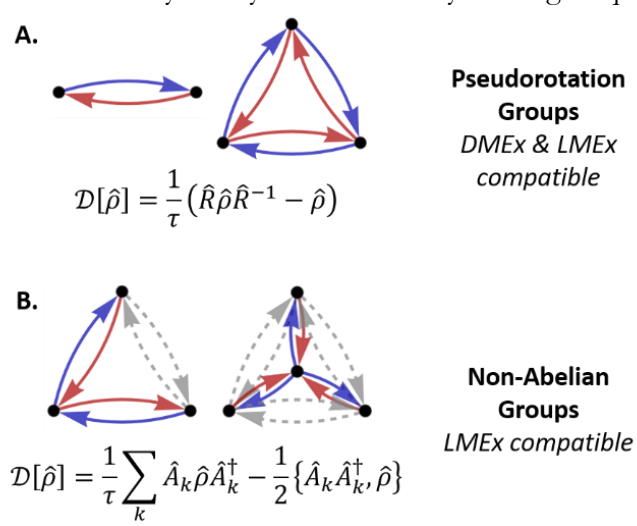

Figure 79: Compatibility of permutation groups with exact master equation formalisms. A. Pseudorotation groups (of order 2 and 3 are shown here) can be described with a dissipator ($\mathcal{D}[\hat{\rho}]$) that rotates ($\hat{R}$) the density matrix basis according to the exchange process. These systems are compatible with both the DMEx and LMEx. **B.** Exact master equations for non-Abelian groups must be described with a Lindbladian dissipator, where the $\hat{A}_k$ operators 'jump' the system to different configurations. Blue arrows are "forward" transitions, red arrows are "backwards" transitions, and the black vertices on the graphs indicate molecular configurations. The gray transitions are those transitions that would be required for the system to be written as a pseudorotation group.

For the case of distinguishable exchange processes, $\hat{\mathcal{L}} = \hat{\mathcal{L}}_k$, and for indistinguishable processes, $\hat{\mathcal{L}}$ is the total Lindbladian. We will refer to this as the infinite-order convergence condition. So long as this condition is satisfied, eq. 6.12 can be written as:

$$\frac{\partial}{\partial t}\hat{\rho} = i[\hat{\rho}, \hat{\mathcal{H}}] + \left\{\sum_k \frac{\hat{\mathcal{L}}_k}{\tau_k} \sum_{n=0}^{\infty} \frac{\lambda_n}{n!}\left(\frac{T}{2\tau_k}\right)^n\right\}\hat{\rho} \tag{6.15}$$

This equation is identical for the case of indistinguishable and distinguishable exchange processes, although the series of λ_n will be different. Now, the term in the brackets only contains constants and is calculated prior to the simulation. Systems that satisfy the infinite-order convergence condition have a closed form solution of the n-sum, which we shall define:

$$\sum_{n=0}^{\infty} \frac{\lambda_n}{n!}\left(\frac{T}{2\tau_k}\right)^n = \Gamma\left(\frac{T}{2\tau_k}\right) \tag{6.16}$$

We call this the exchange generating function, which takes the argument $T/2\tau_k$ and describes how the higher-order dissipator moments can be generated from the leading term in the expansion. This gives the exact Lindblad master equation or LMEx:

$$\frac{\partial}{\partial t}\hat{\rho} = i[\hat{\rho}, \hat{\mathcal{H}}] + \sum_k^N \frac{1}{\tau}\left(\hat{A}_k\hat{\rho}\hat{A}_k^\dagger - \frac{1}{2}\{\hat{A}_k\hat{A}_k^\dagger, \hat{\rho}\}\right)\Gamma\left(\frac{T}{2\tau}\right) \tag{6.17}$$

On first instinct, one would think that $\Gamma(T/2\tau)$ is a complicated function. However, we will show that it is quite simple and, so long as an eigenvalue for higher powers of the Lindbladian may be found, is always a scalar. Thus, eq. 6.17 shows that the action of all higher order dissipators can be rearranged to give a scalar correction to the traditional Lindblad equation of motion, but only if it satisfies the infinite-order convergence condition. Before continuing to derive the conditions where eq. 6.14 is satisfied, we will extend the treatment to the case of non-instantaneous jumps between molecular configurations.

6.2 Lindblad equation for exchange in the non-instantaneous jump limit

In the limit where the coherent degrees of freedom evolve much slower than the molecular rearrangement time during chemical exchange, as is the limit of NMR, we may assume that the system instantaneously jumps between molecular configurations. However, other areas of spectroscopy, such as vibrational spectroscopy, belong to a regime where the coherent degrees of freedom are on the order of the time required for molecular rearrangement. In that case, the model of instantaneous jumps between configurations will no longer suffice and, as such, the correlation functions $g_k(\tau)$ are no-longer δ-correlated. We will refer to this as the non-instantaneous jump limit (NJL). We will use all the assumptions laid out in Section 6.1 except for the assumption that molecules instantaneously jump between sites.

Prior to continuing the derivation, it is beneficial to explore the form of the $\hat{A}_k$ operators. The Lindblad equation is very efficiently expressed in terms of a Hilbert-Fock tensor space, where the Hilbert (or Liouville) space describes the quantum degrees of freedom and the Fock space describes the dissipative degrees of freedom. For chemical exchange, there is no population flux in the system as the ensemble dynamics are stationary. Therefore, the $\hat{A}_k$ are readily constructed from creation ($\hat{a}_k^\dagger$) and annihilation ($\hat{a}_k$) operators as

$$\hat{A}_k = i \exp\left(\frac{-i\pi}{2}\left(\hat{a}_k + \hat{a}_k^\dagger\right)\right) \tag{6.18}$$

where $\hat{a}_k \equiv |\Pi\rangle\langle\Lambda|$ connects configurations Π and Λ, which are states of the Fock space. The $\hat{A}_k$ operators could be constructed directly from the creation and annihilation operators, however that is a less convenient form.

The stationary assumption allows us to define $t - t_1 = \tau$, giving:

$$\frac{\partial}{\partial t}\rho^{(2)} = -\sum_{jk}\int_0^t d\tau\ \left[A_j(\tau) \otimes F_j(\tau), \left[\hat{A}_k^\dagger \otimes \hat{F}_k, \rho\right]\right] \tag{6.19}$$

In doing this, the operators $\hat{A}_k$ and $\hat{F}_k$ lose time-dependence and thus the equation may be expanded rearranged as:

$$\begin{aligned}\frac{\partial}{\partial t}\rho^{(2)} = &\sum_{jk}\int_0^t d\tau\ \left(A_j(\tau)\rho\hat{A}_k^\dagger - A_j(\tau)\hat{A}_k^\dagger\rho\right)\left\langle F_j(\tau)\hat{F}_k\rho_B\right\rangle \\ &+ \int_0^t d\tau\ \left(\hat{A}_k^\dagger\rho A_j(\tau) - \rho\hat{A}_k^\dagger A_j(\tau)\right)\left\langle \hat{F}_k F_j(\tau)\rho_B\right\rangle\end{aligned} \tag{6.20}$$

The double sum permits us to freely reindex the second term in eq. 6.20 as:

$$\begin{aligned}\frac{\partial}{\partial t}\rho^{(2)} = &\sum_{jk}\int_0^t d\tau\ \left(A_j(\tau)\rho\hat{A}_k^\dagger - A_j(\tau)\hat{A}_k^\dagger\rho\right)\left\langle F_j(\tau)\hat{F}_k\rho_B\right\rangle \\ &+ \int_0^t d\tau\ \left(\hat{A}_j^\dagger\rho A_k(\tau) - \rho\hat{A}_j^\dagger A_k(\tau)\right)\left\langle \hat{F}_j F_k(\tau)\rho_B\right\rangle\end{aligned} \tag{6.21}$$

The stationary assumption (3) and the assumption that different exchange processes are uncorrelated (4) permits us to define the stochastic dynamics in $F_k(t)$ as a zero-mean Gaussian process. Doing so permits us to rearrange the correlation function under Isserlis' theorem as:

$$\left\langle F_j(\tau)\hat{F}_k\rho_B\right\rangle = \left\langle F_j(\tau)\hat{F}_k\right\rangle\langle\rho_B\rangle + \left\langle F_j(\tau)\rho_B\right\rangle\left\langle\hat{F}_k\right\rangle + \left\langle\hat{F}_k\rho_B\right\rangle\left\langle F_j(\tau)\right\rangle \tag{6.22}$$

Due to the stationary assumption (3), only the first term survives averaging. Furthermore, $\langle\rho_B\rangle = \hat{E}$ (the identity matrix) by definition. The second correlation function may be rearranged using the permutation under the trace (after using Isserlis' theorem) as:

$$\left\langle\hat{F}_j F_k(\tau)\right\rangle = \left\langle\hat{F}_j e^{-i\hat{\mathcal{H}}_0\tau}\hat{F}_k e^{i\hat{\mathcal{H}}_0\tau}\right\rangle = \left\langle e^{i\hat{\mathcal{H}}_0\tau}\hat{F}_j e^{-i\hat{\mathcal{H}}_0\tau}\hat{F}_k\right\rangle = \left\langle\hat{F}_j(-\tau)\hat{F}_k\right\rangle \tag{6.23}$$

Equations 6.22 and 6.23 allow us to write eq. 6.21 as:

$$\frac{\partial}{\partial t}\rho^{(2)} = \sum_{jk}\int_0^t d\tau\,\left(A_j(\tau)\rho\hat{A}_k^\dagger - A_j(\tau)\hat{A}_k^\dagger\rho\right)\langle F_j(\tau)\hat{F}_k\rangle$$
$$+\int_0^t d\tau\,\left(\hat{A}_j^\dagger\rho A_k(\tau) - \rho\hat{A}_j^\dagger A_k(\tau)\right)\langle F_j(-\tau)\hat{F}_k\rangle \tag{6.24}$$

The $\langle F_j(\tau)\hat{F}_k\rangle$ contains the entire time-dependent component of the exchange interaction and thus dictates both the magnitude of the exchange interaction, giving the exchange rate, as well as the time-correlation of exchange, giving the jump rate τ_c. Specifically, it is proportional to the probability of a single exchange event per unit time, and under the assumption that different exchange processes are uncorrelated (4), we may write this term as:

$$\langle F_j(t)\hat{F}_k\rangle = \delta_{jk}\frac{g_k(t)}{\tau_k} = \delta_{jk}\frac{\exp(-|t|/\tau_c)}{\tau_c\tau_k} \tag{6.25}$$

τ_k is the characteristic lifetime in the two configurations connected by the process $\hat{F}_k$, and its inverse gives the exchange rate between sites. The time-dependent part of the correlation function $g_k(t)$ is even and unit normalized over the region $[0,\infty)$, and we have shown the corresponding form of $g_k(t)$ if it is taken as a single exponential. Thus, we may rewrite eq. 6.24 as:

$$\frac{\partial}{\partial t}\rho^{(2)} = \sum_{k}\int_0^t d\tau\,\left(A_k(\tau)\rho\hat{A}_k^\dagger - A_k(\tau)\hat{A}_k^\dagger\rho\right)\frac{g_k(\tau)}{\tau_k}$$
$$+\int_0^t d\tau\,\left(\hat{A}_k^\dagger\rho A_k(\tau) - \rho\hat{A}_k^\dagger A_k(\tau)\right)\frac{g_k(\tau)}{\tau_k} \tag{6.26}$$

The $\hat{A}_k$ operators have the property:

$$A_k(\tau) = e^{-i\hat{\mathcal{H}}_0\tau}\hat{A}_k e^{i\hat{\mathcal{H}}_0\tau} = e^{i\hat{\mathcal{L}}_k\hat{\mathcal{H}}_0\tau}\hat{A}_k = \hat{A}_k e^{-i\hat{\mathcal{L}}_k\hat{\mathcal{H}}_0\tau} \tag{6.27}$$

Using 6.27, we may rearrange eq. 6.26 as:

$$\begin{aligned}\frac{\partial}{\partial t}\rho^{(2)} = \sum_k \left(\int_0^t d\tau\, e^{i\hat{\mathcal{L}}_k\hat{\mathcal{H}}_0\tau}\frac{g_k(\tau)}{\tau_k}\right)\left(\hat{A}_k\rho\hat{A}_k^\dagger - A_k\hat{A}_k^\dagger\rho\right) \\ +\left(\hat{A}_k^\dagger\rho\hat{A}_k - \rho\hat{A}_k^\dagger\hat{A}_k\right)\left(\int_0^t d\tau\, e^{-i\hat{\mathcal{L}}_k\hat{\mathcal{H}}_0\tau}\frac{g_k(\tau)}{\tau_k}\right)\end{aligned} \tag{6.28}$$

Using the definition of $\hat{A}_k$ (eq. 6.18), we may define the Lindbladian dissipator as

$$\hat{A}_k\rho\hat{A}_k^\dagger - A_k\hat{A}_k^\dagger\rho = \hat{A}_k^\dagger\rho\hat{A}_k - \rho\hat{A}_k^\dagger\hat{A}_k = \frac{1}{2}\left(\hat{A}_k\rho\hat{A}_k^\dagger - \frac{1}{2}\{\hat{A}_k\hat{A}_k^\dagger, \rho\}\right) \equiv \frac{1}{2}\hat{\mathcal{L}}_k\rho, \tag{6.29}$$

and noting that (by eq. 6.18), $\hat{A}_k^\dagger\hat{A}_k = \hat{E}$. The factor of ½ arises as each of the terms in eq. 6.29 only represents half of the total dissipator. For chemical exchange, $\hat{\mathcal{L}}_k$ generates the population inversion between the two sites connected by the $\hat{A}_k$ operator.

The upper limits of the integration in eq. 6.28 are raised to infinity such that the equation describes a full exchange process, i.e., the jump must fully interconvert populations to describe an exchange event. This effectively restricts the value of $\tau_c < \tau_k$. We may now define

$$\hat{\mathcal{J}}_k \equiv \int_0^\infty d\tau\, e^{i\hat{\mathcal{L}}_k\hat{\mathcal{H}}_0\tau} g_k(\tau), \tag{6.30}$$

which is a complex spectral density function, and permits us to rewrite eq. 6.28 as:

$$\frac{\partial}{\partial t}\rho^{(2)} = \sum_k \frac{1}{2\tau_k}\left(\hat{\mathcal{J}}_k\hat{\mathcal{L}}_k\rho + \hat{\mathcal{L}}_k\rho\hat{\mathcal{J}}_k^\dagger\right) \tag{6.31}$$

Equation 6.31 is the most general form of the chemical exchange master equation and exactly represents all the relevant physical effects when the equation of motion is analytically integrated. It is useful to refer to $\hat{\mathcal{J}}_k$ as the jump interaction, which tends to unity for $\tau_c \to 0$ and recovers the traditional master equation for exchange in Lindblad form. Before continuing to derive higher-order corrections to this equation, it is useful to rearrange the complex spectral density function into its real and imaginary components:

$$\hat{\mathcal{J}}_k = \frac{1}{2}\hat{\gamma}_k - i\hat{\pi}_k \tag{6.32}$$

$$\hat{\gamma}_k = \int_{-\infty}^{\infty} d\tau\, e^{i\hat{\mathcal{L}}_k\hat{\mathcal{H}}_0\tau} g_k(\tau) \tag{6.33}$$

$$\hat{\pi}_k = -\int_{0}^{\infty} d\tau \sin\left(\hat{\mathcal{L}}_k\hat{\mathcal{H}}_0\tau\right) g_k(\tau) \tag{6.34}$$

The operators $\hat{\gamma}_k$ and $\hat{\pi}_k$ are real-valued and correspond to the Fourier transform and half sine transform, respectively. Using these definitions in eq. 6.31 and rearranging gives:

$$\frac{\partial}{\partial t}\rho^{(2)} = \sum_k \frac{1}{2}\left\{\hat{\gamma}_k, \frac{\hat{\mathcal{L}}_k\rho}{2\tau_k}\right\} - i\left[\hat{\pi}_k, \frac{\hat{\mathcal{L}}_k\rho}{2\tau_k}\right] \tag{6.35}$$

There are two, novel physical effects that are encapsulated in eq. 6.35. Firstly, the term proportional to $\hat{\pi}_k$ is isomorphic to the Liouville-von Neumann equation and generates coherent evolution in $\hat{\mathcal{L}}_k\rho$ proportional to interactions dictated by $\hat{\mathcal{L}}\hat{\mathcal{H}}_0$, the difference Hamiltonian between exchange sites. The term proportional to $\hat{\gamma}_k$ is most easily interpreted in the eigenbasis of $\hat{\mathcal{L}}\hat{\mathcal{H}}_0$, which may be written as

$$\frac{1}{2}\left\{\hat{\gamma}_k, \frac{\hat{\mathcal{L}}_k\rho}{2\tau_k}\right\}_{mn} = \left(\frac{\hat{\mathcal{L}}_k\rho}{\tau_k}\right)_{mn}\left(\frac{\gamma_m^{(k)} + \gamma_n^{(k)}}{2}\right), \tag{6.36}$$

where $\gamma_m^{(k)}$ is the mth eigenvalue of $\hat{\gamma}_k$. Equation 6.36 shows that each element mn of the exchanging density matrix $\hat{\mathcal{L}}\rho$ is attenuated by the average of the $\gamma_m^{(k)}$ and $\gamma_n^{(k)}$ eigenvalues. This corresponds to a relaxation process of the system that is mediated by the jump interaction and drives $\hat{\mathcal{L}}_k\rho \rightarrow \rho$, the state before exchange. As such, the jump interaction generates both coherent evolution with $\hat{\pi}_k$ as well as dissipative evolution with $\hat{\gamma}_k$. We will examine the impact of these interactions on extracted parameters in a later section.

While isolating the unitary and dissipative components of $\hat{\mathcal{J}}_k$ facilitates analysis of the problem, it will be beneficial later to cast eq. 6.31 in a different form. If we introduce the transformation of a general operator $\hat{O}$

$$\bar{O} = \hat{O}\hat{\mathfrak{J}} + \hat{\mathfrak{J}}\hat{O}^{\dagger}, \tag{6.37}$$

where $\hat{\mathfrak{J}}$ is the matrix of ones and the basis is chosen to be the eigenbasis of $\hat{O}$, then we may rewrite eq. 6.31 as:

$$\frac{\partial}{\partial t}\rho^{(2)} = \sum_k \frac{\hat{\mathcal{L}}_k\rho \circ \bar{\mathcal{J}}_k}{\tau_k} \tag{6.38}$$

The $\circ$ represents the Hadamard (element-by-element) product of the dissipator with the complex spectral density operator. This essentially is an algebraic implementation of eq. 6.36. Importantly, this transformation is only allowed if the basis set is chosen to be the eigenbasis of $\hat{\mathcal{L}}_k\hat{\mathcal{H}}$.

As mentioned previously, eq. 6.31 contains all the relevant physical effects for chemical exchange and is exact in the limit where it may analytically integrated. In this limit, the exchange interaction couples linearly with the coherent degrees of freedom, thus permitting the Dyson series to be truncated to its leading term. However, analytically integrating eq. 6.31

rapidly becomes not feasible as the system size grows. For instance, N coupled three-level systems where there is coherent couplings between each of the N sites span a $3^N N$-dimensional Hilbert-Fock space, which can only analytically diagonalized for $N \leq 6$, as current computational abilities cannot efficiently perform diagonalization in spaces with dimensionalities of approximately $2^{14} = 16{,}384$ states. Instead, it is beneficial to think of this result in terms of a simulation method where the dynamics are numerically integrated over some period T. To avoid violating the assumption of linear coupling between the exchange and coherent degrees of freedom, $T \ll \left\|\hat{\mathcal{H}}_0 + \hat{\mathcal{H}}_1(t)\right\|^{-1}$, which forces the simulation to utilize small integration step sizes. Previously, we overcame this by deriving the closed form solution for the Dyson series in the magnetic resonance limit when the jump time $\tau_c \to 0$ and the jump interaction is negligible. Here, we will show that a closed form solution of the Dyson series is obtainable for all physical limits.

Systems undergoing chemical exchange between multiple sites may be classified based on the distinguishability of the exchange processes. For systems that have distinguishable exchange processes, the self-correlated assumption (4) allows each distinguishable exchange process to be treated identically, as the assumption disallows coupling between process by choice of basis. However, systems may also have indistinguishable exchange processes, such as the rotations of a methyl group. Under such conditions, the self-correlated assumption (4) does not prevent different exchange processes from being coupled. Importantly, any single distinguishable exchange processes is equivalent to the case of indistinguishable processes between two sites. As such, we will pursue the derivation for the more challenging case of indistinguishable processes and reduce it to the statistical case of distinguishable processes as a limit.

We may continue the derivation of higher order exchange interactions starting with fourth-order term of the Dyson series, noting that the stationary assumption only permits even-order terms to be non-zero:

$$\frac{\partial}{\partial t}\rho^{(4)} = \vec{\mathcal{T}} \sum_{jklm} \int_0^t dt_1 \int_0^{t_1} dt_2 \int_0^{t_2} dt_3 \left[\mathcal{H}_j(t), \left[\mathcal{H}_k^\dagger(t_1), \left[\mathcal{H}_l(t_2), \left[\mathcal{H}_m^\dagger(t_3), \rho\right]\right]\right]\right] \tag{6.39}$$

The self-correlated assumption (4) has the repercussion that

$$\hat{F}_j = \hat{F}_k \therefore \left[\hat{F}_j, \hat{F}_k\right] = 0 \; \forall \, jk, \tag{6.40}$$

which permits us to freely factor the stochastic operators from the expression. Importantly, this relation does not extend to the $\hat{A}_k$ operators as they span distinct Fock states. This gives:

$$\frac{\partial}{\partial t}\rho^{(4)} = \vec{\mathcal{T}} \sum_{jklm} \int_0^t dt_1 \int_0^{t_1} dt_2 \int_0^{t_2} dt_3 \left[A_j(t), \left[A_k^\dagger(t_1), \left[A_l(t_2), \left[A_m^\dagger(t_3), \rho\right]\right]\right]\right] \times \left\langle F_j(t) F_k(t_1) F_l(t_2) F_m(t_3) \rho_B \right\rangle \tag{6.41}$$

The time-ordered integrals may be decoupled by dividing by the degeneracy of the time ordering, which for three time-ordered integrals is $3!$:

$$\frac{\partial}{\partial t}\rho^{(4)} = \frac{1}{3!} \sum_{jklm} \int_0^t dt_1 \int_0^t dt_2 \int_0^t dt_3 \left[A_j(t), \left[A_k^\dagger(t_1), \left[A_l(t_2), \left[A_m^\dagger(t_3), \rho\right]\right]\right]\right] \times \left\langle F_j(t) F_k(t_1) F_l(t_2) F_m(t_3) \rho_B \right\rangle \tag{6.42}$$

The four-point correlator may then be factored by Isserlis' theorem as (retaining only non-zero terms):

$$\frac{\partial}{\partial t}\rho^{(4)} = \frac{1}{3!}\sum_{jklm}\int_0^t dt_1 \int_0^t dt_2 \int_0^t dt_3 \left[A_j(t), \left[A_k^\dagger(t_1), \left[A_l(t_2), \left[A_m^\dagger(t_3), \rho\right]\right]\right]\right]$$

$$\times \begin{pmatrix} \langle F_j(t)F_k(t_1)\rangle\langle F_l(t_2)F_m(t_3)\rangle \\ +\langle F_j(t)F_l(t_2)\rangle\langle F_k(t_1)F_m(t_3)\rangle \\ +\langle F_j(t)F_m(t_3)\rangle\langle F_k(t_1)F_l(t_2)\rangle \end{pmatrix} \tag{6.43}$$

As the time-ordered integrals are now decoupled, each term in eq. 6.43 corresponds to a product of two-point correlators that, under the stationary assumption (3), are only dependent on a time-difference and are identical. For eq. 6.43 to be physically valid for chemical exchange, we restrict the indices $j = k$ and $l = m$ such that an exchange event must be completed before another exchange event begins. Using the form of the two-point correlators given in eq. 6.25, raising the upper limits of the integrals acting on the commutators to ∞, and moving the remaining integral out of the commutators, we may write eq. 6.43 as:

$$\frac{\partial}{\partial t}\rho^{(4)} = \sum_{jk}\int_0^\infty d\tau_1 \left[A_j(\tau_1), \left[\hat{A}_j^\dagger, \int_0^\infty d\tau_2 \left[A_k(\tau_2), \left[\hat{A}_k^\dagger, \rho\right]\right] g_k(\tau_2)\right]\right] g_j(\tau_1)$$

$$\times \frac{3}{3!}\frac{1}{\tau_j\tau_k}\int_0^T d\tau_2 \tag{6.44}$$

Note that the self-correlated assumption (4) also has the ramification that $\tau_j = \tau_k$ and $g_j(\tau) = g_k(\tau_2)$. Equation 6.44 has the form of two nested applications of the second-order Dyson term, and thus using eq. 6.31, may be written as:

$$\frac{\partial}{\partial t}\rho^{(4)} = \frac{1}{2}\sum_{jk}\frac{T}{\tau_j\tau_k}\left(\hat{\mathcal{J}}_j\hat{\mathcal{L}}_j\left(\hat{\mathcal{J}}_k\hat{\mathcal{L}}_k\rho + \hat{\mathcal{L}}_k\rho\hat{\mathcal{J}}_k^\dagger\right) + \hat{\mathcal{L}}_j\left(\hat{\mathcal{J}}_k\hat{\mathcal{L}}_k\rho + \hat{\mathcal{L}}_k\rho\hat{\mathcal{J}}_k^\dagger\right)\hat{\mathcal{J}}_j^\dagger\right) \tag{6.45}$$

Using the transformation described by eq. 3.37, we may rewrite eq. 6.45 as:

$$\frac{\partial}{\partial t}\rho^{(4)} = \frac{1}{2}\sum_{jk}\frac{T}{\tau_j\tau_k}\left(\hat{\mathcal{L}}_j\hat{\mathcal{L}}_k\rho \circ \bar{\mathcal{J}}_k \circ \bar{\mathcal{J}}_j\right) \tag{6.46}$$

Equation 6.46 is the form of the fourth-order Dyson term, and describes two exchange events. Importantly, as the integration step $T \to dt$, this term (and all higher order terms) tend to zero, as the exchange and coherent degrees of freedom couple linearly in that limit. Here, we see that the exchange interaction is quadratically coupled to the coherent degrees of freedom.

It will again be convenient to rearrange the form of eq. 6.46 to facilitate further analysis. The Hadamard product is associative, distributive, and commutative, and allows $\bar{\mathcal{J}}_k$ to be essentially treated as a scalar quantity (c.f. eq. 6.38), letting us rearrange eq. 6.46 as:

$$\frac{\partial}{\partial t}\rho^{(4)} = \frac{T}{2}\left(\sum_k \frac{\hat{\mathcal{L}}_k \circ \bar{\mathcal{J}}_k}{\tau_k}\right)^2 \rho \tag{6.47}$$

At this juncture, the higher order Dyson series terms may be calculated using the same procedure as laid out for the fourth-order term, and the entire series may be re-summed as:

$$\frac{\partial}{\partial t}\rho = \sum_{n=0}^{\infty}\left(\frac{T}{2}\right)^n \frac{1}{n!}\left(\sum_k \frac{\hat{\mathcal{L}}_k \circ \bar{\mathcal{J}}_k}{\tau_k}\right)^{n+1} \rho \tag{6.48}$$

For convenience, have changed the indexing to $n = 2m + 2$, where m is the term of the Dyson expansion. Conventionally, this expression is truncated at certain orders to generate a certain correction to the equation of motion. However, if the dissipator satisfies the eigenequation

$$\left(\sum_k \hat{\mathcal{L}}_k\right)^n \left(\sum_k \hat{\mathcal{L}}_k\right)\rho = \lambda_n\left(\sum_k \hat{\mathcal{L}}_k\right)\rho, \tag{6.49}$$

then eq. 6.48 can be rearranged as:

$$\frac{\partial}{\partial t}\rho = \left(\sum_k \frac{\hat{\mathcal{L}}_k \circ \bar{\mathcal{J}}_k}{\tau_k}\right) \circ \sum_{n=0}^{\infty} \frac{\lambda_n}{n!}\left(\sum_k \frac{T\bar{\mathcal{J}}_k}{2\tau_k}\right)^n \rho \tag{6.50}$$

Similar to eq. 6.16, we may define an exchange generating operator

$$\sum_{n=0}^{\infty} \frac{\lambda_n}{n!}\left(\sum_k \frac{T\bar{\mathcal{J}}_k}{2\tau_k}\right)^n = \bar{\Gamma}\left(\frac{T}{2\tau_k}\right), \tag{6.51}$$

which relates all higher powers of the exchange interaction to the leading term. This term additionally couples the jump interaction for each processes with the additional k-sum inside the infinite series. Furthermore, there is only one exchange generating operator for a set of indistinguishable exchange processes. For this case, any $\bar{\mathcal{J}}_k$ is equivalent to $\bar{\mathcal{J}}_l$ up to a similarity transformation, but this was the most efficient representation of the problem. Importantly, as the factors of $\bar{\mathcal{J}}_k$ arise as Hadamard products ($\bar{\mathcal{J}}_k \circ \bar{\mathcal{J}}_l \circ \cdots$), this operator does not require diagonalization and each element may be treated as a separate scalar. This yields:

$$\frac{\partial}{\partial t}\rho = \sum_k \frac{\hat{\mathcal{L}}_k \rho \circ \bar{\mathcal{J}}_k}{\tau_k} \circ \bar{\Gamma}\left(\frac{T}{2\tau_k}\right) \tag{6.52}$$

We have used the commutation property of Hadamard products to rearrange this equation such that it is proportional to eq. 6.38.

If we take eq. 6.52 to the limit of distinguishable molecular processes, which effectively decouples each term in the k-sum and requires that any process obeys the relation

$$\left(\hat{\mathcal{L}}_k\right)^n \left(\hat{\mathcal{L}}_k\right)\rho = \lambda_n \left(\hat{\mathcal{L}}_k\right)\rho, \tag{6.53}$$

where λ_n are the eigenvalues of the individual Lindbladians, then may rewrite the infinite Dyson series as:

$$\frac{\partial}{\partial t}\rho = \left(\sum_k \frac{\hat{\mathcal{L}}_k \circ \bar{\mathcal{J}}_k}{\tau_k}\right) \circ \sum_{n=0}^{\infty} \frac{\lambda_n}{n!}\left(\frac{T\bar{\mathcal{J}}_k}{2\tau_k}\right)^n \rho \tag{6.54}$$

Note that there is not a second summation within the infinite series, and each processes is decoupled from one another. For the case of distinguishable molecular processes, we may define a slightly different exchange generating function:

$$\sum_{n=0}^{\infty} \frac{\lambda_n}{n!}\left(\frac{T\bar{\mathcal{J}}_k}{2\tau_k}\right)^n = \bar{\Gamma}_k\left(\frac{T}{2\tau_k}\right) \tag{6.55}$$

Note that there will be a different exchange generating operator for each distinguishable molecular process. Finally, this yields the exact form of the exchange interaction for this case:

$$\frac{\partial}{\partial t}\rho = \sum_k \frac{\hat{\mathcal{L}}_k \rho \circ \bar{\mathcal{J}}_k}{\tau_k} \circ \bar{\Gamma}_k\left(\frac{T}{2\tau_k}\right) \tag{6.56}$$

It is interesting to examine the various limits of these equations to examine the various levels of theory that may obtained with these equations. In either case, the first term is simply given by the leading order form of the exchange interaction, given by eq. 6.31. In the limit when the integration step size $T \to dt$, these equations both reduce to eq. 6.31. Furthermore, in the limit when the jump time $\tau_c \to 0$, the jump interaction operator $\bar{\mathcal{J}}_k$ reduces to unity. Finally, the traditional chemical exchange master equation in Lindblad form is recovered when the limits $T \to dt$ and $\tau_c \to 0$ are simultaneously imposed.

Hence, we showed that with a minimal number of assumptions that a closed form solution of the Dyson series could be obtained for chemical exchange applicable to any physical limit. In doing so, we derived a new interaction arising from the jump dynamics between sites that is omitted from conventional theory. Furthermore, taking this result to the analytical integration and instantaneous jump limits recovers the traditional master equation

for exchange. In the following sections, we will examine the performance of this framework and the physical ramifications of the jump interaction.

6.3 Systems that satisfy the infinite-order convergence condition

Throughout the derivation in previous sections, we have noted that if the Lindbladians obey the eigenequation

$$\left(\sum_k \hat{\mathcal{L}}_k\right)^n \left(\sum_k \hat{\mathcal{L}}_k\right)\rho = \lambda_n \left(\sum_k \hat{\mathcal{L}}_k\right)\rho, \tag{6.57}$$

that the Dyson series may be written as being proportional to the leading order interaction by a so-called exchange generating function (in the IJL) or an exchange generating operator (in the NJL). Perhaps the easiest method to find system geometries that satisfy eq. 6.57 is to simply computationally evaluate $\mathcal{L}^2\rho \propto \mathcal{L}\rho$ for a set of $\hat{A}_k$ that form different groups of order h. Conveniently, this only requires the Fock-space of the system. If the quadratic Lindbladian is proportional to the leading Lindbladian by a scalar, then all higher order Lindbladians may be written as being proportional to the leading term, thus satisfying eq. 6.57. Two-site exchange always satisfies eq. 6.57. Three set of operators that permit exchange between three configurations are:

$$\{\hat{A}_k\} = \left\{\begin{pmatrix} 0 & 1 & 0 \\ 1 & 0 & 0 \\ 0 & 0 & 1 \end{pmatrix}, \begin{pmatrix} 1 & 0 & 0 \\ 0 & 0 & 1 \\ 0 & 1 & 0 \end{pmatrix}, \begin{pmatrix} 0 & 0 & 1 \\ 0 & 1 & 0 \\ 1 & 0 & 0 \end{pmatrix}\right\} \tag{6.58}$$

These operators correspond to the Fock-space, which is only ever populated on the diagonal elements of the space. The first operator exchanges the first two configurations, the second

operator exchanges the second two configurations, and the third operator exchanges the first and third configurations. Using an arbitrary Fock density matrix of

$$\hat{\rho} = \begin{pmatrix} \rho_1 & 0 & 0 \\ 0 & \rho_2 & 0 \\ 0 & 0 & \rho_3 \end{pmatrix}, \tag{6.59}$$

one can solve the expression

$$\sum_{i \in k} \hat{\mathcal{L}}_i \left(\sum_{j \in k} \hat{\mathcal{L}}_j \hat{\rho} \right) = \lambda \left(\sum_{j \in k} \hat{\mathcal{L}}_j \hat{\rho} \right) \tag{6.60}$$

for λ, which is the scalar relating the linear ($\hat{\mathcal{L}}$) and quadratic ($\hat{\mathcal{L}}^2$) Lindbladians. The indices $i \in k$ and $j \in k$ span subsets of the exchange operators in eq. 6.58. The only groups which directly satisfy eq. 6.57 are pseudorotation groups, for which every state has a transition to every other state. It is convenient to normalize the dissipator by $1/N$, where N is the number of transitions in the group, so that the trace over all ensembles is unity. Under these conditions, the value of λ_n may be expressed in terms of the group order h and $N = (h^2 - h)/2$, as

$$\gamma_n = \left(\frac{-h}{N} \right)^n, \tag{6.60}$$

which makes the exchange generating function

$$\Gamma\left(\frac{T}{2\tau} \right) = \exp\left(\frac{-hT}{2N\tau} \right) \tag{6.61}$$

for pseudorotation groups. Importantly, the case of distinguishable exchange processes simply corresponds to the $h = 2$ case. Similar to the DMEx, we see that the exchange generating function is a simple, scalar correction term to the equation of motion but do so using a far more general set of assumptions.

There are many interesting systems that do not belong to an Abelian pseudorotation group, the simplest of which is the non-cyclic 3-state system (Figure 79B, left). This case does not directly satisfy the infinite order convergence condition and thus does not inherently have an LMEx equation. However, we may consider this case as if it were a $\mathcal{G}^3$ system with two transitions that are removed, which in essence correspond to a $\mathcal{G}^2$ system. As both of the pseudorotation groups satisfy eq. 6.57, it is possible to construct an LMEx based on the difference between the two groups:

$$\frac{\partial}{\partial t}\hat{\rho} = \frac{1}{N}\sum_{k}^{N}\frac{\hat{\mathcal{L}}_k\hat{\rho}}{\tau}\exp\left(\frac{-hT}{2N\tau}\right) - \frac{1}{N}\sum_{j\in k}^{M}\frac{\hat{\mathcal{L}}_j\hat{\rho}}{\tau}\Gamma'\left(\frac{T}{2\tau}\right) \tag{6.62}$$

The first term gives the pseudorotation 'head' group ($\mathcal{G}^3$ in this example, $h = 3; N = 3$) and the second term in the non-Abelian 'forming; group ($\mathcal{G}^2$) where $j \in k$ form a pseudorotation group of order f with $M = (f^2 - f)/2$ transitions ($\mathcal{G}^2$ in this example, $f = 2; M = 1$). The exchange generating function $\Gamma'(T/2\tau)$ is no longer given by 6.61, as it must also consider all pathways that lead to those transitions absent from the head pseudorotation group. Finding the exchange generating function $\Gamma'(T/2\tau)$ requires a slightly different form than 6.61, as the proposed equation of motion is constructed as a difference between groups. Therefore, the function $\Gamma'(T/2\tau)$ arises from the difference mapped by k and $j \in k$. This was explored computationally using a similar method as when defining 6.60 by evaluating:

$$\left(\sum_{k}\hat{\mathcal{L}}_k\hat{\rho}\right)^n - \left(\sum_{j\in k}\hat{\mathcal{L}}_j\hat{\rho}\right)^n = \lambda_n\left(\sum_{k}\hat{\mathcal{L}}_k\hat{\rho} - \sum_{j\in k}\hat{\mathcal{L}}_j\hat{\rho}\right) \tag{6.63}$$

For this equality to hold, λ_n must be the same for both powers of the Lindbladians on the left-hand side of eq. 6.63, such that the desired group formed by the set $\{k - j\}$ transitions is

also an eigenfunction of the left-hand side. Upon evaluation, it became clear that λ_n was not an elementary function that would have an obvious series expansion, as was the case in Abelian systems. Instead, the λ_n series can simply be expanded in terms of a Maclaurin series and plotted, which requires that enough terms be calculated so to ensure series convergence over a desired region. By inspection, we found that the closed form solution of $\Gamma'(T/2\tau)$ for non-Abelian groups formed by linear combinations of Abelian groups, like the $\mathcal{G}^3 - \mathcal{G}^2$ example described above, is:

$$\Gamma'\left(\frac{T}{2\tau}\right) = \exp\left(\frac{-hT}{2N\tau}\right) - \frac{h-f}{f}\left\{\left(1 - \exp\left(\frac{-fMT}{2N\tau}\right)\right)\exp\left(\frac{-(h-f)T}{2N\tau}\right)\right\} \qquad (6.64)$$

Again, we see that the exchange generating function is a scalar correction to the traditional equation of motion. Interestingly, it has very different behavior than the generating functions of single pseudorotation groups (Fig. 80). One of the most pronounced differences is that, while the generating function for Abelian groups is always positive, the generating function for the non-Abelian group is bipolar. Remembering that the generating function relates all higher order Lindbladians to the leading Lindbladian, a bipolar generating function indicates that in certain regimes of $T/2\tau$, the flow of population dictated by the leading Lindbladian is

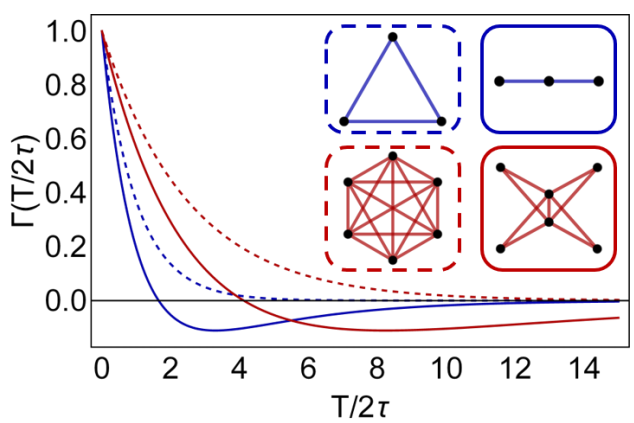

Figure 80: Exchange generating functions for Abelian and non-Abelian groups. The generating functions for the Abelian $\mathcal{G}^3$ (dashed blue), non-Abelian $\mathcal{G}^3 - \mathcal{G}^2$ (solid blue), Abelian $\mathcal{G}^6$ (dashed red), and non-Abelian $\mathcal{G}^6 - \mathcal{G}^4$ (solid red) groups are shown. For reference, the graphs corresponding to these groups are shown inset.

reversed. In both cases, the $\Gamma(\infty)$ condition always tends to zero, which effectively removes exchange from the equation of motion. This happens because if $T \gg \tau$, then it appears as if the system has only undergone an infinite number of exchange events and can be thought of as a repercussion of the stationary approximation. Additionally, larger permutation groups lead to more slowly decaying exchange generating functions, as there are more exchange pathways that must be traversed before the system again appears to be stationary. Taking the difference between Abelian permutation groups is not restricted to using only one non-Abelian forming group, so long as $[\mathcal{G}^n, \mathcal{G}^m] = 0$, and the forming groups may be of different orders ($n \neq m$). In that case, each of the different generating groups will have a unique exchange generating function that is constructed as a summation of terms given by eq. 6.64.

6.4 Error analysis of exact Lindblad Master Equations for exchange

To assess the performance of the LMEx equations, we tested the solution convergence for molecular systems with $\mathcal{G}^3$ (methyl rotation), $\mathcal{G}^3 - \mathcal{G}^2$ (hindered rotation), and $\mathcal{G}^4 - \mathcal{G}^3$ (Berry pseudorotation) exchange dynamics in the IJL. For each condition, a 4 spin-1/2 system was parameterized with the Hamiltonian (units are all rad s^{-1})

$$\begin{aligned} \hat{\mathcal{H}} &= \omega_a \hat{I}_{2z} + \omega_s\left(\hat{I}_{3z} + \hat{I}_{4z}\right) + J_a \hat{I}_{1z}\hat{I}_{2z} \\ &+ J_s\left(\hat{I}_{1z}\hat{I}_{3z} + \hat{I}_{1z}\hat{I}_{4z}\right) + J_r\left(\hat{I}_2 \cdot \hat{I}_3 + \hat{I}_2 \cdot \hat{I}_4\right) \end{aligned} \tag{6.65}$$

and the five parameters ω_a, ω_s, J_a, J_s and J_r were sampled to thoroughly explore the performance. This Hamiltonian was cast in a frame rotating about $\omega_1 \hat{I}_{1z}$, permitting us to drop this term from eq. 6.65. Importantly, we have ensured that the exchange rate was an

order of magnitude larger than the largest possible coupling strength, forcing these systems into the limit where exchange is a strong perturbation.

For error analysis, a ground-truth simulation was calculating using the solution at $T = \tau/500$, where only 0.2% of the ensemble undergoes at least a single exchange per timestep. The solution error was tested for the condition $T = \tau/5$, corresponding to 20% of ensemble undergoing exchange during a single timestep, where τ is the characteristic time of the system ($1/k_{ex}$). Importantly, when 20% of the molecules are allowed to undergo a single exchange, 4% of the ensemble will experience two exchange events during this period. The LMEx accounts for this difference in the exchange generating function, whereas it is not considered in the traditional equation of motion. A special case of this calculation arises when the system is exchange invariant, and as such, the error of the Lindblad and LMEx solutions are identical ($\sigma_{LME} = \sigma_{LMEx}$).

We found that the LMEx generates solutions that are consistently more converged than the those generated by the Lindblad equation (Fig. 81). For the Abelian $\mathcal{G}^3$ group, $\langle\sigma_{LMEx}\rangle = (0.91 \pm 0.62)\%$ whereas $\langle\sigma_{LME}\rangle = (4.0 \pm 1.5)\%$. The non-Abelian $\mathcal{G}^3 - \mathcal{G}^2$ group gives $\langle\sigma_{LMEx}\rangle = (0.55 \pm 0.40)\%$ and $\langle\sigma_{LME}\rangle = (2.37 \pm 0.72)\%$. Finally, the non-Abelian $\mathcal{G}^4 - \mathcal{G}^3$ group yields $\langle\sigma_{LMEx}\rangle = (0.15 \pm 0.12)\%$ and $\langle\sigma_{LME}\rangle = (1.21 \pm 0.70)\%$. These correspond to approximately 5- and 10-fold increases in the convergence radius of the solution for no additional computational cost. As the LMEx rigorously accounts for all moments in exchange, errors that appear in the solution are due to the first-order integration method not encapsulating the time-ordering of the coherent and exchange processes. Even so, the LMEx for any of these systems produces solutions that are, on average, above 99% converged at $T = \tau/5$.

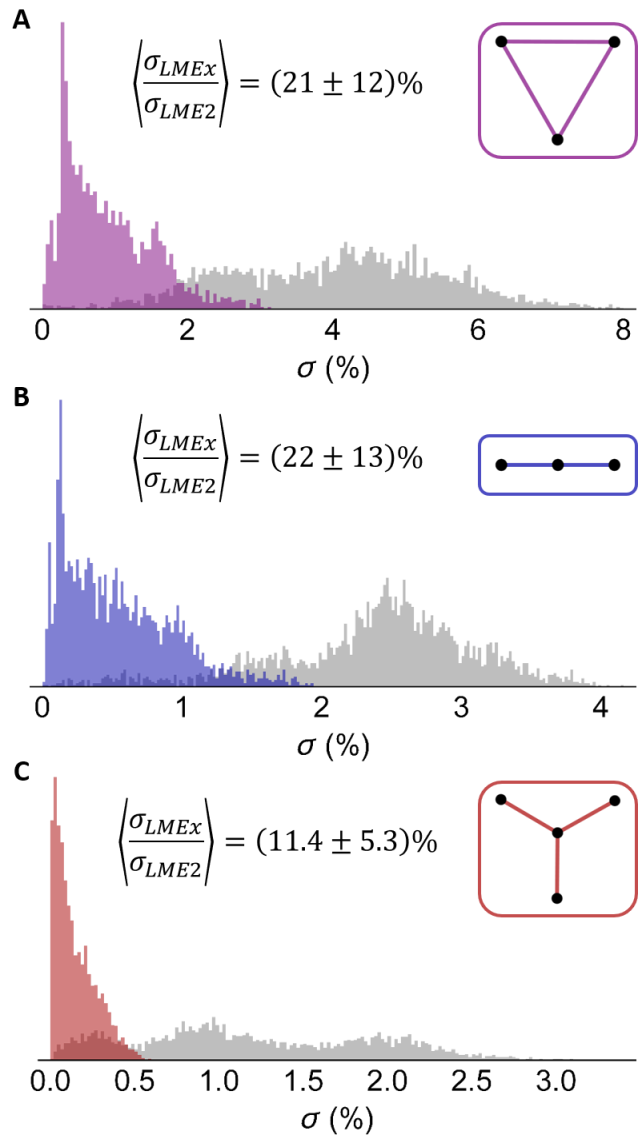

Figure 81: Performance of LMEx equations over the traditional master equation. Exchange dynamics with **A.** Abelian $\mathcal{G}^3$ (blue), **B.** non-Abelian $\mathcal{G}^3 - \mathcal{G}^2$ (purple), and **C.** non-Abelian $\mathcal{G}^4 - \mathcal{G}^3$ groups. The gray histogram indicates the error in the traditional Lindblad equation for the same system parameters. There are no conditions where $\sigma_{Lindblad} > \sigma_{LMEx}$. Solutions were iterated 3200 times for each of the systems to generate the error histograms, and were compared to a solution at $T = \tau/500$ as a ground truth.

Our examination of the error in the NJL follows closely with the same interrogation done for the IJL, but here we must also assess when it is important to utilize each successively more accurate model. Here, we are comparing to a solution that assumes a finite jump time to examine deterioration of the traditional assumption of the instantaneously jump. To

accomplish this, we calculated the dynamics of a three spin-1/2 system with analogous coherent parameters as to those given by eq. 6.65, where the Hamiltonian is:

$$\hat{\mathcal{H}} = \omega_B \hat{I}_{2z} + \omega_C \hat{I}_{3z} + 2\pi \sum_{i<j} J_{ij}\, \hat{I}_i \cdot \hat{I}_j \tag{6.66}$$

In this case, the reference frame is rotated about ω_A, the resonance frequency of the first spin-1/2 nucleus, and there are five adjustable parameters that may be iterated (Fig. 82A). For this

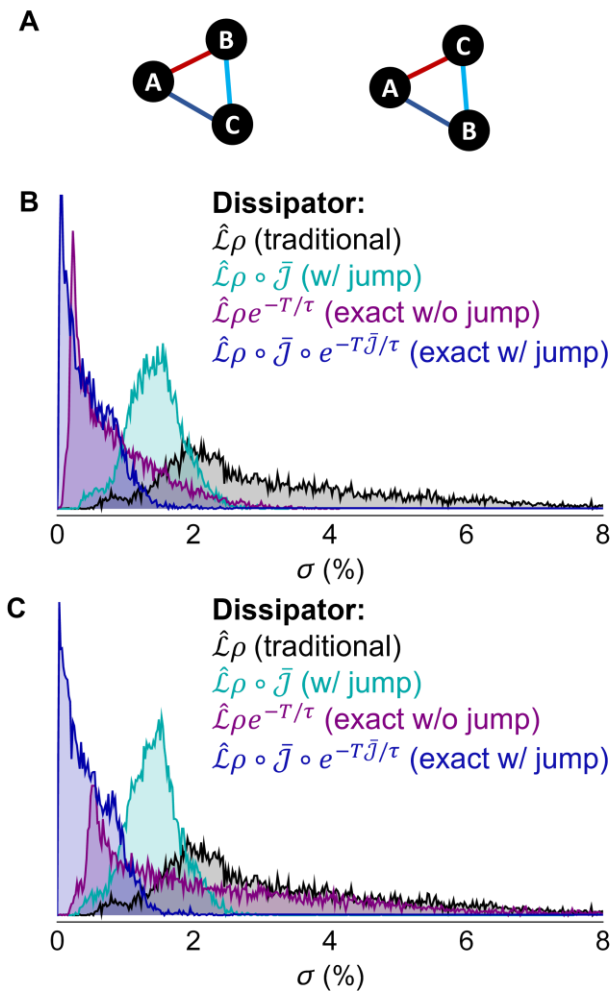

Figure 82: Error analysis in models for exchange in the non-instantaneous jump limit. A. Model three spin-1/2 system that exhibits two-site exchange of two of the spins. Colored lines indicate different spin couplings to be sampled. The simulation was iterated over the same parameter space as the data in **Fig. 81**. Histograms of the solution error in each of the models compared to a system that exhibits non-instantaneous jumps between configurations calculated at a step size of $T = \tau/5$ and using a correlation time of **B.** $\tau_c = \tau/125$ or **C.** $\tau_c = 2\tau/125$. System parameters were iterated 10,000 times over a variety of coherent parameters to generate the histograms.

case, we explored the same case of $T = \tau/5$ and additionally set the correlation time of exchange to be $\tau_c = \tau/125$ (Fig. 82B) and $\tau_c = 2\tau/125$ (Fig. 82C). Of first note is that using the traditional equation of motion for chemical exchange generates solutions that exhibit significant errors for all the tested cases. In comparison, this to the exact equation without correlation (LMEx) exhibits a lower average error and indicates that while the exact treatment of exchange improves the convergence of some simulations that neglecting the time-correlation still introduces significant errors in a large number of systems. The upper limit of these two cases is interesting as it suggests that even under the condition $\tau_c = \tau/125$ that there can be large errors in the solutions from these models. Including correlation in the lowest-order of exchange reduces the upper limit of errors but does not mark an overall improvement in the solution convergence under this condition. Only when including both the exact treatment of exchange and correlation does the model generate solutions that retain a high degree of accuracy when sampling over a wide range of system parameters.

6.5 Applications to coherent optical spectroscopy

The target applications for the case of chemical exchange in the non-instantaneous jump limit are in coherent optical spectroscopies, such as two-dimensional infrared spectroscopy (2DIR). Photons in the mid-infrared (THz frequencies) interrogate vibrational transitions in molecules and can be used to directly study femtosecond to picosecond molecular dynamics. We will review the principles behind optics and 2DIR, and discuss the impact of the non-instantaneous jump limit in the simulation of this system.

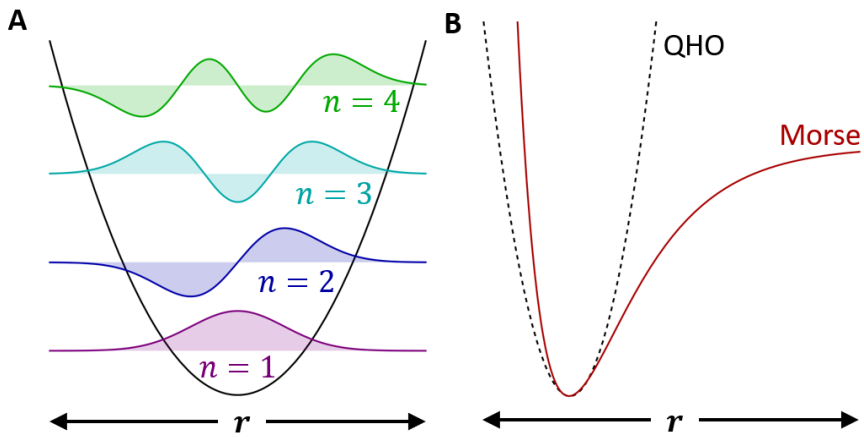

Figure 83: Quantum oscillators. A. Wavefunctions of the quantum harmonic oscillator, which are centered at the energy of each corresponding state. These are parameterized along the internuclear distance $\boldsymbol{r}$. Note that the wavefunctions exceed the confines of the potential, as it is not infinitely higher in energy at any one position. **B.** Realistic bonds do not have a continuously increasing potential as the internuclear distance increases, as the molecule eventually dissociates leading to a constant energy as a function of $\boldsymbol{r}$.

For the purposes of these simulations, we will work with a model system for a vibrating bond. The quantum Harmonic oscillator (QHO) is simplest model for a vibrating bond but is limited based on the shape of the potential (Fig. 83). In a realistic system, the molecule would dissociate as the internuclear distance $\boldsymbol{r}$ is continually increased. As $\boldsymbol{r}$ is increased, the potential energy of the system would asymptotically approach a constant value, with the distance between the bottom of the potential and the asymptote being the dissociation energy (D_e) of the molecule. While the specific shape of the potential would depend on the system, a more realistic model is given by the Morse potential[161], which has the Hamiltonian of the form:

$$\hat{\mathcal{H}} = \frac{1}{2m}\frac{\partial^2}{\partial \boldsymbol{r}^2} + D_e\left[\exp\left(-2\sqrt{\frac{k_e}{2D_e}}\boldsymbol{r}\right) - 2\exp\left(-\sqrt{\frac{k_e}{2D_e}}\boldsymbol{r}\right)\right] \tag{6.67}$$

In this model, k_e is the force constant at the minimum of the potential well. While this appears to be a significantly more complicated form of a potential, its eigenvalues are solvable as

$$E_{\mathrm{v}} = \omega_0\left(\mathrm{v}+\frac{1}{2}\right) - \omega_e x_e\left(\mathrm{v}+\frac{1}{2}\right)^2, \tag{6.68}$$

where $\omega_0 = \sqrt{k_e/m}$ and is the equilibrium resonance frequency and $\omega_e x_e$ is the anharmonicity constant, which modifies the energy levels to reflect the altered potential and is related to the dissociation energy as $\omega_e x_e = \omega_0^2/4D_e$. Furthermore, there are there are $\lambda = \lfloor 2D_e/\omega_0 \rfloor$ bound states of the oscillator. In the Morse oscillator, there are dipole-allowed transitions that can generate $\Delta\mathrm{v} \geq \pm 1$ called overtones, albeit at significantly diminished intensity from the fundamental and at (near) a multiple of the fundamental frequency.

The interaction of the electric field $\boldsymbol{E}(t)$ with the molecular dipole moment operator $\hat{\mu}$ is given as:

$$\hat{\mathcal{H}}_1(t) = \hat{\mu}\cdot\boldsymbol{E}(t) \tag{6.69}$$

The molecular dipolar moment operator $\hat{\mu}$ is well known for a Morse oscillator[161]:

$$\frac{\hat{\mu}_{i<j}}{|\boldsymbol{\mu}|} = \frac{2(-1)^{j-i+1}}{(j-i)\big((2\lambda-1)-i-j\big)}\sqrt{\frac{\left(\lambda-\frac{1}{2}-i\right)\left(\lambda-\frac{1}{2}-j\right)\Gamma(2\lambda-j)j!}{\Gamma(2\lambda-i)i!}}, \tag{6.70}$$

where $\Gamma(x)$ is the Euler gamma function. The electric field magnitude is then related to the pulse energy (E_p) and width (t_p) by:

$$|\boldsymbol{E}| = \sqrt{754\frac{E_p}{t_p}\frac{1}{A_p}} \tag{6.71}$$

A_p is the area of the sample irradiated by the pulse. We will additionally establish that the wavevector $\boldsymbol{k} \parallel \hat{z}$ such that $\boldsymbol{E} \perp \hat{z}$, the electric field is linearly polarized, and oscillates at a frequency ω. For simplicity, we will assume that the dipole moment is collinear with $\boldsymbol{E}$. Thus, the total Hamiltonian is given by (ϕ is the phase of $\boldsymbol{E}$):

$$\hat{\mathcal{H}}(t) = \sum_{\mathrm{v}=0}^{\lambda} E_{\mathrm{v}} + \hat{\mu}|\boldsymbol{E}| \cos(\omega t + \phi) \tag{6.72}$$

We may utilize the rotating frame transformation to make this Hamiltonian time-independent if we assume that the overtone transitions, like $|0\rangle \rightarrow |2\rangle$, are not sufficiently irradiated given the frequency difference between the carrier frequency and bandwidth of the pulse to undergo that transition. As the bandwidth of ultrafast laser pulses is finite and often far from the overtone transition, this is a perfectly adequate approximation. Also noting that we may shift the energy scale as we see fit, we will choose $E_0 = 0\ THz$ and thus we may write the rotating frame optical Hamiltonian:

$$\begin{aligned} \hat{\mathcal{H}} &= \sum_{\mathrm{v}=0}^{\lambda} (E_{\mathrm{v}} - E_0 - \mathrm{v}\omega) + \hat{\mu}|\boldsymbol{E}| \circ \left(\hat{e}_x \cos\phi + \hat{e}_y \sin\phi\right) \\ &= \sum_{\mathrm{v}=0}^{\lambda} \Delta E_{\mathrm{v}} + \hat{\mu}|\boldsymbol{E}| \circ \left(\hat{e}_x \cos\phi + \hat{e}_y \sin\phi\right) \end{aligned} \tag{6.73}$$

We have introduced the polarization directions $\hat{e}_x$ and $\hat{e}_y$, which have the matrix forms:

$$\hat{e}_x = \begin{pmatrix} 0 & 1 & 1 \\ 1 & 0 & 1 \\ 1 & 1 & \ddots \end{pmatrix};\ \hat{e}_y = \begin{pmatrix} 0 & i & i \\ -i & 0 & i \\ -i & -i & \ddots \end{pmatrix}; \tag{6.74}$$

Note that these are Hermitian operators that perform element-wise multiplication of $\hat{\mu}$ given by the Hadamard product, $a \circ b$.

For most molecules, $\omega_0 \approx 12 - 120\ \mathrm{THz}$ and $\omega_e x_e < 1\ \mathrm{THz}$. One of the most common applications of 2DIR is in the study of hydrogen bonding dynamics, where the hydrogen bond effectively increases the mass of the oscillator (Fig. 84). Under these conditions, ω_0 decreases for the hydrogen-bonded species and is often resolvable in a

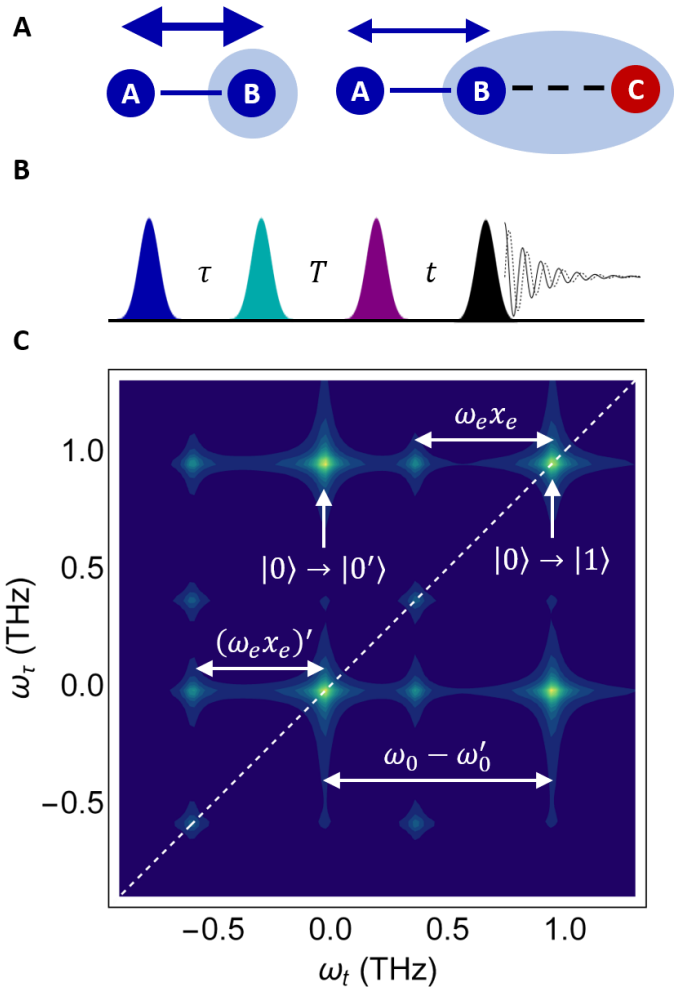

Figure 84: Two-dimensional infrared spectroscopy. A. For a given bond between atoms A and B, there is a net mass of the oscillator that defines the oscillation frequency. Hydrogen bonds will increase the effective mass of the oscillator, thus decreasing the fundamental frequency. **B.** The phase cycling two dimensional infrared spectroscopy pulse sequence uses three, phase-coherent pulses to excite the sample and a fourth pulse to heterodyne the signal. The phases of the excitation pulses may be cycled to isolate the signal of the photon echo. The τ and t delays permit phase evolution of the coherences excited by the first and third pulses, and the T delay allows for exchange to be encoded in the resulting spectrum. **C.** Fourier transforming along the τ and t axes gives the two-dimensional spectrum, where the diagonal is indicated by the dashed line. Off-diagonal peaks indicate transitions that are either coherently-allowed or exchange-allowed. This is a single spectrum at $T = 40\ ps$ in a system with $\tau_{ex} \approx 5\ ps$.

vibrational spectrum. While these effects would still be present in one-dimensional vibrational spectroscopy, such as Fourier Transform Infrared Spectroscopy (FTIR), there is no way to directly access the exchange rate in this experiment. Extracting information on exchange would require lineshape analysis of the spectrum, which is greatly confounded with effects like

inhomogeneous broadening. However, the coherent manipulations required to isolate the exchange degrees of freedom were well known from the NOESY (Nuclear Overhauser Effect SpectroscopY) or EXSY (EXchange SpectroscopY) experiments from NMR. In these experiments, multiple phase-coherent pulses excite the sample such that the NMR spectrum is expanded onto multiple frequency axes, where the diagonal is representative of the 1D spectrum and off-diagonal or cross peaks indicate how different resonances are coupled. This coupling can either be generated by coherent evolution or by incoherent dynamics, such as chemical exchange. This same idea was applied to the optical case (Fig. 84), which lead to the development of two-dimensional infrared spectroscopy as a versatile technique to characterize femtosecond to picosecond dynamics. The 2DIR spectrum boasts a wealth of information, and the cross-peaks that originate from chemical exchange isolate this degree of freedom directly on the picosecond timescale.

As a comparison to NMR, it is interesting to examine how multiple phase-coherent optical pulses are generated, as the hardware in optics is much more constrained than that required to generate waveforms in the radiofrequency domain to arbitrary accuracy. In optics, there are two general approaches to achieve phase-coherent multiple pulse spectroscopy. To see this, we may look at the most general solution of a plane-wave electromagnetic field:

$$\boldsymbol{E}(\boldsymbol{r},t) = E_0 \exp(-i\omega t + \boldsymbol{k}\cdot\boldsymbol{r} + \phi) \tag{6.75}$$

At optical ($nm - \mu m$) wavelengths, phase-coherence can be achieved by spatially overlapping separate beams and selecting for the $\boldsymbol{k}$-vector matched condition that generates the signal. The EXSY experiment essentially generates a spin echo, which in optics is referred to as a photon echo and can be selected by using the $\boldsymbol{k}$-vector matching condition $\boldsymbol{k}_2 + \boldsymbol{k}_3 - \boldsymbol{k}_1$ and

detecting along this axis, often by mixing the emitted photon with a heterodyning field. However, if the $\boldsymbol{k}$-vectors are parallel, Warren and coworkers[162] developed a collinear phase-cycling technique that shifts the phase-coherence of the pulse to the ϕ term by using an acousto-optic modulator (AOM) to generate a train of pulses each with a well-defined phase (Fig. 85). As the $\boldsymbol{k}$-vectors are collinear, multiple coherence pathways are excited simultaneously in addition to the photon echo. However, phase cycling the pulses permits isolation of the photon echo signal from the other, extraneous signals and significantly reduces crowding in the spectrum, and is now a standard method for 2DIR[156].

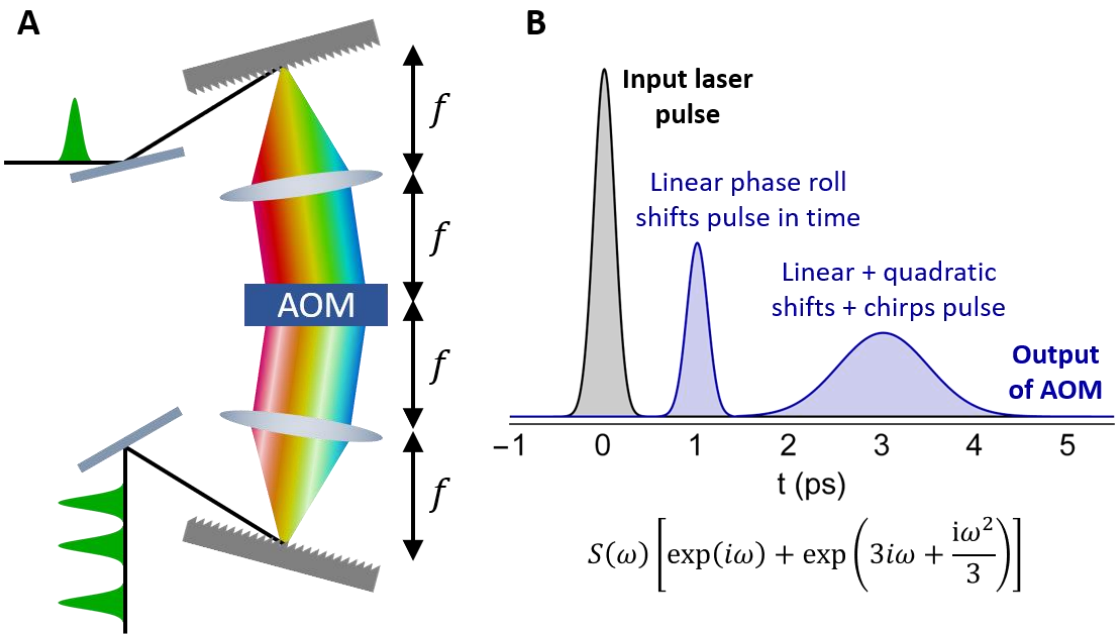

Figure 85: Femtosecond pulse shaping with acousto-optic modulators. A. Femtosecond laser pulses can be shaped by first diffracting the beam collimating it with a lens at a focal length f from the diffraction grating. This generates the Fourier transform of the pulse at a distance f away from the collimating lens, and results in the spectrum of the pulse being dispersed on the AOM crystal. The AOM, which for femtosecond pulse shaping in the visible spectrum is often a medium like TeO_2, acts as a transmission mask when driven with a radiofrequency waveform and can modulate the pulse with a complex phase and amplitude. The first-order diffracted beam is then focused via a second lens (inverting the Fourier transform) onto another diffraction grating to recover the shaped pulses. **B.** As pulse manipulations are performed in the Fourier domain, simple pulse shaping can be thought of in terms of phase-rolls in the pulse spectrum $S(\omega)$. For instance, linear phase-rolls of the spectrum generates a shift in the pulse in time and quadratic phase-rolls generates a chirped pulse.

Optical spectroscopies are also complicated by access to coherent light sources at readily tunable wavelengths. One of the most commonly used light sources is the Ti:Sapphire mode-locked laser, which generates 800 nm femtosecond pulses at a repetition rate of 80 MHz. For coherent vibrational spectroscopy, the 800 nm pulses are often amplified by using chirped pulse amplification and then can be shaped into a pulse train using an AOM (Fig. 86). However, the pulse wavelength must be converted into a mid-infrared pulse. This can be done using an optical parametric amplifier (OPA), which parametrically down-converts the pulse frequency by mixing with a frequency-chirped pulse in a nonlinear medium like β-barium

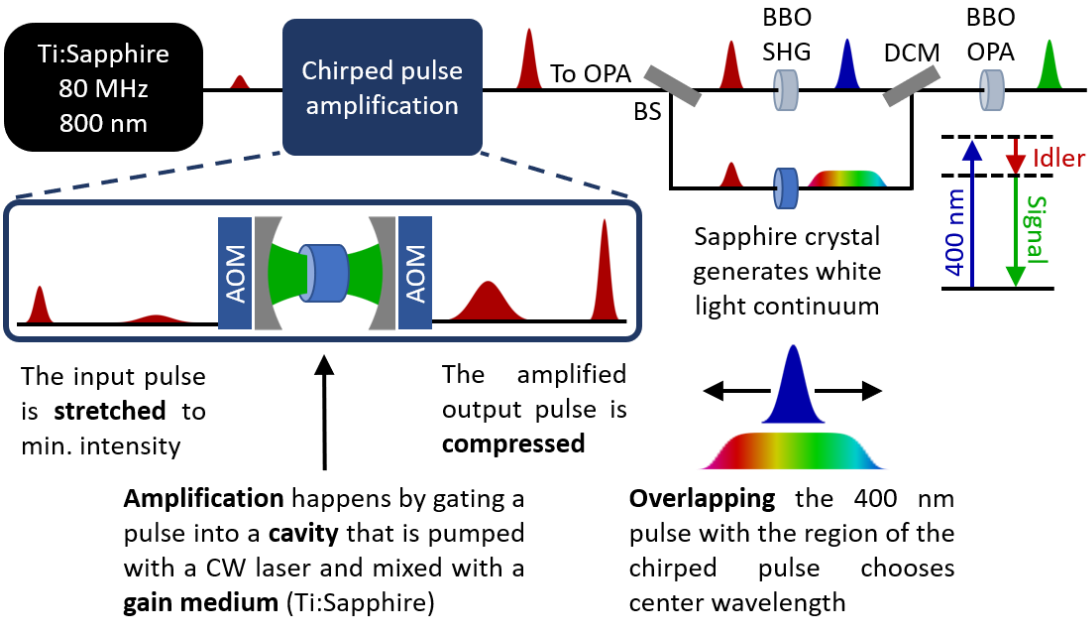

Figure 86: Regenerative amplification and parametric down conversion of optical pulses. The output of the Ti:Sapphire is amplified using Chirped Pulse Amplification, where a pulse is stretched to minimize the peak intensity and then gated into a Q-switched optical cavity with a gain medium (like Ti:Sapphire) that is pumped by a high-power CW laser. The input pulse then causes stimulated emission from the gain medium at the frequency of the input pulse, giving an amplified pulse that is gated out of the cavity. The amplified laser pulse is then recompressed. For applications to vibrational spectroscopy, this pulse can be shaped using an AOM. And then parametrically down converted using an optical parametric amplifier (OPA). If the amplified 800 nm pulse is doubled to 400 nm with a second harmonic generating (BBO) crystal, overlapped with a much weaker, supercontinuum pulse generated by a sapphire, and mixed in a nonlinear medium like BBO, the input pulse may be parametrically down converted in the BBO crystal to generate signal and idler pulses that sum to the energy of the input pulse. Mid-infrared pulses may be generated by using the 800 nm pulse to pump the BBO crystal and isolating the idler as the output.

borate (BBO). To generate a mid-infrared pulse, an amplified 800 nm pulse is passed through a 75/25 beam splitter and the weaker pulse is frequency chirped using a sapphire element, which comes with a commensurate lengthening of the pulse. The stronger of these pulses may optionally be frequency doubled to 400 nm by use of a BBO crystal to generate the second harmonic of the pulse, which provides access to visible wavelengths. Temporally overlapping the 800 nm pulse train with the desired center frequency of the chirped pulse, which is called the signal pulse, determines the wavelength that will be generated by the OPA. The 800 nm and signal pulses are aligned with a birefringent crystal like BBO such that the refractive index of the 800 nm pulse is matched to the refractive index of the signal pulse. The 800 nm (or 400 nm) pulse is then parametrically down-converted into an amplified signal (frequency of chirped pulse) and idler (difference frequency from input and chirped pulse) pulses. With an 800 nm seed pulse, the idler can be tuned to the mid-infrared wavelengths. If the OPA is pumped not with a single seed pulse but a train of seed pulses, then a train of mid-infrared pulses may be generated from the OPA in a similar fashion[163].

We should now have a sufficient basis to examine the impact of chemical exchange in the non-instantaneous jump limit for 2DIR. We will assume that the frequency difference in the fundamental vibrational transition for the hydrogen bonded and free species is approximately $\Delta\omega \approx 1.5\,THz$ Additionally, the anharmonicity constant is assumed to be nearly identical for the two cases because the bond dissociation energy D_e is assumed to not change significantly and is $\omega_e x_e \approx 0.8\,THz$. Finally, the exchange rate between configurations is $k = 0.1\,ps^{-1}$ and we have assumed an exponential correlation function with a characteristic time τ_c. Conveniently, this means that the spectral density operator $\hat{\mathcal{J}}$ is diagonal in the $\{|0\rangle, |1\rangle, |2\rangle, \cdots\}$ eigenbasis and that there is only one exchange pathway in

this system. In accordance with the phase cycling technique published by Warren and coworkers[162], the phases of the four pulses in the sequence were cycled according to

$$S(t) = (XXXP - \bar{X}XXP) + i(YYXP - \bar{Y}YXP), \tag{6.76}$$

where $P = X + iY$. For instance, the notation $\bar{X}XXP$ corresponds to the first pulse being an $\bar{X}$ pulse and then the following two pulses being π out-of-phase with the first pulse, or simply X. The final pulse is the heterodyne pulse which is acquired with either an X or Y phase and the two resulting signals are added to generate a complex-valued signal. After scanning the various time-delays, the resultant signal is then Fourier transformed along the τ and t axes for different values of the mixing time T. Two 2DIR spectra are shown in Fig. 87 for mixing times of $T = 1\ ps$ and $T = 20\ ps$. The diagonal in both spectra are shown by the dashed line, and the solid, horizontal lines indicate the anharmonic separation between the $|0\rangle \rightarrow |1\rangle$ and $|1\rangle \rightarrow |2\rangle$ transitions for both species. The cross-peaks that are circled in Fig. 30 arise from exchange between the two sites and rate at which these cross-peaks appear as a function of the mixing time T is indicative of the exchange rate. For $T < k^{-1}$, not all of the exchange cross-peaks are visible in the spectrum, such as the $(|0\rangle \rightarrow |1\rangle) \rightarrow (|1'\rangle \rightarrow |2'\rangle)$ cross-peak. However, this peak is visible for $T < k^{-1}$ and this condition leads to the appearance of all of the cross-peaks that are accessible through either coherent or exchange pathways. Simulating 2DIR spectra as a function of different exchange correlation times and calculating the deviation from the instantaneous jump limit simulation demonstrates that the IJL assumption is a poor approximation of the actual dynamics in coherent optical experiments (Fig. 87B). Even with $\tau_c < 50\ fs$, the IJL solution is still markedly deviated from the NJL solution but still converge as the jump time $\tau_c \rightarrow 0\ fs$, as is expected. The absolute magnitude of signals

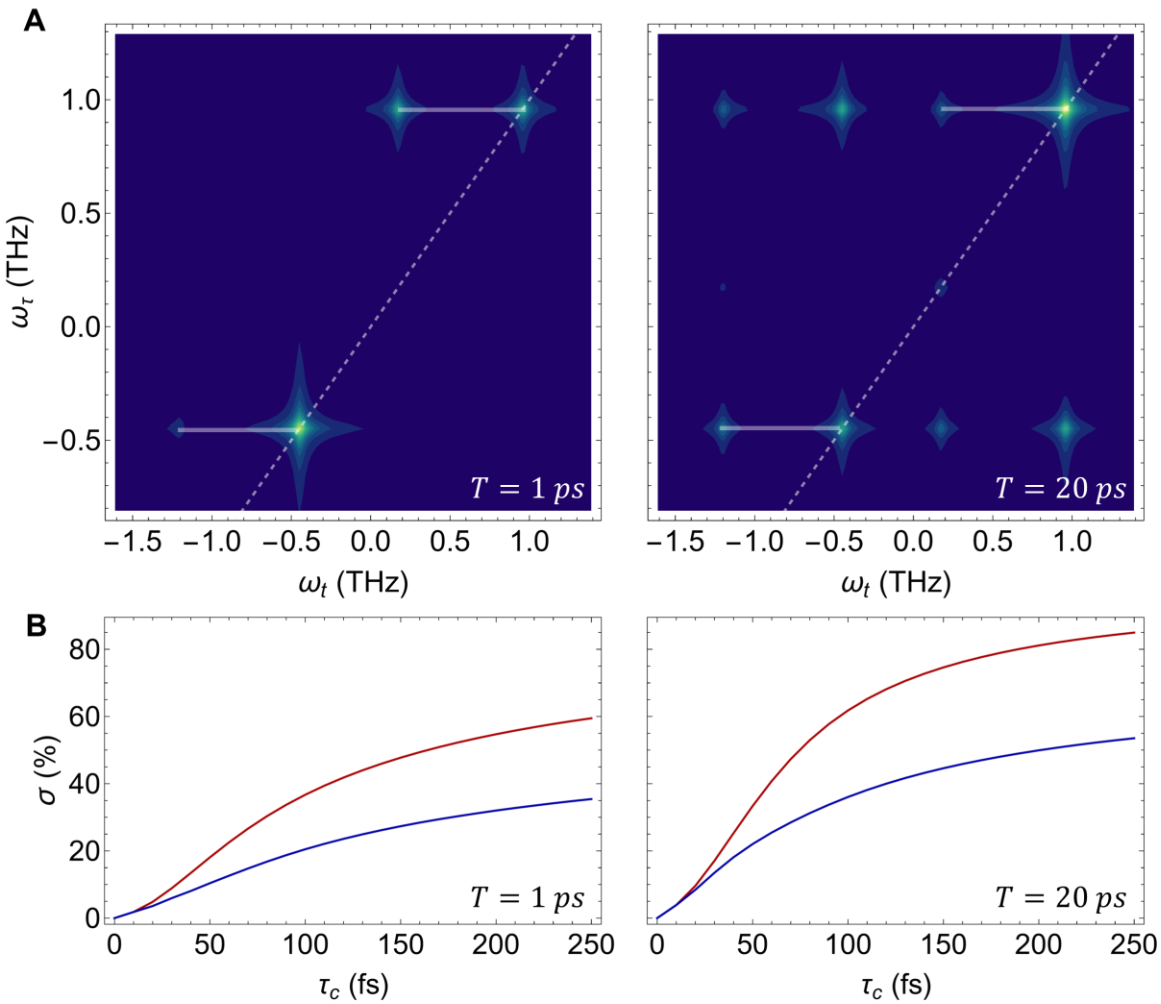

Figure 87: Error in simulated 2DIR spectra in the instantaneous jump limit. A. Simulated 2DIR spectra at mixing times of $T = 1\,ps$ and $T = 20\,ps$ using an exchange rate of $k = 0.1\,ps^{-1}$, corresponding to an average lifetime of 7 ps. **B.** The error (σ, RMSD) in the instantaneous jump limit 2DIR spectrum as a function of the exchange correlation time τ_c used to calculate the non-instantaneous jump limit 2DIR spectrum. The red lines indicate the real error and the blue lines indicate the error when the amplitude of the spectrum is not included in the calculation.

is rarely known from experiment, so it is also pertinent to compare the solution errors without the amplitude. This is done by simply fitting the two solutions to one another and recording the minimum deviation. For two simulations that are different by a scalar factor, this process would completely eliminate the solution error. However, 80% of the error found by absolute comparison was retained for the amplitude normalized comparison (blue line, Fig. 87B), suggesting that the structure of the solutions is much more than a scalar factor removed from

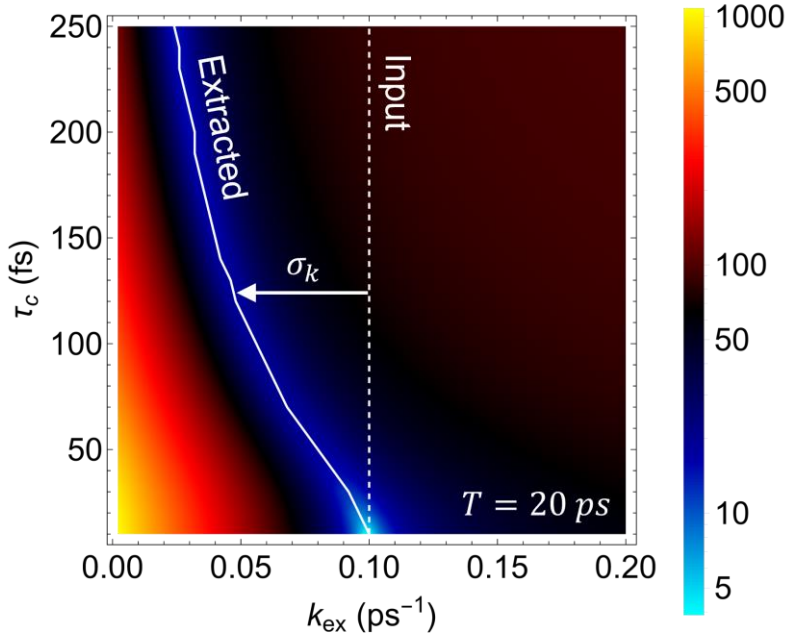

Figure 88: Predicting and extracting exchange rates from 2DIR spectra. To assess the error in the predicted exchange rate of an IJL simulation as a function of the correlation time, a series of IJL simulations were calculated varying $k = [0.0, 0.2] ps^{-1}$ at $T = 20\ ps$ and fitting the resulting 2DIR spectrum to the NJL spectrum at $k = 0.1\ ps^{-1}$ for $\tau_c = [0, 250] fs$. The rate extracted from the IJL simulation deviates from the input rate as the jump time increases. We observe significant deviations even for $\tau_c < 50\ fs$, which will lead to a significant self-consistency error σ_k, as was used to evaluate the DMEx errors. The color bar is RMSD between the IJL and NJL simulations.

the instantaneous jump limit solution. The divergence of these solutions indicates that even rapid molecular reorientation times can generate large differences in the predicted 2DIR spectrum.

We examined the impact of a finite jump time τ_c on the exchange rate that would be extracted by the traditional master equation (Fig. 88). To do this, we used an IJL simulation at a range of exchange rates that are be compared to an NJL simulation using $k = 0.1\ ps^{-1}$ at and a variable jump time. All simulations were compared for $T = 20\ ps$, where the correlation time has a strong impact on the error of the IJL simulation (Fig. 87). The relative difference in the exchange rates predicted by the IJL relative to the NJL at a given jump time is then characterized by σ_k, which was used to assess self-consistency errors in the DMEx. Over the jump time range $\tau_c = [0, 250] fs$, we find that $\langle \sigma_k \rangle = (-48 \pm 24)\%$. Even when restricted

to the range, $\tau_c = [0, 100] fs$, $\langle \sigma_k \rangle = (-22 \pm 16)\%$, and both cases represent significant deviations in the exchange rate predicted by the IJL for a finite jump time. The errors are negative as $\|\bar{\mathcal{J}}\| \leq 1$. We see that as the jump time tends to zero, that the IJL and NJL simulations converge at the same predicted rate. Furthermore, the deviation at the exchange rate minimum is $\langle \sigma \rangle = (15.4 \pm 3.4)\%$, meaning that even varying the exchange rate does not eliminate the differences between the IJL and NJL models, as this would essentially assume that every element of $\hat{\mathcal{L}}\hat{\rho}$ was attenuated equally, whereas $\bar{\mathcal{J}}$ attenuates the elements of $\hat{\mathcal{L}}\hat{\rho}$ differently.

Here, we demonstrate that exchange in the non-instantaneous jump limit can dramatically impact the results of theoretical predictions in coherent optical experiments. In the limit where the exchange correlation time is much faster than the difference Hamiltonian between the configurations, the instantaneous jump limit solution is adequate. However, this limit rapidly deteriorates for exchange correlation times that are on the order of tens of femtoseconds. The additional computational cost of calculating this effect is relatively minor, and is significantly offset by using the LMEx solution to improve solution convergence. Furthermore, physical effects such as differential energy barriers between the ground and excited vibrational states naturally arise from this treatment.

6.6 Conclusions

Here, we have demonstrated that an exact Lindblad master equation (LMEx) for chemical exchange may be derived with a minimal number of foundational assumptions, and that it is valid in any physical limit. The resulting form of master equation reduces to the LMEx in the

instantaneous jump limit and can be further reduced to recover the traditional form of the chemical exchange interaction. A new 'jump' interaction was discovered from this derivation, which generates both dissipation as well as dynamic frequency shifts for systems with a finite jump time.

We have found that Abelian pseudorotation groups give rise to a scalar exchange generating function and that linear combinations of these groups permit construction of non-Abelian exchange generating functions. Finally, we have assessed the performance of this framework both in the instantaneous jump limit and found the limitations of the $\tau_c \to 0$ limit. As an extension of this, we have demonstrated that the non-instantaneous jump limit for chemical exchange can significantly affect the dynamics in two-dimensional infrared spectroscopies. In doing so, we have examined systematic deviations in predicted behavior for finite jump times that can have significant ramifications in extracting physical constants from experimental spectra.

Chapter 7: Conclusions

Magnetic resonance techniques permeate the physical and natural sciences. With ever-decreasing limits of detection, new applications for these methods are in constant development. Recently, the ability to generate $B_0 \approx 30T$ superconducting magnetic fields is another step towards being able to analyze increasingly-complex systems, and the introduction of commercial rubidium vapor magnetometers has made zero and ultralow field (ZULF) NMR accessible to a much wider audience. Hyperpolarization methods are on the forefront of the techniques to boost signals in magnetic resonance across all its applications. However, a significant barrier to incorporating hyperpolarization into a laboratory or preclinical setting is both the cost and need for specialized equipment. Signal Amplification By Reversible Exchange, or SABRE, is an exciting hyperpolarization technique, as it is a fraction of the cost of the preeminent hyperpolarization methods and requires limited to no specialized equipment. Later, SABRE was extended to heteronuclei (X-SABRE), which offer significantly longer lifetimes and polarization potential than ^{1}H.

An archetype of optimizing magnetic resonance experiments is coupling pencil-and-paper theory to computational modeling of the system, both of which are backed by decades of theoretical efforts. X-SABRE is a particularly complex system, containing multiple subsystems that interact through chemical exchange and exhibit nonlinear effects that often dominate the hyperpolarization dynamics. Our initial attempts to apply this ideology to SABRE revealed that the traditional theory unifying quantum dynamics and chemical

exchange formulated by Binsch[92] was founded on incorrect statistical assumptions, and X-SABRE exists in a regime that challenged these assumptions. Here, we completely re-interrogated the theory for quantum evolution with chemical exchange, and found that Binsch's expressions are recovered in the lowest order of perturbation theory. However, we demonstrated that the expansion of the chemical exchange interaction could be derived exactly, and formulated the exact Dissipative Master Equation (DMEx) theory of chemical exchange. Most importantly, this can be incorporated into any existing computational formalism for chemical exchange for no additional computational cost, as the exact equation of motion is proportional to the traditional equation by a scalar factor. While chemical exchange was largely investigated first in magnetic resonance, it is a major focus of studies in other disciplines such as ultrafast multidimensional spectroscopy. To make our findings applicable to the broader audience, we derived an exact Lindblad Master Equation (LMEx) for the exchange interaction and extended it to the non-instantaneous jump limit, such that it accurately encapsulated the ultrafast physics pertinent to optical techniques.

With the ability to exactly express the chemical exchange interaction, we were able to formulate a robust computational framework for simulating the SABRE system. Our exhaustive DMExFR2 model is capable of efficiently simulating any system while including all relevant physical effects. We found that even neglecting a single interaction will significantly alter the resulting polarization predicted by simulation, and thus any attempt to extract meaningful physical parameters must be simulated with a robust model. This computational framework was supported by extensive experimental evidence generated through a new generation of X-SABRE experiments, which unveiled the underlying coherent dynamics. Simultaneously observing both the coherent and exchange degrees of freedom was quintessential in confirming the validities of the DMExFR2 model.

Of the various X-SABRE methods, experiments performed directly in the detection field are the most likely to be translated into conventional NMR techniques such as biomolecular NMR and NMR-based metabonomics. However, the high field X-SABRE experiments were limited to only hyperpolarize ^{15}N-pyridine, which is of little interest for biological systems. Our robust and efficient computational framework for X-SABRE coupled with analytical theory permitted for the expansion of high field X-SABRE techniques to potentially span the entire target scope with the ^{1}H decoupled LIGHT-SABRE variants. However, a significant difficulty with this experiment was that specific molecular parameters that were difficult or impossible to measure had to be known *a priori*. To address this, we developed the broadband X-SABRE experiment, which in addition to not requiring knowledge of specific molecular parameters was the first X-SABRE experiment to demonstrate simultaneous hyperpolarization of multiple targets at high magnetic field. The ability to hyperpolarize multiple targets simultaneously was the only remaining barrier limited by the spin physics to coupling X-SABRE to biomolecular NMR, as the SABRE scope spans both the amino acid and nucleotide functional groups.

While high field X-SABRE is perhaps the most likely to be coupled to conventional NMR techniques, ultralow field X-SABRE is certainly the target for optimizing hyperpolarization for clinical applications. We showed new methods for controlling spin interactions in ultralow magnetic fields, such as pumping the field between an ultralow and high magnetic field to control the coherent dynamics of non-magnetized states. Expanding on this idea led to work with shaping the magnetic field to enhance hyperpolarization by controlling the magnitude and phase of the heteronuclear couplings. Using this could potentially overcome experimental barriers such as hyperpolarizing in the presence of nearby quadrupolar nuclei. Finally, we expanded ultralow field X-SABRE to utilize orthogonal

magnetic fields and showed that doing so can greatly improve hyperpolarization in both conventional exchange regimes as well as in the previously inaccessible fast exchange regime, with hyperpolarization predicted at $P{\sim}1\%$ for ligand exchange rates up to $k_N = 500\ s^{-1}$. This would greatly expand the scope of potential X-SABRE targets to include those that bind the iridium catalyst too weakly to be hyperpolarized by conventional techniques.

The future of X-SABRE as a hyperpolarization method lies in the balance between theoretical, computational, and experimental efforts. Due to the complexity of the system, it is likely that any one of these efforts alone will not be particularly fruitful in the absence of the others. However, the work presented here greatly simplifies access to both the computational and experimental access to X-SABRE. As such, the field is poised to take the next steps towards optimizing hyperpolarization efficiency and coupling the technique to conventional applications.

Appendix A: Numerical simulations of the SABRE system

The entire collection of simulations presented here were calculated using an in-house simulation package that was constructed in Mathematica. There are many different types of simulations that may be constructed based on the system. Instead of writing out the simulation code for each of these cases, we will instead walk through the code for a (3+1)Y X-SABRE simulation, which contains all of the various components that would be needed to construct any other system within this framework. Furthermore, we will write this in the Mathematica coding language and explain each step such that it could be implemented in other coding languages. Code will be written like `this`. We will be begin by setting up the spin system and then review the code that runs the simulation. The simulation core that defines the underlying code is available for free by contacting jacob.lindale@duke.edu and is included in full in Appendix C.

A.1 Setting up a (3+1)Y simulation

There are only two things that one must know to understand the following Mathematica coding: the list (or vector) construction is described by curly braces, `{}`, and the iterator in Mathematica can either be a `For` loop or a `Table`. We will begin by defining the spin system of the iridium-bound species, which requires a list of designators for each of the spin angular

momenta of the various nuclei, which here is called **spins**. For 3 spin-1/2 nuclei, this variable looks like:

```
spins = Table[h, {n, 1, 3}];
```

The output of the table would look like:

```
spins = {h, h, h};
```

The semicolon at the end of the line suppresses the output. At this point, we will define the Larmor frequencies of each of the spin-1/2 nuclei, and effectively assign them a specific nuclide. For flexibility, we will define this as a function, which has the general structure:

```
F[a_]:= 3a
```

The green-colored characters are those that correspond to the arguments of the function. This function takes the argument **a** and returns the value **3a**. Note that functions do not generate an output when they are defined, so no semicolon is necessary. The Larmor frequencies of each nucleus may then be coded into a function as:

```
larmorFreq[B0_]:= {γH, γH, γN}B0
```

This takes the argument of the magnetic field, which is distributive over the list of gyromagnetic ratios. Current options for nuclei are ^{1}H (**γH**), ^{2}D (**γD**), ^{13}C (**γC**), ^{14}N (**γN14**), ^{15}N (**γN**), ^{19}F (**γF**), ^{31}P (**γP**), and ^{129}Xe (**γXe**). By convention, each of these gyromagnetic ratios are in units of $Hz/\mu T$ or equivalently MHz/T. This list also defines the order of each of the spins in the system; the two ^{1}H are spins 1 and 2, and the ^{15}N is spin 3. These spin indices will be used throughout the setup of the system.

The next step is to define the couplings in the system and the magnitude of each of the couplings. For the (3+1)Y system, there are three J-couplings that are present in solution. The simulation package can take clusters of different J-coupled nuclei, such as if one subset

of nuclei had a separate J-coupling network from another set. To define each of the clusters, one simply defines a list with all of the various spin indices belonging to a given cluster. For the (3+1)Y X-SABRE system the three nuclei all belong to the same cluster. Furthermore, there are two isomers of this complex, which will be delineated by **_1** or **_2** in the code. The J-couplings for isomer 1 may be written as:

```
Jcouplings1={{1, 2, 3}};
```

The simulation code will build each of the J-couplings as the unique permutations of the indices in each cluster ordered by the first index. For instance, it will build J_{12}, J_{13}, and J_{23} in that order. For each cluster, each of the values of the couplings need to be defined in the order described above. For isomer 1, spin 2 is coupled to spin 3 and spin 1 is only coupled to spin 2. This gives the J-coupling magnitude list:

```
Jvalues1={{-9.2, 0, -25.41}};
```

The J-couplings in this list correspond to the couplings in the ^{15}N-acetonitrile/^{14}N-pyridine complex. It is beneficial to also examine how this code would change if the system were altered, such as adding the methyl ^{1}H on the ^{15}N-acetonitrile. The code to this point is:

```
spins=Table[h,{n,1,6}];
larmorFreq[B0_]:={γH, γH, γN, γH, γH, γH}B0
Jcouplings1={{1, 2, 3}, {3, 4, 5, 6}};
Jvalues1={{-9.2, 0, -25.41},{-1.69, -1.69, -1.69, 0, 0, 0}};
```

Note that instead of classifying all 6 spin-1/2 nuclei in the same cluster, because there are no couplings between the methyl ^{1}H (spins 4-6) and the hydrides (spins 1 and 2) that we can simply define a second cluster that adds only the couplings between the ^{15}N and the methyl

group. The first three J-couplings in the second cluster are the three J_{NH} couplings to the methyl group and the final three are the internal methyl ^{1}H couplings, which are set to zero.

At this point, we may build the Hamiltonian of isomer 1, which will be the sum of the Zeeman and J-coupling terms (units s^{-1}):

```
H1[B0_]:= LarmorN[spins, larmorFreq[B0]]
   + ScalarCouplingStrongN2[Jcouplings1, Jvalues1, spins]
```

The **LarmorN** and **ScalarCouplingStrongN2** functions build the operators that construct the Hamiltonian and use the Zeeman basis by convention. These are both functions that are defined within the simulation core. Finally, we may calculate the propagator for this Hamiltonian:

```
U1[B0_, Δ_]:= SparseArray@MatrixExp[2 π I H1[B0]Δ/1000]
```

The **@** sign applies the function preceding it (**SparseArray**) to the function following it (**MatrixExp**). Using sparse arrays greatly reduces computational time for large spin systems, as it only defines the elements of a matrix that are non-zero. By convention, we utilize a time-step **Δ** in milliseconds, hence dividing the Hamiltonian by 1000. Here, it is beneficial to note that spaces are interpreted by Mathematica as multiplications and the symbol **π** is obtained by using esc+p+esc.

Similarly, we may define the system for isomer 2 of the iridium-bound species, where spins 1 and 3 are coupled and spin 2 is only coupled to spin 1. It is useful to use the same indexing established by **spins** to construct isomer 2, but simply change the J-couplings:

```
Jcouplings2={{1, 2, 3}};
Jvalues2={{-9.2, -25.41, 0}};
```

```
H2[B0_]:= LarmorN[spins, larmorFreq[B0]]
   + ScalarCouplingStrongN2[Jcouplings2, Jvalues2, spins]
U2[B0_, Δ_]:= SparseArray@MatrixExp[2 π I H2[B0]Δ/1000]
```

Having built the spin systems of the bound species, we must also build the spin system of the free hyperpolarization target, and will have the suffix **_F**. In the (3+1)Y system, this is only a single spin-1/2 nucleus, and its Hamiltonian may be built directly:

```
HF[B0_]:= γN B0 OperatorNF[1, {1,z}]
UF[B0_, Δ_]:= SparseArray@MatrixExp[2 π I HF[B0]Δ/1000]
```

The function **OperatorNF** is the easiest method to build product operators, and takes the first argument of the number of nuclei in the system, and the second argument is a list that specifies the index, total spin, and spin component operator that is desired. In this case, there is only a single spin in the free species (first argument) and we want to calculate the operator $\hat{I}_{1z}$ in this system (the second argument). In a three-spin system, the operator $\hat{I}_{1z}\hat{I}_{3x}$ may be built as:

```
I1zI3z = OperatorNF[3, {1,z,3,x}]
```

Similarly, if spin 3 was a spin-1 nucleus, this operator would be:

```
I1zI3z = OperatorNF[3, {1,z,3,xo}]
```

where **_o** is added to define a spin-1 nucleus or **_oh** is added to define a spin-3/2 nucleus.

We can now establish the initial states of the system. The parahydrogen bath will be set to 100% enriched parahydrogen and the hyperpolarization target will have an initial spin density proportional to unity, assuming that the thermal polarization is negligibly small:

```
ρH20 = SparseArray[ρSinglet];
ρ0F = IdentityMatrix[2]/2];
```

```
ρ0 = SparseArray[KroneckerProduct[ρH20, ρ0F]];
```

As the density matrix of 100% enriched singlet is used frequently, it is simply defined in the core as **ρSinglet**. The argument of the **IdentityMatrix** function is the dimensionality of that matrix, and the **KroneckerProduct** function forms the tensor space. The **ρ** character may be written by typing esc+r+esc.

The simulations are built to monitor the expectation value of a single operator over the course of the calculation. For hyperpolarization experiments, this is often the $\hat{I}_z$ component of the target spin. To construct these operators for both the target nucleus in the bound and free species, we will again use the **OperatorNF** function:

```
OP = OperatorNF[3, {1,z}];
OPfree = OperatorNF[1, {1,z}];
```

Naturally, the code may be modified to extract multiple expectation values simultaneously, if desired.

At this point, we have defined all of the required elements of the code to dictate coherent evolution. As such, we will move onto the dissipative interactions, such as relaxation and exchange. To accomplish either of these, we will need to take the partial trace over certain spin indices to isolate the sub-systems of either the hydrides or the hyperpolarization target. For a system of only spin-1/2 nuclei, the function

```
ρTrN = PartialTr[ρ, N];
```

takes the density matrix **ρ** and traces over the first **N** spin indices. For instance, to trace over the hydride spins of either bound species isomers, which correspond to spins 1 and 2, and retain only the target spins we can write:

```
ρTarget = PartialTr[ρ, 2];
```

The function **PartialTr** only works to remove the first **N** spins. To trace over a specific spin, we must rearrange the indexing of the density matrix, which can be done with the function

```
permuteSpins = MoveSpins[Length[spins], {i}, {f}];
```

The **MoveSpins** function generates the appropriate basis set transformation matrix that reindexes the system by moving the list of initial indices **{i}** to be in the position of the indices **{f}**. To make this computationally efficient, we also calculate the transpose of **permuteSpins**. For the (3+1)Y system, we want to trace over the target index to yield the parahydrogen density matrix **ρH2**, which is given by:

```
permuteSpins = MoveSpins[Length[spins], {3}, 164];
permuteSpinsTr = Transpose[permuteSpins];
ρH2 = PartialTr[permuteSpinsTr.ρ.permuteSpins, 1];
```

In doing this, we move spin 3 (the target spin) to be reindexed as spin 1, and then trace over that index to yield **ρH2**. It is beneficial to collect all of the **PartialTr** functions into an overarching function, which we define as:

```
ρTr[ρ_]:= Module[{ρH2, ρTarget},
   ρH2 = PartialTr[permuteSpinsTr.ρ.permuteSpins, 1];
   ρTarget = PartialTr[ρ, 2];
   {ρH2, ρTarget}
]
```

A Module in Mathematica is a higher-level coding form of a function that collects multiple lines of code together into an overall structure. The first argument **{ρH2, ρTarget}** defines these quantities as local variables and avoids writing them to the global notebook, reducing

computation time. The output of **ρTr** is then a list of the different sub-systems extracted by the **PartialTr** function.

The next step requires that we define how the system is exchanging, which is accomplished by building functions that reconstruct the density matrix after an exchange event (c.f. Chapter 3 for individual exchange pathways). Overall, these functions are specific to different types of systems. For the (3+1)Y system, the exchange functions take the arguments **ρ1** (density matrix of isomer 1) and **ρ2** (density matrix of isomer 2), which are **ρTr[ρ1]** and **ρTr[ρ2]**, respectively. As such, both **ρ1** and **ρ2** have two elements, which may be selected from a list by using **[[1]]** or **[[2]]**. They also take the arguments of the free-species density matrix **ρf**, the parahydrogen ensemble density matrix **ρH**, and the hydride association rate **kaH**.

```
MixDensityRebind[ρ1_, ρ2_, ρf_, ρH_, kaH_]:=
   (1-kaH)KroneckerProduct[(ρ1[[1]]+ρ2[[1]])/2, ρf]
   + (kaH)KroneckerProduct[ρH, ρf]

MixDensityRebindC[ρ1_, ρ2_, ρf_, ρH_, kaH_]:=
   (1-kaH)KroneckerProduct[(ρ1[[1]]+ρ2[[1]])/2,
   (ρ1[[2]]+ρ2[[2]])/2]
   + (kaH)KroneckerProduct[ρH, (ρ1[[2]]+ρ2[[2]])/2]

MixDensityH2[ρ1_, ρ2_]:= (ρ1[[1]]+ρ2[[1]])/2

MixDensityFree[ρ1_, ρ2_]:= (ρ1[[2]]+ρ2[[2]])/2
```

The function **MixDensityRebind** generates the density matrix after it rebinds a ligand from the free species subsystem, and **MixDensityRebindC** generates the density matrix if the

coligand of a Y-system exchanges and the complex isomerizes. Similarly, **MixDensityH2** and **MixDensityFree** calculate the density matrices corresponding to the hydrides that exchange and the target ligand that dissociate from the complex. For an X-system, there are fewer functions that must be defined to generate exchange, which will be listed here for completeness. We will assume a (4+1)X system, which requires the exchange functions:

```
permuteSpins = {MoveSpins[Length[spins], {3}, 164],
   MoveSpins[Length[spins], {3}, 164]};
permuteSpinsTr = Tr/@permuteSpins;

ρTr[ρ_]:= Module[{ρH2A, ρH2B, ρTargetA, ρTargetB},
   ρH2A = PartialTr[permuteSpinsTr[[1]].ρ.permuteSpins[[1]], 1];
   ρH2B = PartialTr[permuteSpinsTr[[2]].ρ.permuteSpins[[2]], 1];
   ρTargetA = PartialTr[permuteSpinsTr[[2]].ρ.permuteSpins[[2]], 3];
   ρTargetB = PartialTr[ρ, 3];
   {ρH2A, ρH2B, ρTargetA, ρTargetB}
]

MixDensityRebind[ρ_, ρf_, ρH_, kaH_]:=
   ((1-kaH)KroneckerProduct[ρ[[1]], ρf]
   + (kaH)KroneckerProduct[ρH, ρ[[3]], ρf]
   +(1-kaH)KroneckerProduct[ρ[[2]], ρf]
   + (kaH)KroneckerProduct[ρH, ρf, ρ[[4]])/2

MixDensityFree[ρ_]:= (ρ[[3]]+ρ [[4]])/2
```

Importantly, given the construction of these functions, only **ρTr** must be modified to change the system and the **MixDenisty_** functions are independent of every system parameter aside from the system geometry (X/Y). Also, the notation **/@** applies the function preceding **/@** to each element of the list after the **/@**, and is known as a **Map**.

The final step required in system setup is to define the relaxation functions that drive the system back to its thermal equilibrium. As mentioned in Chapter 3, relaxation is implemented as a boundary value problem. For relaxation at ultralow field, we assume that $T_1 = T_2$, simplifying the form of the boundary values for relaxation. Importantly, we do not relax the singlet state of the parahydrogen, but allow the triplet manifold of this species to thermalize. The relaxation function for the free species is:

```
RelaxFree[ρ_, Δ_]:= (1 - Δ/(1000 T1))ρ + (Δ/(1000 T1))ρ0F
```

The value of T_1 is used in place of the variable **T1** in units of seconds. For the relaxation of the bound species, we must first build the basis set transformation to cast **ρ** into the singlet-triplet basis on the hydrides. The relaxation function is then:

```
Ust = KroneckerProduct[(Flatten/@st),IdentityMatrix[2]];
UstT = Transpose[Ust];


RelaxBound[ρ_, Δ_]:= (1 - Δ/(1000 T1))ρ
   + (Δ/(1000 T1))RelaxTriplet[Ust.ρ.UstT]
```

By convention, the basis set transformation matrices (**Ust** and **UstT**) that give the singlet-triplet basis set must be given these variable names.

At this point, all of the setup required for the simulation has been complete. Naturally, each part of this setup may be modified to model the desired system. Here, we have described

a simple but robust system that explores all facets of the simulations used throughout this work. Now, we are ready to explore the foundational code that runs the X-SABRE simulation.

A.2 The DMExFR2 code

Having built the system and its various interactions, we may now explore the code that actually calculates the dynamics. We will split out the various sections of the code to discuss what they do to the system, and will use the Y-system as a demonstration, understanding that the X-system will only deviate in which exchange functions are called. This code is the most exhaustive and generalized version of the DMExFR2 code, which contains both ligand and coligand exchange pathways, as well as ligand and hydrogen rebinding capabilities. It is important to note that these simulations were built with the intention of performing parallel computation on the simulation itself, so the data structure within the simulation is reasonably straightforward to interpret.

We call this the DMExFR2DualH function, which has the inputs:

```
DMExFR2DualH[U1_, U2_, Ufree_, ρ0_, ρfree0_, kdN_, kaH_, conc_,
   concH2_, tf_, loops_]:= Module[{…}, …]
```

The variables **U1**, **U2**, and **Ufree** are the propagator lists for the simulation, **ρ0** and **ρfree0** are the initial density matrices of the bound and free species, **kdN** and **kaH** are the ligand dissociation and parahydrogen association rates, **conc** and **concH2** are the $[Ir]/[S]$ and $[Ir]/[H_2]$ fractions, respectively, **tf** is the number of steps to be taken for each element of the propagator list, and **loops** is the number of loops of the propagator list to be calculated.

For instance, to expose the system to a field Bevo for a time tp and then to a field Bd for a time tp, a propagator list for **U1** and time list **tf** would be:

```
U1 = {U1[Bevo], U1[Bd]};
tl = {tp, td}/Δt
```

The variable **Δt** is the simulation step size. The **DMExFR2DualH** code is built within a module, where all of the internal variables are made to be local by writing them in the first argument of the Module, which will be reviewed at the end of this section.

The first step of the simulation is to assemble the entire list of propagators and times that will be used for the whole simulation. This is done by

```
Ul1 = Loops[U1, loops];
Ul2 = Loops[U2, loops];
Ulfree = Loops[Ufree, loops];
tl = Loops[tf, loops];
```

For instance, **Ul1** for 2 loops would be:

```
U1 = {U1[Bevo], U1[Bd]};
Ul1 = {U1[Bevo], U1[Bd], U1[Bevo], U1[Bd]};
```

The next step is to define the initial states of the system within the simulation core:

```
state1 = ρ0;
state2 = ρ0;
ρfree = ρfree0;
ρH2 = ρH20;
```

For each time-step taken by the simulation, we will append the expectation value of the system to 'buckets' that will contain the magnetization on the bound and free species, defined by:

```
magnetizationbound = {};
magnetizationfree = {};
```

These are both empty lists at the start of the simulation. The next step will be to establish the exchange rates modified by the DMEx, which are simply:

```
modkdN = kdN Exp[-kdN/2000];
modkdC = modkdN;
modkaH = kaH Exp[-kaH/2000];
```

For simplicity, we have set the coligand exchange rate to the ligand exchange rate.

The next portion of the code actually calculates evolution of the system, and is constructed as a double **For** loop of the form:

```
For[j=1, j<=Length[tl], j++,
   For[i=1; ρ1 = state1; ρ2 = state2, i<=tl[[j]], i++,
      ...
   ];
   ρ1 = state1;
   ρ2 = state2;
]
```

The first **For** loop indexes through each element of the propagator list, determining essentially which field conditions are used during each period of time. The second **For** loop actually calculates evolution for these periods of time, and at the end of that loop, the states of the two iridium-bound isomers are updated.

Now, we will examine how evolution through the second For loop is calculated. The **DMExFR2DualH** simulation uses a first order integration method, where the first step is to

perform evolution of each of the subsystems. In this example, the parahydrogen bath is expressed in its eigenbasis and thus does not evolve. The evolution of each of the subsystems is then calculated as:

```
For[i=1; ρ1 = state1; ρ2 = state2, i<=tl[[j]], i++,
   ρ1 = ConjugateTranspose[Ul1[[j]]].ρ1.Ul1[[j]];
   ρ2 = ConjugateTranspose[Ul2[[j]]].ρ2.Ul2[[j]];
   ρfree = ConjugateTranspose[Ulfree[[j]]].ρfree.Ulfree[[j]];
   ...
];
```

For brevity, we will use ellipses to denote parts of the code that we either have not yet introduced or have already discussed. The next step in the simulation is to calculate the various `ρTr` functions for the iridium-bound species. It is also advantageous to create 'copies' of the density matrices of the free and parahydrogen species at this point. This gives:

```
For[i=1; ρ1 = state1; ρ2 = state2, i<=tl[[j]], i++,
   ...
   ρTraced1 = ρTr[ρ1];
   ρTraced2 = ρTr[ρ2];
   ρfreetemp =  ρfree;
   ρH2temp =  ρH2;
   ...
];
```

After calculating each of the partial traces on the various sub-systems, the next stage requires imposing exchange on the system, which is carried out as:

```
For[i=1; ρ1 = state1; ρ2 = state2, i<=tl[[j]], i++,
   ...
   ρH2 = ρH2 + (modkaH concH2/1000)
      *(MixDensityH2[ρTraced1, ρTraced2]- ρH2);
   ρfree = ρfree + (modkdN conc/1000)
      *(MixDensityFree[ρTraced1, ρTraced2]- ρfree);
   ρ1 = (1-modkdN/1000-modkdC/1000)ρ1
      + modkdN/1000*MixDensityRebind[ρTraced1, ρTraced2, ρfreetemp,
         ρH2temp, modkaH/modkdN]
      + modkdC/1000*MixDensityRebindC[ρTraced1, ρTraced2, ρfreetemp,
         ρH2temp, modkaH/modkdN]
   ρ2 = (1-modkdN/1000-modkdC/1000)ρ2
      + modkdN/1000*MixDensityRebind[ρTraced1, ρTraced2, ρfreetemp,
         ρH2temp, modkaH/modkdN]
      + modkdC/1000*MixDensityRebindC[ρTraced1, ρTraced2, ρfreetemp,
         ρH2temp, modkaH/modkdN]
   ...
];
```

The next stage is to perform relaxation of the various subsystems, which is accomplished simply by:

```
For[i=1; ρ1 = state1; ρ2 = state2, i<=tl[[j]], i++,
   ...
   ρfree = RelaxFree[ρfree];
   ρ1 = RelaxBound[ρ1];
```

```
    ρ2 = RelaxBound[ρ2];
    ...
];
```

Finally, the magnetization at the end of each step must be appended to the appropriate bucket. This is constructed as:

```
For[i=1; ρ1 = state1; ρ2 = state2, i<=tl[[j]], i++,
    ...
    Append[magnetizationbound, 0.5conc(Tr[ρ1.OP]+Tr[ρ2.OP])/(1+conc)];
    Append[magnetizationfree, 0.5 Tr[ρfree.OPfree]/(1+conc)];
    ...
];
```

We use the convention that each subsystem is unit-normalized, which gives rise to the factors of the concentrations when calculating the final polarization of the system. At the end of the double `For` loop, the output of the simulation is simply the sum of the bound and the free magnetization.

A.3 Examples of simulations

To simulate a time-course of the hyperpolarization dynamics of a coherently pumped SABRE-SHEATH experiment, we can use the input:

```
200 DMExFR2DualH[{U1[-0.5], U1[-50]}, {U2[-0.5], U2[-50]}, {UF[-0.5],
      UF[-50]}, ρ0, ρfree0, Δt*16, Δt*2, 1/20, 0, {22, 350}/Δt, 100]
```

The simulation output is multiplied by 200 to convert from the expectation value to percent polarization. This example performs the simulation for 100 loops of the pulse sequence

described by the propagator lists. Naturally, the number of loops can be adjusted so that the simulation is calculated for a certain experiment time by simply dividing the total time by the time of each loop and rounding the resulting fraction. In addition to simply running a time-course, one of the most typical simulations is to examine a field dependence of the X-SABRE hyperpolarization. In this case, we will use a **ParallelTable** to make parallel computation of the simulation easy:

```
ParallelTable[
   200 Last@DMExFR2DualH[{U1[Bevo], U1[-50]}, {U2[Bevo], U2[-50]},
   {UF[Bevo], UF[-50]}, ρ0, ρfree0, Δt*16, Δt*2, 1/20, 0, {22, 350}/Δt,
   100],
{Bevo, -10, 10 , 0.1}];
```

This **ParallelTable** iterates the simulation over the fields ranging from -10 to 10 μT in steps of 0.1 μT. These two code structures are the most commonly encountered simulations that are used for X-SABRE simulations, and any simulation will result from a combination of the various elements described in this Appendix.

Appendix B: Numerical evaluation of spin operator pathways

A particularly useful computational tool that was developed in this work is the ability to search the entire spin operator pathway space for X-SABRE systems, which aided in the development of the experiments summarized in Chapters 4 and 5. The code is written out explicitly below:

```
searchLiouvillePath[ρ_, H_, order_] :=
 Module[{dρ, comm, dProjections, projections, dStates, i, powerDependences,
   initialStates, pos, commNorms, opNorms, reSort, fullStates, pDepTemp, graphEntries,
   graphVals, reNorm, reNormOperators, commG, powerCorrections, termsL,
   termsLcorrected, termsR, termsRcorrected, activeTerms, termCount},

  dρ = {{ρ}};
  dStates = {};
  powerDependences = {{1}};
  termCount = {{1}};
  graphEntries = {};

  For[i = 1, i ≤ order, i++,

   Print[Style["Derivative " <> ToString[i] <> ":", Bold]];

   If[i == 1,

    initialStates = Table[Rationalize@Chop[Tr[ρ.LiouvilleOperators[[j]]]],
      {j, 2, Length@LiouvilleOperators}];

    AppendTo[dStates, {Total[stateNamesN[[2 ;;]] * initialStates]}];

   ];

   AppendTo[dρ, {}];
   AppendTo[termCount, {}];
```

```
dProjections = Table[

  comm = Table[Chop[I Commute[dρ[[i, 1]], H[[n, 2, m]]]], {m, 1, Length[H[[n, 2]]]}];

  activeTerms = If[# == 0 IdentityMatrix[Length[ρ]], 0, 1] & /@ comm;
  AppendTo[termCount[[i + 1]], Total@activeTerms];

  comm = Total@comm;

  If[comm == 0 IdentityMatrix[Length[ρ]], None,

   AppendTo[dρ[[i + 1]], comm];
   projections = Table[Chop[Tr[comm.LiouvilleOperators[[j]]]],
     {j, 2, Length@LiouvilleOperators}];
   projections = If[# ≠ 0, Sign[#] 1, 0] & /@ projections
  ],

  {l, 1, Length[dρ[[i]]]}, {n, 1, Length@H}];

termCount = If[Length[#] ≥ Length@H, Partition[#, Length@H], #] & /@ termCount;

fullStates = Map[DeleteCases[Null],
  Table[If[dProjections[[l, m]] // ListQ,
    Total[stateNamesN[[2 ;;]] * dProjections[[l, m]]]], {l, 1, Length[dρ[[i]]]},
   {m, 1, Length@dProjections[[l]]}]];

AppendTo[dStates, fullStates];

pos =
 Table[DeleteCases[None][Table[If[dProjections[[l, n]] // ListQ, n, None],
    {n, 1, Length@dProjections[[l]]}]], {l, 1, Length[dρ[[i]]]}];

pDepTemp = Table[H^T[[1, pos[[j]]]], {j, 1, Length@pos}];

 graphVals =
  Join @@ Table[{

     Simplify[dStates[[2 i - 1, m(*indexes starting state,
         Length@dStates[[2i-1]]*)]]] →
      Simplify@fullStates[[m, n(*number of terms generated from that starting state,
         max 4*)]],

     pDepTemp[[m, n]],
```

```
      If[Length[dStates[[2 i - 1, m]]] <
        (Map[DeleteCases[0], termCount[[i + 1]]][[m, n]] * Length[fullStates[[m, n]]]),
       Map[DeleteCases[0], termCount[[i + 1]]][[m, n]],
       1]

     },

     {m, 1, Length[dStates[[2 i - 1]]]}, {n, 1, Length[fullStates[[m]]]}];

  AppendTo[graphEntries, graphVals];
  graphEntries = DeleteDuplicates[Partition[Flatten@graphEntries, 3]];
  Print["The number of graph terms in derivative " <> ToString[i] <> " is: " <>
    ToString[Length[graphEntries]]];

  reSort = GatherBy[{Flatten@fullStates, Flatten@pDepTemp, dρ[[i + 1]]}ᵀ, First];

  reSort = Total /@ reSort / Length /@ reSort;

  AppendTo[dStates, reSortᵀ[[1]]];

  AppendTo[powerDependences, reSortᵀ[[2]]];
  dρ[[i + 1]] = reSortᵀ[[3]]

 ];

reNormOperators = ParallelTable[

  termsLcorrected =
   If[Head[graphEntriesᵀ[[1(*operator*), j(*term*), 1(*lhs*)]]] === Plus,

    Total@Table[

      termsL =
       Table[Numerator@(Rationalize@graphEntriesᵀ[[1(*operator*), j
            (*term*), 1(*lhs*), n]]),
        {n, 1, Length[graphEntriesᵀ[[1, j(*term*), 1(*lhs*)]]]}];

      If[Length[Union[Norm /@ (termsL /. opRules)]] == 1,
       graphEntriesᵀ[[1(*operator*), j(*term*), 1(*lhs*), m]],
       If[Norm[termsL[[m]] /. opRules] < Max[Norm /@ (termsL /. opRules)], 1, 1/4]
        (termsL[[m]] / Denominator[graphEntriesᵀ[[1(*operator*), j(*term*),
             1(*lhs*), m]]])]
      , {m, 1, Length[graphEntriesᵀ[[1, j(*term*), 1(*lhs*)]]]}],
```

```
    graphEntries[[1(*operator*), j(*term*), 1(*lhs*)]]];

  termsRcorrected =
   If[Head[graphEntries[[1(*operator*), j(*term*), 2(*rhs*)]]] === Plus,

    Total@Table[
      termsR =
       Table[Numerator@(Rationalize@graphEntries[[1(*operator*), j
            (*term*), 2(*rhs*), n]]),
        {n, 1, Length[graphEntries[[1, j(*term*), 2(*rhs*)]]]}];

      If[Length[Union[Norm /@ (termsR /. opRules)]] == 1,
       graphEntries[[1(*operator*), j(*term*), 2(*rhs*), m]],
       If[Norm[termsR[[m]] /. opRules] < Max[Norm /@ (termsR /. opRules)], 1, 1/4]
        (termsR[[m]] / Denominator[graphEntries[[1(*operator*), j(*term*),
             2(*rhs*), m]]])]

      , {m, 1, Length[graphEntries[[1, j(*term*), 2(*rhs*)]]]}],

    graphEntries[[1(*operator*), j(*term*), 2(*rhs*)]]];

  powerCorrections =
   If[
    (*Identify multi-operator terms*)
    Head[graphEntries[[1(*operator*), j(*term*), 1(*lhs*)]]] === Plus
     && Head[graphEntries[[1(*operator*), j(*term*), 2(*rhs*)]]] === Plus,

    (*Normal action loop*)
    If[Length[Union[Norm /@ (termsL /. opRules)]] == 1 &&

   Length[Union[Norm /@ (termsR /. opRules)]] == 1 &&
   Norm[(termsL[[1]] /. opRules)] < Norm[(termsR[[1]] /. opRules)],
   If[graphEntries[[3, j]] > 1, 2, 1]/4, 1],

 (*Single operator loop*)
 If[
  (Head[graphEntries[[1(*operator*), j(*term*), 1(*lhs*)]]] === Times
     ∨ Head[graphEntries[[1(*operator*), j(*term*), 1(*lhs*)]]] === Symbol)
   && Head[graphEntries[[1(*operator*), j(*term*), 2(*rhs*)]]] === Plus,
```

```
(*LHS single*)
If[Norm[(graphEntries^T[[1(*operator*), j(*term*), 1(*lhs*)]] /. opRules)] <
  Norm[(termsR[[1]] /. opRules)],

 If[graphEntries^T[[3, j]] > 1, 2, 1]
                                 4
                                    , 1],

If[
 Head[graphEntries^T[[1(*operator*), j(*term*), 1(*lhs*)]]] === Plus
  && (Head[graphEntries^T[[1(*operator*), j(*term*), 2(*rhs*)]]] === Times
    ∨ Head[graphEntries^T[[1(*operator*), j(*term*), 2(*rhs*)]]] ===
     Symbol),

 (*RHS single*)
 If[Norm[(termsL[[1]] /. opRules)] <
    Norm[(graphEntries^T[[1(*operator*), j(*term*), 2(*rhs*)]] /.
       opRules)] &&
   Norm[(termsL[[1]] /. opRules)] ≠
    Norm[(graphEntries^T[[1(*operator*), j(*term*), 2(*rhs*)]] /. opRules)],
  If[graphEntries^T[[3, j]] > 1, 2, 1]
                                 4
                                    , 1],

 (*LHS & RHS single*)
 If[Norm[(graphEntries^T[[1(*operator*), j(*term*), 1(*lhs*)]] /.
      opRules)] <
   Norm[(graphEntries^T[[1(*operator*), j(*term*), 2(*rhs*)]] /. opRules)],

  If[graphEntries^T[[3, j]] > 1, 2, 1]
                                 4
                                    , 1]
 ]

]

];

{termsLcorrected → termsRcorrected, graphEntries^T[[2, j]] powerCorrections},

{j, 1, Length[graphEntries^T[[1(*operator*)]]]}];

graphEntries = Rationalize@reNormOperators;

graphEntries

]
```

Using this code is significantly easier than the code itself. For instance, the setup and calculations of the heterogeneous catalysts discussed in the conclusion of Chapter 6 was:

```
LiouvilleOperators =
  Join @@ Join @@ Table[OperatorNF[3, {1, i, 2, j, 3, k}] / Norm[OperatorNF[3, {1, i, 2, j, 3, k}]], {i, {u, x, y, z}},
     {j, {u, x, y, z}}, {k, {u, x, y, z}}];

stateNames =
  Join[{"E"},
   StringDelete["u"][
     KetNames[KetNames[{"u", "I1x", "I1y", "I1z"}, {"u", "I2x", "I2y", "I2z"}],
      {"u", "Sx", "Sy", "Sz"}]][[2 ;;]]];

stateNamesN = (ToExpression /@ stateNames);

LiouvilleOperators2 =
  Join @@ Join @@ Table[OperatorNF[3, {1, i, 2, j, 3, k}], {i, {u, x, y, z}},
     {j, {u, x, y, z}}, {k, {u, x, y, z}}];

opRules = Table[stateNamesN[[i]] → LiouvilleOperators2[[i]], {i, 1, Length@stateNamesN}];
```

Here, we have setup the operators that span a 3 spin-1/2 system, define the names of these operators and define rules for naming them to be used in the code. All variable names must be conserved for the code to work. The generic Hamiltonian is written as:

```
HSS = {
   {Δ, {OperatorNF[3, {3, z}]}},
   {dHHzz, {OperatorNF[3, {1, z, 2, z}]}},
   {dHHxx, {OperatorNF[3, {1, x, 2, x}]}},
   {dHHyy, {OperatorNF[3, {1, y, 2, y}]}},
   {dHHxyyx, {OperatorNF[3, {1, x, 2, y}] + OperatorNF[3, {1, y, 2, x}]}},
   {dHHxzzx, {OperatorNF[3, {1, x, 2, z}] + OperatorNF[3, {1, z, 2, x}]}},
   {dHHyzzy, {OperatorNF[3, {1, y, 2, z}] + OperatorNF[3, {1, z, 2, y}]}},
   |
   {dNHzz, {OperatorNF[3, {1, z, 3, z}]}},
   {dNHxx, {OperatorNF[3, {1, x, 3, x}]}},
   {dNHyy, {OperatorNF[3, {1, y, 3, y}]}},
   {dNHxyyx, {OperatorNF[3, {1, x, 3, y}] + OperatorNF[3, {1, y, 3, x}]}},
   {dNHxzzx, {OperatorNF[3, {1, x, 3, z}] + OperatorNF[3, {1, z, 3, x}]}},
   {dNHyzzy, {OperatorNF[3, {1, y, 3, z}] + OperatorNF[3, {1, z, 3, y}]}}

  };
```

Only the terms that have the same spatial dependence are summed in this format, permitting the action of each of the operators to be delineated from every other operator. Finally, the first four derivatives of the solid state coherence pathways may be searched by:

```
ρ0 = SparseArray@KroneckerProduct[ρSinglet, 1/2 IdentityMatrix[2]];

spinOperatorPathwaySolid = searchLiouvillePath[ρ0, HSS, 4];
Derivative 1:
The number of graph terms in derivative 1 is: 6
Derivative 2:
The number of graph terms in derivative 2 is: 77
Derivative 3:
The number of graph terms in derivative 3 is: 627
Derivative 4:
The number of graph terms in derivative 4 is: 3765
```

The code outputs the number of terms in the coherence pathway graph as a function of the number of derivatives. Given the large number of terms in the Hamiltonian for this case, there are many terms that are extracted from the coherence pathways. The output of the `searchLiouvillePath` function can be used to plot a graph of the coherence pathways, on which calculations may be run, such as interrogating the shortest distance between an initial and a desired state.

References

1. A. Abragam, *The principles of nuclear magnetism.* (Oxford, Clarendon Press., 1961).

2. J. S. Waugh, L. M. Huber and U. Haeberlen, Physical Review Letters **20** (5), 180-182 (1968).

3. H. Y. Carr and E. M. Purcell, Physical Review **94**, 630-638 (1954).

4. H. Oschkinat, C. Griesinger, P. J. Kraulis, O. W. Sorensen, R. R. Ernst, A. M. Gronenborn and G. M. Clore, Nature **332** (6162), 374-376 (1988).

5. N. Bloembergen and R. V. Pound, Physical Review **95** (1), 8 (1954).

6. E. Hahn, Physical Review **80** (4), 580-594 (1950).

7. O. W. Sorensen, G. W. Eich, M. H. Levitt, G. Bodenhausen and R. R. Ernst, Progress in Nuclear Magnetic Resonance Spectroscopy **16**, 163-192 (1983).

8. M. Levitt, Nature **294** (5839), 379-380 (1981).

9. V. Daggett and M. Levitt, Current Opinion in Structural Biology **4** (2), 291-295 (1994).

10. I. J. Kimsey, K. Petzold, B. Sathyamoorthy, Z. W. Stein and H. M. Al-Hashimi, Nature **519** (7543), 315-320 (2015).

11. N. K. Logothetis, J. Pauls, M. Augath, T. Trinath and A. Oeltermann, Nature **412** (6843), 150-157 (2001).

12. V. S. Zotev, A. N. Matlashov, P. L. Volegov, I. M. Savukov, M. A. Espy, J. C. Mosher, J. J. Gomez and R. H. Kraus, Journal of Magnetic Resonance **194** (1), 115-120 (2008).

13. A. Konkel, D. E. Warren, M. C. Duff, D. N. Tranel and N. J. Cohen, Frontiers in Human Neuroscience **2** (2008).

14. J. L. Stewart, S. L. Warren, J. N. Spielberg, A. S. Engels, W. Heller and G. A. Miller, Psychophysiology **45**, S85-S85 (2008).

15. J. Kurhanewicz, M. G. Swanson, S. J. Nelson and D. B. Vigneron, J Magn Reson Imaging **16** (4), 451-463 (2002).

16. A. C. Westphalen, G. D. Reed, P. P. Vinh, C. Sotto, D. B. Vigneron and J. Kurhanewicz, J Magn Reson Imaging **36** (2), 430-437 (2012).

17. B. L. Koelsch, K. R. Keshari, T. H. Peeters, P. E. Larson, D. M. Wilson and J. Kurhanewicz, Analyst **138** (4), 1011-1014 (2013).

18. Bruker, https://www.bruker.com/en/news-and-events/news/2020/successful-installation-of-worlds-first-12-ghz-nmr-system-enables-novel-functional-structural-biology-research.html.

19. A. Abragam and M. Goldman, Reports on Progress in Physics **41** (3), 395 (1978).

20. J. H. Ardenkjaer-Larsen, B. Fridlund, A. Gram, G. Hansson, L. Hansson, M. H. Lerche, R. Servin, M. Thaning and K. Golman, Proc. Natl. Acad. Sci. U.S.A. **100** (18), 10158-10163 (2003).

21. S. E. Day, M. I. Kettunen, F. A. Gallagher, D. E. Hu, M. Lerche, J. Wolber, K. Golman, J. H. Ardenkjaer-Larsen and K. M. Brindle, Nature Medicine **13** (11), 1382-1387 (2007).

22. F. A. Gallagher, M. I. Kettunen, S. E. Day, D. E. Hu, J. H. Ardenkjaer-Larsen, R. Zandt, P. R. Jensen, M. Karlsson, K. Golman, M. H. Lerche and K. M. Brindle, Nature **453** (7197), 940-943 (2008).

23. S. J. Nelson, J. Kurhanewicz, D. B. Vigneron, P. E. Larson, A. L. Harzstark, M. Ferrone, M. van Criekinge, J. W. Chang, R. Bok, I. Park, G. Reed, L. Carvajal, E. J. Small, P. Munster, V. K. Weinberg, J. H. Ardenkjaer-Larsen, A. P. Chen, R. E. Hurd, L. I. Odegardstuen, F. J. Robb, J. Tropp and J. A. Murray, Sci. Transl. Med. **5** (198), 198ra108 (2013).

24. G. Pileio, S. Bowen, C. Laustsen, M. C. D. Tayler, J. T. Hill-Cousins, L. J. Brown, R. C. D. Brown, J. H. Ardenkjaer-Larsen and M. H. Levitt, Journal of the American Chemical Society **135** (13), 5084-5088 (2013).

25. R. Schmidt, C. Laustsen, J. N. Dumez, M. I. Kettunen, E. M. Serrao, I. Marco-Rius, K. M. Brindle, J. H. Ardenkjaer-Larsen and L. Frydman, J Magn Reson **240**, 8-15 (2014).

26. C. von Morze, R. A. Bok, G. D. Reed, J. H. Ardenkjaer-Larsen, J. Kurhanewicz and D. B. Vigneron, Magn Reson Med (2013).

27. C. R. Bowers, M. G. Pravica and D. P. Weitekamp, Abstracts of Papers of the American Chemical Society **197**, 34-Coll (1989).

28. C. R. Bowers and D. P. Weitekamp, Journal of the American Chemical Society **109** (18), 5541-5542 (1987).

29. C. R. Bowers and D. P. Weitekamp, Phys. Rev. Lett. **57** (21), 2645-2648 (1986).

30. E. Y. Chekmenev, J. Hovener, V. A. Norton, K. Harris, L. S. Batchelder, P. Bhattacharya, B. D. Ross and D. P. Weitekamp, Journal of the American Chemical Society **130** (13), 4212-+ (2008).

31. E. Y. Chekmenev, V. A. Norton, D. P. Weitekamp and P. Bhattacharya, Journal of the American Chemical Society **131** (9), 3164-+ (2009).

32. S. Appelt, A. B. Baranga, C. J. Erickson, M. V. Romalis, A. R. Young and W. Happer, Physical Review A **58** (2), 1412-1439 (1998).

33. W. C. Chen, T. R. Gentile, Q. Ye, T. G. Walker and E. Babcock, J. Appl. Phys. **116** (1), 014903 (2014).

34. W. Happer, E. Miron, S. Schaefer, D. Schreiber, W. A. van Wijngaarden and X. Zeng, Physical Review A **29** (6), 3092-3110 (1984).

35. P. Nikolaou, A. M. Coffey, M. J. Barlow, M. Rosen, B. M. Goodson and E. Y. Chekmenev, Anal. Chem. **86** (16), 8206–8212 (2014).

36. T. G. Walker and W. Happer, Rev. Mod. Phys. **69** (2), 629-642 (1997).

37. R. W. Adams, J. A. Aguilar, K. D. Atkinson, M. J. Cowley, P. I. Elliott, S. B. Duckett, G. G. Green, I. G. Khazal, J. Lopez-Serrano and D. C. Williamson, Science **323** (5922), 1708-1711 (2009).

38. R. W. Adams, S. B. Duckett, R. A. Green, D. C. Williamson and G. G. R. Green, J. Chem. Phys. **131** (19) (2009).

39. J. A. Aguilar, R. W. Adams, S. B. Duckett, G. G. R. Green and R. Kandiah, Journal of Magnetic Resonance **208** (1), 49-57 (2011).

40. M. J. Cowley, R. W. Adams, K. D. Atkinson, M. C. R. Cockett, S. B. Duckett, G. G. R. Green, J. A. B. Lohman, R. Kerssebaum, D. Kilgour and R. E. Mewis, J. Am. Chem. Soc. **133** (16), 6134-6137 (2011).

41. J. B. Hovener, N. Schwaderlapp, R. Borowiak, T. Lickert, S. B. Duckett, R. E. Mewis, R. W. Adams, M. J. Burns, L. A. Highton, G. G. Green, A. Olaru, J. Hennig and D. von Elverfeldt, Anal Chem **86** (3), 1767-1774 (2014).

42. L. S. Lloyd, R. W. Adams, M. Bernstein, S. Coombes, S. B. Duckett, G. G. Green, R. J. Lewis, R. E. Mewis and C. J. Sleigh, Journal of the American Chemical Society **134** (31), 12904-12907 (2012).

43. M. E. Gemeinhardt, M. N. Limbach, T. R. Gebhardt, C. W. Eriksson, S. L. Eriksson, J. R. Lindale, E. A. Goodson, W. S. Warren, E. Y. Chekmenev and B. M. Goodson, **59** (1), 418-423 (2020).

44. J. Bae, Z. Zhou, T. Theis, W. S. Warren and Q. Wang, Science advances **4** (3), eaar2978 (2018).

45. J. F. P. Colell, A. W. J. Logan, Z. Zhou, R. V. Shchepin, D. A. Barskiy, G. X. Ortiz, Q. Wang, S. J. Malcolmson, E. Y. Chekmenev, W. S. Warren and T. Theis, J Phys. Chem. Phys. C Cover Article **just accepted** (2017).

46. D. A. Barskiy, R. V. Shchepin, C. P. N. Tanner, J. F. P. Colell, B. M. Goodson, T. Theis, W. S. Warren and E. Y. Chekmenev, ChemPhysChem, DOI: 10.1002/cphc.201700416 (2017).

47. J. F. P. Colell, M. Emondts, A. W. J. Logan, K. Shen, J. Bae, R. V. Shchepin, G. X. Ortiz, P. Spannring, Q. Wang, S. J. Malcolmson, E. Y. Chekmenev, M. C. Feiters, F. P. J. T. Rutjes, B. Blümich, T. Theis and W. S. Warren, J. Am. Chem. Soc. **139** (23), 7761-7767 (2017).

48. Z. Zhou, J. Yu, J. F. P. Colell, R. Laasner, A. Logan, D. A. Barskiy, R. V. Shchepin, E. Y. Chekmenev, V. Blum, W. S. Warren and T. Theis, J. Phys. Chem. Lett. **8** (13), 3008-3014 (2017).

49. D. A. Barskiy, R. V. Shchepin, A. M. Coffey, T. Theis, W. S. Warren, B. M. Goodson and E. Y. Chekmenev, J. Am. Chem. Soc. **138** (26), 8080-8083 (2016).

50. T. Theis, G. X. Ortiz, Jr., A. W. Logan, K. E. Claytor, Y. Feng, W. P. Huhn, V. Blum, S. J. Malcolmson, E. Y. Chekmenev, Q. Wang and W. S. Warren, Sci. Adv. **2** (3), e1501438 (2016).

51. T. Theis, M. L. Truong, A. M. Coffey, R. V. Shchepin, K. W. Waddell, F. Shi, B. M. Goodson, W. S. Warren and E. Y. Chekmenev, J. Am. Chem. Soc. **137** (4), 1404-1407 (2015).

52. T. Theis, M. Truong, A. M. Coffey, E. Y. Chekmenev and W. S. Warren, J. Magn. Reson. **248**, 23-26 (2014).

53. R. Kaptein, Chem. Phys. Lett. **2** (4), 261-267 (1968).

54. W. de Boer and T. O. Niinikoski, Nuclear Instruments and Methods **114** (3), 495-498 (1974).

55. W. Boer, M. Borghini, K. Morimoto, T. O. Niinikoski and F. Udo, Journal of Low Temperature Physics **15** (3-4), 249-267 (1974).

56. A. Abragam and M. Goldman, Reports on Progress in Physics **41** (3), 395-467 (1978).

57. V. S. Bajaj, C. T. Farrar, M. K. Hornstein, I. Mastovsky, J. Vieregg, J. Bryant, B. Eléna, K. E. Kreischer, R. J. Temkin and R. G. Griffin, Journal of Magnetic Resonance **160** (2), 85-90 (2003).

58. K. Golman, J. H. Ardenkjær-Larsen, J. S. Petersson, S. Månsson and I. Leunbach, Proc. Natl. Acad. Sci. USA **100** (18), 10435-10439 (2003).

59. S. J. Nelson, D. Vigneron, J. Kurhanewicz, A. Chen, R. Bok and R. Hurd, Appl Magn Reson **34** (3-4), 533-544 (2008).

60. T. Maly, G. T. Debelouchina, V. S. Bajaj, K.-N. Hu, C.-G. Joo, M. L. Mak–Jurkauskas, J. R. Sirigiri, P. C. A. van der Wel, J. Herzfeld, R. J. Temkin and R. G. Griffin, The Journal of Chemical Physics **128** (5), - (2008).

61. A. B. Barnes, G. De Paëpe, P. C. A. van der Wel, K. N. Hu, C. G. Joo, V. S. Bajaj, M. L. Mak-Jurkauskas, J. R. Sirigiri, J. Herzfeld, R. J. Temkin and R. G. Griffin, Applied Magnetic Resonance **34** (3-4), 237-263 (2008).

62. M. E. Halse and P. T. Callaghan, Journal of Magnetic Resonance **195** (2), 162-168 (2008).

63. T. Maly, G. T. Debelouchina, V. S. Bajaj, K. N. Hu, C. G. Joo, M. L. Mak-Jurkauskas, J. R. Sirigiri, P. C. A. van der Wel, J. Herzfeld, R. J. Temkin and R. G. Griffin, Journal of Chemical Physics **128** (5) (2008).

64. Y. Matsuki, T. Maly, O. Ouari, H. Karoui, F. Le Moigne, E. Rizzato, S. Lyubenova, J. Herzfeld, T. Prisner, P. Tordo and R. G. Griffin, Angewandte Chemie-International Edition **48** (27), 4996-5000 (2009).

65. S. E. Korchak, A. S. Kiryutin, K. L. Ivanov, A. V. Yurkovskaya, Y. A. Grishin, H. Zimmermann and H. M. Vieth, Applied Magnetic Resonance **37** (1-4), 515-537 (2010).

66. Ü. Akbey, W. T. Franks, A. Linden, S. Lange, R. G. Griffin, B.-J. van Rossum and H. Oschkinat, Angew. Chem. Int. Ed. **49** (42), 7803-7806 (2010).

67. L. Lumata, A. K. Jindal, M. E. Merritt, C. R. Malloy, A. D. Sherry and Z. Kovacs, J Am Chem Soc **133** (22), 8673-8680 (2011).

68. S. Hu, H. A. Yoshihara, R. Bok, J. Zhou, M. Zhu, J. Kurhanewicz and D. B. Vigneron, Magn Reson Imaging **30** (10), 1367-1372 (2012).

69. A. P. Chen, M. J. Albers, C. H. Cunningham, S. J. Kohler, Y. F. Yen, R. E. Hurd, J. Tropp, R. Bok, J. M. Pauly, S. J. Nelson, J. Kurhanewicz and D. B. Vigneron, Magn Reson Med **58** (6), 1099-1106 (2007).

70. S. J. Kohler, Y. Yen, J. Wolber, A. P. Chen, M. J. Albers, R. Bok, V. Zhang, J. Tropp, S. Nelson, D. B. Vigneron, J. Kurhanewicz and R. E. Hurd, Magn Reson Med **58** (1), 65-69 (2007).

71. C. H. Cunningham, A. P. Chen, M. J. Albers, J. Kurhanewicz, R. E. Hurd, Y. F. Yen, J. M. Pauly, S. J. Nelson and D. B. Vigneron, J Magn Reson **187** (2), 357-362 (2007).

72. J. Kurhanewicz and D. B. Vigneron, Magn Reson Imaging Clin N Am **16** (4), 697-710, ix-x (2008).

73. C. H. Cunningham, A. P. Chen, M. Lustig, B. A. Hargreaves, J. Lupo, D. Xu, J. Kurhanewicz, R. E. Hurd, J. M. Pauly, S. J. Nelson and D. B. Vigneron, J Magn Reson **193** (1), 139-146 (2008).

74. J. Kurhanewicz, R. Bok, S. J. Nelson and D. B. Vigneron, J Nucl Med **49** (3), 341-344 (2008).

75. M. J. Albers, R. Bok, A. P. Chen, C. H. Cunningham, M. L. Zierhut, V. Y. Zhang, S. J. Kohler, J. Tropp, R. E. Hurd, Y.-F. Yen, S. J. Nelson, D. B. Vigneron and J. Kurhanewicz, Cancer Res. **68** (20), 8607-8615 (2008).

76. Y. Chen, R. W. Dorn, M. P. Hanrahan, L. Wei, R. Blome-Fernández, A. M. Medina-Gonzalez, M. A. S. Adamson, A. H. Flintgruber, J. Vela and A. J. Rossini, Journal of the American Chemical Society **143** (23), 8747-8760 (2021).

77. M. P. Hanrahan, J. L. Stein, N. Park, B. M. Cossairt and A. J. Rossini, The Journal of Physical Chemistry C **125** (5), 2956-2965 (2021).

78. C. R. Bowers and D. P. Weitekamp, Phys. Rev. Lett. **57** (21), 2645-2648 (1986).

79. M. G. Pravica and D. P. Weitekamp, Chemical Physics Letters **145** (4), 255-258 (1988).

80. C. R. Bowers and D. P. Weitekamp, Solid State Nuclear Magnetic Resonance **11** (1-2), 123-128 (1998).

81. R. W. Adams, J. A. Aguilar, K. D. Atkinson, M. J. Cowley, P. I. P. Elliott, S. B. Duckett, G. G. R. Green, I. G. Khazal, J. Lopez-Serrano and D. C. Williamson, Science **323** (5922), 1708-1711 (2009).

82. R. V. Shchepin, J. R. Birchall, N. V. Chukanov, K. V. Kovtunov, I. V. Koptyug, T. Theis, W. S. Warren, J. G. Gelovani, B. M. Goodson and S. Shokouhi, Chemistry–A European Journal (2019).

83. G. Zhang, J. F. P. Colell, T. Glachet, J. R. Lindale, V. Reboul, T. Theis and W. S. Warren, **58** (32), 11118-11124 (2019).

84. N. M. Ariyasingha, J. R. Lindale, S. L. Eriksson, G. P. Clark, T. Theis, R. V. Shchepin, N. V. Chukanov, K. V. Kovtunov, I. V. Koptyug, W. S. Warren and E. Y. Chekmenev, The Journal of Physical Chemistry Letters **10** (15), 4229-4236 (2019).

85. R. V. Shchepin, L. Jaigirdar, T. Theis, W. S. Warren, B. M. Goodson and E. Y. Chekmenev, The Journal of Physical Chemistry C **121** (51), 28425-28434 (2017).

86. A. W. Logan, T. Theis, J. F. Colell, W. S. Warren and S. J. Malcolmson, Chem. Eur. J. **22** (31), 10777-10781 (2016).

87. M. L. Truong, T. Theis, A. M. Coffey, R. V. Shchepin, K. W. Waddell, F. Shi, B. M. Goodson, W. S. Warren and E. Y. Chekmenev, J. Phys. Chem. C **119** (16), 8786-8797 (2015).

88. R. V. Shchepin, M. L. Truong, T. Theis, A. M. Coffey, F. Shi, K. W. Waddell, W. S. Warren, B. M. Goodson and E. Y. Chekmenev, J. Chem. Phys. Lett. **6** (10), 1961-1967 (2015).

89. J. R. Lindale, S. L. Eriksson, C. P. Tanner, Z. Zhou, J. F. Colell, G. Zhang, J. Bae, E. Y. Chekmenev, T. Theis and W. S. Warren, Nature communications **10** (1), 395 (2019).

90. M. Haake, J. Natterer and J. Bargon, Journal of the American Chemical Society **118** (36), 8688-8691 (1996).

91. J. S. Waugh, in *eMagRes* (2007).

92. G. Binsch, Journal of the American Chemical Society **91** (6), 1304-1309 (1969).

93. A. G. Redfield, IBM Journal of Research and Development **1** (1), 19-31 (1957).

94. S. Goudsmit, Uhlenbeck, G. E., Physica **6**, 273-290 (1926).

95. W. Gerlach and O. Stern, Zeitschrift für Physik **9** (1), 349-352 (1922).

96. P. A. M. Dirac and R. H. Fowler, Proceedings of the Royal Society of London. Series A, Containing Papers of a Mathematical and Physical Character **117** (778), 610-624 (1928).

97. M. H. Levitt, Wiley, 710 (2001).

98. A. I. Bykov, M. I. Dolotenko, N. P. Kolokolchikov, V. D. Selemir and O. M. Tatsenko, Physica B: Condensed Matter **294-295**, 574-578 (2001).

99. S. Ahn, S. Lee and W. S. Warren, Molecular Physics **95** (5), 769-785 (1998).

100. W. S. Warren and S. Ahn, Journal of Chemical Physics **108** (4), 1313-1325 (1998).

101. M. A. Mccoy and W. S. Warren, Journal of Chemical Physics **93** (1), 858-860 (1990).

102. W. S. Warren, W. Richter, A. H. Andreotti and B. T. Farmer, Science **262** (5142), 2005-2009 (1993).

103. S. Lee, W. Richter, S. Vathyam and W. S. Warren, Journal of Chemical Physics **105** (3), 874-900 (1996).

104. V. Acosta, M. P. Ledbetter, S. M. Rochester, D. Budker, D. F. J. Kimball, D. C. Hovde, W. Gawlik, S. Pustelny, J. Zachorowski and V. V. Yashchuk, Physical Review A **73** (5) (2006).

105. C. Bengs and M. H. Levitt, Journal of Magnetic Resonance **310**, 106645 (2020).

106. I. Kuprov, J Magn Reson **209** (1), 31-38 (2011).

107. J. S. Waugh, Hammel, P. C., Kuhns, P. L., Gonen, O., Bull. Mag. Res. **11**, 97-102 (1989).

108. J. I. Kaplan, The Journal of Chemical Physics **29** (2), 462-462 (1958).

109. J. Kaplan, The Journal of Chemical Physics **28** (2), 278-282 (1958).

110. S. Alexander, The Journal of Chemical Physics **37** (5), 967-974 (1962).

111. S. Alexander, The Journal of Chemical Physics **37** (5), 974-980 (1962).

112. H. M. McConnell, **28** (3), 430-431 (1958).

113. R. Kubo, Nuovo Cimento **6**, 1063 (1957).

114. R. A. Sack, Molecular Physics **1** (2), 163-167 (1958).

115. F. J. Dyson, Physical Review **75** (3), 486-502 (1949).

116. J. R. Lindale, S. L. Eriksson, C. P. N. Tanner and W. S. Warren, Science Advances **6** (32), eabb6874 (2020).

117. A. N. Pravdivtsev, I. V. Skovpin, A. I. Svyatova, N. V. Chukanov, L. M. Kovtunova, V. I. Bukhtiyarov, E. Y. Chekmenev, K. V. Kovtunov, I. V. Koptyug and J.-B. Hövener, The Journal of Physical Chemistry A **122** (46), 9107-9114 (2018).

118. P. M. Richardson, A. J. Parrott, O. Semenova, A. Nordon, S. B. Duckett and M. E. Halse, Analyst **143** (14), 3442-3450 (2018).

119. K. V. Kovtunov, A. Svyatova, I. Skovpin, N. Chukanov, I. Koptyug, E. Chekmenev, J. Hoevener and A. Pravdivtsev, Chemistry–A European Journal (2019).

120. S. Knecht, A. S. Kiryutin, A. V. Yurkovskaya and K. L. Ivanov, Molecular Physics, 1-10 (2018).

121. K. V. Kovtunov, L. M. Kovtunova, M. E. Gemeinhardt, A. V. Bukhtiyarov, J. Gesiorski, V. I. Bukhtiyarov, E. Y. Chekmenev, I. V. Koptyug and B. M. Goodson, Angewandte Chemie International Edition **56** (35), 10433-10437 (2017).

122. R. V. Shchepin, D. A. Barskiy, A. M. Coffey, T. Theis, F. Shi, W. S. Warren, B. M. Goodson and E. Y. Chekmenev, ACS Sens. (2016).

123. T. Theis, G. X. Ortiz , A. W. J. Logan, K. E. Claytor, Y. Feng, W. P. Huhn, V. Blum, S. J. Malcolmson, E. Y. Chekmenev, Q. Wang and W. S. Warren, Sci. Adv. **2** (3), e1501438 (2016).

124. A. N. Pravdivtsev, A. V. Yurkovskaya, H. Zimmermann, H.-M. Vieth and K. L. Ivanov, RSC Adv. **5** (78), 63615-63623 (2015).

125. T. Theis, N. M. Ariyasingha, R. V. Shchepin, J. R. Lindale, W. S. Warren and E. Y. Chekmenev, The journal of physical chemistry letters **9** (20), 6136-6142 (2018).

126. G. X. O. J. Thomas Theis, Angus W.J. Logan, Kevin E. Claytor, Yesu Feng, William P. Huhn, Volker Blum, Steven J. Malcolmson, Eduard Y. Chekmenev, Qiu Wang, Warren S. Warren, Science Advances **to be published** (2016).

127. R. V. Shchepin, B. M. Goodson, T. Theis, W. S. Warren and E. Y. Chekmenev, ChemPhysChem **18** (15), 1961-1965 (2017).

128. A. N. Pravdivtsev, A. V. Yurkovskaya, H.-M. Vieth and K. L. Ivanov, J. Phys. Chem. B **119** (43), 13619-13629 (2015).

129. J. R. Lindale, C. P. N. Tanner, S. L. Eriksson and W. S. Warren, Journal of Magnetic Resonance **307**, 106577 (2019).

130. J. R. Lindale, Eriksson, S. L., Warren, W. S., arXiv:2107.13040 [physics.chem-ph] (2021).

131. T. Theis, Y. Feng, T. Wu and W. S. Warren, J. Chem. Phys. **140** (1) (2014).

132. A. N. Pravdivtsev, A. V. Yurkovskaya, H. Zimmermann, H.-M. Vieth and K. L. Ivanov, Chem. Phys. Lett. **661**, 77-82 (2016).

133. S. Knecht, A. S. Kiryutin, A. V. Yurkovskaya and K. L. Ivanov, Journal of Magnetic Resonance **287**, 10-14 (2018).

134. D. M. Wilson, R. E. Hurd, K. Keshari, M. Van Criekinge, A. P. Chen, S. J. Nelson, D. B. Vigneron and J. Kurhanewicz, Proceedings of the National Academy of Sciences of the United States of America **106** (14), 5503-5507 (2009).

135. J. K. Nicholson and J. C. Lindon, Nature **455** (7216), 1054-1056 (2008).

136. N. Shanaiah, M. A. Desilva, G. A. N. Gowda, M. A. Raftery, B. E. Hainline and D. Raftery, Proceedings of the National Academy of Sciences of the United States of America **104** (28), 11540-11544 (2007).

137. J. K. Nicholson and I. D. Wilson, Nature Reviews Drug Discovery **2** (8), 668-676 (2003).

138. F. Loaiza, Lim, K-T., Warren, W. S., Health Care Instrumentation (189-194) (1986).

139. I. Rechenberg, presented at the Simulationsmethoden in der Medizin und Biologie, Berlin, Heidelberg, 1978 (unpublished).

140. C. P. N. Tanner, J. R. Lindale, S. L. Eriksson, Z. Zhou, J. F. P. Colell, T. Theis and W. S. Warren, **151** (4), 044201 (2019).

141. B. A. Rodin, J. Eills, R. Picazo-Frutos, K. F. Sheberstov, D. Budker and K. L. Ivanov, Physical Chemistry Chemical Physics **23** (12), 7125-7134 (2021).

142. J. Eills, J. W. Blanchard, T. Wu, C. Bengs, J. Hollenbach, D. Budker and M. H. Levitt, The Journal of Chemical Physics **150** (17), 174202 (2019).

143. M. Emondts, M. P. Ledbetter, S. Pustelny, T. Theis, B. Patton, J. W. Blanchard, M. C. Butler, D. Budker and A. Pines, Phys Rev Lett **112** (7), 077601 (2014).

144. X. Li, et. al., (2021).

145. S. L. Eriksson, Lindale, Jacob. R., Li, Xiaoqing, Warren, W. S., arXiv:2107.04687 [physics.chem-ph] (2021).

146. A. M. Stokes, J. W. Wilson and W. S. Warren, Journal of Magnetic Resonance **223**, 31-40 (2012).

147. R. T. Branca, E. R. Jenista and W. S. Warren, Journal of Magnetic Resonance **209** (2), 347-351 (2011).

148. E. R. Jenista, G. Galiana, R. T. Branca, P. S. Yarmolenko, A. M. Stokes, M. W. Dewhirst and W. S. Warren, Journal of Magnetic Resonance **204** (2), 208-218 (2010).

149. E. R. Jenista, R. T. Branca and W. S. Warren, Journal of Magnetic Resonance **196** (1), 74-77 (2009).

150. R. T. Branca, G. Gallana and W. S. Warren, Journal of Magnetic Resonance **187** (1), 38-43 (2007).

151. W. Richter, M. Richter, W. S. Warren, H. Merkle, P. Andersen, G. Adriany and K. Ugurbil, Magnetic Resonance Imaging **18** (5), 489-494 (2000).

152. D. J. Schaefer, D. E. Favre, M. Wilhelm, S. J. Weigel and B. F. Chmelka, Journal of the American Chemical Society **119** (39), 9252-9267 (1997).

153. P. Selter, M. B. Schmithorst and B. F. Chmelka, Adsorption **27** (5), 857-874 (2021).

154. P. D. Lauren, A. N. Rebecca and T. Andrei, Opt. Lett. **32** (20), 2966--2968 (2007).

155. Y. S. Kim and R. M. Hochstrasser, Proceedings of the National Academy of Sciences of the United States of America **102** (32), 11185 (2005).

156. M. K. Petti, J. P. Lomont, M. Maj and M. T. Zanni, The Journal of Physical Chemistry B **122** (6), 1771-1780 (2018).

157. A. Kossakowski, Reports on Mathematical Physics **3** (4), 247-274 (1972).

158. V. Gorini, A. Kossakowski and E. C. G. Sudarshan, Journal of Mathematical Physics **17** (5), 821-825 (1976).

159. G. Lindblad, Communications in Mathematical Physics **48** (2), 119-130 (1976).

160. L. ISSERLIS, Biometrika **12** (1-2), 134-139 (1918).

161. P. M. Morse, Physical Review **34** (1), 57-64 (1929).

162. P. F. Tian, D. Keusters, Y. Suzaki and W. S. Warren, Science **300** (5625), 1553-1555 (2003).

163. H.-S. Tan and W. S. Warren, Opt. Express **11** (9), 1021-1028 (2003).

164. T. M. Zagar, J. Oleson, Z. Vujaskovic, M. W. Dewhirst, O. I. Craciunescu, K. L. Blackwell, L. Prosnitz, E. Jones and R. M. http://informahealthcare.com/doi/abs/10.3109/02656736.2010.487194, International Journal of Hyperthermia **26** (7), 612-617 (2010).